DEVELOPMENT OF A COMPACT COLD-ATOM ATOMIC CLOCK BASED ON COHERENT POPULATION TRAPPING

by

ERIC M. BLANSHAN

B.A., University of Chicago, 2008

M.S., University of Colorado, 2011

A thesis submitted to the

Faculty of the Graduate School of the

University of Colorado in partial fulfillment

of the requirements for the degree of

Doctor of Philosophy

Department of Physics

2014

This thesis entitled:
Development of a Compact Cold-Atom Atomic Clock Based on Coherent Population Trapping
written by Eric M. Blanshan
has been approved for the Department of Physics

_____
Prof. Andreas Becker

_____
Dr. John Kitching

Date _____

The final copy of this thesis has been examined by the signatories, and we find that both the content and the form meet acceptable presentation standards of scholarly work in the above mentioned discipline.

Blanshan, Eric M. (Ph.D., Physics)

Development of a Compact Cold-Atom Atomic Clock Based on Coherent Population Trapping

Thesis directed by Dr. John Kitching

Field-grade atomic clocks capable of primary standard performance in compact physics packages would be of significant value in a variety of applications ranging from network synchronization and secure communications to GPS hold-over and inertial navigation. A cold-atom coherent population trapping (CACPT) clock featuring laser-cooled ^{87}Rb atoms and pulsed Ramsey interrogation is a strong candidate for this technology if the principal frequency shifts can be controlled and the performance degradation associated with miniaturization can be overcome. In this thesis, research focused on the development of this type of compact atomic clock is presented. To address the low atom numbers obtained in small cold-atom sources, experiments were performed in which an atomic beam was decelerated with bichromatic stimulated laser forces and loaded into a mm-scale magneto-optical trap, increasing the atom number by a factor of $12.5\times$. A CACPT clock using the high-contrast lin||lin optical interrogation technique was developed and achieved a stability of 7×10^{-13} after one hour of integration. Doppler shifts in the clock are explained using a simple kinematic model and canceled by interrogating the atoms with a counter-propagating CPT configuration. Finally, a thorough characterization of the AC-stark effect in lin||lin CPT was performed. Observed shifts are explained in terms of contributions from coherent CPT-generating couplings and population transfer effects caused by optical pumping from incoherent light. Measurements are compared with existing and new theoretical treatments, and a laser configuration is identified that reduces clock drift from light shifts to $< 1 \times 10^{-14}$ for the current system.

Dedication

To my parents.

agreeing to be my titular adivsor at the university.

My friends in Boulder have been hugely important in providing a life outside of lab that made graduate school much more manageable. Between softball, camping, skiing, grilling, brewing, coffee trips from NIST, or movie nights, we have had a lot of good times, and I thank them for that. I also want to acknowledge my Iowa and Chicago friends of over a decade now. I always look forward to our yearly trips. In particular, I want to thank Dana. The support you've shown during the last two and a half years is amazing. I'm excited to see where this road takes us.

Finally, I want to thank my family as I would never have accomplished this without you. Through the unconditional love and support during the good times and the hard times, you've always been there when I needed it. So to my parents, Kevin and Dee, sister, Kelsey, and all of my grandparents, I can not thank you enough.

Disclaimer

The views, opinions, and/or findings contained in this article/presentation are those of the author(s)/ presenter(s) and should not be interpreted as representing the official views or policies of the Department of Defense or the U.S. Government. Approved for Public Release, Distribution Unlimited.

Contents

List of Tables

<h1 style="text-align: center">List of Figures</h1>

CHAPTER 1

INTRODUCTION

Measuring the passage of time has been a central interest of civilizations for thousands of years. Techniques have evolved over the centuries from simple sundials based on the Earth's rotation through mechanical devices featuring springs or pendulums to modern, state of the art optical lattice clocks that would neither gain nor lose a second in five billion years [1, 2]. This progression of clock technology has been ardently driven by the desire to perform fundamental physics experiments and realize advanced applications requiring precise timing information. The impressive performance of modern frequency standards has enabled careful tests of general relativity [3], searches for variation in the fine structure constant [4], and introduced discussion of redefining the SI second in terms of optical clock transitions [5, 6]. While the future of atomic clocks in fundamental experiments is bright [7], in the applications domain, the steady reduction of the size and power required by modern frequency references has caused a remarkable expansion of their use in everyday life. State of the art technology featured in telecommunication and computer networks, global navigation satellites, and defense systems all rely on precise timing information, and the development of compact, high performance, field-grade atomic clocks will improve the portability of current systems and spur innovative new applications.

The work performed for this thesis falls into the applied category, focusing on the development of an atomic clock with the capability for primary standard performance in a robust and highly miniaturized physics package. A series of proof of principle experiments were performed with table-top systems to demonstrate that such a clock is realizable, and that frequency biases would not preclude 10^{-13} level frequency stability. The remainder of this chapter will provide the context for these experiments, including a summary of frequency standard principles, an overview of compact atomic clocks, an introduction to the compact clock program at NIST within which my Ph.D. work was performed, and an overview of the goals and achievements presented in this thesis.
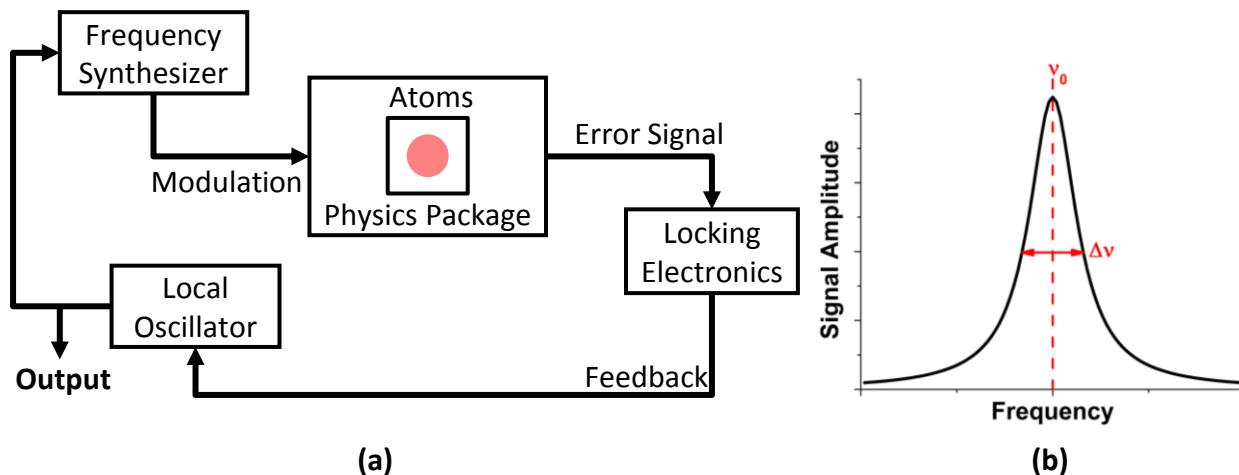
Figure 1.1: (a) Generic block diagram for an atomic clock. Modulation can be applied to the atoms in various ways, including via a microwave cavity or through the injection current of a laser diode. (b) Example atomic line; the resonance quality factor for any clock is the ratio of the central frequency to the linewidth: $Q \equiv \nu_0/\Delta\nu$.

1.1 Fundamentals of Atomic Frequency Standards

During the mid 20$^{\text{th}}$ century, the development of frequency standards based on atomic transitions led to the definition of the SI second as the duration of 9,192,631,770 periods of oscillation between the ground state hyperfine levels of ^{133}Cs [8]. The ability to define the unit of time in terms of a natural constant that can be independently measured in labs around the world was a breakthrough for the metrology community and was only possible due to the ever-improving accuracy and stability of atomic clocks. The intrinsic stability of an atomic clock arises from electronically locking the frequency of a local oscillator (LO), typically a temperature-compensated (TCXO) or ovenized quartz crystal oscillator (OCXO), to the resonance frequency of an atomic transition. Through this process, environmental factors that directly affect the crystal resonance are bypassed as the LO is driven at a frequency determined by feedback from the atomic system of choice. While biases affecting the crystal are avoided, frequency shifts of the atomic transition become critically important, and the latter third of this thesis will address this issue in our cold-atom coherent population trapping (CACPT) atomic clock.

Every atomic clock features some variations of a few basic components, including a local oscillator, frequency synthesizer, physics package, and control electronics (Fig. 1.1 (a)). For microwave

atomic clocks, the synthesizer generates microwaves near the resonance frequency for driving transitions between the ground state hyperfine levels of Rb ($F = 1, 2$) or Cs ($F = 3, 4$). The microwave signal can be applied to the atoms through different techniques, including direct excitation in cavity-based clocks or through modulation of an interrogation laser for CPT clocks. Depending on the clock configuration, atoms respond to the applied microwave radiation with a Lorentzian absorption or transmission line as a function of modulation frequency (Fig. 1.1 (b)), from which a dispersive error signal can be derived. The error signal is fed into a loop filter that provides feedback to the voltage controlled crystal oscillator acting as the LO, locking the output frequency to the atomic resonance.

Frequency corrections applied to the LO provide information on the fractional frequency stability of the clock. This is generally the figure of merit for the performance of a frequency standard and quantifies the variation in the measured frequency over an averaging period. This information is framed in terms of the Allan deviation [9], a two-sample deviation providing a statistical interpretation of frequency fluctuations based on the difference between subsequent frequency measurements [10]: $\sigma_y(\tau) = \sqrt{\frac{1}{2}\langle(\overline{y}_2 - \overline{y}_1)^2\rangle}$. In this expression, $\overline{y}_i$ is a series of subsequent discrete clock frequency measurements averaged over an integration time τ: $\overline{y}_i = \frac{1}{\tau}\int_{t_i}^{t_i+\tau} y(t)dt$. A plot of the Allan deviation vs. averaging time (τ) illustrates the frequency stability of the clock at different integration time intervals and can be used to identify the types of noise mechanisms present in the system. Allan deviations characterizing the CACPT clock will be presented in later chapters.

The statistical expression for the Allan deviation above can be mapped to experimentally relevant physical processes in a manner that is useful for determining the fundamental performance limits for an atomic clock [11]:

$$\sigma_y(\tau) = \frac{1}{\pi Q}\sqrt{\frac{T_c}{\tau}}\left(\frac{1}{N_{at}} + \frac{1}{N_{at}n_{ph}} + \frac{2\sigma_{\delta N}^2}{N_{at}^2} + \gamma\right)^{\frac{1}{2}}. \tag{1.1}$$

In this expression, τ is the measurement time, T_c is the clock cycle time, $Q \equiv \nu_0/\Delta\nu$ is the resonance quality factor, N_{at} is the atom number, n_{ph} is the number of detected photons per atom, $\sigma_{\delta N}^2$ is the uncorrelated atom number fluctuation in the detection system, and γ is the contribution from frequency noise in the local oscillator operating in a pulsed mode [12, 13]. The first term corresponds to quantum projection noise, the second to photon shot-noise in the detection system,

and the third to detection noise related to atom number fluctuations. In the CACPT clock discussed in this thesis, the dominant contribution to the Allan deviation is noise from the laser system and local oscillator; however, for a given cycle time and atom number, the quantum projection noise represents the fundamental limit for clock stability imposed by the in-deterministic nature of the quantum system [14]:

$$\sigma_y(\tau) = \frac{1}{\pi Q}\sqrt{\frac{T_c}{\tau}}\sqrt{\frac{1}{N_{at}}}. \tag{1.2}$$

If technical noise and unstable frequency shifts can be suppressed, then Eq. 1.2 provides the best-case stability for an atomic clock without using squeezing techniques [15].

Accordingly, the choice of atomic species and interrogation configuration for an atomic clock is particularly important as the quality factor and available atom number significantly impacts $\sigma_y(\tau)$. The interrogated atom number varies widely depending on the type of atomic frequency reference, ranging from a single ion in quantum logic clocks [16] to 10^9 atoms in some laser-cooled atomic fountains [17]. Due to the scaling of radiative forces with device size, careful attention to the atom number is critical for compact atomic clocks featuring laser-cooled atoms. Maximizing the trapped atom number to suppress the projection noise stability limit was the first project of my Ph.D. and is discussed in the first third of this thesis. The quality factor of the clock resonance provides a second method for lowering the fundamental stability limit. Due to the Fourier relationship between the excited state lifetime and the natural linewidth of a transition ($\Delta\nu \propto 1/\tau$), the best clock systems are those that drive high energy transitions to very long-lived states. Strontium optical lattice clocks function in this regime and achieve Q-factors exceeding 10^{14} by operating at optical transition frequencies ($\nu_0 \sim 10^{14}$ Hz) on a doubly-forbidden $^1S_0 - ^3P_0$ transition with a mHz scale natural linewidth [2, 18]. For microwave atomic clocks, Q-factors are generally $\sim 10^{10}$ due to the hyperfine ground state transition frequencies in alkali atoms falling below 10 GHz. Despite the lower quality factor, state of the art cryogenic Cs fountains are able to reach a long-term stability of 4.4×10^{-16} through superior control of environmental and technical effects [19]. However, the excellent performance of the cryogenic fountain may be approaching the achievable improvement limit for microwave frequency standards due to fundamental issues such as gravitational restrictions on the Ramsey interaction time for ground-based clocks and cold-atom collision effects [20].

A summary of current atomic clock stabilities published within the last two years is presented in

4

Table 1.1, including a commercially available microwave standard, a laboratory microwave standard, and two optical lattice clocks. The high pace of improvement in optical frequency standards is

Table 1.1: Recent Frequency Standard Stability Summary

Frequency Standard	Fractional Instability	Integration Time (s)	Reference
Cesium Beam Clock 5071A	1.0×10^{-14}	4.0×10^5	[21]
Cesium Atomic Fountain	4.4×10^{-16}	3.5×10^4	[19]
Strontium Optical Lattice Clock	3.0×10^{-18}	1.0×10^4	[2]
Ytterbium Optical Lattice Clock	1.6×10^{-18}	2.5×10^4	[1]

likely to continue in the next several years, and a new proposal based on nuclear magnetic dipole transitions in $^{229}\text{Th}^+$ offers the tantalizing possibility of a nuclear clock with a frequency stability of 1×10^{-19} [22]. While the performance of these advanced standards is outstanding, they are currently prohibitively expensive, complicated, and difficult to operate for use in most applications. With continued improvements in time transfer technology and increased operation time, optical lattice clocks will likely be able to participate in the time scale in the future, but for the moment, they remain laboratory systems only. For the numerous applications that could benefit from improved frequency references, microwave atomic clocks remain the best option and the focus of very active research and commercial development efforts.

1.2   Miniature Atomic Clocks

One of the earliest efforts to reduce the size, weight, and power (SWAP) requirements of microwave atomic clocks was launched in 1992 by the Westinghouse Science and Technology Center, which proposed and built a compact laser-pumped Cesium atomic clock [23, 24]. The ultimate goal of these early projects was to simplify the complicated techniques and equipment necessary to stabilize atomic frequency standards such that a battery powered, portable atomic clock with a stability exceeding that of quartz oscillators was achievable. Such a clock would also need a cost point on the order of $1000-$2000 to make the added expense for the improved stability over low-cost temperature-compensated quartz crystal oscillators attractive. The realization of an inexpensive device operating on ~150 mW in a ~ 25 cm^3 package would open up a multitude of defense and commercial applications.

An improved frequency reference generating reliable intrinsic timing knowledge in hand-held

GPS receivers would reduce the search time necessary to obtain high-correlation code agreement between a receiver and satellite, enabling rapid acquisition of the P(y) code without first locking to the jamming-susceptible course/acquisition (C/A) signal [25, 26]. It would also eliminate the need to synchronize receiver and satellite time variables, reducing the number of unknowns in the position algorithm such that a 3D position fix is achievable with signal reception from only three satellites [27]. Each of these advantages would improve performance in hostile and signal dense environments as well as in GPS-denied areas such as indoors or urban combat zones, where weak signals can significantly impede acquisition.

With the rise of the information age, ever-increasing data transfer rates and the sheer quantity of data flowing around the globe have made stable and accurate timing systems a critical component for communications and infrastructure network synchronization. Code-division multiple access (CDMA) cellular telephone networks, for example, require a common time between base stations accurate to < 3 μs as base stations distinguish themselves from one another by unique time offsets at the beginning of each code transmission [28]. Drifts in base station time approaching 10 μs are sufficient to cause handovers between adjacent stations to fail, triggering a coverage loss in the area. Constraints on the power grid have required a transition to the "Smart Grid", in which usage over large sectors is monitored in real-time. This is accomplished with phasor measurement units (PMU) that record a series of voltages at specific times at multiple points throughout the grid [29]. This information is analyzed to efficiently allocate power and avoid blackouts caused by system strain. The time stamping in PMUs requires an accuracy of <27 μs to ensure correct sequencing of voltage measurements throughout the grid [30]. For both of these examples, the accuracy requirements are met by GPS timing signals; however, in the case of either intentional or unintentional disruption of GPS access, power grid and telecommunications stations must rely on the hold over capability of local oscillators to maintain synchronization. Cost requirements in industry tend to preclude the use of high-end commercial frequency standards, however low cost atomic clocks that still exceed TCXO performance could be widely used to improve the hold over capability of infrastructure base stations [31]. These and other interesting applications, including computer networks for high frequency trading, underwater seismic exploration, autonomous vehicle systems, electronic warfare systems, and high-bandwidth communication systems [32, 33], spurred new efforts in the early 2000s to realize a low SWAP atomic clock.

1.2.1 Chip Scale Atomic Clock Program

The focus within the metrology community on the development of compact, robust atomic clocks was organized and driven by the launch of the Chip Scale Atomic Clock (CSAC) program by the Defense Advanced Research Projects Agency (DARPA) Micro-Technology Office (MTO) in 2001. The ambitious program lived up to the mantra of "DARPA hard" with targets of < 1 cm^3 package volume, < 30 mW power usage, and a stability of $< 1 \times 10^{-11}$ at one hour, goals that required significant innovation to achieve [32]. The path forward required integrating microelectromechanical systems (MEMS) techniques with coherent population trapping (CPT) to produce chip-scale devices featuring all-optical interrogation of a microwave frequency clock resonance [34, 35]. While compact CPT atomic clocks had been previously proposed [36], a device was not feasible until vertical-cavity surface-emitting lasers (VCSELs) first became available at the 852 nm wavelength of the Cesium D$_2$ line [37, 38]. A CSAC prototype based on these concepts was developed at NIST (Fig. 1.2 (a)) and by 2004, exhibited a fractional frequency stability of $\sigma_y(1 \text{ s}) = 2.5 \times 10^{-10}$ and consumed just 75 mW of power in a 9.5 mm^3 physics package [39]. The device featured a custom vapor cell designed and manufactured at NIST using MEMS techniques and anodic bonding [40]. The cell contained both Cesium and a mixture of high pressure buffer gas to generate long interrogation times by reducing decoherence from wall-collisions.

The CSAC program proved to be a very nice demonstration of a complete DARPA effort, taking an idea from an initial concept all the way to a commercial product. Working in parallel to NIST and other program competitors, Microsemi Corporation (formerly known as Symmetricom) in a collaboration with Draper Laboratory, produced a prototype CSAC featuring a similar vertical stack of chip-scale components as in the NIST design. Working through the four program phases from 2001-2011, Microsemi successfully engineered the prototype into a reliable, commercially available chip-scale atomic clock with an accuracy of 5×10^{-11} (calibrated at shipment) and stability of $\sigma_y(1 \text{ hr}) = 5 \times 10^{-12}$ that operates on < 120 mW of power in a 35 g, < 17 cm^3 package (Fig. 1.2 (b)) [41]. This clock exceeds the stability of TCXOs (OCXOs) by nearly four (two) orders of magnitude on long time scales and can be purchased for $\sim \$1500$, opening the door to many of the applications discussed above.

While the short term performance of the CSAC is sufficient for many applications, drifts due to
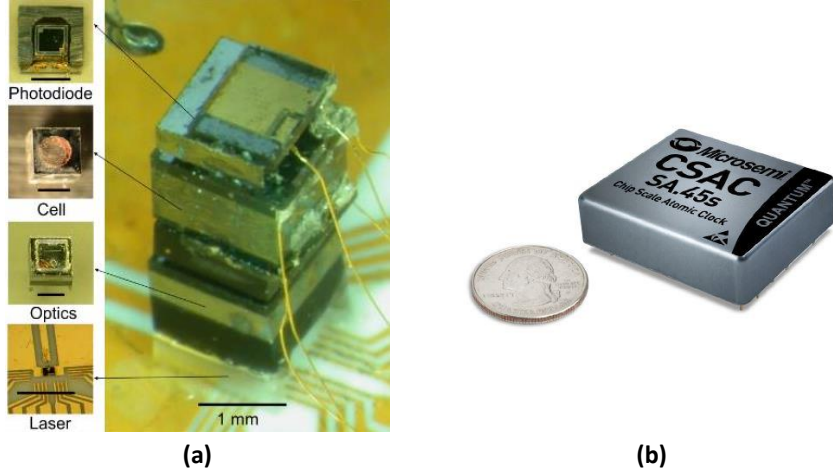
Figure 1.2: (a) NIST CSAC prototype consisting of a VCSEL, optics block, vapor cell, and photodiode in a 4.2 mm tall stack. Solid black lines correspond to 1 mm lengths [39]. (b) Commercially available 17 cm^3 CSAC produced by Microsemi Corporation. Requires < 120 mW of power and produces 10 MHz and 1 PPS output with $\sigma_y(1\text{ s}) = 2.5 \times 10^{-10}$ [41]. Photograph from Microsemi product website.

the high pressure buffer gas used to generate long coherence times and reduce Doppler effects limit the long term fractional frequency stability. The instability emerges from temperature-dependent pressure shifts of the clock frequency caused by collisions between alkali atoms and the buffer gas [42]. Mixtures of inert gases such as nitrogen and argon typically compose the buffer gas as the sign and magnitude of the linear and quadratic temperature coefficients is species dependent. Proper selection of the mixture ratio can reduce the temperature dependence of the buffer gas shift or the magnitude of the shift itself. Generally, the mixture is chosen to limit stability-degrading changes in resonance frequency from temperature fluctuations, resulting in potentially large, but stable residual shifts that primarily limit the accuracy of the clock [43]. While improvements in production techniques have reduced these effects [44], the long term stability is still limited by drift from buffer gas and AC-stark shifts at the level of 3×10^{-11}/month [45]. This precludes the use of CSACs in demanding applications that require an accuracy $\sim 1 \times 10^{-11}$ and is one of the principal reasons why vapor cell clocks are secondary frequency references that require periodic calibration.

1.2.2 Integrated Micro-Primary Atomic Clock Technology Program

To push compact atomic clock technology toward primary standard performance, DARPA launched the Integrated Micro-Primary Atomic Clock Technology (IMPACT) program in 2008.

Table 1.2: CSAC and IMPACT Program Goals

Device Metric	CSAC	IMPACT
Power	30 mW	50 mW
Volume	1 cm^3	< 5 cm^3
Stability @ $\tau = 1$ hr	1×10^{-11}	$1 \times 10^{-13\dagger}$

[†]Calculated from formal time loss metrics in Broad Agency Announcement [46]

The ultimate goal of the program was to build upon the knowledge acquired during the successful CSAC effort and develop a compact atomic clock that could rival a state of the art commercial Cesium beam clock. As shown in the comparison of the two programs given in Table 1.2, IMPACT sought to improve the fractional frequency stability by two orders of magnitude over the CSAC with only 50% more power and a 5 cm^3 package. Fig. 1.3 illustrates where the final phase performance goals of the IMPACT program fell within the big-picture framework at DARPA as well as relative to other existing clocks. As shown, achieving such a compact primary standard would require a three orders of magnitude reduction in size and power over a 5071A beam clock, while actually improving the fractional frequency stability at one hour over the standard performance model [21].

For a successful program, a fundamental change in the atomic physics approach was necessary as a vapor cell clock was very unlikely to meet the ambitious performance specifications for IMPACT. Various techniques were adopted, including using laser cooled atoms [47–49], trapped ions [50], and Kerr optical frequency combs in microelectromechanical systems (MEMS) resonators [51]. The clock research and development reported in this thesis was performed at NIST as a seedling participant in the IMPACT program. The laser-cooling approach was chosen for the atom source, while the all-optical interrogation scheme implemented in the CSAC was maintained. This combination of techniques ensured long atom-field interaction times and microwave-free interrogation while removing the buffer gas shifts that render vapor cell clocks fundamentally inaccurate. An introduction to the IMPACT research performed at NIST over the last six years and an overview of the accompanying thesis chapters is presented in the next section.

1.3 IMPACT at NIST: Thesis Overview

As part of the IMPACT efforts at NIST, my Ph.D. work encompassed two different projects related to the realization of a compact clock featuring laser-cooled atoms in a magneto-optical
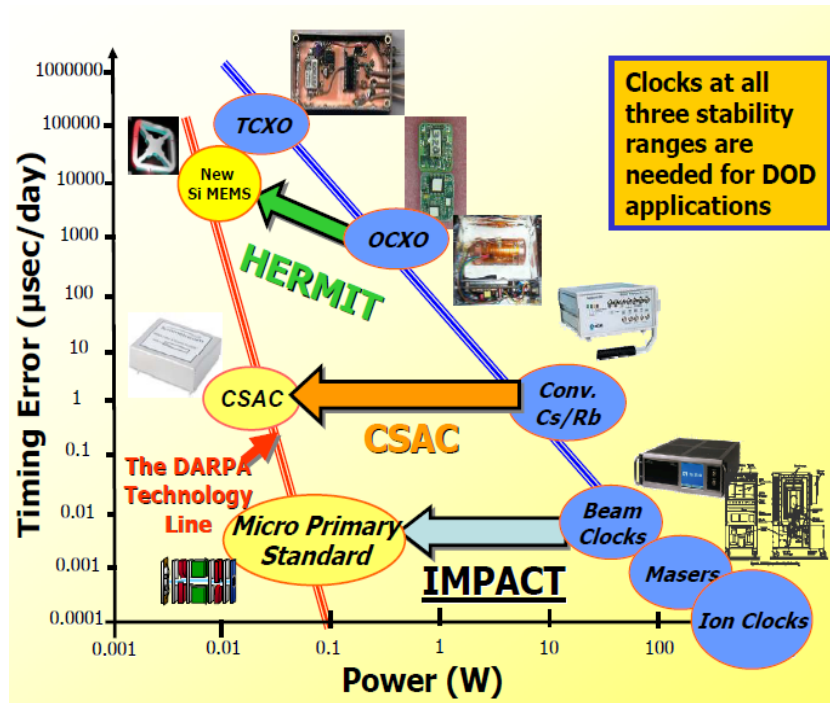
(a)
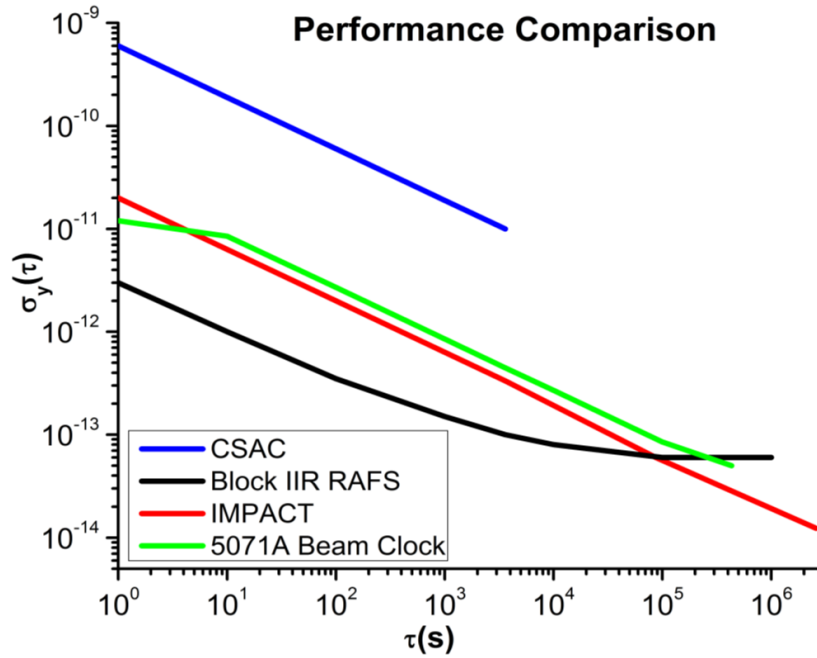
(b)

Figure 1.3: (a) Summary of DARPA oscillator and clock programs and goals for technology minia-turization. Figure courtesy of Amit Lal, former DARPA-MTO. Approved for Public Release, Distribution Unlimited. (b) A comparison of fractional frequency stabilities between a commercial Cs beam clock, the GPS Rb atomic frequency standards, CSACs, and the IMPACT program goal.

10

trap and coherent population trapping interrogation. The first experiment focused on developing an atom source for chip-scale cold-atom devices in which the trapped atom number exceeded the standard limit for traditional loading techniques. The second project entailed the realization of a second-generation CACPT clock and the characterization and mitigation of the two main frequency biases in this type of standard. These experiments will be introduced and motivated in this section.

1.3.1 Bichromatic Forces and Compact Magneto Optical Traps

Since first demonstrated in the late 1980s [52], the magneto-optical trap (MOT) has been a centerpiece of neutral atom laboratories, providing a cold-atom source for experiments ranging from Bose-Eisenstein condensates [53] to ultra-cold molecules [54] and quantum information [55]. A MOT operates by creating a restoring force through radiative pressure and the Zeeman effect. Three pairs of mutually orthogonal counter-propagating laser beams are aligned to intersect at the center of the quadrupole magnetic field generated by a single set of anti-Helmholtz coils. Each of the laser beams is red-detuned by $\sim 1.5\gamma$ from the unperturbed atomic resonance, where γ is the natural linewidth, and the polarization is circular and opposite between each counter-propagating pair. When the polarizations are set correctly relative to the quantization axis of the quadrupole field, the Zeeman shift is such that for any displacement away from the center of the field, there is an imbalance in the radiation pressure caused by the transition selection rules that results in a net force toward the center of the trap. This position dependence causes atoms that enter the laser field to be slowed and guided to the center by spontaneous optical forces. The relative simplicity of trapping atoms in this manner, coupled with the energy dissipation that allows temperatures of $\sim 100\mu$K to be achieved from a thermal vapor, has lead to very wide spread use of MOTs. More detailed explanations of MOT physics can be found in the literature [56–58].

While the atom number captured in a MOT is always a signal to noise ratio (S/N) concern for tabletop fundamental science experiments, sufficient numbers are easily achieved by using large trapping beams. In the growing field of atom-based sensors, this luxury is not available, and careful attention must be paid to the expected and actual number of trapped atoms. To calculate the steady-state atom number (N_{ss}), the rate of atoms entering the trap volume with velocities below the maximum that can be trapped (v_{cap}) is balanced with the loss rate from different mechanisms, primarily collisions with the background vapor. Solving the rate equation for a 3D vapor-loaded

MOT, one obtains the following steady state atom number [59]:

$$N_{ss} \simeq \frac{V^{2/3}}{\sigma\sqrt{6}} \left(\frac{v_{cap}}{\bar{v}}\right)^4, \tag{1.3}$$

where V is volume of the trap formed by the intersecting laser beams, σ is the collisional loss cross-section, and $\bar{v}$ is the mean velocity of atoms in the background vapor. For a MOT loaded from an atomic beam rather than a vapor, the expression is changed slightly to account for the difference in loading area:

$$N_{ss} \simeq \frac{A_b}{\sigma\sqrt{\pi}} \left(\frac{v_{cap}}{\bar{v}}\right)^4, \tag{1.4}$$

where A_b is the cross-sectional area of the atomic beam ($\propto d_b^2$, where d_b is the atomic beam diameter) and $\bar{v}$ is the mean velocity in the atomic beam. This expression is valid when both the diameter of the atomic beam is smaller than the laser beam diameter and the primary loss mechanism is collisions with the incident atomic beam.

Many previous experiments have observed the strong dependence of N_{ss} on the diameter of the trapping beams (d) [59–61]. This arises from the combined effects of the trap size (proportional to d^2) and the capture velocity, which has a diameter dependence determined by the radiative force in the MOT. A simple model of the restoring force within the trap assumes a radiative force that is independent of the atomic velocity: $F = \hbar k R_{sc}$, where k is the photon wave number and R_{sc} is the photon scattering rate. With this force, simple kinematics show that the capture velocity is $v_{cap} = \sqrt{2dR_{sc}\hbar k/m}$, where m is the mass of the atom. From Eq. 1.4, this results in a steady state atom number proportional to d^4. This scaling, or more accurately $N_{ss} \propto d^{3.6}$ from a more thorough treatment [60, 61], has been observed experimentally for trapping volumes exceeding 1 cm^3. For smaller MOTs with trapping beam diameters of a few mm, recent experimental work using pyramidal traps and traditional 3D MOTs have observed a stronger $N_{ss} \propto d^6$ dependence [62, 63]. This strong scaling of the atom number with beam diameter arises from a damping radiative force proportional to velocity: $F = \alpha v$, where α is the damping constant and v is the atomic velocity. This is the same drag force slowing low velocity atoms ($v < \delta/k$) in an optical molasses and results in a capture velocity proportional to the beam diameter, causing $N_{ss} \propto d^6$ for $d <$3 mm [63].

The rapid scaling of the trapped atom number with laser beam diameter has particularly serious ramifications for cm^3-scale atomic devices, where the trapping volumes are on the order of tens of

cubic millimeters. To achieve the IMPACT program goals while leaving some room for instability from other noise sources, a quantum projection noise limited performance of $1 \times 10^{-12}/\sqrt{\tau}$ is reasonable. If we assume modest clock parameters such as a cycle time of 100 ms and $Q = 1.5 \times 10^8$, then Eq. 1.2 dictates that $\sim 10^6$ atoms are needed; according to Eq. 1.3, this corresponds to a trapping beam diameter of $\sim$5 mm. Since this is likely too large for a complete device meeting the final program goals, the first experiment of my Ph.D. focused on a technique to overcome these difficult scaling restrictions.

The experiment concept was based on a common loading technique for a MOT in which atoms are trapped from a slowed atomic beam [64]. Various Doppler shift compensation methods have been successfully employed, including a spatially varying magnetic field (Zeeman slower) [65] or sweeping the frequency of the slowing laser (chirping) [66]. However, for these techniques, the length scale required to efficiently slow atoms from thermal velocities to a reasonable MOT capture velocity is on the order of 1 m for alkali atoms. This length scale is determined by the mean velocity of the atoms and the maximum spontaneous force of $F_{spont} = \hbar k \gamma / 2$ and is not practical for a cm-scale atomic device. To demonstrate a compact atom source loaded from an atomic beam, we employed a deceleration technique based on stimulated emission that is capable of significantly exceeding the magnitude of the spontaneous force by scattering photons much faster than the natural lifetime limited rate of $\gamma / 2$ [67, 68]. The bichromatic forces in our technique will be introduced in Chapter 2, while the experiment apparatus, data, and conclusions will be presented in Chapters 3 and 4. The results from this study were published in 2012 in Physical Review A [69].

1.3.2 Phase II Cold-Atom Coherent Population Trapping Clock

Since the motivations for developing a compact atomic clock were discussed above, this section will present our approach to the program as well introduce the two main frequency shifts considered in this thesis. The CACPT clock features a unification of three techniques in a configuration designed to achieve the goals of the IMPACT program: laser-cooled atoms, coherent population trapping, and Ramsey interrogation. As mentioned above, the use of cold atoms in lieu of buffer gas preserves the long interaction times necessary for narrow clock fringes while avoiding the pressure shifts that restrict the long-term stability of vapor cell clocks. The CACPT clock transition is between the $|F = 1\rangle$ and $|F = 2\rangle$ ground state hyperfine levels of ^{87}Rb, which are separated by a

microwave frequency of $\sim$6.835 GHz. While classic Ramsey spectroscopy featuring two spatially or temporally separated $\pi/2$ microwave pulses is a direct interrogation option [70], the required microwave cavity places a restriction on the minimum size of the final device. To avoid such a limitation, a coherent population trapping resonance is used to interrogate the microwave transition optically. Finally, while avoiding the direct use of microwaves, the CACPT clock does rely on the Ramsey technique to generate narrow fringes while minimizing power broadening. Interrogating the atoms in this pulsed fashion also suppresses AC-stark perturbations, which are another stability-limiting effect in CSACs. We successfully integrated each of these techniques and demonstrated the first CACPT clock in 2013 [48]. Since then, a second-generation system was constructed in which the volume of the physics package was reduced from ~ 150 cm^3 to ~ 80 cm^3. The new system was thoroughly characterized and optimized to improve the short and long-term fractional frequency stability. Chapter 5 will present the fundamentals of coherent population trapping, the Phase II CACPT apparatus and operation procedures, and the current best performance of the system. A publication reporting the CACPT clock performance obtained in our second generation system will be prepared in early 2015.

At the beginning of this project, most of the risk inherent with the cold-atom CPT approach arose from potential Zeeman, Doppler, and AC-stark shifts, the principal frequency biases for this type of clock. While plans were in place to mitigate each of these frequency shifts, it was unclear what degree of suppression the techniques would provide and whether it would be sufficient to make this scheme a viable option for an IMPACT device. Frequency biases arise when various physical effects introduce a phase shift of the Ramsey fringes to which the clock is locked. The ratio of the fractional phase shift to the width of a complete Ramsey fringe ($\Delta\nu_R = 1/T_R$, where T_R is the Ramsey time) gives the frequency shift: $\Delta\nu_i = \Delta\phi_i/(2\pi T_R)$, where i corresponds to the physical effect under consideration. For the CACPT clock, the Zeeman effect from the magnitude and fluctuations of ambient magnetic fields causes both a loss of S/N due to the particular CPT scheme employed as well as frequency shifts and instability. This can be managed through magnetic shielding and reduction of field gradients and is discussed in Section 5.1.3. In vapor cell clocks, the high pressure buffer gas reduces the motion of atoms participating in the clock sequence, effectively eliminating Doppler shifts. By exchanging buffer gas for laser cooling in the CACPT clock, suppression of atom motion and cloud expansion during the interrogation sequence is lost,

and Doppler shifts are re-introduced. To reduce this effect, the CACPT clock features a counter-propagating CPT interrogation configuration that uses light with the same optical phase to both pump atoms into the clock state and probe its evolution [48]. This scheme and the results of experiments to characterize its effectiveness are discussed in Chapter 6 and were published in Physical Review A in 2013 [48]. Even with time-separated Ramsey interrogation, AC-stark shifts, or light shifts [71–73], are still a concern for clocks based on coherent population trapping resonances. The AC-stark effect arises from a coupling between the atom and the time varying electric field of the laser, introducing a perturbation in the Hamiltonian that shifts the energy eigenstates. For a simple two-level atom and a monochromatic laser field, the energy shift is given by $\Delta\omega = \pm\hbar\Omega^2/4\delta$, where Ω is the Rabi frequency and δ is the detuning of the light field [56]. This traditional shift, proportional to intensity, has been observed in many systems; however, the response in the CACPT clock is more nuanced. Contributions from coherent and incoherent laser light combine to form complicated light shifts with the potential to significantly affect the long-term frequency stability of the clock. A thorough characterization of the AC-stark effect in the CACPT clock as well as a laser configuration that effectively eliminates the shift is presented in Chapter 7. The results of our light shift study were submitted for publication in the fall of 2014 [74].

CHAPTER 2

BICHROMATIC FORCE THEORY

Many different techniques have been developed over the last three decades to slow, trap, and cool atoms for fundamental experiments in atomic physics. With the relatively new interest in atom-based sensors, these techniques are being adapted to increase efficiency and simplify technical requirements. For a compact atomic device based on a beam loaded magneto-optical trap, achieving sufficient atom number to reach the demanding S/N requirements of sensing applications is a challenge. A very strong force acting over a wide velocity class is necessary to slow a large fraction of the velocity distribution in a reasonably short distance. This chapter will present a brief overview of potential forces for use in such a device and will discuss the theory and characteristics of the bichromatic force that was studied in our experiment.

2.1 Overview of Optical Forces

The simplest and most widely employed laser cooling technique uses spontaneous emission to both slow and cool an atomic sample. For an atomic beam, this force is generated by the absorption of a photon from a laser overlapped with the beam and oriented opposite of the longitudinal velocity component. The laser is red-detuned from the transition frequency between two states such that the Doppler shift will bring the laser frequency into resonance for a certain velocity class determined by the linewidth of the laser and the absorption cross section. Atoms in this velocity range absorb a photon from the laser and are excited to the upper state, receiving a momentum kick of $\hbar \vec{k}$, where $|\vec{k}| = 2\pi/\lambda$ is the laser wave number. After a period determined by the excited state lifetime (τ), the atom decays to the ground state through spontaneous emission. This sequence generates a net force in the direction of $\vec{k}$ as the momentum reduction during absorption is along the direction of laser propagation while the photon from the spontaneous decay event is emitted randomly within a solid angle of 4π. On average, this results in a net momentum transfer opposing the velocity of the atomic beam (Fig. 2.1). For a laser detuning δ, intensity I, and saturation intensity I_{sat}, the
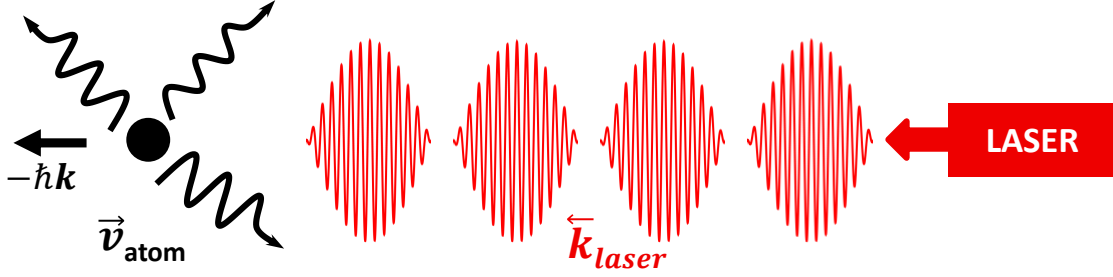
Figure 2.1: Schematic for the spontaneous optical force. The red packets represent laser photons detuned below the transition frequency, and the black oscillating lines represent photons emitted over an $\Omega = 4\pi$ solid angle from spontaneous decay. Averaging the momentum transfer from laser absorption and spontaneous emission results in a net force opposite the atomic velocity vector.

net force is given by [56]:

$$F_{spont} = \hbar k \frac{\gamma}{2} \frac{I/I_{sat}}{1 + I/I_{sat} + 4\delta^2/\Gamma^2} = \hbar k R_{scatt}.$$ (2.1)

This force saturates at large intensities, approaching a maximum of $F_{spont}^{max} = \hbar k \gamma/2$ that is limited by the lifetime of the excited state. Despite the technical simplicity of this slowing mechanism, the limited force magnitude results in deceleration distances on the order of 1-2 m for a thermal beam and requires additional complexities to maintain Doppler resonance over large velocity classes (Section 1.3.1). These issues would likely preclude its use in a compact device.

While advanced techniques capable of reaching sub-Doppler limit temperatures with spontaneous emission have been developed, such as polarization-gradient cooling or Sisyphus cooling [75], these forces are still limited in magnitude by the rate of spontaneous decay. These methods are very valuable in ultra-cold atom experiments but are inadequate for slowing an atomic beam. To exert a force sufficient to slow a thermal beam over cm-scale lengths, circumventing the spontaneous decay rate is necessary. The dipole force provides one means of accomplishing this, taking advantage of the atomic response to spatially-dependent light shifts within an intensity gradient to generate a force that can exceed F_{spont}. The simplest case to consider is the limit of large optical detunings. In this regime, the force is given by the standard $\vec{F}_{dip} = -\nabla U_{dip}$, where the dipole potential is just the shift in energy levels caused by the AC-stark effect (Section 1.3.2): $U_{dip} = \hbar \Omega_R^2/4\delta$. In this expression, the Rabi frequency (Ω_R) is defined in terms of the field intensity as:

$$\Omega_R = \gamma \sqrt{\frac{I}{2I_{sat}}}. \tag{2.2}$$

Thus, the dipole force for large detunings is [56]:

$$\vec{F}_{dip} = -\nabla \left(\frac{\hbar \Omega_R^2}{4\delta} \right) = -\frac{\hbar \gamma^2}{8 \delta I_{sat}} \nabla I. \tag{2.3}$$

Near the high intensity extrema of the potential, ∇I is negative such that dipole forces drive atoms toward high intensity nodes for negative detunings and away from them for positive detunings. This detuning control of the force orientation has enabled the realization of dipole force traps in which atoms are bound at the focus of a high intensity laser beam [76] as well as the optical tweezers technique in which macroscopic objects are controlled via the dipole force [77]. Furthermore, since the slope of the light shift potential scales with the intensity of the applied field, there is not an intrinsic limit on the magnitude of the force. However, for the sinusoidal intensity dependence of a standing wave, the intensity gradient is symmetric about zero resulting in no dipole force when averaged over a wavelength. Generating a net force requires modifying the technique such that the dipole force is "rectified" and does not vanish under spatial averaging. This can be accomplished by adding a second standing wave at a much larger detuning than the primary field [78, 79]. The secondary beam is sufficiently far detuned to not independently drive transitions, but rather provides an additional light shift that modulates the detuning of the primary field. The resulting effective detuning dependence of the dipole force in Eq. 2.3 is now given by [57]:

$$\delta_{eff}(\vec{r}) = \delta_p + \frac{\gamma^2}{8\delta_s I_{sat}} I(\vec{r}), \tag{2.4}$$

where δ_{eff} is the effective detuning, $\delta_{p,s}$ is the detuning of the primary and secondary fields respectively, and $I(\vec{r})$ is the spatially-dependent intensity of the secondary field. The dipole force is now $\propto \nabla I_p / \delta_{eff}$; with the proper choice of δ_s and the phase between primary and secondary fields, it is possible to configure the system such that both the effective detuning and intensity gradient of the primary field flip signs at the same position. This forces F_{dip} to keep the same sign over the interaction length, breaking the symmetry and producing a net force that can significantly exceed $\hbar k \gamma / 2$. However, due to the sensitivity of this arrangement to the detunings of the primary and secondary

fields, strong dipole forces can only be achieved over a narrow velocity class before Doppler shifts render the technique inoperable [57]. Accordingly, a different rectification mechanism is necessary to generate the large forces and broad velocity range desired for a compact atomic beam device.

Such a mechanism is provided by a similar configuration featuring two overlapped standing waves but operating in a different parameter regime where the two fields have equal intensities and are symmetrically detuned about the atomic resonance. Balancing the two fields in this manner results in strong optical forces that act over a broad velocity class. This aptly named bichromatic force relies on a repeated sequence of absorption and stimulated emission, occurring at a much faster rate than allowed by spontaneous decay, to transfer photons between counter-propagating laser beams. When optimized, this process can exert a force $\sim 10\times$ greater than the spontaneous force over a velocity range $\sim 50\gamma/k$ [80]. Bichromatic forces have been used to slow and deflect Rb [81, 82], collimate and slow metastable He [83], slow a Cs atomic beam [80], and have been discussed as a mechanism for decelerating molecules [84]. In theory, the magnitude of the bichromatic force has no fundamental limitation but rather is practically limited by the laser power that can be applied at the proper frequencies. The square force profile is also well suited for application in a beam-loaded MOT due to the transitions between a large applied force and no applied force occurring within a very narrow velocity range. With careful control of the frequencies, the force profile can be positioned such that atoms are slowed from a broad velocity class down to the capture velocity of a compact MOT over short interaction lengths. These characteristics and a theoretical description of the bichromatic force will be discussed in the remaining sections of this chapter.

2.2 Theoretical Description of the Bichromatic Force

This section introduces the theoretical framework for the bichromatic force, including an intuitive model, a calculation of the force profile from the optical Bloch equations, and a discussion of the center velocity.

2.2.1 π-Pulse Model

An intuitive physical description of the bichromatic force is provided by the π-pulse model in which the bichromatic field produces coherent transitions between atomic states in an optical analogy to spin-flip techniques [85]. In this picture, shown schematically in Fig. 2.2, an atom with
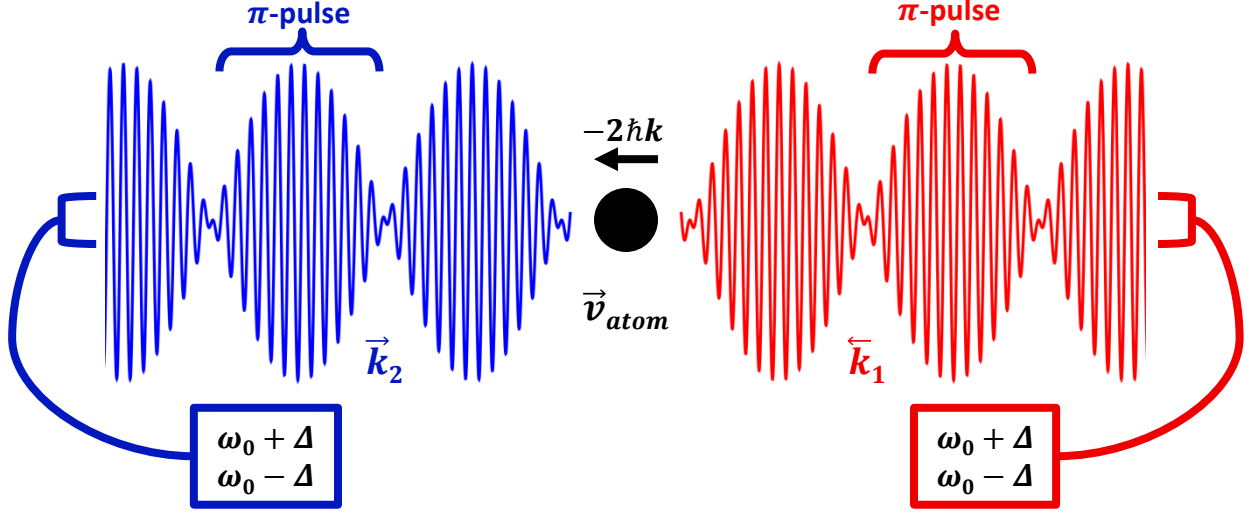
Figure 2.2: Diagram of the π-pulse model of the bichromatic force. Counter-propagating π-pulses produce $2\hbar k$ momentum loss per absorption/stimulated emission cycle. Due to the high repetition rate Δ/π, a force greatly exceeding the spontaneous force can be generated and used to decelerate an atomic beam over small distances.

velocity $\vec{v}_{atom}$ interacts with two counter-propagating bichromatic fields with equal intensities and frequencies symmetrically detuned around the atomic resonance: $\omega_0 \pm \Delta$ with $\Delta \sim 200$ MHz for our experiment. The bichromatic beams are aligned along the axis of the atom velocity and establish opposing pulse trains at the beat frequency 2Δ. To configure the counter-propagating pulse trains such that each pulse coherently drives transitions to or from the excited state, the intensity of each beam is tuned to match the π-pulse condition [57]:

$$\int_{-\pi/2\Delta}^{\pi/2\Delta} 2\Omega_R \cos\left(\Delta t\right) \; \mathrm{dt} = \pi, \tag{2.5}$$

where Ω_R is the Rabi frequency and Δ is the detuning of the bichromatic field. This condition arises from the optical Bloch equations for a two-level atom interacting with a laser field. In this case, a complete 180° rotation of the Bloch vector, corresponding to a population inversion between the ground and excited states, is caused by a coherent pulse with an envelope area of π [86]. Solving the integral equation in Eq. 2.5 provides the required ratio between intensity and detuning:

$$\Omega_R = \gamma\sqrt{\frac{I}{2I_{sat}}} = \frac{\pi}{4}\Delta. \tag{2.6}$$

When the bichromatic field meets the condition in Eq. 2.6, each of the pulses in the counter-propagating trains become optical π-pulses that will coherently excite or trigger stimulated emission depending on the internal atomic state. A slowing sequence occurs when the relative phase between the bichromatic beams is such that the atom absorbs a pulse from the counter-propagating beam ($\vec{k}_1$ in Fig. 2.2) and transitions to the excited state, receiving a momentum kick opposite its motion. Immediately after the absorption, a pulse from the co-propagating beam ($\vec{k}_2$ in Fig. 2.2) interacts with the atom and causes it to emit a photon into the co-propagating beam, providing a second momentum kick opposite the atom's velocity. This sequence of absorption and stimulated emission results in a $2\hbar k$ momentum loss per cycle. Due to the high bichromatic repetition rate of Δ/π (from the beat envelope $\propto \cos{(\Delta t)}$), these cycles occur much faster than the spontaneous scattering rate ($\gamma/2$) and lead to a very large ideal force given by the product of the momentum transfer per cycle and the repetition rate [57]:

$$F_{bc}^{ideal} = \frac{2\hbar k \Delta}{\pi}. \tag{2.7}$$

For reasonable laser parameters, the force in Eq. 2.7 can greatly exceed F_{spont}, however this analysis has not yet considered the disruptive effects of spontaneous emission. If spontaneous decay occurs while the atom is in the excited state after absorbing a pulse from bichromatic beam $\vec{k}_1$, then it will be in the ground state for its subsequent interaction with a pulse from $\vec{k}_2$. In this configuration, the atom will now absorb the pulse from $\vec{k}_2$ and will undergo stimulated emission into $\vec{k}_1$, receiving momentum kicks that increase its velocity. Because of this sequence, the natural decay of the atom becomes a disruptive effect that reverses the direction of the applied bichromatic force. The probability of a spontaneous event occurring before stimulated emission depends on the relative phase, $\delta\phi$, between the counter-propagating bichromatic beams. For $\delta\phi = 0$ or π, the force averages to zero as the system will spend equal time periods in each configuration. To break the spatial symmetry and establish a strong net force, the relative phase must be set such that absorption from $\vec{k}_1$ is immediately followed by stimulated emission into $\vec{k}_2$, minimizing the time spent in the excited state. This will suppress the occurrence of spontaneous emission and produce an average decelerating force by maximizing the time spent in the desired configuration. Numerically, this occurs at $\delta\phi \sim \pi/2$, where sufficient directional asymmetry is present to generate a strong force without introducing excessive overlap between subsequent π-pulses [57, 80, 87]. At

this relative phase, the system applies a decelerating force 75% of the time and an accelerating force for the remaining 25%, resulting in a net force that is half the expected value from Eq. 2.7:

$$F_{bc} = \frac{\hbar k \Delta}{\pi}.$$

(2.8)

This expression reveals the lack of a fundamental limit for the bichromatic force magnitude; it continues to grow with increasing beat frequency as long as sufficient laser power is available to meet the π-pulse requirement of Eq. 2.6. The magnitude of the bichromatic force given in Eq. 2.8 has been confirmed by multiple numerical calculations, however experimental measurements tend to be between 65%-80% of this prediction [57, 80, 82].

Table 2.1: Bichromatic and Spontaneous Force Comparison

Parameter	Bichromatic Force	Spontaneous Force
Force Magnitude	$\sim \dfrac{\hbar k \Delta}{\pi}$	$\dfrac{\hbar k \gamma}{2}$
Velocity Range	$\sim \dfrac{\Delta}{k}$	$\dfrac{\gamma}{k}$

Table 2.1 provides a comparison of the bichromatic and spontaneous forces. The velocity class over which the bichromatic force is active can not be calculated within the π-pulse model but rather requires the more sophisticated dressed-atom treatment in which superpositions of the energy levels coupled by the radiation field are used to analyze the system [75, 88]. From this type of calculation, the width of the velocity class can be attributed to the combined effects of Doppler and AC-stark shifts [57].

The increase in force magnitude and addressed velocity class achieved with the bichromatic force relative to the spontaneous force scales with the ratio of the RF detuning of the bichromatic field to the natural linewidth of the atom under consideration: Δ/γ. For our experiments, Δ is on the order of 200 MHz, while the linewidth of the D2 transition in ^{87}Rb is ~ 6 MHz, implying that bichromatic forces should provide a significant advantage in our system.

2.2.2 Bichromatic Force Profiles

The bichromatic force profile can be calculated by numerically solving the optical Bloch equations for a two-level atom interacting with the counter-propagating laser fields. This technique arises from the density matrix formalism of quantum mechanics, where the evolution of the system due to interaction with a Hamiltonian H is given by:

$$\dot{\rho} = -\frac{i}{\hbar}[H, \rho],\tag{2.9}$$

where for a two-level system, the density matrix for ground state $|1\rangle$ and excited state $|2\rangle$ is given by:

$$\rho = \begin{pmatrix} \rho_{22} & \rho_{21} \\ \rho_{12} & \rho_{11} \end{pmatrix}.\tag{2.10}$$

In this expression, ρ_{ii} is the population fraction of $|i\rangle$ and ρ_{ij} is the coherence between $|i\rangle$ and $|j\rangle$. The above expressions hold true for pure quantum states, however the presence of spontaneous emission in the bichromatic process requires adding a term to Eq. 2.9 to account for the natural decay of the excited state [57]:

$$\dot{\rho} = -\frac{i}{\hbar}[H, \rho] + \left(\frac{d\rho}{dt}\right)_{spont},\tag{2.11}$$

where [57]:

$$\left(\frac{d\rho}{dt}\right)_{spont} = \begin{pmatrix} -\gamma\rho_{22} & -\frac{\gamma}{2}\rho_{21} \\ -\frac{\gamma}{2}\rho_{12} & \gamma\rho_{22} \end{pmatrix}.\tag{2.12}$$

Spontaneous emission introduces a term into the density matrix equations that modifies the level populations and reduces the coherence between the ground and excited states, i.e. disrupting the coherent population inversion that the bichromatic force relies on.

The Hamiltonian for the system has the standard form for an atom in a radiation field. For electric dipole transitions, this is $H = H_0 + H'$, where H_0 is the unperturbed atomic Hamiltonian, and $H' = -\vec{d} \cdot \vec{E}(\vec{r}_0)$ is the perturbation from the laser field. In this expression, $\vec{d}$ is the dipole moment, and $\vec{E}(\vec{r}_0)$ is the total electric field at the position of the atomic dipole [86]. With the Rabi frequency (Eq. 2.2) written in terms of the electric field,

$$\Omega_R = \vec{d} \cdot \vec{E}\left(\vec{r}_0\right)/\hbar, \tag{2.13}$$

the perturbation Hamiltonian becomes [86]:

$$H' = -\frac{\hbar}{2} \begin{pmatrix} 0 & \Omega_R \\ \Omega_R^* & 0 \end{pmatrix}. \tag{2.14}$$

To derive the density matrix system of equations from Eq. 2.11, the total electric field of the combined counter-propagating bichromatic components is needed. For resonant bichromatic fields aligned along the $\hat{z}$-axis, there are two frequency components $\omega_{1,2}$ traveling in opposite directions with wave vectors $k_{1,2} = \pm k$ and field amplitudes $|E_{1,2}|$. The total field is then:

$$|\vec{E}_{bc}\left(z,t\right)| = \text{Re}\left[E_1 e^{i(kz-\omega_1 t)} + E_1 e^{-i(kz+\omega_1 t)} + E_2 e^{i(kz-\omega_2 t)} + E_2 e^{-i(kz+\omega_2 t)}\right]. \tag{2.15}$$

The phase difference between counter-propagating beams is included by a $\pi/4$ phase added to each traveling-wave component such that the relative phase delay is $\delta\phi = \pi/2$. The total electric field becomes:

$$|\vec{E}_{bc}\left(z,t\right)| = \text{Re}\left[E_1 e^{i(kz-\omega_1 t+\phi/4)} + E_1 e^{-i(kz+\omega_1 t-\phi/4)} + E_2 e^{i(kz-\omega_2 t+\phi/4)} + E_2 e^{-i(kz+\omega_2 t-\phi/4)}\right]. \tag{2.16}$$

After inserting the bichromatic frequencies ($\omega_1 = \omega_0 + \Delta$, $\omega_2 = \omega_0 - \Delta$) and assuming equal beam intensities to meet the π-pulse condition ($E_1 = E_2 \equiv E_0$), the final bichromatic electric field is:

$$|\vec{E}_{bc}\left(z,t\right)| = \text{Re}\left[E_0 e^{-i\omega_0 t}\left(e^{i(kz-\Delta t+\phi/4)} + e^{-i(kz+\Delta t-\phi/4)} + e^{i(kz+\Delta t+\phi/4)} + e^{-i(kz-\Delta t-\phi/4)}\right)\right]. \tag{2.17}$$

By combining similar exponential terms, this can be reduced to a more compact form where the spatial and temporal dependence is given by $\cos\left(kz\right)\cos\left(\Delta t\right)\cos\left(\omega_0 t - \phi/4\right)$.

With the electric field defined, the next step in deriving the optical Bloch equations for the system is to apply the rotating wave approximation. This removes the rapid oscillations of the electric field at the atomic resonance frequency ω_0 by shifting to a rotating frame. It is then possible to write down the time evolution of each component of the density matrix in terms of the

Rabi frequency. Combining Eqs. 2.10 - 2.14 and 2.17, the density matrix equations including the decoherence from spontaneous emission are [87, 89]:

$$\begin{aligned}
\dot{\rho}_{11} &= -\frac{i}{2}\left(\rho_{12}\Omega_R - \rho_{21}\Omega_R^*\right) + \gamma\rho_{22} \\
\dot{\rho}_{22} &= \frac{i}{2}\left(\rho_{12}\Omega_R - \rho_{21}\Omega_R^*\right) - \gamma\rho_{22} \\
\dot{\rho}_{12} &= \frac{i\Omega_R^*}{2}\left(\rho_{22} - \rho_{11}\right) - \frac{\gamma}{2}\rho_{12} \\
\dot{\rho}_{21} &= -\frac{i\Omega_R}{2}\left(\rho_{22} - \rho_{11}\right) - \frac{\gamma}{2}\rho_{21}.
\end{aligned}$$

(2.18)

The optical Bloch equations can now be written down through a variable substitution using the components of the Bloch vector. This approach takes advantage of the similarities between a spin 1/2 particle and a two level atomic system, adopting the formalism by defining a Bloch vector analogous to the spin vector from magnetic resonance theory [86]. The components of the vector are combinations of the coherences and population fractions from the density matrix [56]:

$$\begin{aligned}
u &= \rho_{12} + \rho_{21} \\
v &= i\left(\rho_{21} - \rho_{12}\right) \\
w &= \rho_{22} - \rho_{11}.
\end{aligned}$$

(2.19)

With this definition, much of the formalism from magnetic resonance theory can be directly used for two-level atoms in a resonant optical field [86]. Substituting the Bloch vector components for the density matrix elements in Eq. 2.18, we obtain the optical Bloch equations for the bichromatic force:

$$\begin{aligned}
\dot{u} &= -\frac{\gamma}{2}u - \text{Im}\left(\Omega_R\right)w \\
\dot{v} &= -\frac{\gamma}{2}v + \text{Re}\left(\Omega_R\right)w \\
\dot{w} &= \text{Im}\left(\Omega_R\right)u - \text{Re}\left(\Omega_R\right)v - \gamma\left(w + 1\right).
\end{aligned}$$

(2.20)

The magnitude of the force exerted on the atom can be calculated from Ehrenfest's theorem and basic relations from quantum mechanics [57]:

$$F = \langle\dot{p}\rangle = \frac{i}{\hbar}\langle[H, p]\rangle = -\langle\nabla H\rangle = -\text{Tr}\left(\rho\nabla H\right).$$

(2.21)

Inserting the electric dipole Hamiltonian and using the variable definitions in Eq. 2.19, the force due to the bichromatic field is given by:

$$\vec{F}_{bc} = \frac{\hbar}{2} \left[u \nabla \left(\text{Re} \left(\Omega_R \right) \right) + v \nabla \left(\text{Im} \left(\Omega_R \right) \right) \right]. \tag{2.22}$$

Using Eqs. 2.13 and 2.17, the real and imaginary parts of the Rabi frequency and its gradient can be explicitly written down:

$$\text{Re} \left(\Omega_R \right) = 4\omega_R \cos(kz) \cos(\Delta t) \cos(\phi/4)$$

$$\text{Im} \left(\Omega_R \right) = 4\omega_R \sin(kz) \sin(\Delta t) \sin(\phi/4)$$

$$\nabla \left[\text{Re} \left(\Omega_R \right) \right] = -4k\omega_R \sin(kz) \cos(\Delta t) \cos(\phi/4) \tag{2.23}$$

$$\nabla \left[\text{Im} \left(\Omega_R \right) \right] = 4k\omega_R \cos(kz) \sin(\Delta t) \sin(\phi/4),$$

where ω_R is the traveling wave Rabi frequency of each individual field component, and Ω_R is the Rabi frequency of the total electric field. Finally, the complete system of equations that must be solved to calculate the bichromatic force profile is found by substituting the expressions in Eq. 2.23 into the optical Bloch equations (Eq. 2.20) and the force derived from Ehrenfest's theorem [87, 89]:

$$\dot{u} = -\frac{\Gamma}{2} u - 4\omega_R \sin(kz) \sin(\Delta t) \sin(\phi/4) w$$

$$\dot{v} = -\frac{\Gamma}{2} v + 4\omega_R \cos(kz) \cos(\Delta t) \cos(\phi/4) w$$

$$\dot{w} = 4\omega_R \sin(kz) \sin(\Delta t) \sin(\phi/4) u - 4\omega_R \cos(kz) \cos(\Delta t) \cos(\phi/4) v - \Gamma \left(w + 1 \right) \tag{2.24}$$

$$F_{bc} = -2\hbar k \omega_R \left[\sin(kz) \cos(\Delta t) \cos(\phi/4) u - \cos(kz) \sin(\Delta t) \sin(\phi/4) v \right].$$

The force profile as a function of velocity is calculated from the system of equations in Eq. 2.24 using the constant velocity approximation, where the position dependence is exchanged for velocity dependence with the substitution of $z = vt$. In the numerical solution, a discrete velocity is chosen and the system of equations (2.24) is solved, with the force calculated by averaging the results from incrementally stepping through a long period of time. This is repeated over the full velocity range to calculate the force profile.

Using Fortran code provided to us by the authors of [81, 82], we have calculated the bichromatic force profile for different combinations of relative phase (ϕ), Rabi frequency (Ω_R), and bichromatic

detuning (Δ). The strong dependence of the force magnitude and velocity class on these critical parameters is demonstrated by the variation in calculated profiles plotted in Fig. 2.3. The optimum phase for a strong force occurs at $\phi = 90°$ and degrades rapidly, with lobes arising in the profile and a 50% reduction in magnitude at just a $\pm 20°$ deviation.
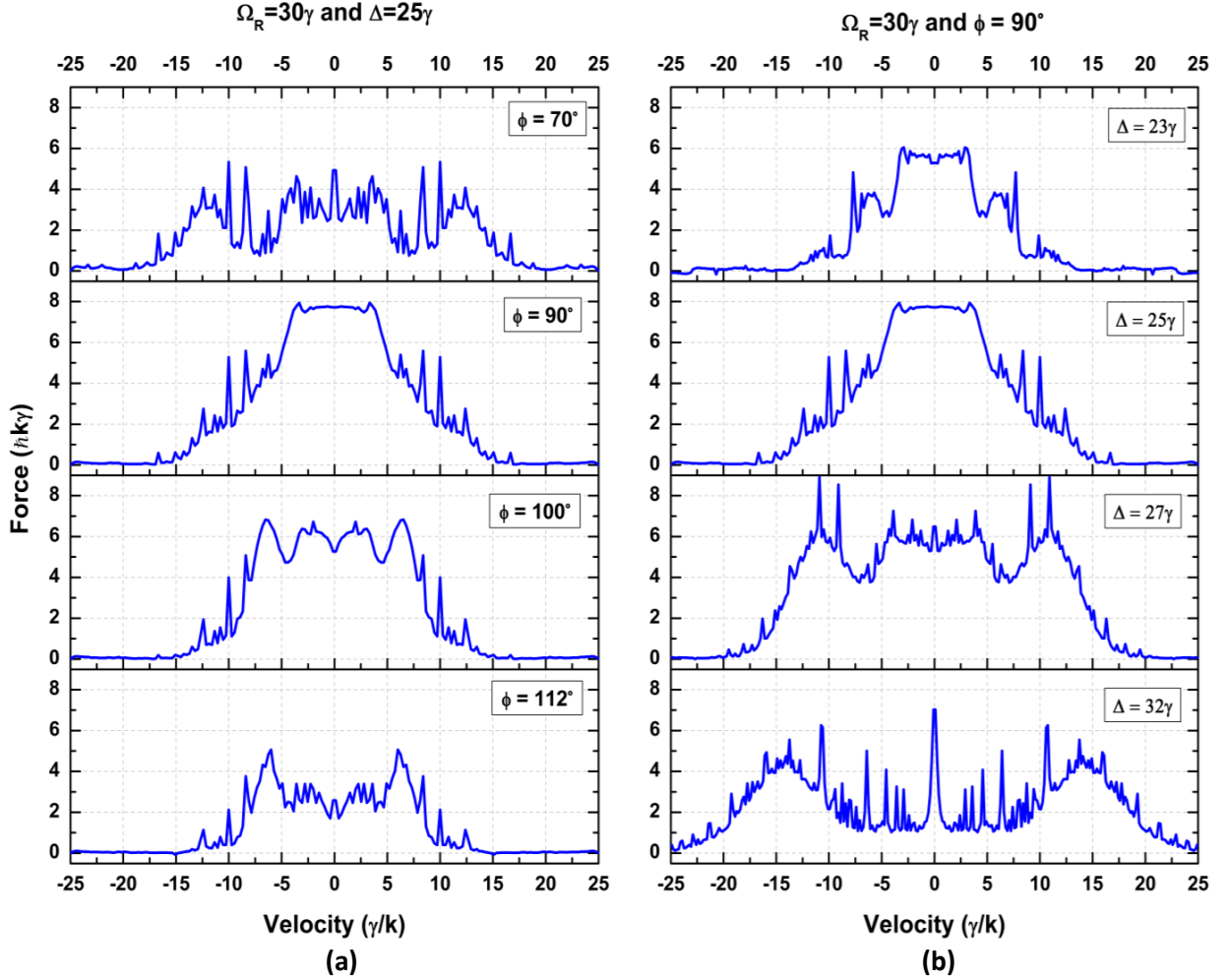
Figure 2.3: Bichromatic force profiles calculated by numerical integration of the optical Bloch equations and plotted for (a) varied relative phase between the counter-propagating beams and (b) varied detuning of the bichromatic field. Proper relative phase and optical detuning values are necessary for a strong stimulated force that does not average to zero over time.

These numerical solutions also reveal that the relationship between the Rabi frequency and optical detuning is not as simple as presented in the π-pulse model, where for $\Omega_R = 30\gamma$, Eq. 2.6 predicts that the optimum force should occur for $\Delta = 38\gamma$. From column (b) in Fig. 2.3, it is clear that the optimum ratio of Ω_R to Δ is not $\pi/4$ as for $\Delta = 32\gamma$ (20% below the π-pulse condition),

the force profile is $\sim 50\%$ smaller than the maximum magnitude and large lobes have appeared in the velocity dependence that decrease the slowing efficiency of the force. Rather, the optimum force profile occurs at $\Delta = 25\gamma$ or a ratio of Ω_R to Δ of 1.2. This deviation of the optimum force from the π-pulse condition has been verified experimentally [80–82], and while it can not be explained in the π-pulse model, it does arise in the doubly dressed atom description of the bichromatic force, where the relationship is found to be $\Omega_R = \sqrt{3/2}\Delta$ [90, 91].

The importance of properly matching the Rabi frequency to the detuning is emphasized by the set of force profiles calculated for the parameters in our experiment: $\Delta = 20\gamma$. For this optical detuning, the optimum force profile occurs for $\Omega_R = 24.5\gamma$, shown in the middle pane of Fig. 2.4. This is the theoretical force profile used in most of our atomic beam and MOT experiments.
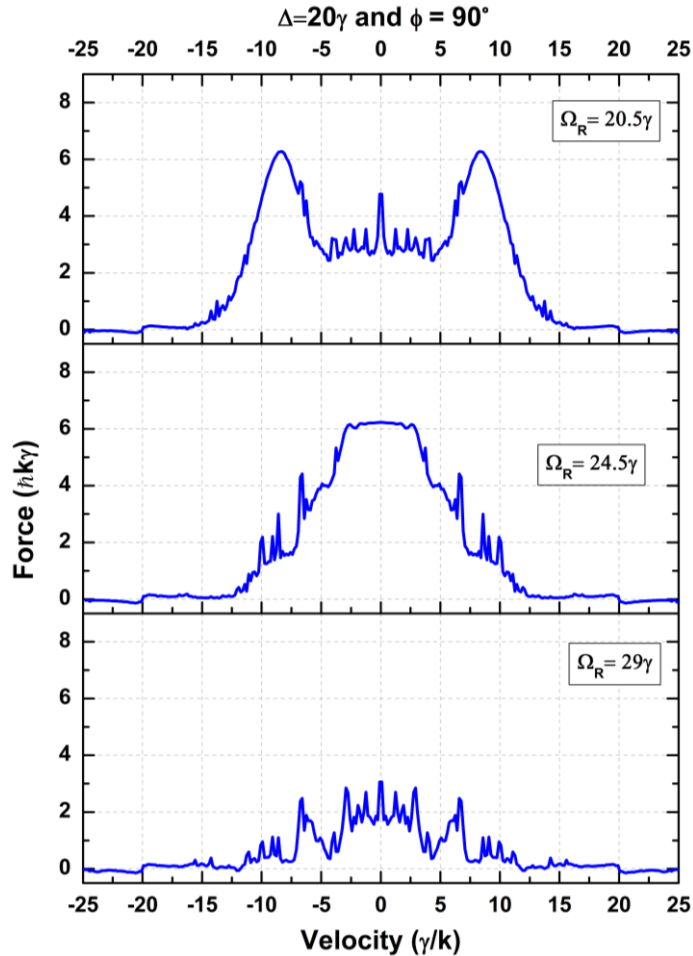
Figure 2.4: Force profiles for $\Delta = 20\gamma$, the detuning used in most of our measurements. Tuning the intensity of the bichromatic field such that a strong force (unlike the bottom pane) without lobes in the velocity dependence (unlike the top pane) was important for the atom number experiments.
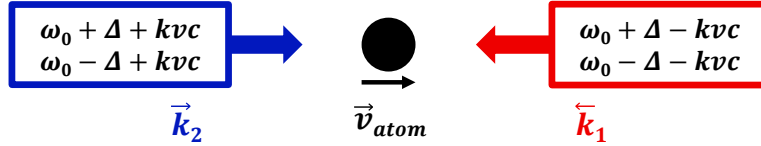
Figure 2.5: Bichromatic frequency components needed to center the force profile at v_c instead of $v = 0$.

2.2.3 Doppler Shifted Force Profiles

Each of the bichromatic force profiles plotted in section 2.2.2 is centered on $\vec{v} = 0$, implying that for a bichromatic field aligned with the $\hat{z}$-axis, the force will be exerted equally on atoms moving in both the $\pm\hat{z}$ direction. For an atomic beam experiment in which each atom has a longitudinal velocity in the $+\hat{z}$ direction, half of this force profile has no effect. To remedy this situation, the center velocity of the force (v_c) must be shifted along the velocity axis such that the entire force profile addresses the atomic beam. This is achieved by Doppler shifting each pair of counter-propagating bichromatic fields in opposite directions. The frequency components propagating opposite the atomic beam are red-detuned by an additional factor $\delta_D = -kv_c$, while the components traveling in the same direction as the atoms are blue-detuned by $\delta_D = +kv_c$. The relative orientation of the four bichromatic frequency components is shown in Fig. 2.5.

By configuring the frequencies in this manner, the force profile is centered at velocity v_c and controlled via the RF frequency δ_D. A set of three Doppler shifted force profiles is shown in Fig. 2.6, where the center velocity varies from 10 m/s to 110 m/s. For ^{87}Rb, this corresponds to an RF frequency shift of between $2\pi \times 13$ MHz and $2\pi \times 140$ MHz. Frequency shifts in this range are easily achieved with an acousto-optical modulator in the beam path of the bichromatic light, providing a very simple means of tuning the center velocity of the force profile. This is a particularly valuable control for a MOT atom number experiment, where the most gain is achieved by placing the force profile such that the lowest velocity edge lies exactly at the capture velocity of the MOT. In this case, the bichromatic force will address the maximum number of atoms that can be slowed to that particular capture velocity for a given Rabi frequency and optical detuning. For the compact MOTs considered in our experiments, typical capture velocities were in the range of $v_{cap} = 5 - 15$ m/s. With such small capture velocities, the force profile in the middle of Fig. 2.6 is optimal. High center velocities will not slow atoms enough to be trapped, while a low center velocity will actually
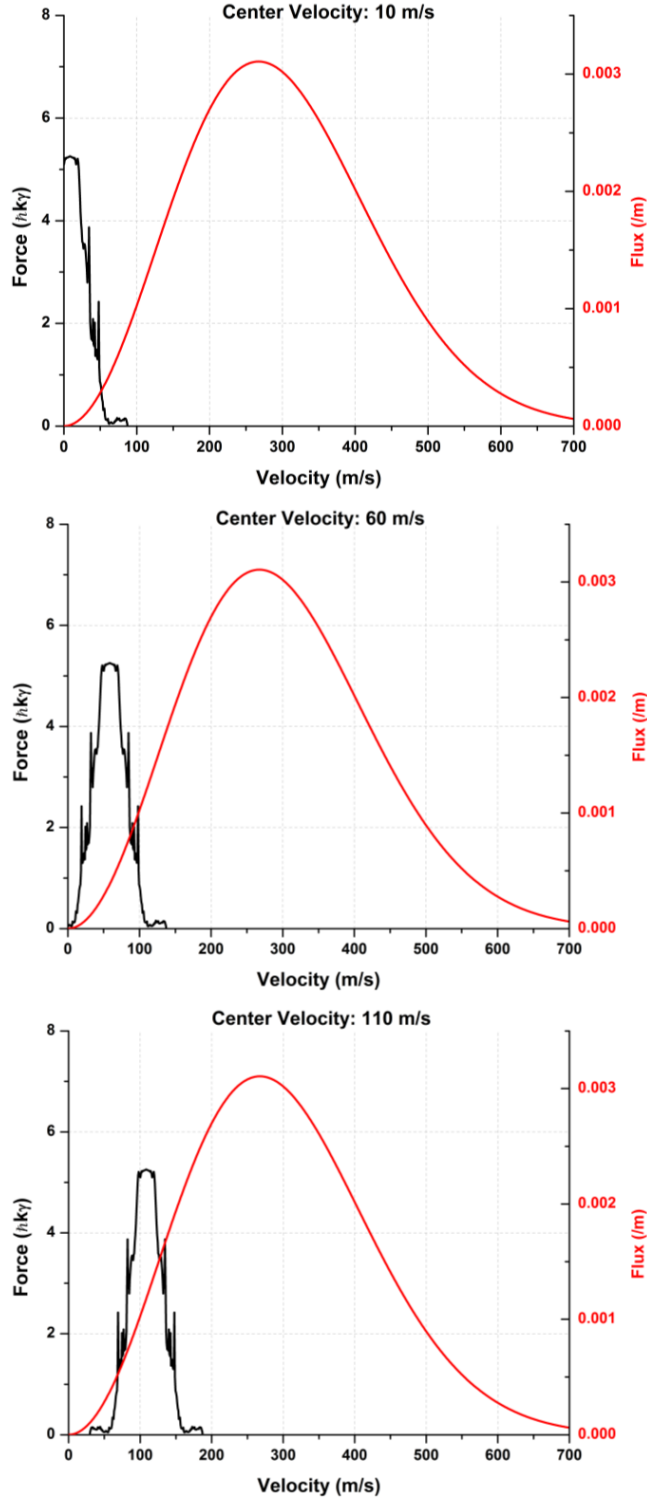
Figure 2.6: Bichromatic force profiles for $\phi = 90°$, $\Delta = 16.8\gamma$, $\Omega_R = 20\gamma$, and varied kv_c such that the center velocity of the force profile from top to bottom is 10 m/s, 60 m/s, and 110 m/s. Plotted with each force profile is the Maxwell-Boltzmann distribution for a Rb atomic beam with $T = 100°$C. To shift the velocity profile by 50 m/s for ^{87}Rb, the frequency must be shifted by $kv_c = 2\pi \times 64$ MHz.

stop atoms and accelerate them away from the trapping region. This illustrates the need to balance all of the bichromatic parameters such that a strong and broadly acting force profile is achieved and positioned such that the maximum number of atoms is slowed to the desired capture velocity. This will be discussed further in later chapters.

CHAPTER 3

BICHROMATIC SLOWING APPARATUS

The table top apparatus for our compact MOT experiments was designed to explore how bichromatic slowing scaled with miniaturization in terms of the laser power required to generate a strong optical force and the interaction length necessary to slow atoms to the low capture velocities of mm-scale MOTs. This experiment required designing and building an ultra-high vacuum chamber (UHV) with a Rb atomic beam, developing the required lasers and optics for the trapping and slowing light, and constructing a detection and data acquisition system. Each of these components will be discussed in this chapter. A post-doctoral researcher, Dr. Tara Cubel-Liebisch, and I worked together on the bichromatic slowing apparatus discussed in this chapter and on the data collection and analysis presented in Chapter 4. Tasks were divided efficiently throughout the experiment. During the construction phase, for example, I constructed lasers, designed the vacuum chamber, and wrote control software while she designed the optics layouts, performed early modeling, etc.

3.1   Vacuum Chamber

The UHV chamber for the bichromatic slowing experiment was designed to facilitate measurements of both atomic beam velocity profiles as well as compact MOT atom numbers. The system featured a high pressure Rb oven and a large science chamber separated by a collimating package that generated an atomic beam flowing vertically along the direction of gravity. Individual components were primarily selected from standard parts manufactured from vacuum-compatible stainless steel connected via knife-edge flanges and copper gaskets. A CAD rendering of the full UHV chamber with labels for the main functional components is shown in Fig. 3.1.

To reach ultra-high vacuum pressures, a sequence of pumping and baking steps is necessary as no single pump is capable of operating from atmospheric pressure down to the UHV range. A pumping station with both roughing and turbomolecular pumps was attached to the all-metal bake-out valve on the lower arm of the system. The roughing pump was engaged first, reducing the system pressure from atmosphere down to $\sim 10^{-3}$ torr. Once the initial chamber evacuation
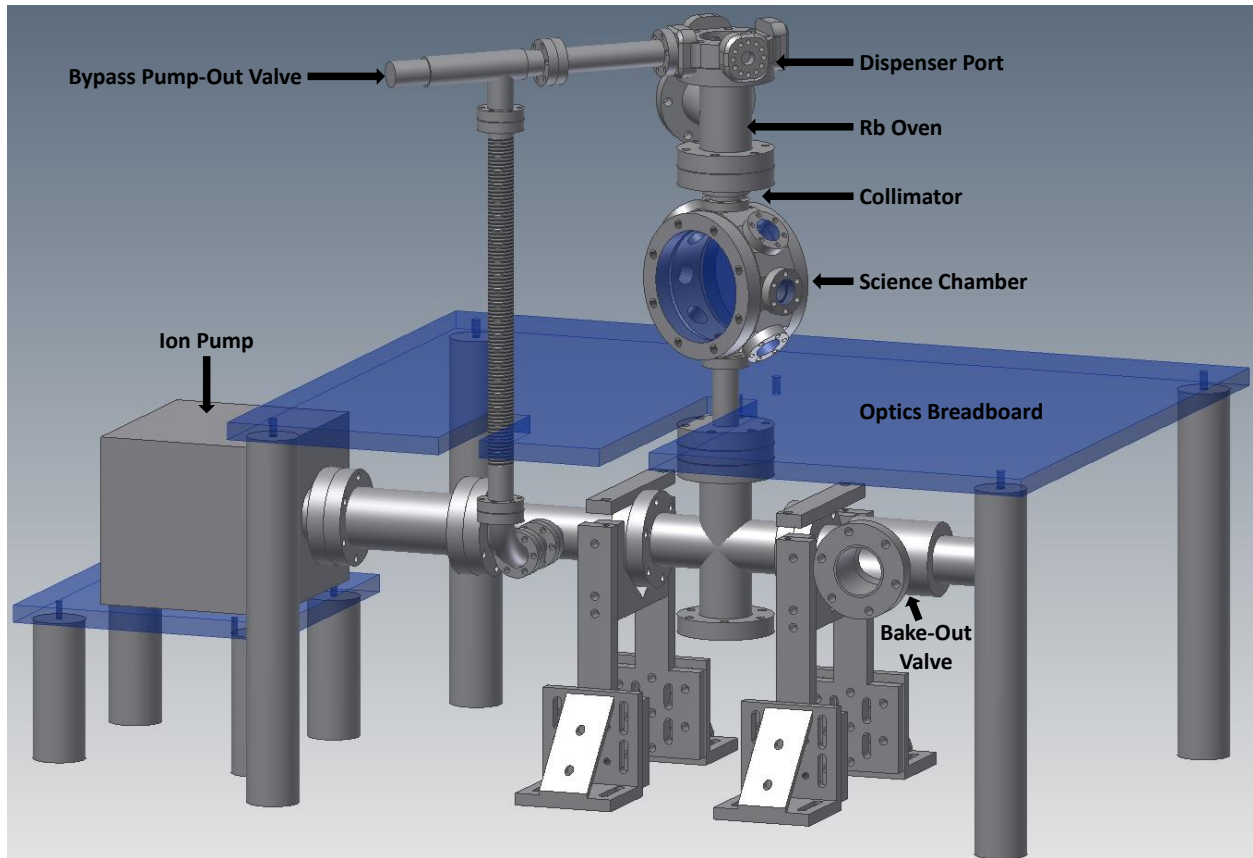
Figure 3.1: CAD rendering of the UHV chamber for bichromatic slowing experiments. The system featured a 150°C Rb oven, an atomic beam collimator, and a science chamber with sufficient optical access for both atomic beam and MOT experiments.

was complete, the turbo pump was activated and brought the system pressure to $\sim 10^{-7}$ torr. At this stage, if the turbo pump struggles to reach its pressure limit, leak detection is performed using Helium or isopropyl alcohol to check the seals throughout the system. After tightening any leaking connections and reaching the limit of the turbomolecular pump, the 20 L/s ion pump connected to the opposite end of the lower arm was turned on. Before reaching the final UHV system pressure, the chamber was uniformly heated to ~ 150°C to drive off residual molecules that adsorbed to the inner walls of the chamber. Baking the system rapidly increases the pump down rate by forcing these molecules off the chamber walls at one time, avoiding constant desorption that would prevent UHV pressures from being attained. In this system, the bake out temperature was restricted to < 150°C due to the low melting point (~ 156°C) of an indium seal used in the collimation package. This evacuation procedure, and the placement of a graphite chip in the lower arm to absorb excess Rb, enabled the bichromatic system to reach and maintain UHV pressures below the 10^{-9} level.
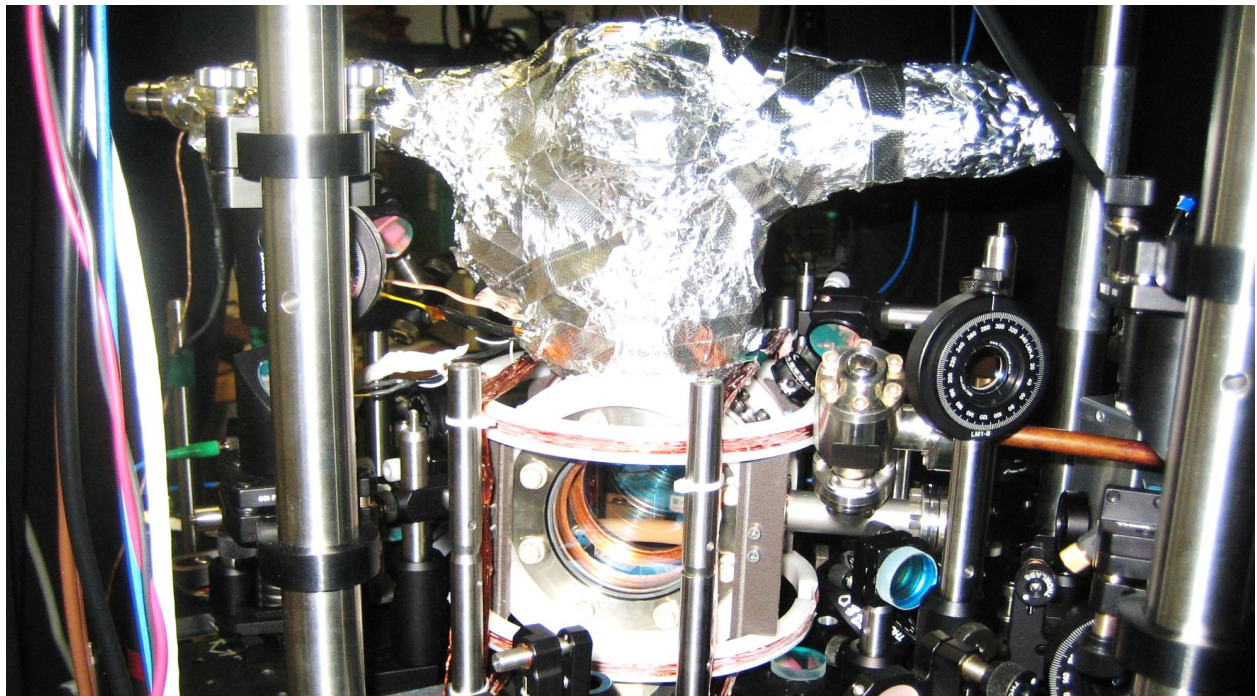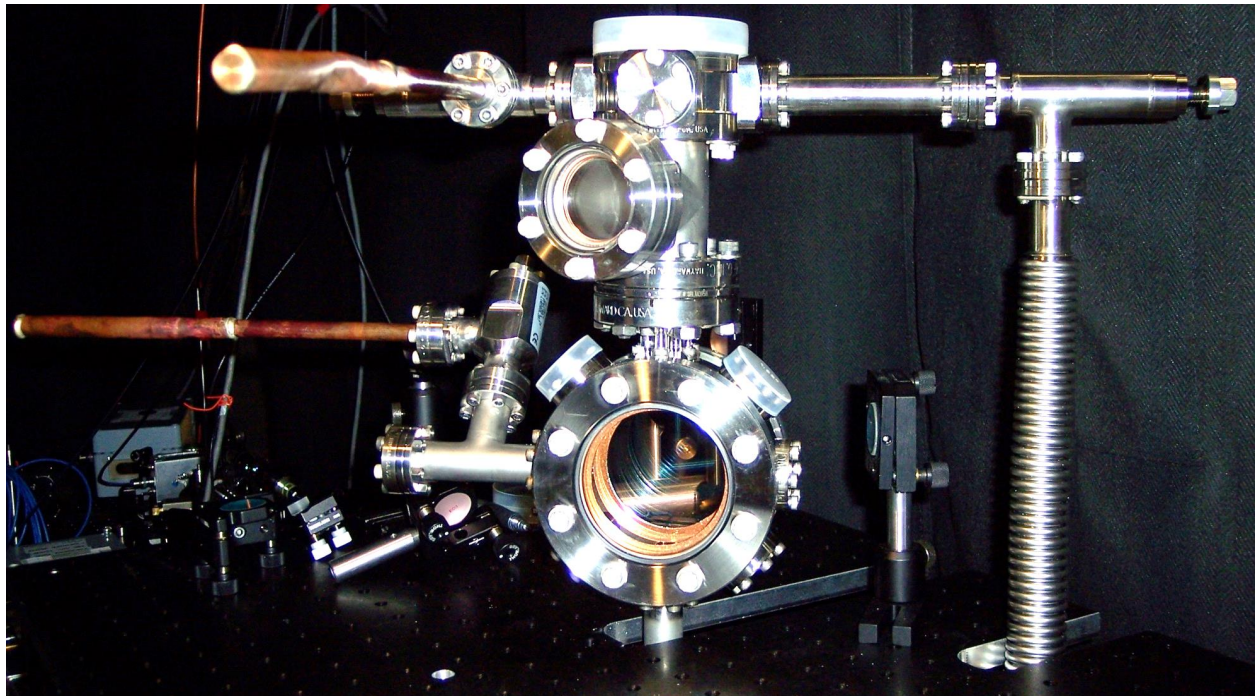
Figure 3.2: Photograph of the UHV chamber for the bichromatic slowing experiments with (bottom) and without (top) heat tapes and foil wrapping for the Rb oven. In the top photo, note the crimped copper tube where the Rb ampule was broken to provide alkali vapor for the atomic beam.

The atomic beam was generated from a rubidium oven located above the science chamber. The home-built Rb dispenser consisted of a glass ampule filled with metallic rubidium placed inside a sealed copper tube with a 1.33" diameter con-flat flange on one end. The dispenser was bolted to the side of the oven and released Rb vapor after the sealed copper tube was crimped, cracking the glass ampule. The oven was uniformly heated to 150°C by wrapping the entire upper part of the chamber with heat tapes and encasing it in aluminum foil. This created a hot, high-pressure Rb vapor that formed an atomic beam by flowing through the collimating package into the science cell. The assembled chamber, with and without the heat tape and foil wrappings, is shown in Fig. 3.2. The system was designed with an all-metal bypass valve connecting the oven to the lower arm of the chamber with a flexible bellows; this allowed the oven to be pumped out through a separate path that did not include the collimating apertures.

The atomic beam collimator was mounted inside a 2.75" diameter to 1.33" diameter reduction flange connecting the Rb oven to the low pressure science chamber. It consisted of two 500 μm apertures separated by 25 mm within a Vespel mounting structure (Fig. 3.3 (a)). Vespel is a high-performance plastic well-suited for vacuum applications due to low out-gassing and high structural stability over a broad thermal range. This collimator design produced an expanding atomic beam with a $1/e^2$ diameter of 2.2 mm at the center of the science cell, 50 mm from the second aperture. To prevent excessive absorption of the bichromatic, repump, and probe laser light within the oven, a neodymium permanent magnet was attached to the collimator above the first aperture (Fig. 3.3 (c)). This produced a strong magnetic field that Zeeman shifted the cooling transition (magnetic response of 1.4 MHz/G) within the oven, reducing the beam absorption. This permanent field was ~ 50 G at the top aperture and decreased to approximately zero at the center of the experiment chamber. The contribution of the neodymium magnets to the total magnetic field will be discussed again in the context of the Zeeman shifted bichromatic force in the following chapter.

The science cell was designed with sufficient optical access for both atomic beam velocity profile and MOT atom number measurements. It consisted of a 4.5" diameter spherical octagon chamber with the top and bottom 1.33" ports providing UHV access for the atomic beam and bichromatic light. Anti-reflection (AR) coated windows were mounted to the remaining six 1.33" and two 4.5" ports, providing enough beam paths for a traditional MOT, absorption imaging, and florescence detection to be simultaneously realized (Fig 3.2). To improve the optical quality of the chamber
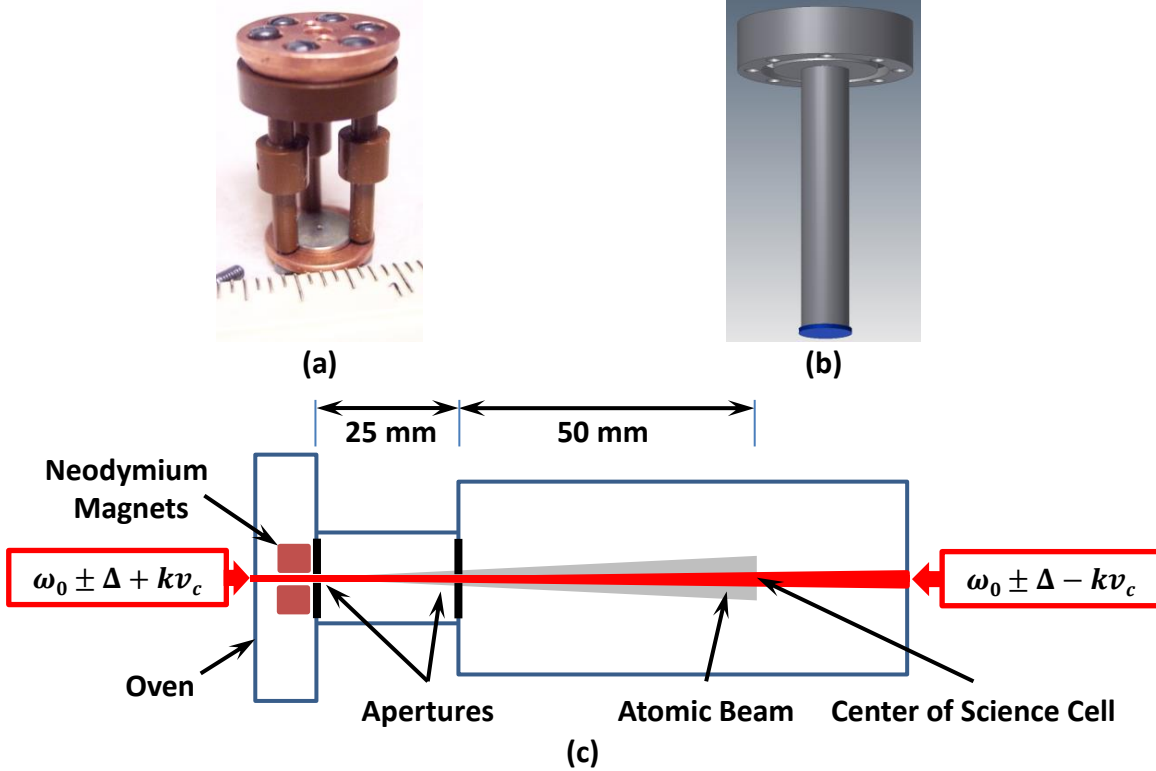
Figure 3.3: (a) Photograph of the atomic beam collimator showing the Vespel mounting structure and the lower 500 μm aperture. (b) CAD rendering of the upper inverted window. (c) Schematic diagram of atomic beam apparatus.

for the bichromatic beam path, inverted windows were inserted both at the top and bottom of the system. These windows consisted of a stainless steel tube with a view port at one end attached to a 2.75" conflat flange (Fig. 3.3 (b)). By coupling the bichromatic beams into the system via inverted windows, the path length within the oven and lower arm of the vacuum chamber that the bichromatic light had to travel through was minimized, reducing absorption in the rubidium vapor. For the top window, an evacuated glass cylinder was placed inside the steel tube to reduce beam distortion within the inverted window from hot air generated by the oven. This improved the beam quality and mode-matching between the counter-propagating bichromatic beams.

3.2 Lasers and Optics

Three diode lasers were used in the optics system for the bichromatic slowing experiments. For both atomic beam and compact MOT studies, one laser provided the bichromatic slowing field, one functioned as a repump laser preventing atoms from accumulating in the $|F = 1\rangle$ ground state,
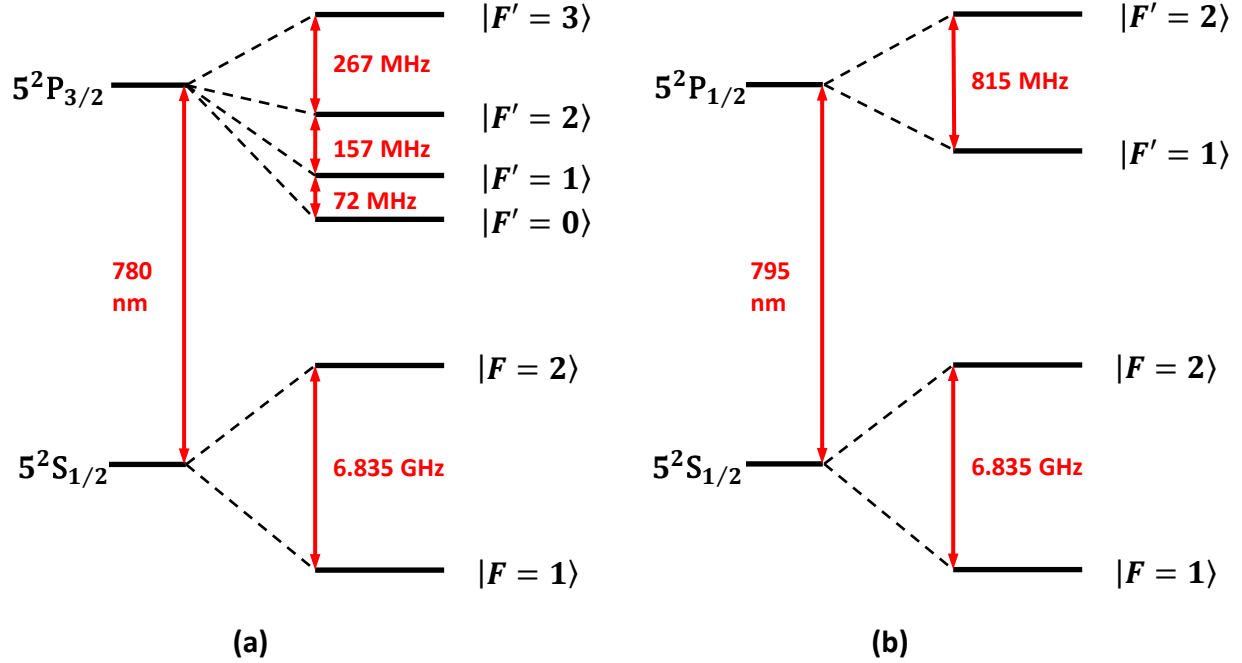
Figure 3.4: Energy level diagram for the D2 (a) and D1 (b) lines of ^{87}Rb. Transition frequencies from [92].

and one laser served as either a probe for the atomic beam or trapping laser for the MOT.

3.2.1 Probe and Repump Lasers

In experiments designed to characterize the bichromatic force, the Maxwell-Boltzmann distribution of the atomic beam was measured by detecting fluorescence from a probe laser tuned to the $|F = 2\rangle \rightarrow |F' = 3\rangle$ cycling transition on the D2 line of ^{87}Rb (Fig. 3.4 (a)). The probe was a home-built extended cavity diode laser (ECDL) based on a single-mode Sanyo diode with 80 mW of output power at $\lambda = 780$ nm. The diode was mounted in a three-pin, 5.6 mm diameter TO package and was temperature and current controlled with standard NIST electronics. The external cavity layout within the laser housing is shown in Fig. 3.5 (a). This laser was constructed in the Littman-Metcalf configuration [93, 94], in which a fixed diffraction grating selects a fraction of the beam and directs it toward a tunable mirror, while the remaining light forms the laser output. The mirror directs the first diffraction order back into the laser diode, providing wavelength selection through optical feedback. This configuration is advantageous as the direction of the laser output is fixed, simplifying downstream optics alignment and providing stable fiber-coupling into the apparatus.
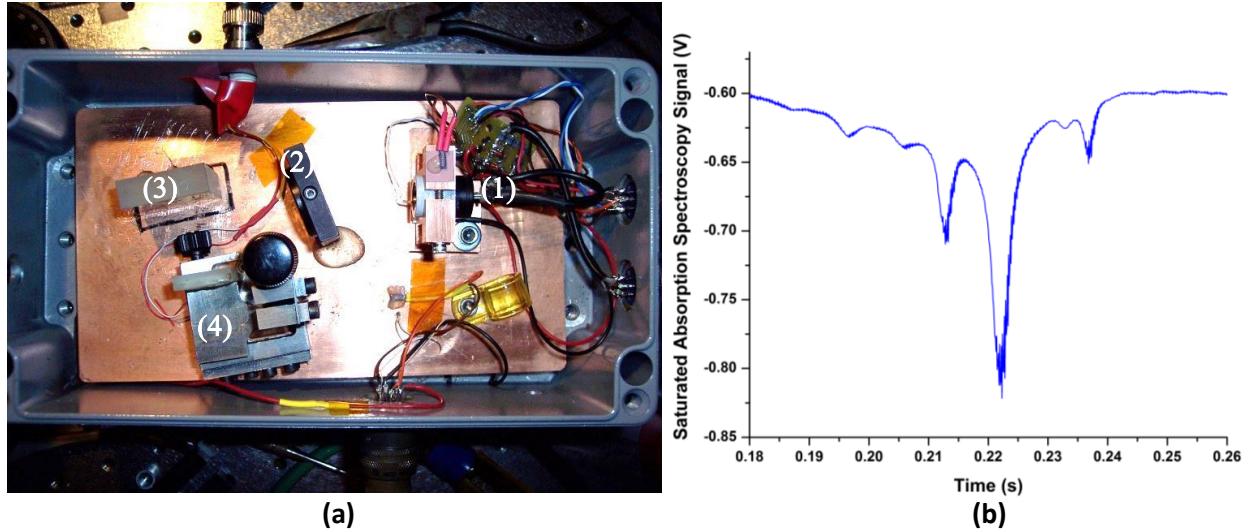
Figure 3.5: (a) Photograph of probe ECDL showing the laser diode (1), half-wave plate (2), diffraction grating (3), and wavelength selection mirror (4). (b) Saturated absorption spectroscopy signal for the probe laser scanning over the D2 manifold of ^{87}Rb. The $|F = 2\rangle \rightarrow |F' = 3\rangle$ cycling transition is on the far right of the scan and the largest two peaks are the $|F = 2', 3'\rangle$ and $|F = 1', 3'\rangle$ cross-over resonances, respectively.

The ECDL probe frequency was set by coarsely tuning the wavelength selection mirror until the laser output was sufficiently close to a transition to cause fluorescence in a Rb vapor cell in the saturated absorption setup. A piezoelectric actuator on the mirror mount with a high voltage control circuit was then used to fine-tune the laser frequency and scan over the D2 manifold. The saturated absorption signal from one such scan is shown in Fig. 3.5 (b), where $|F = 2\rangle \rightarrow |F' = 1, 2, 3\rangle$ transitions and the cross-over resonances are clearly visible. The probe light was combined with the repump and bichromatic lasers and coupled into the system through an optical fiber.

Roughly half-way through the bichromatic slowing experiments, the system was upgraded to directly load compact MOTs from the slowed atomic beam. As part of this process, the sensitive ECDL probe laser was exchanged for a robust distributed Bragg reflector (DBR) type diode from Vescent Photonics (the "MOT laser"). DBR diodes are particularly convenient as no external grating or moving parts are required for frequency control; rather, the diode is a two-part structure with an etched Bragg mirror following the gain medium that provides wavelength dependent feedback with a very small cavity length. Single-mode frequency tuning over tens of GHz is accomplished via the injection current. The diode was commercially mounted in a temperature controlled housing with a built-in anamorphic prism pair to correct the elliptical shape of the beam and had a maximum

38

output power of 40 mW (Fig. 3.6 (a)).

The MOT laser was locked to the $|F = 1', 3'\rangle$ cross-over transition with a saturated absorption spectroscopy setup using current modulation and NIST locking electronics. Cross-over resonances arise in saturated absorption spectroscopy of multi-level atoms when the high intensity pump beam acting on one transition creates a population reduction through optical pumping that decreases the absorption of the probe beam acting on a second transition. The resonances appear at a frequency exactly in between the two real transitions [56]. In our case, locking to the $|F = 1', 3'\rangle$ cross-over resonance red-detuned the laser frequency by ~ 212 MHz (Fig. 3.4 (a)). This frequency was brought back toward resonance by passing the MOT laser through an acousto-optic modulator (AOM) in a double-pass configuration [95]. AOMs are commonly used in optical systems to precisely shift the frequency of a laser over a range of hundreds of MHz. In a double pass configuration, the incident beam passes through the AOM and is shifted by plus or minus δ_{AOM}. A mirror retro-reflects the diffracted beam back through the AOM, shifting the frequency again such that the laser has a total frequency shift of plus or minus $2\delta_{AOM}$. On each trip through the modulator, the un-shifted component was blocked such that only the twice-diffracted beam passed through the system. For the MOT laser, the AOM had an RF frequency of $\delta_{AOM} \sim +106$ MHz such that after the double-pass arm, the trapping light was nearly on resonance with the $|F = 2\rangle \rightarrow |F' = 3\rangle$ cycling transition. Configuring the optics in this way provided easy control of the MOT laser detuning through the frequency of the voltage controlled oscillator (VCO) that generated the RF modulation for the AOM. The detuning of the trapping light is an important parameter of the scattering force and was continually optimized throughout the compact MOT experiments. After the double-pass, the MOT light was coupled into a polarization-maintaining optical fiber and sent to the UHV system.

Repump lasers are necessary in most cold-atom experiments to prevent atom loss caused by population transfer to the lower ground state hyperfine level ($|F = 1\rangle$ for Rb). With the MOT, probe, and bichromatic lasers all driving transitions from the $|F = 2\rangle$ ground state to the $5^2P_{3/2}$ excited manifold, atoms initially in the $|F = 1\rangle$ ground state and atoms that decay there via spontaneous emission will not interact with any of these fields. This results in atom loss that prevents a MOT from forming and precludes effective slowing by bichromatic forces. In our experiment, the repump light was provided by an 80 mW Eagleyard diode laser operating at 795 nm (Fig. 3.6 (b)). This was a distributed feedback (DFB) diode laser that was injection-current tuned and locked
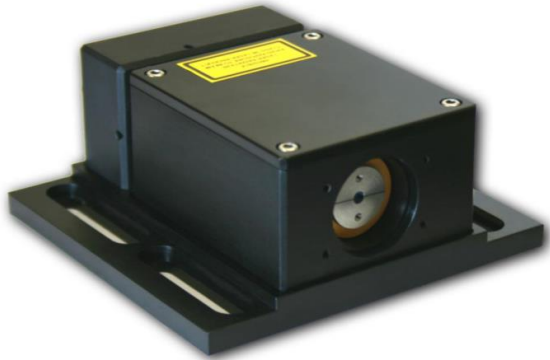
(a)   **(b)**

Figure 3.6: (a) Photograph of MOT DBR laser showing the commercial package. Lock stability was greatly improved over the home-built probe system shown in Fig. 3.5 (a). Image from Vescent Photonics website. (b) Photograph of the Eagleyard D1 DFB diode laser used as a repump in our bichromatic experiments. Image from Eagleyard Photonics website.
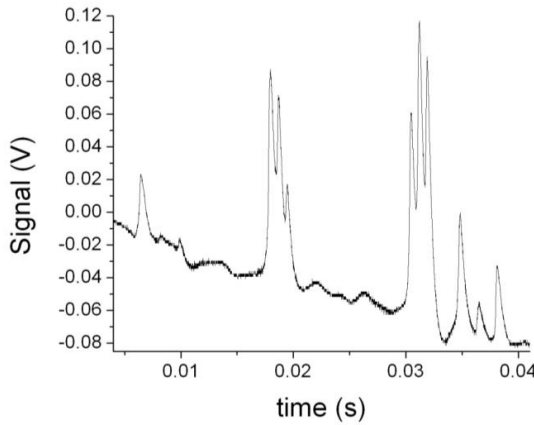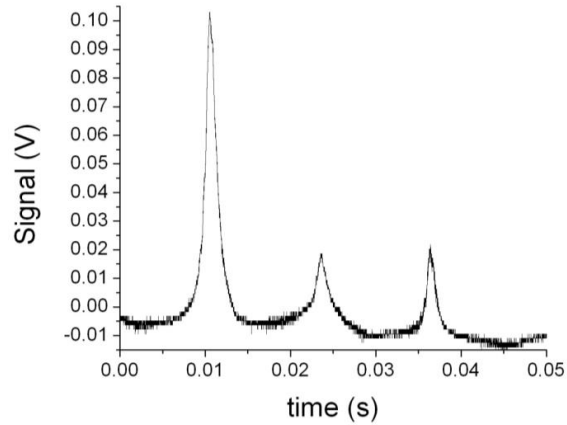
(a)   **(b)**

Figure 3.7: (a) Broad frequency scan of the D1 line for both ^{87}Rb and ^{85}Rb. From left to right, the transitions are ^{87}Rb $|F = 1\rangle \to |F' = 2, 1\rangle$, ^{85}Rb $|F = 2\rangle \to |F' = 3, 2\rangle$, ^{85}Rb $|F = 3\rangle \to |F' = 3, 2\rangle$, and ^{87}Rb $|F = 2\rangle \to |F' = 2, 1\rangle$. (b) Narrow frequency scan of the $|F = 1\rangle \to |F' = 2, 1\rangle$ transitions and the cross-over resonance for ^{87}Rb. The repump is locked to the strongest saturated absorption peak ($|F = 1\rangle \to |F' = 2\rangle$).

with a NIST lock-in amplifier and loop filter to the $|F = 1\rangle \rightarrow |F' = 2\rangle$ transition on the D1 line (Fig. 3.4) using a saturated absorption spectroscopy setup. Broad and narrow frequency scans of the repump laser spectrum are shown in Fig. 3.7. For the atomic beam experiments, the repump laser passed through an AOM with $\delta_{AOM} \sim 200$ MHz that was tuned for maximum diffraction efficiency into the -1 order. This red-detuned the repump light so that it would be centered in the Maxwell-Boltzmann distribution of the atomic beam. To further increase the number of atoms the repump laser could address, modulation was applied at $f_{mod} = 10$ MHz to the high-bandwidth port of the injection current controller to broaden the laser line. These effects combined to significantly improve the fluorescence signal size of our velocity distribution measurements. After the AOM, the repump laser was combined with the bichromatic and probe light and coupled into a polarization-maintaining optical fiber.

3.2.2   Bichromatic Laser and Optics Layout

The four frequencies forming the bichromatic standing wave were generated from a single high power laser diode and three different AOMs. One AOM created the $\pm\Delta$ frequency shifts, while the other two provided the additional $\pm kv_c$ offset that placed the force profile at a non-zero center velocity. Synthesizing the laser frequencies in this manner enabled independent control of Δ and kv_c such that the width and center velocity of the bichromatic force profile could be separately optimized for both beam slowing and MOT-loading experiments. A diagram of the optics layout for the bichromatic beam paths is shown in Fig. 3.8.

The bichromatic light was produced by a Photodigm DBR laser diode operating on the D2 line with 80 mW of single-mode output power and a sub-MHz linewidth. The diode was packaged in a TO-8 can with a built-in thermoelectric cooler and thermistor to manage the heat sensitivity of the device. As an additional precaution against overheating, the DBR was mounted in a custom copper mount designed to provide extra thermal conductivity to the aluminum heat sink and laser enclosure. Thermal paste or a single layer of Sil-Pad (composite material with high thermal conductivity) was applied between each component to improve the heat transfer away from the diode. The bichromatic laser box and TO-8 diode are shown in Fig. 3.9 (a).

The bichromatic light first passed through an optical isolator and polarizing optics to prevent feedback and generate a clean polarization before entering the first AOM. This AOM operated at
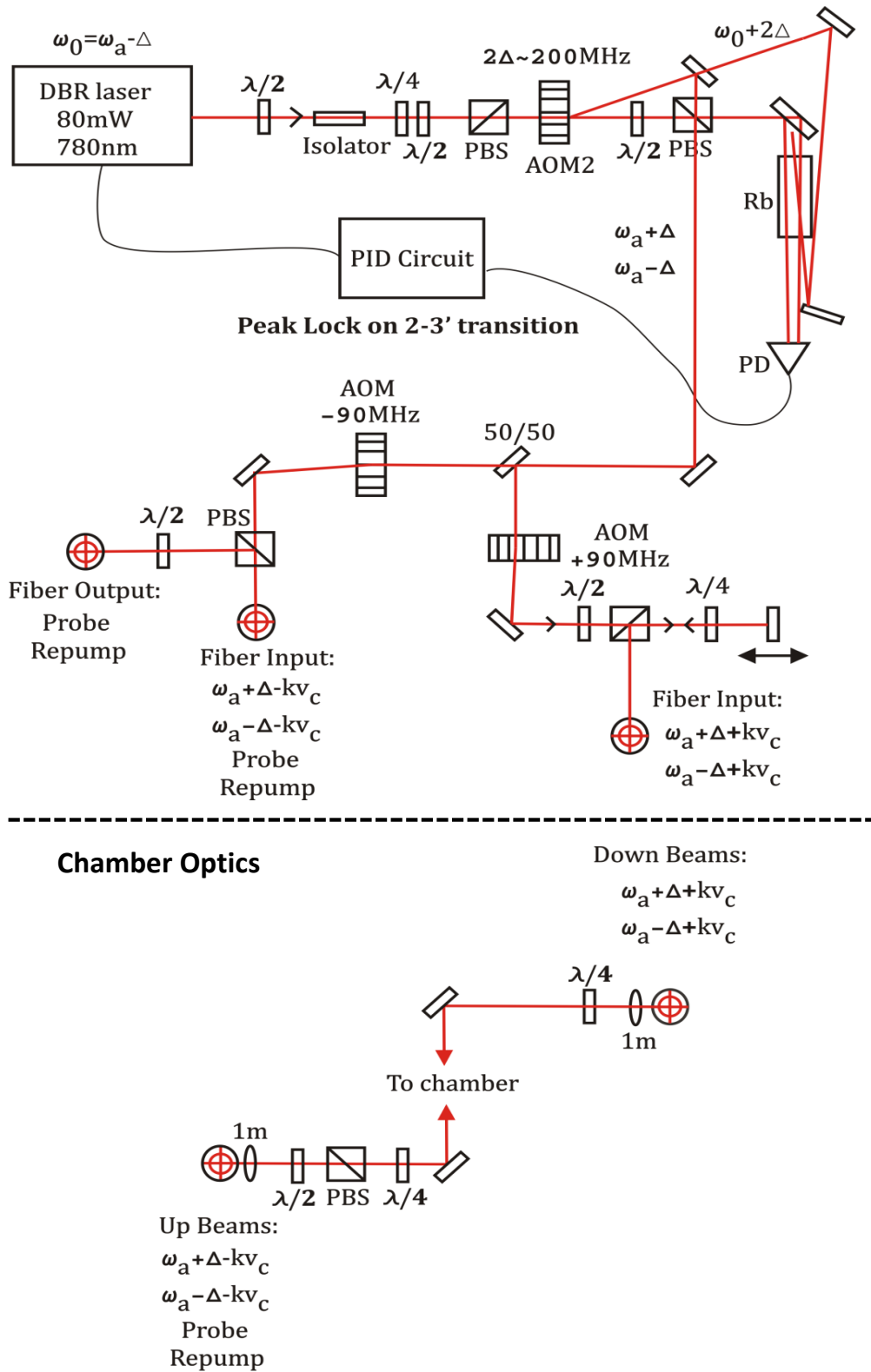
Figure 3.8: Optics layout used to generate the four bichromatic laser frequencies and couple the beams into the apparatus. Diagram courtesy of T.C. Liebisch.
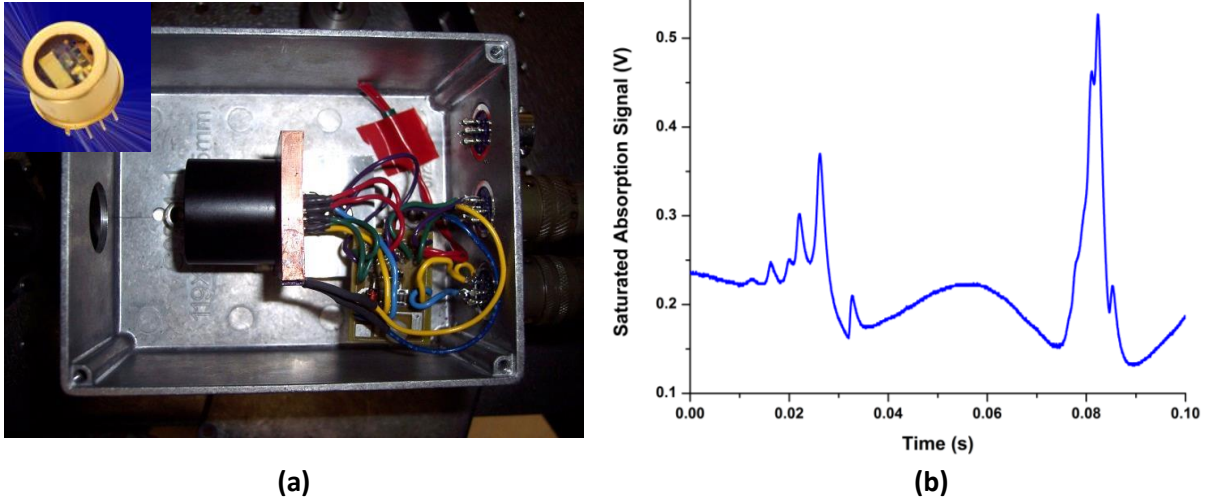
Figure 3.9: (a) Photograph of the home-built mount, protection board, and housing for the bichromatic laser. The diode was clamped against the copper heat sink/mount by the wired socket connector in the center of the image. The black lens tube held the collimating lens and screwed into the copper mount. Thermal paste was applied between each metal component to improve heat transfer to the box. Inset: Photograph of Photodigm DBR in TO-8 package (image from Photodigm website). (b) Saturated absorption spectroscopy signal for the bichromatic laser showing the $|F = 2\rangle \rightarrow |F'\rangle$ manifolds for ^{87}Rb (left manifold) and ^{85}Rb (right manifold).

an RF frequency of $\delta_{AOM} = 2\Delta \sim 200$ MHz and was tuned to diffract roughly 50% of the optical power into the $+1$ order while leaving the other half in the un-shifted 0th order. A small fraction of each AOM order was picked off and directed toward a saturated absorption spectroscopy setup, while the remaining light from both frequency components was combined on a polarizing beam splitter (PBS) and sent downstream. The spectroscopy configuration for the bichromatic laser was unique in that the pump beam, generated from the $+1$ order of the AOM, and the probe beam, generated from the 0th order, were separated in frequency by the AOM modulation of 2Δ.

The effect of this scheme is clarified by calculating the resonance condition for a saturation absorption spectroscopy peak. There will be an increase in transmission when the velocity class that the probe and pump beams interact with is the same: $v_{pump} = -v_{probe}$, where we assume the beams have minimal angular deviation from a perfect counter-propagating configuration. The selected velocity class is given by [56]:

$$v_{select} = \frac{\omega - \omega_a}{|\vec{k}|}, \tag{3.1}$$

where ω is the light frequency, ω_a is the resonant frequency for an atomic transition, and $|\vec{k}|$ is the amplitude of the wave vector. With the laser frequency ω_L, the pump and probe frequencies are then $\omega_L + 2\Delta$ and ω_L, respectively. Inserting these into the resonance condition gives:

$$\frac{\omega_L + 2\Delta - \omega_a}{k} = -\left(\frac{\omega_L - \omega_a}{k}\right)$$
$$\omega_L + 2\Delta - \omega_a = -\omega_L + \omega_a \qquad (3.2)$$
$$\omega_L = \omega_a - \Delta.$$

The frequency offset between probe and pump beams results in the laser lock being red-detuned from the atomic resonance by half the AOM RF frequency: $\omega_a - \Delta$. Using this saturated absorption spectroscopy configuration, the bichromatic laser was locked to the $|F = 2\rangle \rightarrow |F' = 3\rangle$ transition frequency on the D2 line using a NIST lock-in amplifier and loop filter such that ω_a was the resonance frequency of the cycling transition. Accordingly, the two output beams from the first AOM at frequencies ω_L and $\omega_L + 2\Delta$ when written relative to the atomic resonance were $\omega_a \pm \Delta$. These two frequencies established the standing wave beat of the bichromatic force, and the RF detuning of this AOM determined the width of the force profile and the power required for the Rabi frequency to match the π-pulse condition.

After the locking optics, the two frequency components of the bichromatic beam were sent downstream to a 50/50 beam splitter, where they were divided evenly into two separate arms. Each beam then passed through a second AOM with an RF frequency of $\delta_{AOM} = kv_c \sim 90$ MHz. One AOM was tuned to maximize the diffraction efficiency of the +1 order to shift the frequency by $+kv_c$, while the second AOM was aligned to maximize the -1 order, shifting the beam by $-kv_c$. The frequency of these two AOMs provided the mechanism for shifting the bichromatic force profile along the velocity axis of the atomic beam. The pair of AOMs was controlled by a single VCO to ensure that the frequency and phase of the RF modulation generating the optical frequency shift was exactly equal for both beams. In the $+kv_c$ arm, a mirror mounted on a translation stage formed an optical delay line used to set the relative phase between the counter-propagating bichromatic beams. As discussed in Section 2.2.1, the relative phase between the two beams was critical for establishing a strong net bichromatic force that opposed the atomic beam.

The $\pm kv_c$ components were then coupled into separate polarization-maintaining optical fibers.
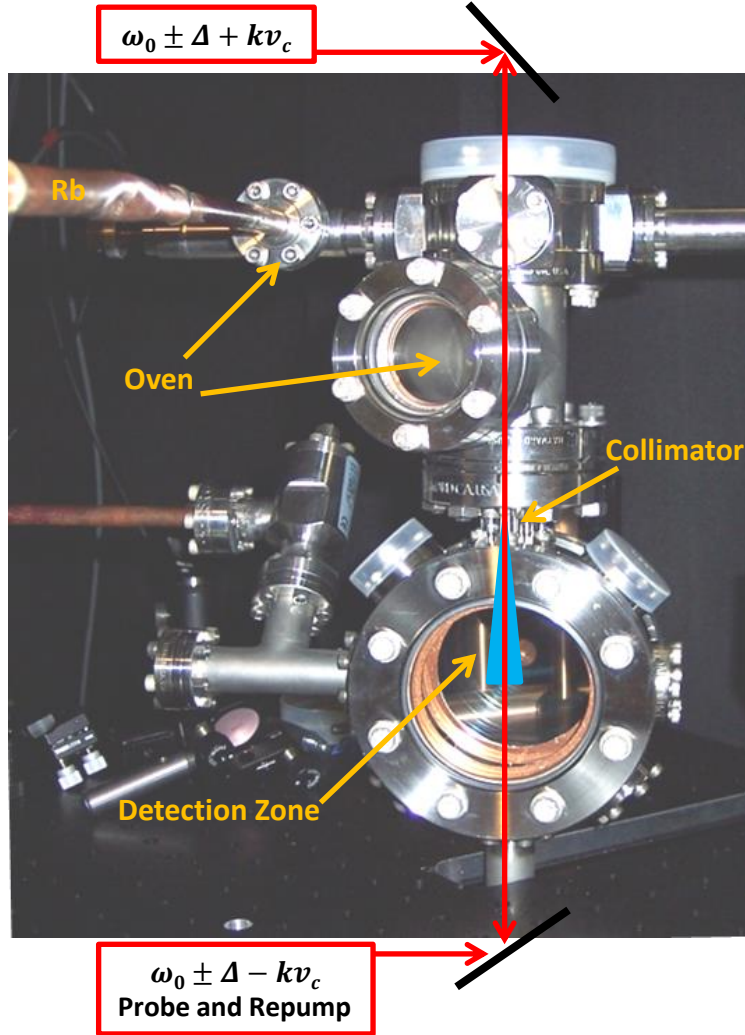
Figure 3.10: Bichromatic, probe, and repump beam paths (red) relative to the UHV chamber. Major components are labeled and the atomic beam is shown in blue.

In the $-kv_c$ arm, the probe and repump light was combined with the $-kv_c$ bichromatic frequency components on a PBS and coupled into a single fiber. This fiber led to the vacuum chamber, where the output coupler directed the probe, repump, and $-kv_c$ bichromatic light through polarizing optics and into the chamber from the bottom, opposite the direction of the atomic beam. The $+kv_c$ fiber had an output coupler on the elevated breadboard shown in Fig. 3.2. The beam also passed through optics to set the polarization and was then directed into the apparatus from the top, oriented to co-propagate with the atomic beam. The polarizing optics at the output of each fiber generated circularly polarized bichromatic laser beams to efficiently drive the $|F = 2\rangle \rightarrow |F' = 3\rangle$ cycling transition, a nearly ideal two-level system. Before entering the chamber, each bichromatic

frequency component had 1.3 mW of power, for a total optical slowing power of 5.2 mW. In order to increase the Rabi frequency of the bichromatic field without using a high-power laser diode, and to ensure that the beams completely cleared the 500 μm apertures in the collimating assembly, both $\pm k v_c$ beams passed through a 1 m focal length lens. This long focal length produced a gradually changing intensity profile that focused down to a diameter of 0.32 mm ($1/e^2$) in between the apertures and slowly expanded throughout the science chamber. Before assembling the vacuum system, we verified on the bench that 100% of the light could be transmitted through the collimator with this optics configuration. The orientation of the bichromatic beams, as well as the probe and repump, is shown with the vacuum chamber in Fig. 3.10.

3.3   Signal Detection

In both atomic beam and MOT atom number experiments with the bichromatic force, signals of interest were collected either by fluorescence detection or absorption imaging. Most experimental data was collected from fluorescence, while absorption imaging was used to characterize certain aspects of the system. These detection schemes are discussed in this section.

3.3.1   Atomic Beam Detection

For the series of experiments used to explore and optimize the effectiveness of the bichromatic slowing force, most data was derived from the collection of fluorescence photons from the atomic beam. As discussed above, the probe laser was coupled into the $-k v_c$ bichromatic fiber and injected in the system longitudinally, opposing the atomic beam. The power of the probe was kept low (< 10 μW or $< 5 \times I_{sat}$) to avoid distorting the measured velocity distribution. A ramp voltage was applied to the probe, sweeping the frequency over the ^{87}Rb $|F = 2\rangle \rightarrow |F'\rangle$ manifold. As the probe frequency shifted into resonance with different velocity classes within the atomic beam, atoms in the resonant class would absorb probe photons, excite to the upper state, and eventually decay via spontaneous emission. The fluorescence from this cycle was recorded over the full scan of the probe frequency and used to calculate the velocity distribution of the atomic beam.

Fluorescence was measured using a Hamamatsu H5783-20 photo-multiplier tube (PMT) mounted inside a lens tube with a 25.4 mm diameter, short focal length plano-convex collection lens at the

end. The PMT was chosen over a standard photodiode due to a few advantageous properties including high gain, fast response time, and a large dynamic range; it had a 200 kHz bandwidth and a collection sensitivity of 0.5 V/nW of fluorescence. The PMT was mounted directly next to the science chamber and pointed through one of the large 4.5" windows, maximizing the solid angle over which it could collect fluorescence.

The fluorescence signal from the PMT was sent to a National Instruments PCI-6281 data acquisition (DAQ) card that was the interface between the experiment and the LabVIEW control software. The LabVIEW program was written to control experiment parameters, including pulse sequences and laser intensities/frequencies, as well as to collect and analyze fluorescence and calibration data. For the atomic beam experiment, both the absorption recorded by the photodiode in the saturated absorption spectroscopy setup for the probe laser and the fluorescence signal from the atomic beam were recorded. The probe scan over the $|F = 2\rangle \rightarrow |F'\rangle$ manifold (top-left pane of Fig. 3.11) was used to calibrate the time-axis of the recorded fluorescence from the atomic beam and convert it to frequency. First, the computer recorded both signals and the user partitioned the probe spectroscopy scan data with cursors, selecting the $|F = 2\rangle \rightarrow |F' = 3\rangle$ transition and $|F = 2', 3'\rangle$ cross-over resonance (top-right pane of Fig. 3.11). The software applied a double-peak Lorentzian fit to the two resonances (bottom-left pane of Fig. 3.11) to identify the center of each feature and used the known 133 MHz separation to calibrate the time axis of the probe scan. This provided a time to frequency conversion for the recorded atomic beam fluorescence signal, which was displayed in the software and exported as volts vs. frequency data for later analysis (bottom-right pane of Fig. 3.11). This software dramatically improved our ability to quickly analyze experiment data and was particularly valuable for optimizing the bichromatic force based on atomic beam measurements.

To obtain a high signal to noise (S/N) ratio fluorescence measurement of the atomic beam velocity profile, the slowing and probe laser beams could not be simultaneously turned on. Inadvertent pulse overlap resulted in significantly reduced and distorted signals due to spontaneous emission occurring as part of the bichromatic slowing process that was uncorrelated with the probe frequency scans. To avoid this complication, the experiment operated with a pulse sequence tuned to ensure that the slowing and probe fields were temporally isolated. The timing sequence for each of the lasers and the detection system is shown in Fig. 3.12 (a). This series of pulses switched on
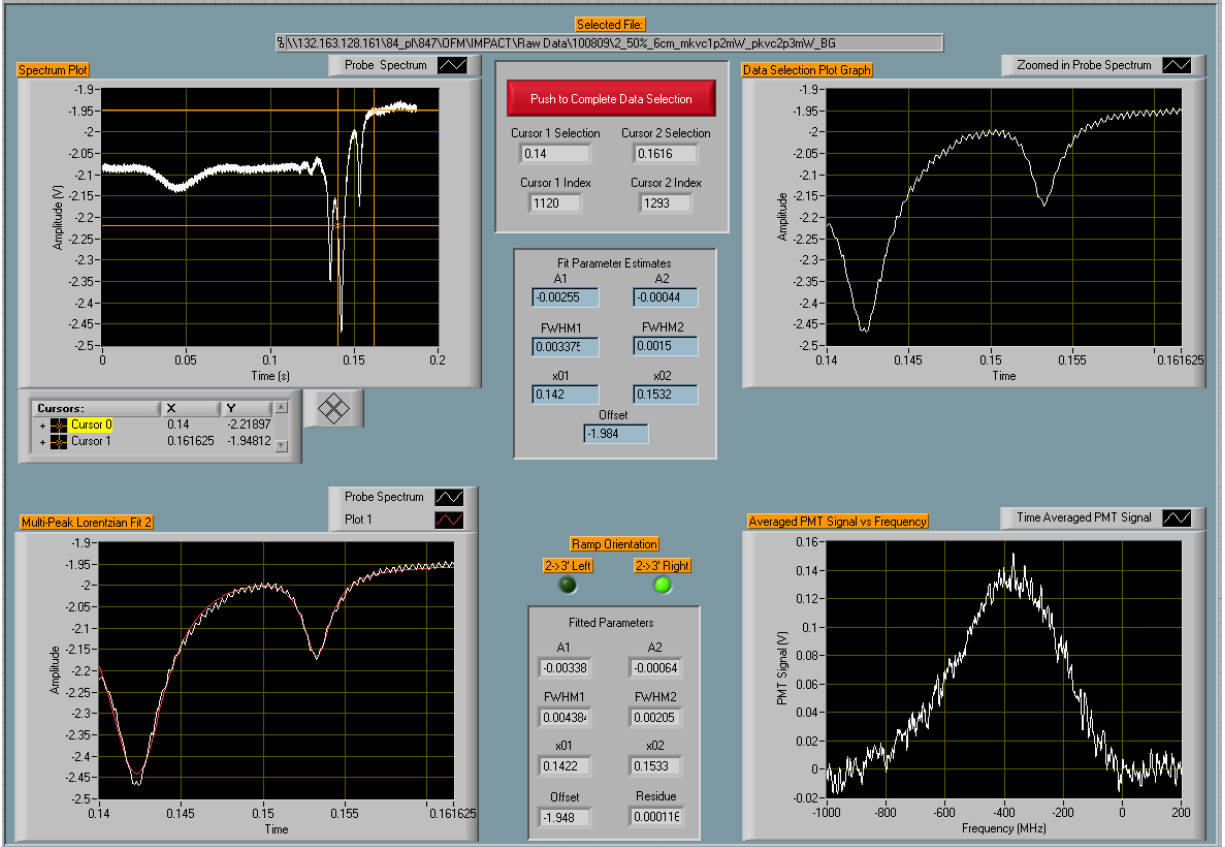
Figure 3.11: Front panel screen shot of the LabVIEW control program used for atomic beam experiments. The software recorded the probe scan from the saturated absorption spectroscopy setup (top-left pane) and used a multi-peak Lorentzian fit to calibrate the frequency axis of the atomic beam fluorescence collected during the probe scan (bottom-right pane).

the probe laser at the same time that the bichromatic laser was shut off, while the PMT signal was collected over a shorter time period in the middle of the probe pulse. Reducing the PMT collection period such that it was completely within the probe pulse guaranteed that transients from the rise and fall time of the laser pulses did not affect the data.

The light pulses in this experiment were generated by rapidly jumping the RF frequency of the AOMs in the probe, repump, and bichromatic beam paths such that δ_{AOM} was outside the bandwidth of the device. This has the effect of exponentially decreasing the diffraction efficiency of the AOM, effectively turning off the modulated output. Since AOM switching times are on the order of hundreds of ns, this technique is well suited for the tens of μs-long pulses used in this experiment. To switch the frequency of the VCO driving each AOM, a multi-channel multiplexer circuit was built that used a TTL pulse to jump between two arbitrary voltages corresponding to
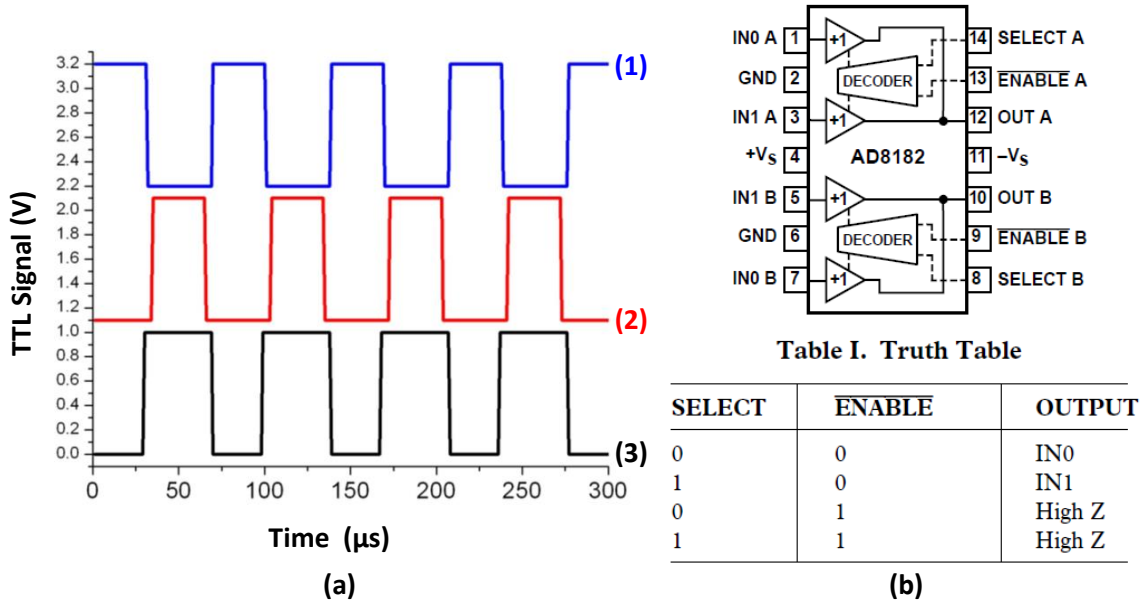
Figure 3.12: (a) Timing diagram for the atomic beam detection sequence showing the TTL control pulses for the bichromatic and repump light (1, blue), the PMT (2, red) and the probe laser (3, black). Each component is on when the TTL is high. The sequences have been offset vertically from one another for clarity. A lock-in amplifier referenced to the TTL pulses for the PMT was used to improve the S/N in the atomic beam detection. (b) Functional block diagram and truth table for the AD8182 multiplexer chip taken from Analogue Devices supporting documentation.

the desired "on" and the far detuned "off" AOM frequencies. The circuit featured several AD8182 multiplexer chips (Fig. 3.12 (b)) that output one of two voltages depending on whether the TTL at the select port was high or low. The output voltages were controlled by potentiometers, enabling continuous control of the VCO voltage and thus, the AOM RF frequency. This same technique was used to control the PMT fluorescence collection. The PMT collected continuously, but the signal voltage was connected to one of the input ports (IN0) of a multiplexer chip while the other (IN1) was grounded. The output of the chip was connected to the DAQ input such that a TTL from the software on the select port would determine when the PMT signal was collected and when it was blanked. All of the TTL signals in the experiment were generated by a NI PCI-6534 digital input/output (DIO) card controlled by the LabVIEW program. During typical operation, the pulse durations were on the order of 30 μs long.

Example atomic beam data collected with this fluorescence detection scheme is shown in Fig. 3.13, including a calibration figure and a fitted measurement of the Maxwell-Boltzmann distribution used to verify that the temperature of the Rb oven is roughly $100°$C.

(a) **(b)**
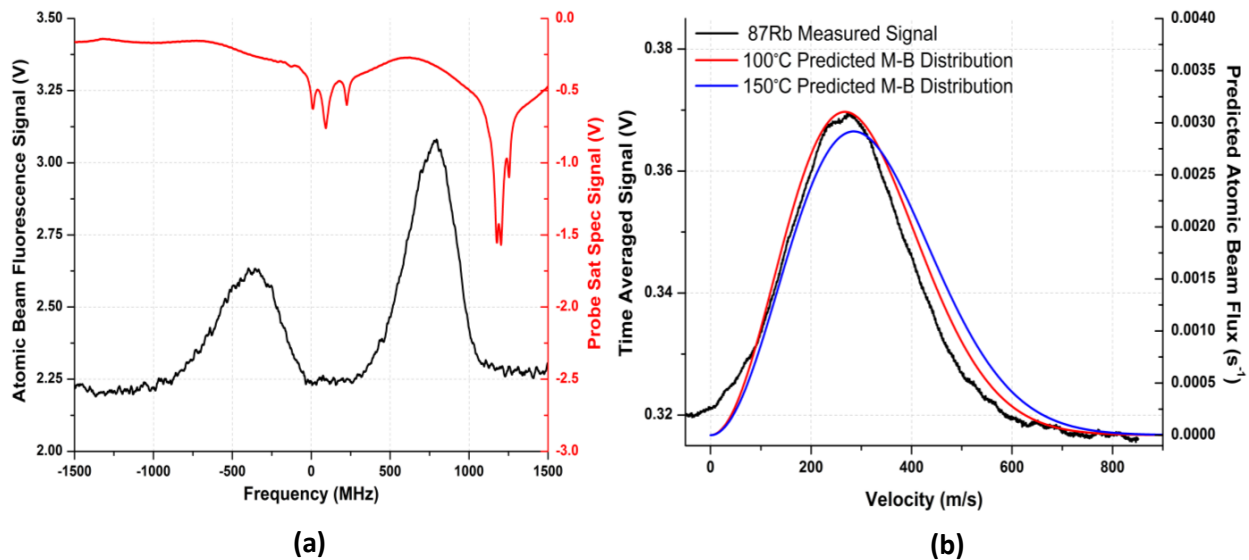
Figure 3.13: (a) Example calibration showing the atomic beam fluorescence signal (black) and the probe saturated absorption spectroscopy scan (red). (b) Measurement of the Maxwell-Boltzmann velocity distribution of the atomic beam compared with theoretical predictions for a 100°C and 150°C atomic beam. The two theory curves are plotted against the right axis while the experimental data is plotted against the left axis. From this type of measurement, we have determined that our oven is operating at approximately 100°C.

(a) **(b)**
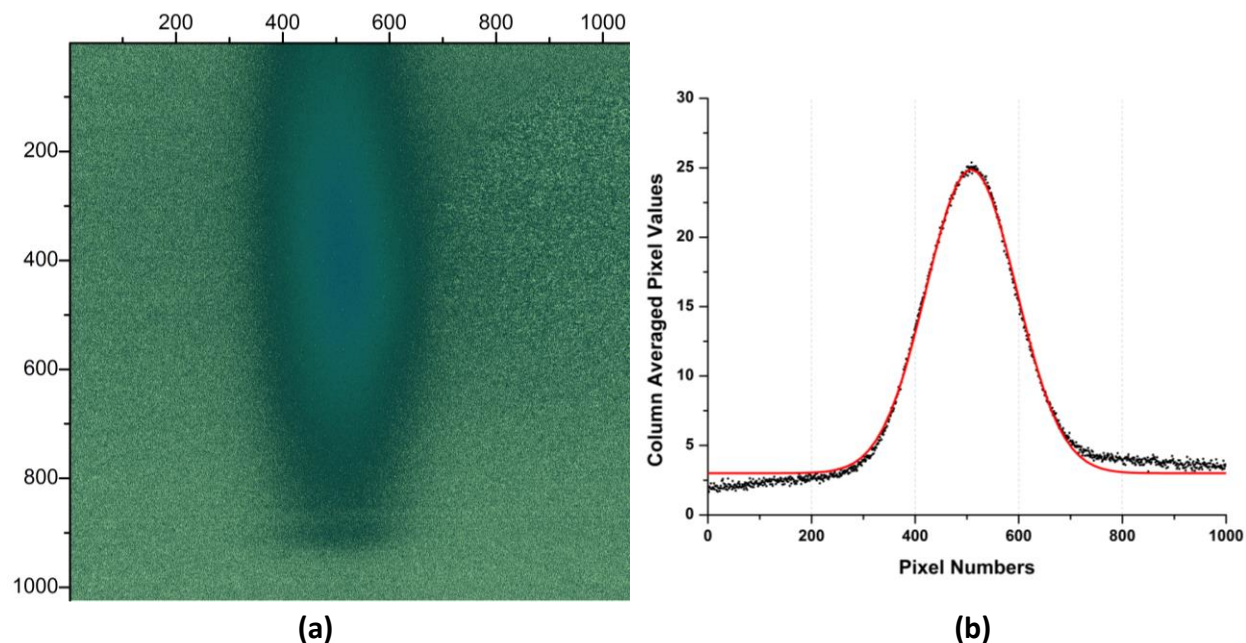
Figure 3.14: (a) Background-subtracted absorption image of the atomic beam taken in the low gain video mode with the Pixelfly CCD camera and a 15 s exposure. (b) Average column value over the range of horizontal pixels and a Gaussian fit. From this fit, the diameter of the atomic beam was determined to be ~ 2.25 mm.

To spatially characterize the atomic beam, an absorption imaging system was assembled by switching the probe laser fiber to an output coupler that directed the beam horizontally through the science chamber. Upon exiting, the beam passed through a neutral density filter and was aligned onto a Pixelfly CCD camera with a 1:1 lens system attached. The laser pulses for the absorption imaging sequence were controlled by the software and multiplexer circuit in the same manner described above. The Pixelfly camera was a high quality 12 bit CCD with a quantum efficiency of up to 65% and exposure times ranging from several μs to tens of seconds. The camera is computer controlled via a PCI board and was integrated into the LabVIEW software (see Section 3.3.2). Imaging the atomic beam required three separate images to be collected: one image with the probe on resonance with the atomic transition, one image with the probe far detuned from resonance, and a final image with the probe laser turned off. The second image was subtracted from the first to remove unabsorbed probe light and create a difference in the pixel values at the location of the atomic beam, while the third image was used to remove any stray-light background. The probe beam was circularly polarized with a power on the order of tens of μW.

An absorption image of the atomic beam collected using this procedure is shown in Fig. 3.14 (a). From this type of measurement, the diameter of the beam can be calculated by performing a column average, fitting the result to a Gaussian function (3.14 (b)), and multiplying the diameter $(1/e^{-2})$ by the 6.45 μm pixel width. This was done for several images of the atomic beam with the average $1/e^{-2}$ diameter found to be $\bar{d}_{beam} = 2.25 \pm 0.01$ mm.

3.3.2 MOT Detection

In the compact MOT experiments, fluorescence detection was the primary data acquisition technique used to measure the main characteristics of interest: the atom number and loading rate. The same photomultiplier tube and data acquisition hardware described in the previous section were used, and new LabVIEW software was written to control the experiment and collect data. No probe laser was needed for these measurements as both the atom number and loading rate could be extracted from the fluorescence generated by atoms interacting with the cooling light as they were trapped during the MOT loading process. Accordingly, the PMT signal was not blanked with multiplexer electronics during these measurements, and data was collected continuously as the MOT formed.

The MOT experiment control software integrated the sequence generation code with analysis capabilities for the loading curves. The user could program TTL control pulses for the lasers, coils, and detection system into the sequencer and then continuously run the sequence. From the detection panel, the number of MOTs to average was selected, and the program would display each individual loading curve in one plot and the running average in second plot. After completing the specified number of averages, the program would run a routine to fit the fluorescence curve to an exponential loading function and would export the raw data and fit parameters. The loading rate and atom number could then be extracted from this data.

To determine the atom number and loading rate from the fluorescence signal, the collected data was fit to the following expression for the atom number as a function of time:

$$N(t) = N_0 \left(1 - e^{-t/\tau}\right), \tag{3.3}$$

where N_0 is the voltage corresponding to the steady state atom number (N_{ss}), and τ is the loading time, defined as the e^{-1} time constant or the time required for the MOT to reach $\sim 63\%$ of the steady state atom number. Three parameters are needed to calculate the atom number from the amplitude of the fit: the power emitted per atom (P_{atom}), the PMT response (α_{PMT}), and the collection efficiency of the detection configuration (ϵ). With this information, the atom number is given by:

$$N_{SS} = \frac{N_0}{\epsilon P_{atom} \alpha_{PMT}}. \tag{3.4}$$

The response of the Hamamatsu PMT was $\alpha_{PMT} = 0.5$ V/nW. The collection efficiency is a geometric factor given by the fraction of total solid angle around the MOT covered by the collection lens. For a lens of radius r_L located a distance d_L from the MOT, the collection efficiency is then:

$$\epsilon = \frac{\pi r_L^2}{4\pi d_L^2}. \tag{3.5}$$

For our system, the collection lens was 25.4 mm in diameter and located 150 mm from the center of the chamber, giving a collection efficiency of $\epsilon = 1.79 \times 10^{-3}$. This was eventually improved by switching to a 50 mm diameter collection lens. Accurately calculating the power per atom is challenging as the transition probabilities between all of the Zeeman sublevels in the ground
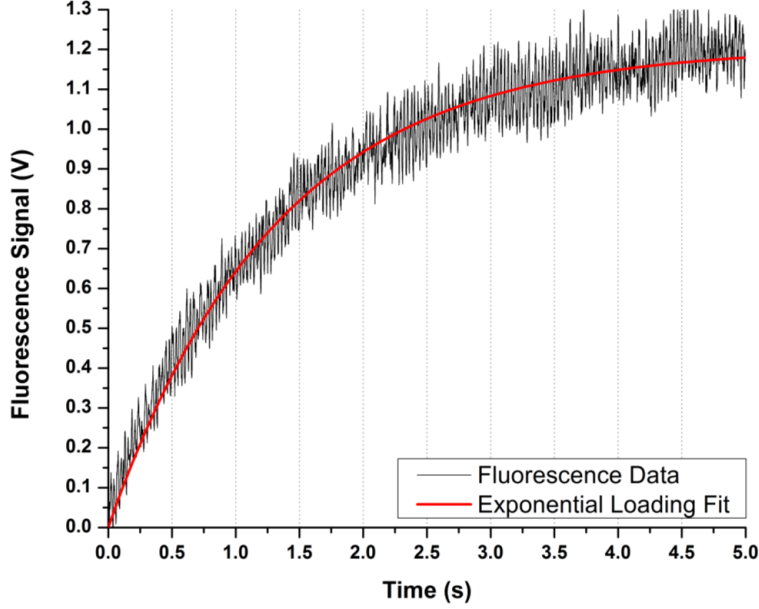
Figure 3.15: Fluorescence loading curve (black) of an early MOT. The data was fit to the exponential given in Eq. 3.3 from which the loading rate and atom number were determined. For this curve, 2×10^6 atoms were trapped in a loading time of 1.32 s using MOT light with 1.3 mW per beam and detuned by $\sim 2\gamma$, 200 μW of repump, and a gradient of $\sim$ 10 G/cm.

and excited states are needed. Experimentally, this involved calculation is typically avoided by assuming averaged Clebsch-Gordan coefficients, C_1 and C_2, and calculating the power from the following [96]:

$$P_{atom} \cong \hbar\omega \frac{\Gamma}{2} \frac{\frac{1}{2}C_1^2\Omega_{tot}^2}{\delta^2 + \frac{1}{4}\Gamma^2 + \frac{1}{2}C_2^2\Omega_{tot}^2}. \tag{3.6}$$

In this expression, Ω_{tot} is the Rabi frequency of the trap including the intensity contributions from the six individual MOT beams, and δ is the detuning of the MOT laser. For our calculation, the experimentally measured value for Cs, $C_1^2 = C_2^2 = 0.73$, was used [96]. Combining Eqs. 3.3-3.6, we can calculate the atom number and loading rate (N_{ss}, τ) from fits to the fluorescence loading curve. An example of a single shot MOT loading curve is shown in Fig. 3.15 along with the exponential fit.

While most of our MOT data was collected via fluorescence detection, we did design and implement an absorption measurement capability as well. The system used the same CCD camera, probe laser, and 1:1 imaging configuration described in Section 3.3.1, however new LabVIEW software was developed to integrate the imaging and MOT loading sequences (Fig. 3.16). As

53
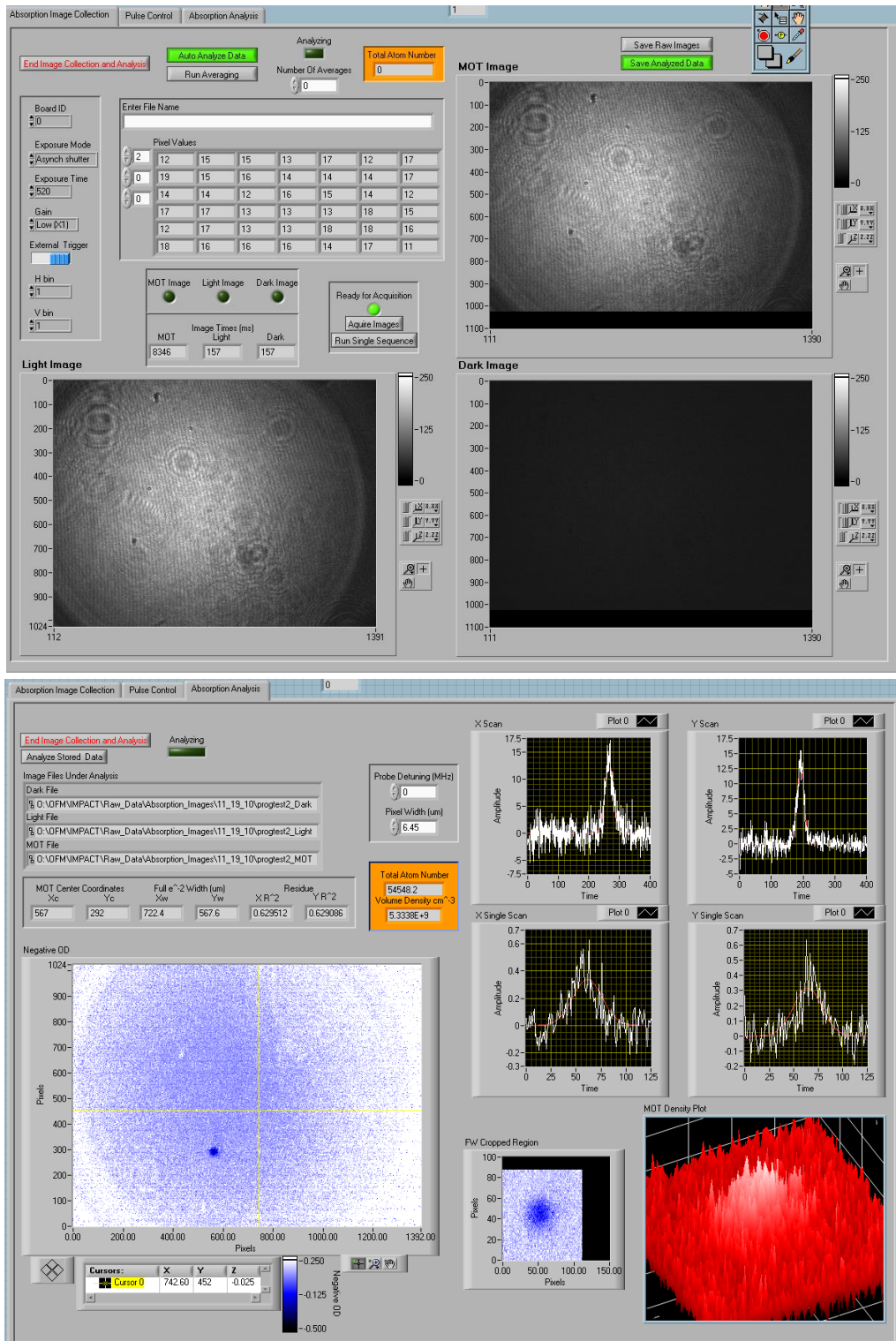
Figure 3.16: Collection (top) and analysis (bottom) panes for the MOT absorption imaging software. The dark blue spot in the lower pane is the MOT.

before, three images were required to remove background effects and determine the absorption. The first image was collected with the MOT present, while the second image was collected with the detuning ramped to remove the MOT and image the probe beam. The final image was taken with all lasers off to remove background effects. The timing for the lasers, magnetic fields, and image collection was controlled by coding the sequence into the pulse control pane which would trigger the DIO to send TTLs to the appropriate channels. The absorption image collection panel controlled the CCD settings and displayed the individual images, while the analysis panel performed the image subtraction and column/row averaging to identify the center point of the MOT. The software then automatically cropped the image and determined the atom number from Beer's law describing the intensity loss due to absorption:

$$I\left(z\right) = I_0 e^{-n\sigma z}, \tag{3.7}$$

where n is the atomic number density, σ is the absorption cross-section, I_0 is the initial intensity, and z is the position along the beam. From this, the atom number was calculated by solving for n, writing down the absorption cross section as a function of detuning, removing the background noise, and summing the contribution from each pixel that imaged the MOT:

$$N_{ss} = \sum_{pixels} \frac{A_{pixel}}{\sigma_0} \left[1 + 4\left(\frac{\delta}{\Gamma}\right)^2 \right] \ln\left(\frac{I_{light} - I_{dark}}{I_{MOT} - I_{dark}}\right). \tag{3.8}$$

In this equation, A_{pixel} is the pixel area, σ_0 is the resonant cross section, δ is the probe detuning, I_{MOT} is the image with the trapped atoms, I_{light} is the image with the probe on but far detuned, and I_{dark} is the background image with all laser beams turned off.

While this procedure provided an efficient means of taking data, it was vulnerable to noise issues in the image subtraction and exhibited shot-to-shot fluctuations. Fluorescence detection provided higher S/N and was used for the small MOTs measured in our experiment. However, we did use the absorption setup to characterize the MOT position relative to the atomic beam. Two example images are shown in Fig. 4.15 (b).

CHAPTER 4

BICHROMATIC EXPERIMENT RESULTS

This chapter summarizes the results of our bichromatic slowing experiments [69]. Measurements of the atomic beam velocity distribution used to explore the capabilities of the technique and optimize the force profile will be presented, along with measurements of the MOT atom number and loading rate enhancements testing the scalability of the technique for potential use in a compact device.

4.1   Atomic Beam Measurements

The goal of the atomic beam experiments was to optimize the effect of the bichromatic force on the Maxwell-Boltzmann velocity distribution of the atomic beam while minimizing the interaction length and required optical power to stay within the spirit of the IMPACT program. Previous experiments using the bichromatic force obtained impressive results, slowing an 80°C Cesium atomic beam such that 1% of the flux had a velocity below 35 m/s [80]. However, to manipulate the distribution to this degree, the authors used 160 mW of bichromatic optical power and performed the slowing over a 10 cm interaction length. The question our experiment sought to answer was whether similar results could be obtained using just $\sim 4\%$ of the optical power to slow an atomic beam over an interaction length of less than one cm and subsequently load it into a MOT. The measurements below reveal that this is indeed possible.

4.1.1   Bichromatic Force Characterization

For reasons discussed in Section 4.1.2, the strongest signal in our atomic beam experiments with the bichromatic force came with the relative phase between the counter-propagating slowing beams set to $\phi = -\pi/2$, corresponding to an accelerating force exerted in the same direction as the atomic beam velocity. All of the data in this section was collected with this relative phase to provide the largest signal to noise ratio for optimizing the bichromatic force profile, center velocity, and detection parameters. Unless otherwise noted, the force profile was centered at 74 m/s
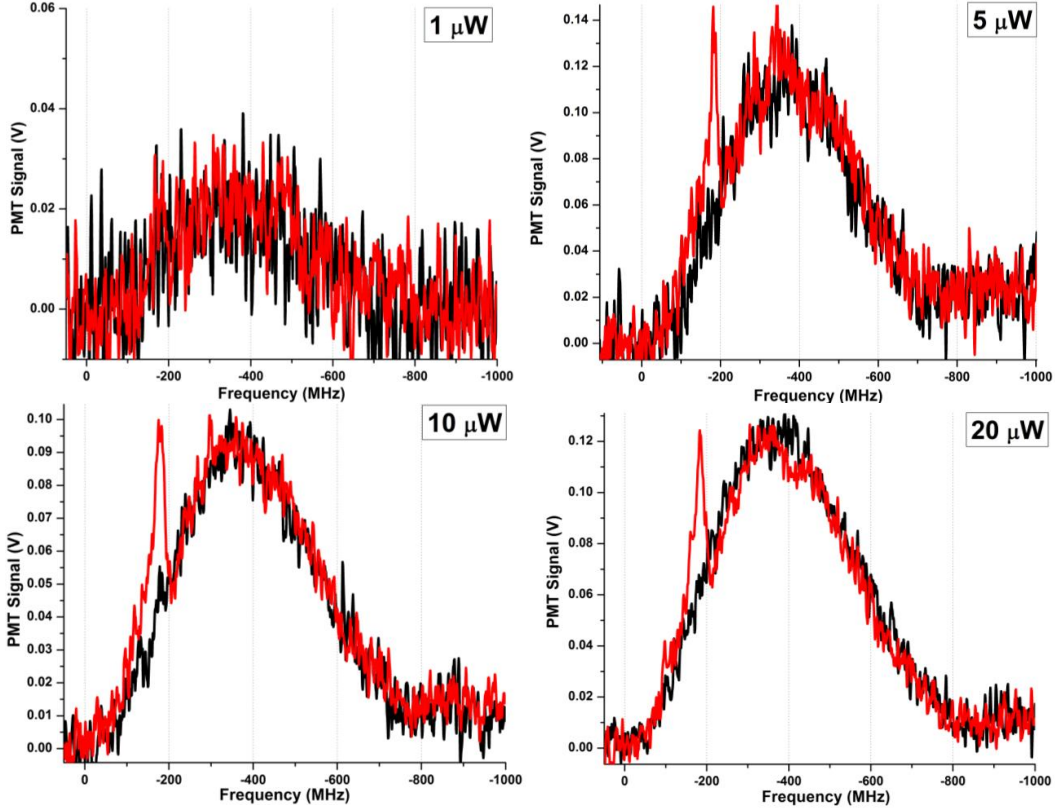
Figure 4.1: Atomic beam measurements with (red) and without (black) bichromatic forces applied for varied probe laser power.

corresponding to a $\pm k v_c$ AOM frequency of 95 MHz. The peak appearing in velocity distributions modified by the bichromatic force arose from atoms within the target velocity class being accelerated and deposited at the high frequency/velocity edge of the force profile. This is the signal used to optimize the force.

Characterization measurements of the velocity distribution for varied probe laser power were performed to ensure that the detection system did not distort the data, either through a large intensity causing broadening of the detection transition or an unclean polarization driving transitions other than $|F = 2\rangle \rightarrow |F' = 3\rangle$ for different velocity classes. A representative sample of this data is shown in Fig. 4.1. Based on these results, the optimum probe power was determined to be $\sim 5 - 10$ μW, corresponding to $2 - 4\times$ the saturation intensity. While the S/N ratio was slightly better for higher probe powers, the distribution began to distort due to interactions with off-resonant transitions (20 μW data in Fig. 4.1).

Setting the Rabi frequency as a function of bichromatic detuning (Δ) such that the π-pulse
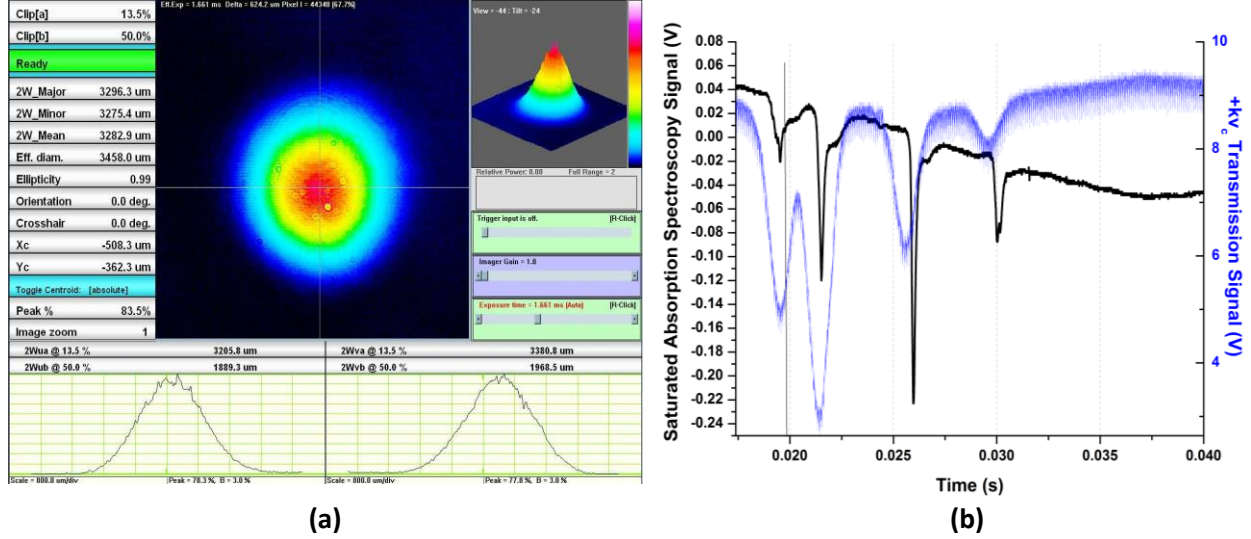
Figure 4.2: (a) Laser beam profiler output for the $+kv_c$ beam after passing through the system. (b) Absorption of the $+kv_c$ beam after passing through the system (blue) and the saturated absorption spectroscopy signal used to identify the transition manifolds (black).

condition is approximately satisfied was important for generating a strong bichromatic force. As mentioned in Chapter 2, the optimum value was best determined experimentally as it differed slightly from the theoretical prediction. Complicating matters in our system were the 500 μm apertures and the Rb oven the bichromatic beams had to pass through to transit the system. While we verified 100% transmission before constructing the UHV chamber, it was unclear whether all the bichromatic power was passing through the system with it fully assembled and if the beam mode was affected. To check this, a laser beam profiler was used to measure the intensity profile of both the $\pm kv_c$ lasers after exiting the vacuum chamber. The output of the profiler (Fig. 4.2 (a)) revealed that both beams maintained a clean Gaussian profile after passing through the system; there was no clipping on the apertures, and the windows were not introducing distortion. However, as shown by the data in Fig. 4.2 (b), the absorption of the $+kv_c$ beam in the 100°C Rb oven was significantly larger than expected, approaching 40% on the $|F = 2\rangle \rightarrow |F'\rangle$ manifold used for cooling. To account for this and apply a balanced bichromatic field, the counter-propagating intensities were set at a ratio of $I_{-kv_c}/I_{+kv_c} = 0.6$. These measurements helped reduce errors in the applied Rabi frequency of the bichromatic fields.

With the system-dependent balance between the counter-propagating beams measured, the optimal Rabi frequency for a given bichromatic detuning could be experimentally determined by
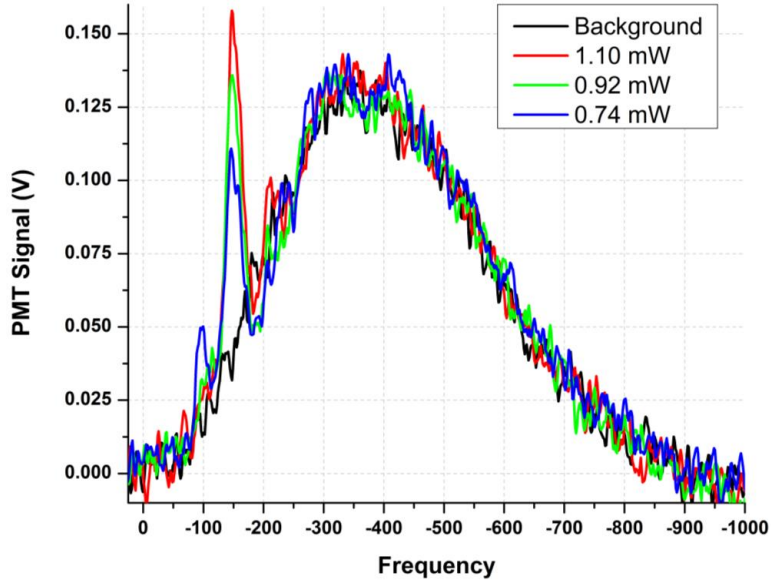
Figure 4.3: Atomic beam measurements for varied bichromatic laser intensity, showing the dependence of the force on the applied Rabi frequency. Here, the bichromatic beat frequency was $2\Delta = 2\pi \times 177$ MHz $\to \Delta = 15\gamma$, and the power labels are for the $-kv_c$ frequency component.

varying the absolute intensity and observing the effect on the velocity distribution. For the data shown in Fig. 4.3, the AOM generating the bichromatic beat frequency was operating at 177 MHz, giving a bichromatic detuning of $\Delta = 0.5 \times 2\pi \times 177$ MHz $= 15\gamma$ when written in terms of the natural linewidth. The number of atoms accelerated by the bichromatic force grew until saturating at ~ 1.1 mW of laser power in each bichromatic frequency component. For a beam waist of ~ 0.2 mm at the center of the science chamber, this corresponds to $\Omega_R = 16\gamma$ and falls within the experimentally reported range [80, 81]. Based on repeated measurements of this type, the experiment typically operated with ~ 1.2 mW of optical power in each bichromatic beam.

The relative phase between the counter-propagating beams was a critical factor for both the magnitude and direction of the bichromatic force. In our experiment, the phase was coarsely set by the placement of the output fiber couplers relative to the chamber center and fine-tuned with a phase delay mirror mounted on a linear translation stage in the $+kv_c$ beam path. Varying the position of this mirror resulted in small changes of the relative phase, while for large adjustments, a series of optical fibers cut to custom lengths allowed for changes of 180° and a few other increments. To set the relative phase, two home-built fast photodetectors based on Hamamatsu 1.5 GHz PIN type photodiodes were used to directly measure the time delay between counter-propagating beams. The
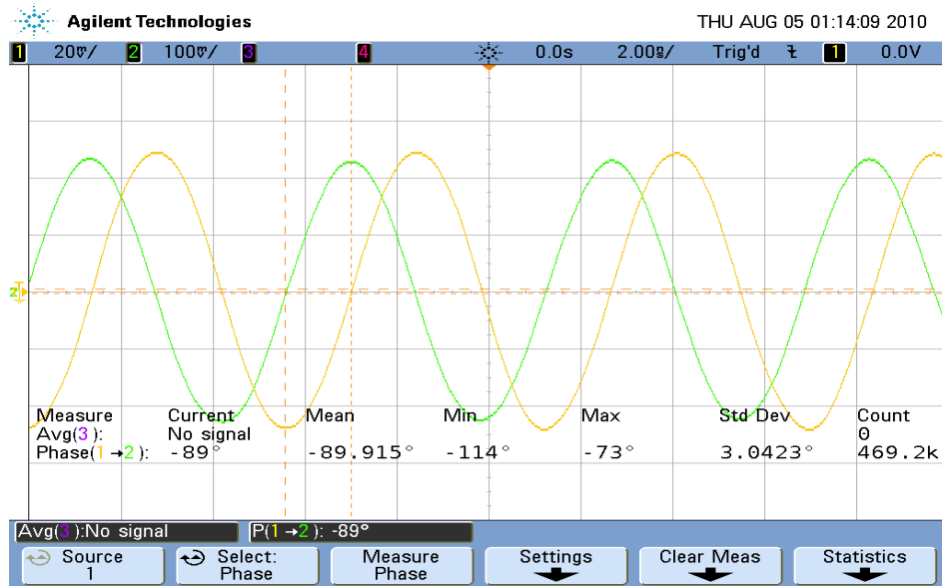
Figure 4.4: Oscilloscope trace of the beat signal for $+kv_c$ (yellow) and $-kv_c$ (green) showing a $\delta\phi = -\pi/2$ phase delay between the two beams. Data was measured using home-built high speed photodetectors placed equidistant from the center of the science chamber.
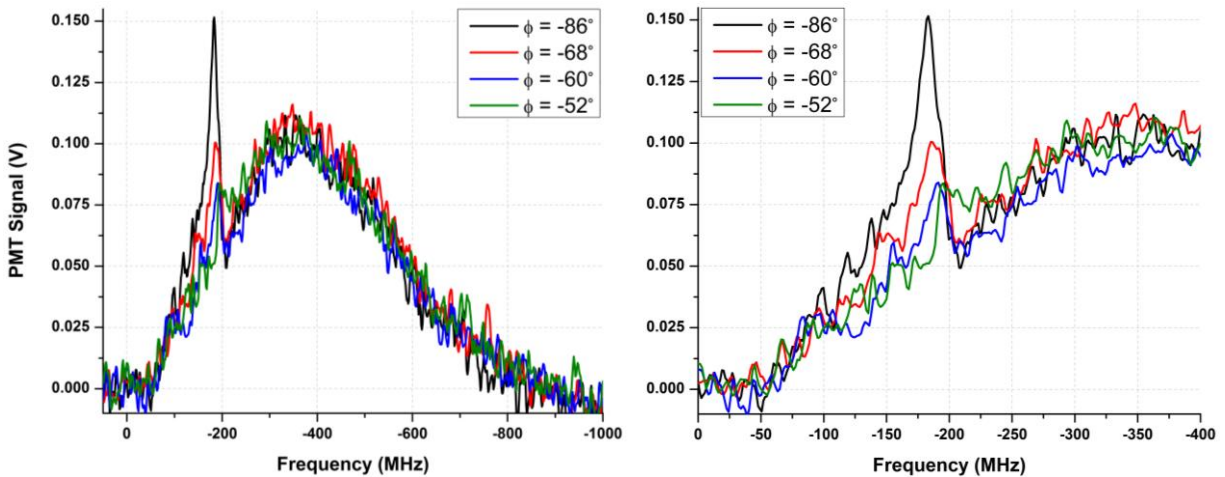
Figure 4.5: Velocity profile measurements for varied relative phase between counter-propagating bichromatic beams. The signal was optimum at roughly $\delta\phi = -\pi/2$ as expected from the π-pulse model and numerical simulations. The right hand plot is a narrow-band view of the same data.

photodetectors were placed at equal distances from the center of the science chamber, measured along the beam paths. Using a 500 MHz oscilloscope, traces of the beat frequency ($2\Delta = 177$ MHz) were recorded independently for both the $\pm kv_c$ beams and the relative phase between them was measured. The phase delay mirror position was tuned based on the real time measurements of the phase difference. Example traces collected during this optimization are shown in the screenshot in Fig. 4.4. We estimate that with this technique, the phase was set within $10°$ of the desired value with errors coming from the placement of the photodetectors and cable delays. With the phase roughly set, the bichromatic signal was used to fine-tune the position of the delay mirror. This final optimization addressed the different phases applied to the atomic beam over the long interaction length with the bichromatic light, providing information not available through the direct delay measurement. Fig. 4.5 shows the result of one series of phase measurements using the bichromatic signal. There was a significant increase in the number of accelerated atoms as the phase approached $-\pi/2$. For small phase changes on the order of $5°$ around the $-\pi/2$ maximum, the effect on the signal was insignificant. With the optimum position of the phase delay mirror identified for a $-\pi/2$ phase difference, switching to a decelerating phase was accomplished by changing the optical fiber delivering the $+kv_c$ light to the chamber.

For the bichromatic force to efficiently drive stimulated transitions between $|F = 2\rangle$ and $|F' = 3\rangle$, the circular polarization of both counter-propagating beams must have the same handedness. This is shown by the measurements in Fig. 4.6, where in one trace both beams were σ^+ polarized and in the other trace, the quarter-wave plate for the $-kv_c$ beam was rotated by $90°$, changing its polarization to σ^-. Whether both beams were σ^+ or σ^- polarized also impacted the magnitude of the bichromatic force through magnetic field effects. This will be discussed later in this chapter.

This subsection has illustrated the importance of properly setting the key bichromatic force parameters, including the relative phase, center velocity, Rabi frequency, bichromatic detuning, and polarization. Generally, the interplay between these different parameters could result in complicated force profiles that produced misleading data as certain parameters would compensate when others were incorrectly tuned. In practice, we achieved the best results by iteratively optimizing each parameter with the bichromatic signal until no further gains were observed. By checking values obtained in this manner against absolute measurements, we were able to verify that we had not walked into a local optimum of the parameter space.
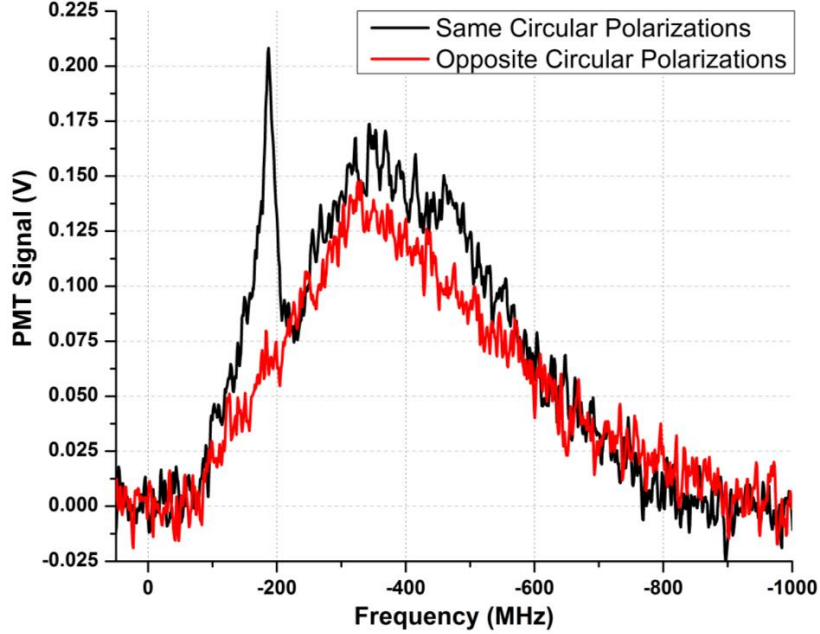
Figure 4.6: Atomic beam measurements for $\pm k v_c$ having the same (black) and opposite (red) circular polarizations.

4.1.2 Optimized Atomic Beam Results and Detection Limitations

The characterization of the parameter space and detection system described above facilitated measurements of the velocity distribution of the atomic beam with an optimized bichromatic force acting upon it. The results of these measurements are shown in Fig. 4.7 for a force acting along the direction of the atomic beam ($\phi = -\pi/2$) and one opposing it ($\phi = +\pi/2$). A force profile calculated from the optical Bloch equations for the parameters of this measurement is plotted with the data. The theoretical force has a magnitude of $F_{BC} = \hbar k \Delta/\pi \cong 4.7 \hbar k \gamma$ or nine times the maximum spontaneous force. However, as discussed in Chapter 2, careful measurements of the force suggest that the actual magnitude is $2/3$ of the expected ideal value [82].

The effect of the bichromatic field on the velocity distribution is clearly visible at the edges of the force profile for both $\phi = \pm\pi/2$. The change can be quantified in each case by integrating the fluorescence signal over a small velocity class just outside the active region of the force and comparing it with the same velocity class in the unaltered Maxwell-Boltzmann distribution. For $\phi = -\pi/2$, this analysis revealed a 300% increase in the number of atoms with a longitudinal velocity between 120 m/s and 140 m/s. While this illustrates the potential of the bichromatic

62
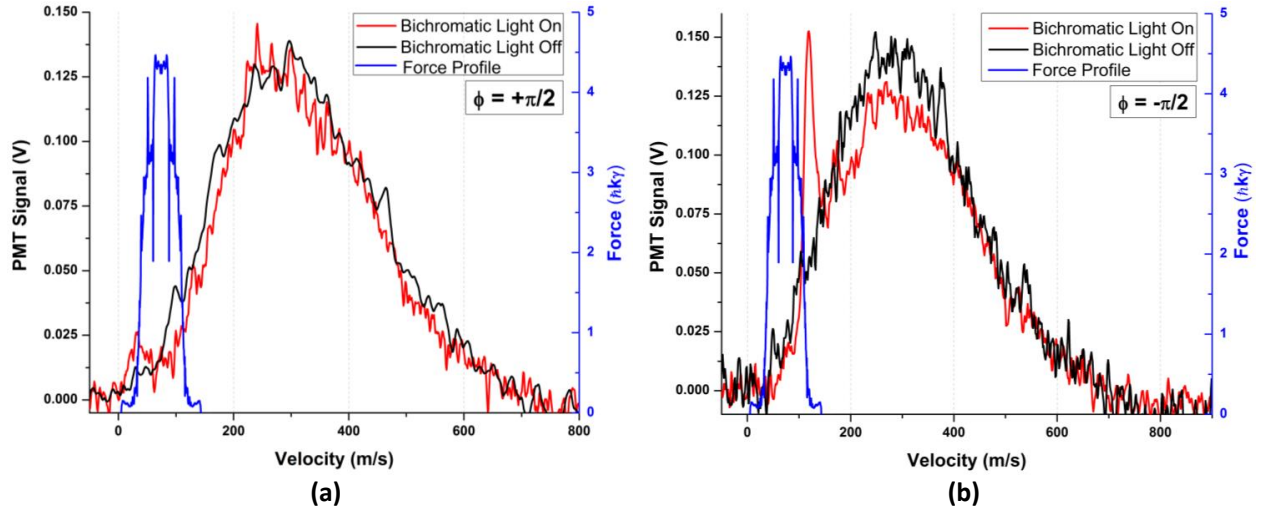
Figure 4.7: Atomic beam measurements for a bichromatic force applied with $\phi = +\frac{\pi}{2}$ (left) and $\phi = -\frac{\pi}{2}$ (right), along with a numerically calculated force profile matching the experiment parameters. Slowing case: $\Delta = 15\gamma$, $\Omega_R = 19.2\gamma$, and $kv_c = 74$ m/s. Accelerating case: $\Delta = 15\gamma$, $\Omega_R = 16.6\gamma$, and $kv_c = 74$ m/s.

force, increasing the flux of atoms in a low velocity class relevant for a compact MOT was the primary interest. This was accomplished in the slowing phase ($\phi = +\pi/2$) measurement, where a $\sim 10\times$ increase in the number of atoms with velocities below 13 m/s was observed. The data presented in Fig. 4.7 demonstrates qualitatively similar behavior to that observed in previous experiments with atomic beams slowed by bichromatic forces [80] but used only a few percent of the optical power, achieving the initial goals of the project.

While the results of our atomic beam experiments were promising, we had expected more significant improvement in the atom flux at low velocities suitable for capture in a small MOT. The predicted force profile should interact with 2.5% of the Maxwell-Boltzmann distribution and should slow all of these atoms down ~ 10 m/s. The fact that our data did not reflect this degree of interaction with the bichromatic field revealed a pair of detection issues in our large tabletop apparatus.

As discussed previously, the bichromatic beams were focused through the UHV chamber in order to pass through the apertures within the atomic beam collimator. Due to the size of the table-top apparatus and to maintain a gradual change in the intensity profile such that the Rabi frequency did not drastically vary over the interaction length, 1 m focal length lenses were used. This resulted in a beam waist that varied from 0.16 mm at the apertures to 0.21 mm at the center
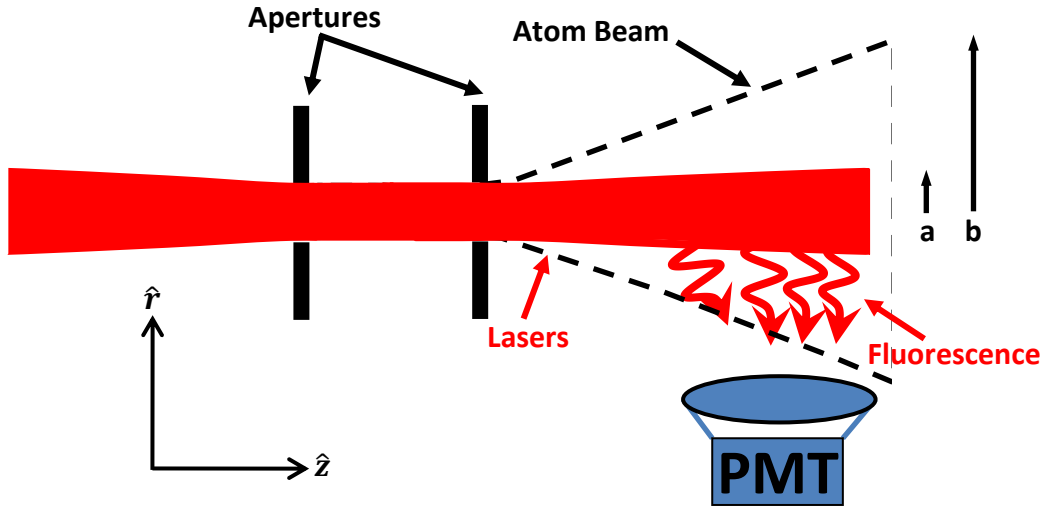
Figure 4.8: Diagram illustrating the mode mismatch between the laser beams and the atomic beam. The laser beam waist at the center of the chamber (a) was 0.21 mm, while the atomic beam (b) had expanded to a radius of 1.1 mm at the same location, introducing a detection bias in our atomic beam measurements.

of the science chamber. However, as illustrated by the absorption measurements presented in Chapter 3, the atomic beam at the center of the chamber had expanded to a diameter of $\sim$2.2 mm, revealing a significant mode-mismatch between the bichromatic/probe laser beams and the atomic beam. This mode discrepancy introduced a measurement bias as only atoms with a low ratio of radial to longitudinal velocities (v_r/v_z in Fig. 4.8) would remain within the laser field long enough to scatter probe photons and be detected by the PMT. Since the bichromatic force only affected the longitudinal atom velocity, the divergence angle of addressed atoms changed by a factor of $\sim v_i/v_f$, where v_i and v_f are the initial and final longitudinal velocities, respectively. Accordingly, the divergence angle for accelerated atoms decreased (smaller v_r/v_z), while it increased for slowed atoms (larger v_r/v_z), resulting in the peak height imbalance between the $\phi = \pm\pi/2$ data in Fig. 4.7. Furthermore, since the repump laser was coupled into the $-kv_c$ bichromatic fiber, the force was active over the entire path length of the laser beam, including the segment within the collimating assembly. Atoms slowed between the apertures would also exhibit a larger divergence angle and would be blocked by the second aperture in the collimator, never reaching the science chamber to be detected.

In addition to the bias leading to preferential detection of accelerated over decelerated atoms, the mode mismatch also reduced the effectiveness of the bichromatic force itself. Half of the atoms
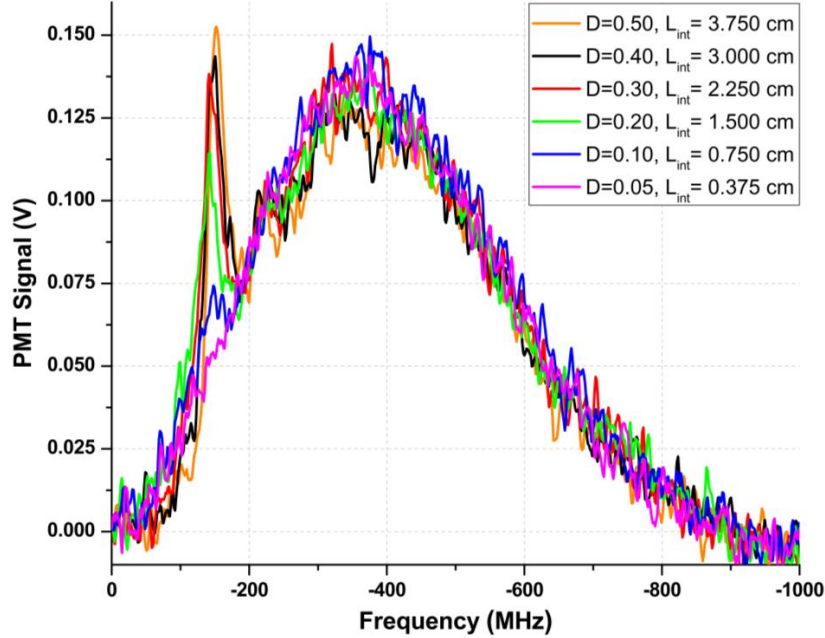
Figure 4.9: Atomic beam measurements with the bichromatic force applied with $\phi = -\pi/2$. The duty cycle of the applied force was varied from 5-50% with $\Delta = 15\gamma$, $\Omega_R = 16.6\gamma$, and $kv_c = 95$ MHz. As shown by the blue 10% curve, the bichromatic force had an effect on the distribution for interaction lengths below 1 cm.

in the atomic beam never interacted with the bichromatic field due to the difference between the aperture diameter and the atomic beam waist at the end of the collimator. By the center of the science chamber, the fraction of atoms within the laser beam fell to only 16%. As discussed later in this chapter, poor mode-matching was one factor contributing to our applied bichromatic force being reduced by $\sim 4\times$ over the theoretical prediction.

4.1.3 Interaction Length Experiment

Since the primary goal of this project was to test the scalability of the bichromatic force for potential use in a compact cold-atom source for atomic devices, a set of experiments were performed in which the interaction length between the bichromatic force and the atomic beam was varied. This was accomplished by reducing the length of the bichromatic pulse in the timing sequence (Fig. 3.12), changing the duty cycle (D) at which the force was applied. The maximum slowing length with the bichromatic and repump lasers applied longitudinally was $L_b = 7.5$ cm, corresponding to the length of the collimator and the distance from the second aperture to the center of the science chamber (Fig. 3.3 (c)). The effective interaction length was then defined by the product of the

65

maximum length and the bichromatic duty cycle: $L_{int} = DL_b$. For this set of measurements, the probe pulse length was 30 μs, and the pulse duration of the bichromatic beams ranged from 1.5-30 μs, varying the duty cycle from 5-50% and the interaction length from 0.375-3.75 cm. The data for this experiment is shown in Fig. 4.9. The peak of accelerated atoms shows a clear dependence on the interaction length with the bichromatic field, growing from 0.375 cm through the 3.75 cm case. The clear and reproducible signature of accelerated atoms at an interaction length of only 7.5 mm (blue trace) was an important result for this project. This length scale is within the range of interest for a chip-scale device and showed promise for the MOT experiments discussed in the next section.

4.2   Compact MOT Experiments

The atomic beam measurements discussed above were important for characterizing the bichromatic force in our system and performing preliminary scaling tests; however, applying the technique to achieve a large atom number in a compact trap was the ultimate goal from a chip-scale sensor perspective. If realized, large N_{ss} MOTs in compact physics packages would provide a valuable cold-atom source that could directly improve S/N ratios in atomic clocks, gyroscopes, etc. From an experimental perspective, switching from atomic beam measurements to MOT experiments had the added benefit of reducing the measurement bias from poor mode-matching that hindered some of the bichromatic force results in the previous section.

To test the feasibility of using bichromatic forces in a small cold-atom source, we performed a series of experiments in which both the interaction length of the bichromatic light with the atomic beam and the capture velocity of the MOT were varied. By loading MOTs with low capture velocities from an atomic beam slowed over several mm by a bichromatic field, we were able to simulate using the technique in a chip-scale system. The effectiveness was then determined by measuring the atom number and loading rate of the traps. As a control for the experiments, MOTs were loaded from the atomic beam slowed by bichromatic forces and spontaneous forces. This provided a useful comparison for determining whether the technical requirements needed to implement bichromatic slowing were warranted relative to a simple spontaneous slowing beam. To reduce issues stemming from the divergence angle of the slowed atomic beam and to avoid
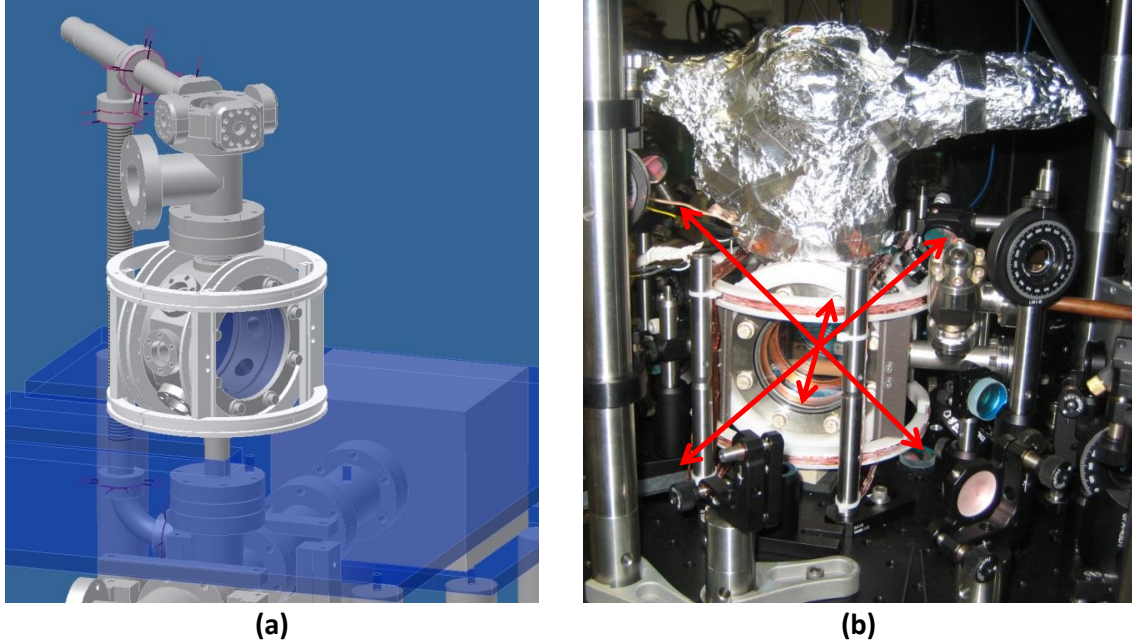
Figure 4.10: (a) CAD rendering of the coil guides for the MOT and vertical bias fields. (b) Image of upgraded system with magnetic field coils, MOT optics, and arrows showing the orientation of the trapping beams.

the difficulties of aligning mm-scale trapping lasers, the MOT was constructed with 6.6 mm $1/e^2$ diameter fiber output collimators. Despite the large beam size, testing the scalability down to sub-mm MOTs was accomplished through a reduction of the optical power used in the trap. By not fully saturating the trapping force, the capture velocity was reduced such that it was equivalent to a fully saturated trap formed from smaller diameter laser beams. This technique was very useful from an experimental perspective as aligning and optimizing a trap with mm-diameter beams is a difficult process in a large system. Additionally, small trapping beams would have exacerbated the transverse spreading issue in our apparatus.

4.2.1 Apparatus Modifications

A series of upgrades were performed on the bichromatic system to enable the compact MOT experiments. Four sets of magnetic field coils were added to the vacuum chamber; one pair in the anti-Helmholtz configuration to generate the quadrupole field for the MOT and three pairs of orthogonal Helmholtz coils to control the bias fields in each direction. The MOT and vertical bias coils were wound onto circular coil guides machined out of Teflon and screwed together around
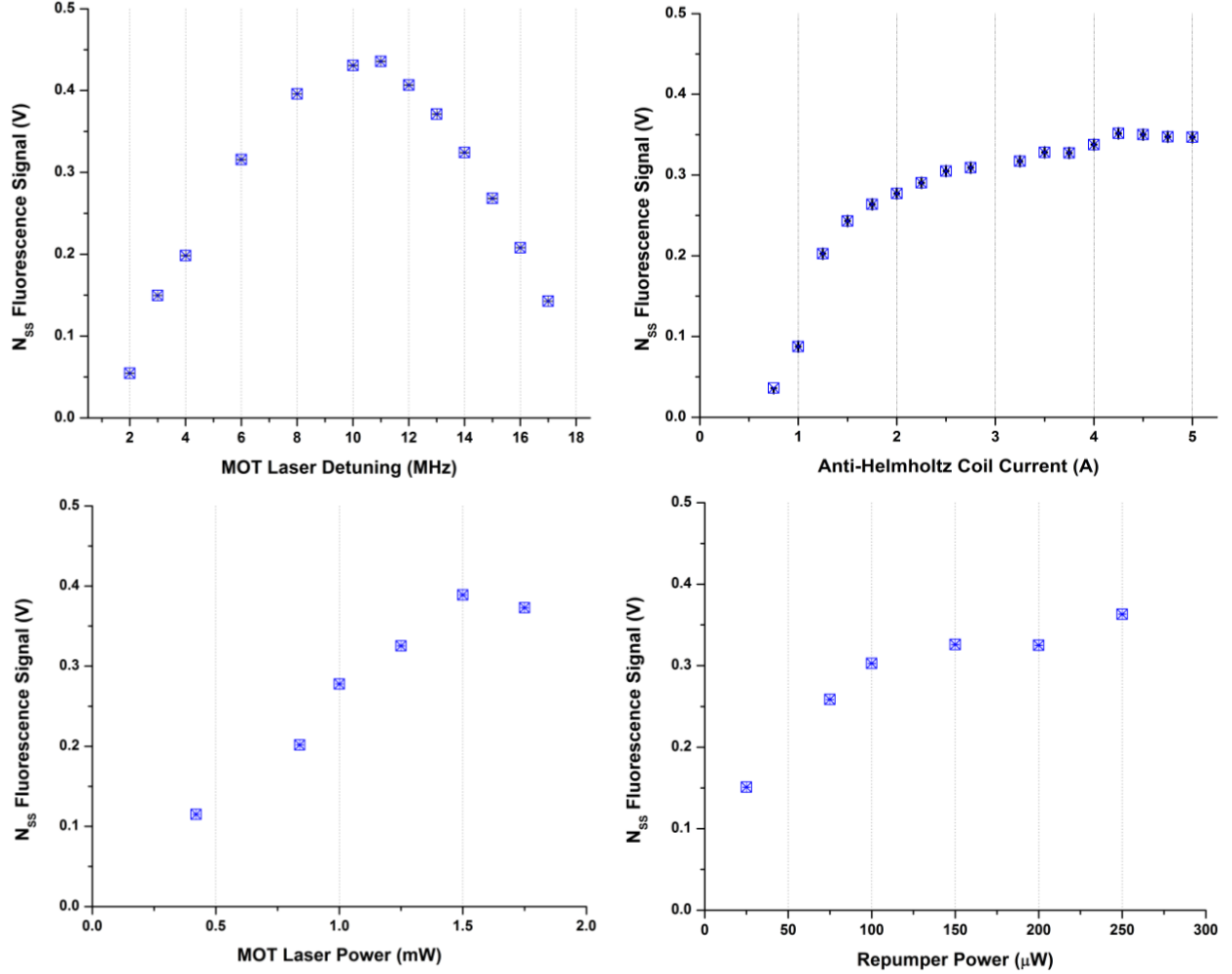
Figure 4.11: MOT optimization data for laser detuning (top-left), current through the MOT anti-Helmholtz coils (top-right), laser power (bottom-left), and repump power (bottom-right).

the chamber (Fig. 4.10). The remaining two sets of bias coils were rectangular in shape and slid around the Teflon frame; they were sufficiently large that edge effects from the rectangular shape were minimal. Mirrors, polarizing beam splitters, linear polarizers, and quarter wave plates were assembled on the upper breadboard and used to split the MOT laser light into three balanced beams and direct them into the system with the correct polarizations. Two beams entered along the 45° axes of the octagonal chamber, while the third beam passed through the 4.5" window along the axis of the anti-Helmholtz coils. Each beam was retro-reflected to form the trap.

After completing the system upgrade and obtaining our first MOT, an optimization sequence was performed to determine how many atoms could be captured with saturated trapping beams. Characterization data of the steady state atom number as a function of MOT laser intensity and

detuning, quadrupole gradient, and repump power was collected (Fig. 4.11). After optimizing each of the parameters, $\sim 2 \times 10^6$ atoms were trapped with 1.30 mW of cooling light per beam, 200 μW of repump power, 4 A flowing through the anti-Helmholtz coils producing a gradient of ~ 10 G/cm, and a detuning of $\delta_{MOT} = 11$ MHz $\sim 2\gamma$. This atom number served as the baseline for the initial set of MOT experiments.

4.2.2 Enhancement Model and Signature

To assist in interpreting the atom number data, a model was developed in which the fraction of atoms in the atomic beam that would be captured in a compact MOT was calculated for a thermal beam, a beam slowed with bichromatic forces, and a beam slowed by spontaneous forces. Calculating the captured fraction as a function of duty cycle or interaction length in each of these cases produced an expected signature for this type of experiment. For an ideal system, the bichromatic slowing force is 100% effective as long as the interaction time (τ_{int}) is greater than or equal to the critical slowing time (τ_c), defined as the length of time an atom must interact with the bichromatic light to be slowed to the minimum active velocity of the force profile, v_{min}, from the maximum active velocity, v_{max}:

$$\tau_c = \frac{m\,(v_{max} - v_{min})}{F_{BC}} = \frac{3\pi m\,(v_{max} - v_{min})}{2\hbar k\Delta}, \tag{4.1}$$

where m is the mass of an ^{87}Rb atom, and the bichromatic force has been adjusted by the 2/3 factor. For the bichromatic force profile corresponding to $\Delta \sim 15\gamma$, $\Omega_R \sim 17\gamma$, and $kv_c = 74$ m/s, the critical slowing time is $\tau \cong 150$ μs. This is converted to a critical duty cycle (D_c) by using kinematic expressions to calculate the minimum interaction length necessary to fully slow an atom and dividing by the maximum interaction length allowed by the system design:

$$L_{int}|_{min} = v_{max}\tau_c - \frac{F_{BC}}{2m}\tau_c^2 \cong 8.7 \text{ mm}$$
$$D_c = \frac{L_{int}|_{min}}{L_b} \cong 0.12. \tag{4.2}$$

Based on this analysis, we would expect an ideal bichromatic force to slow every atom within the force profile to the minimum active velocity for all duty cycles exceeding 12%, corresponding to an interaction length of 8.7mm in our apparatus. Below this critical value, the captured fraction should decrease to the thermal number by a 0% duty cycle. For the spontaneous slowing, the minimum
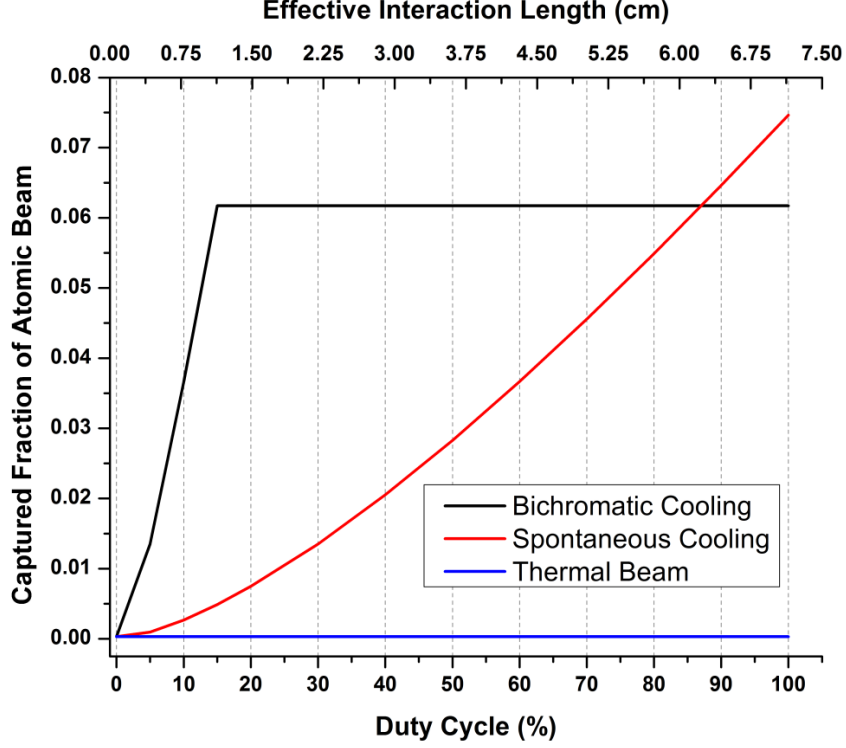
Figure 4.12: Calculations of the expected captured atom fraction of a thermal $100°\text{C}$ atomic beam (blue) and of the same beam slowed by spontaneous forces (red) and bichromatic forces (black). The captured fraction from the thermal beam is 3.2×10^{-4}. See text for discussion.

interaction length needed to slow every atom within its addressed velocity class is greater than the maximum interaction length in our system ($L_b = 7.5$ cm) such that the captured fraction should continue to increase over the entire range of duty cycles.

These intuitive conclusions were confirmed by the modeling results shown in Fig. 4.12, where the captured fraction for each case is plotted versus duty cycle. For these calculations, the capture velocity was $v_{cap} = 20$ m/s, and the bichromatic force parameters were $\Delta \sim 15\gamma$, $\Omega_R \sim 17\gamma$, and $kv_c = 74$ m/s. The spontaneous slowing curve was calculated with 1 mW of optical power and a detuning of -115 MHz, close to the parameters of the spontaneous beam in our experiment.

While this signature was qualitatively useful, to quantitatively analyze the data, we developed a model for the atom number enhancement of a MOT loaded from an atomic beam slowed by optical forces over a MOT loaded from a thermal beam. For an atomic beam subject to a force $\xi\times$ stronger than the maximum spontaneous force, $F = \xi\hbar k\gamma/2$, the maximum atomic velocity that can be slowed to the capture velocity of a MOT in an interaction length L is:

$$v_{max}^2 = v_{cap}^2 + 2\frac{F}{m}\Delta z \tag{4.3}$$

$$v_{max} = \sqrt{v_{cap}^2 + \frac{\xi\hbar k\gamma L}{m}}.$$

By slowing the atomic beam before loading it into a MOT, the captured atom number is larger than the number loaded from a thermal beam by the enhancement factor $E \equiv N_{ss1}/N_{ss2}$, where N_{ss1} is the atom number loaded from a slowed atomic beam, and N_{ss2} is loaded from a thermal beam. Since the slowing force effectively raises the capture velocity of the MOT, substituting Eq. 4.3 for the capture velocity in the atom number expression from Eq. 1.4 allows the enhancement to be written as:

$$E = \frac{N_{ss1}}{N_{ss2}} \simeq \frac{\frac{A_b}{\sigma\sqrt{\pi}}\left(\frac{\sqrt{v_{cap}^2 + \frac{\xi\hbar k\gamma L}{m}}}{v_{avg}}\right)^4}{\frac{A_b}{\sigma\sqrt{\pi}}\left(\frac{v_{cap}}{v_{avg}}\right)^4} = \frac{\left(v_{cap}^2 + \frac{\xi\hbar k\gamma L}{m}\right)^2}{v_{cap}^4} = \left(1 + \frac{\xi\hbar k\gamma L}{mv_{cap}^2}\right)^2. \tag{4.4}$$

To link this expression to the diameter of the laser beams used in the MOT, we can write down the capture velocity in terms of the saturated MOT beam diameter (d_{sat}) and the spontaneous decay scattering force ($F_{spont} = \hbar k\gamma/2$):

$$v_f^2 - v_{cap}^2 = -2\frac{F_{spont}}{m}d_{sat}\Big|_{v_f=0}$$
$$mv_{cap}^2 = 2\left(\frac{\hbar k\gamma}{2}\right)d_{sat}. \tag{4.5}$$

Rearranging, we have:

$$d_{sat} = \frac{mv_{cap}^2}{\hbar k\gamma}. \tag{4.6}$$

Substituting this into Eq. 4.4, we obtain a compact form for the enhancement:

$$E = \left(1 + \frac{\xi L}{d_{sat}}\right)^2. \tag{4.7}$$

The above equations have assumed an ideal force applied in a continuous manner. Adapting this theory to incorporate a force applied in a pulsed operation mode over a maximum interaction length L_b with a duty cycle D requires substituting $L \to L_b D$ for the interaction length. Secondly,

the slowing length was limited by the partial spatial overlap between the atomic beam and the bichromatic lasers caused by the imperfect mode-matching in our large apparatus. This effect shortens the interaction length by an additional factor η, which was a function of our particular experiment design. Including these two effects in Eq. 4.8, the enhancement expected in our system becomes:

$$E = \left(1 + \frac{\xi \eta L_b D}{d_{sat}}\right)^2.$$ (4.8)

These approximate scaling arguments will be used to interpret the experimental data presented in later sections.

4.2.3 MOT Experiment Results

In a typical experiment, fluorescence curves for MOTs loaded from an atomic beam slowed by bichromatic and spontaneous forces were recorded as a function of duty cycle. A slowing sequence was 60 μs in duration, and the fraction of time the slowing light was on varied from 0-60 μs. The spontaneous slowing beam was a single counter-propagating laser, red-detuned by $-17.5\gamma \cong 105$ MHz, with a saturation parameter of 1200 and a power-broadened linewidth of $\sim 35\gamma$ (velocity FWHM of 164 m/s). The light was coupled into the system through the $-kv_c$ fiber, such that the mode matched the bichromatic laser beams. To verify that the spontaneous slowing was fully saturated, the MOT number enhancement as a function of applied power in the spontaneous beam was measured (data shown in Fig. 4.13 (a)).

A representative example of an early MOT loading measurement exhibiting the qualitative signature from the above discussion is shown in Fig. 4.13 (b). As expected, the spontaneous enhancement grew steadily with effective slowing length due to the large, power broadened velocity class it addressed and the relatively weak magnitude of the force. For this measurement, the bichromatic force parameters were $\Delta \sim 15\gamma$ and $\Omega_R \sim 17\gamma$, resulting in a peak enhancement of ~ 3.25 that saturated at a duty cycle of roughly 40%. This critical duty cycle is roughly 3.5$\times$ larger than the expected value, indicating that the bichromatic force was not optimized in this data.

The decrease in the bichromatic atom number enhancement at high duty cycles was an interesting feature in this data set. This decrease in the enhancement indicated that for high duty cycles, even the non-ideal bichromatic force profile was strong enough to complete the deceleration near
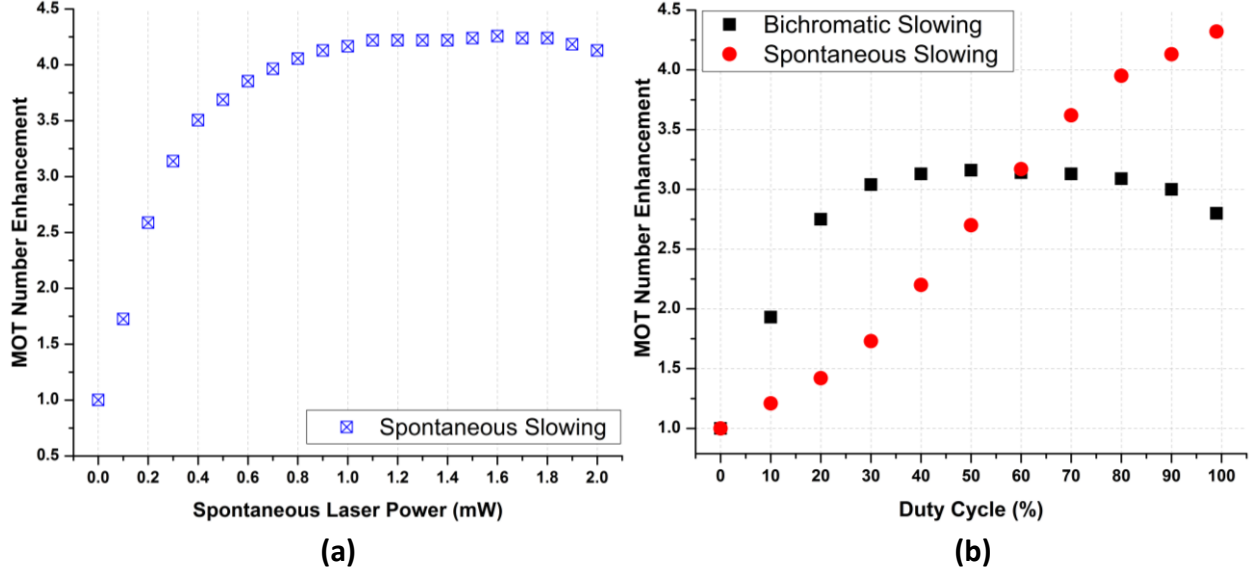
Figure 4.13: (a) Optimization data confirming that the atom number enhancement for a spontaneously slowed beam saturated above ~ 0.75 mW. (b) Results of early MOT experiments showing atom number enhancement for both spontaneous and bichromatic slowing.

the apertures, leaving sufficient time for the atom's transverse velocity to carry it away from the trapping region. A second option for explaining this feature is that the bichromatic force profile was sufficiently broad, due to poor parameter optimization, that the low velocity edge crossed zero ($v_{min} < 0$). In this case, the force at high duty cycles would continue to decelerate the atom until the velocity was reversed, at which point the force would accelerate the atom away from the trap. Regardless of the mechanism, the low enhancement and presence of this decrease at large duty cycle indicated that the force profile and the transverse velocity issue both required attention.

To re-optimize the bichromatic force profile for MOT loading experiments, enhancement as a function of interaction length was measured for variations in center velocity, bichromatic beat frequency, Rabi frequency, relative phase, MOT magnetic gradient, and MOT laser power, among others. These tests provided valuable information used to tune the system and obtain the optimum enhancement discussed later in this section. Enhancement data for varied kv_c is shown in Fig. 4.14, where measurements were made for two different bichromatic beat frequencies. Both the atom number and loading rate enhancement exhibited a strong dependence on the center frequency of the force profile. If set too low on the velocity axis of the Maxwell-Boltzmann distribution, the enhancement was suppressed both by the smaller number of atoms within the active range of the
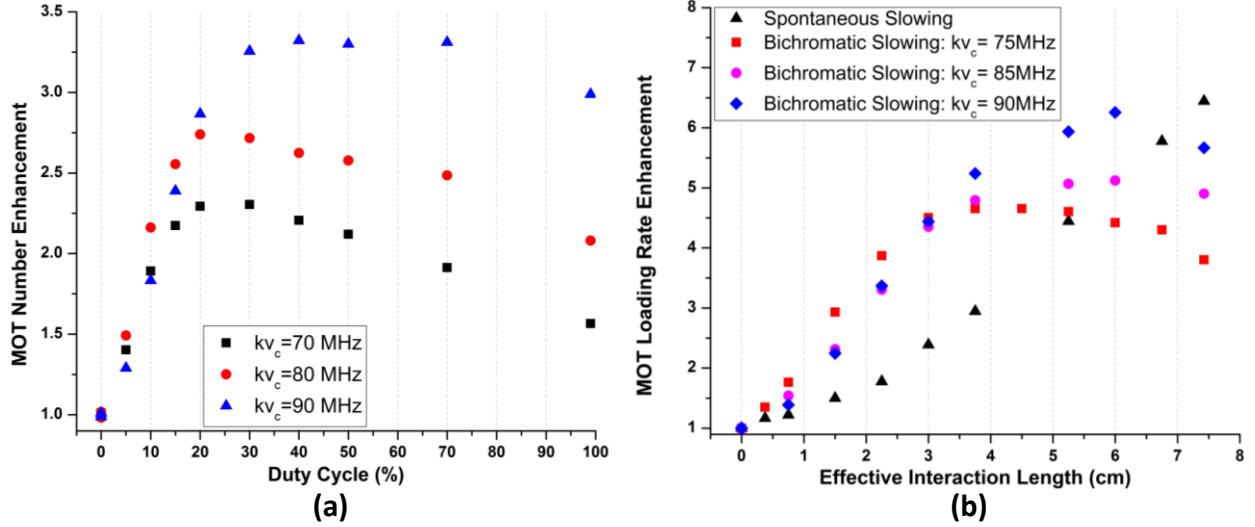
Figure 4.14: (a) Atom number enhancement vs. duty cycle for different center frequencies of the force profile. For this measurement, $2\Delta = 240$ MHz. (b) Loading rate enhancement vs. effective interaction length for varied center frequency with $2\Delta = 190$ MHz.

force and by atoms being stopped and accelerated away from the trap if v_{min} crossed zero. As the center frequency was raised, the enhancement grew, and the effective interaction length where the enhancement began to decrease due to these detrimental effects was increased. These trends appear in both plots in Fig. 4.14. Not shown in this data set is the effect of placing the force profile at too high of a center velocity. In this case, the enhancement decreases over the full interaction range as the lower edge of the addressed velocity class is higher in velocity than the capture velocity of the MOT ($v_{min} > v_{cap}$). This was observed for $kv_c \gtrsim 110$ MHz.

The enhancement provided by bichromatic slowing exhibited a dependence on the magnetic fields in the system. The atom number enhancement with the MOT bias coils tuned to null the background field and set to optimize the enhancement are shown in Fig. 4.15. The larger enhancement occurs when the bias fields are tuned such that the MOT is shifted to the periphery of the atomic beam, decreasing collisional losses from the thermal beam and partly compensating for the shallow trap depth of the unsaturated MOT. This effect is also partly due to Zeeman shifts of the force profile that will be discussed in Section 4.2.4.

Rabi frequency optimization measurements are shown in Fig. 4.16, along with a comparison of the MOT number enhancement for two different bichromatic force profiles with $\Delta = 15.7\gamma$ and 20γ. The data in (a) exhibits fairly limited dependence of the enhancement on the bichromatic Rabi

74
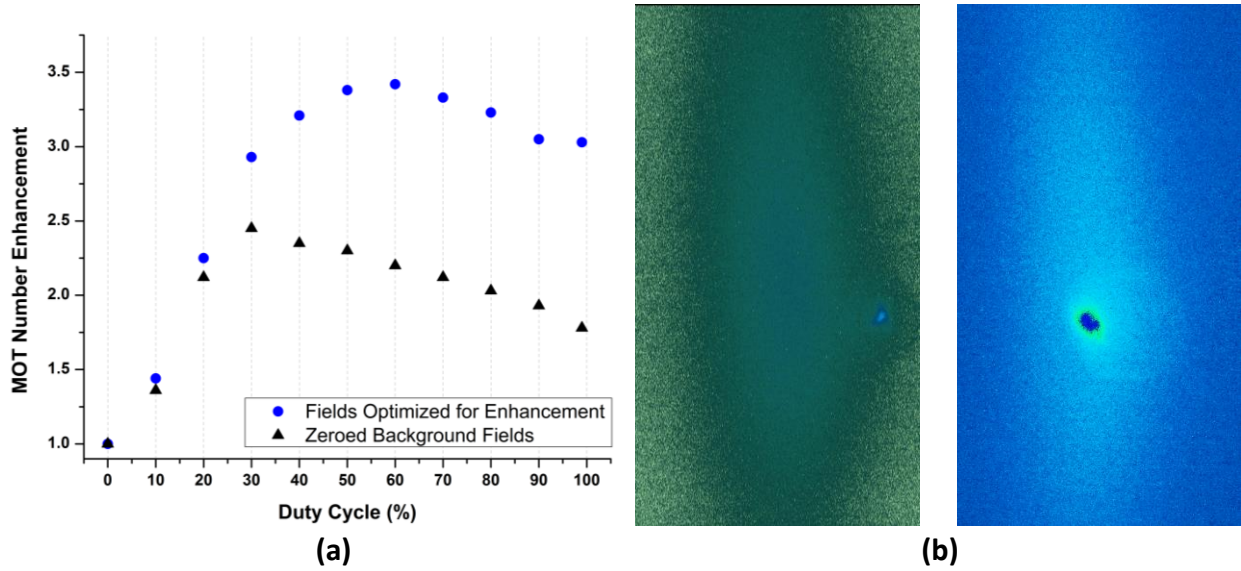
Figure 4.15: (a) Atom number enhancement vs. duty cycle for bias fields tuned to zero the background magnetic fields (black) and to optimize the enhancement (blue). (b) Absorption images showing the position of the MOT (blue/dark blue spot) relative to the atomic beam for fields set to optimize enhancement (left) and to zero the background field (right).
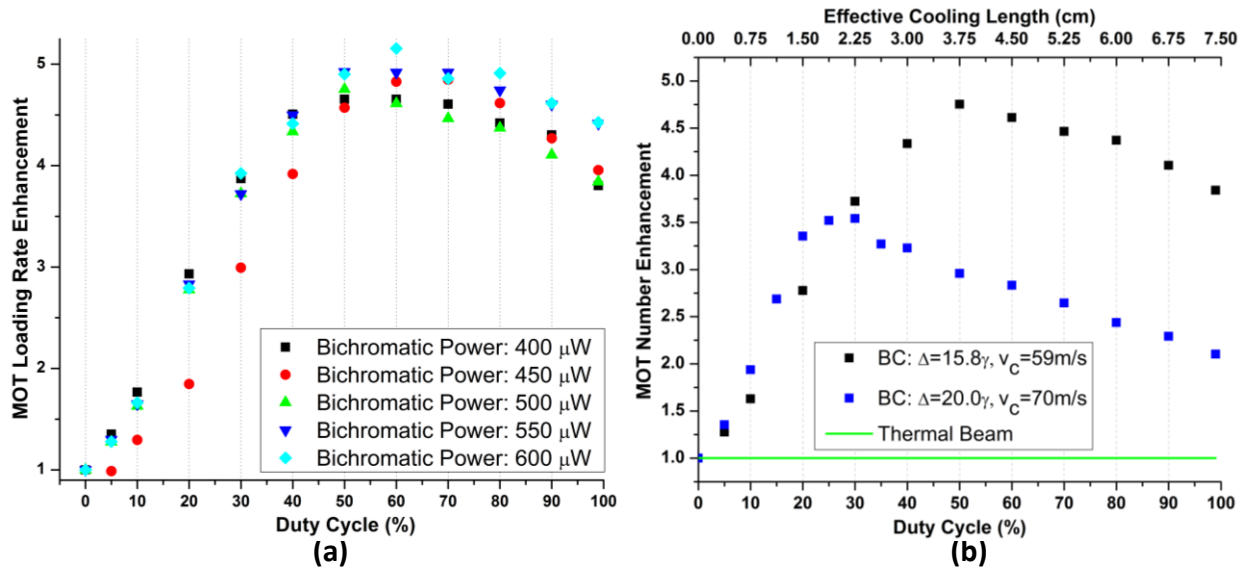
Figure 4.16: (a) Loading rate enhancement vs. duty cycle for varied bichromatic power. The dependence on the Rabi frequency was not as strong as on other parameters. (b) Atom number enhancement vs. effective interaction length for two bichromatic beat frequencies. Despite generating a stronger force, the $\Delta = 20\gamma$ enhancement was worse than for $\Delta = 15.7\gamma$ due to the transverse velocity issues.

frequency, however due to the interplay between the different force parameters, this type of optimization was performed frequently to verify that the proper power was used for a given MOT capture velocity, bichromatic beat frequency, and center velocity. In Fig. 4.16 (b), the atom number enhancement for the two force profiles highlights the transverse velocity issue in these experiments. Despite generating a bichromatic force profile that was $\sim 30\%$ stronger and broader than the force for $\Delta = 15.7\gamma$, the enhancement for $\Delta = 20\gamma$ with an optimized kv_c was significantly worse for duty cycles exceeding 30%. This was again due to the transverse velocity spread of atoms that were slowed near the apertures of the system. While the enhancement for the $\Delta = 20\gamma$ force profile was still $2.6\times$ larger than spontaneous slowing at an interaction length of 1.5 cm, this performance did not meet expectations. The transverse velocity issue required a resolution for improved enhancement over a broad range of interaction lengths to be achieved.

To verify our hypothesis that transverse spreading of slowed atoms was responsible for the atom loss at high duty cycles, a test was performed in which a quadrupole magnetic field was used to guide atoms along the slowing beam axis to the trapping region. Two neodymium permanent magnets were mounted outside the science chamber in the configuration shown in Fig. 4.17 (a). This external field interacted with the magnetic dipole moment of the atoms, exerting a force that reduced the transverse beam spread [97]. The data from this experiment (Fig. 4.17 (b)) showed a significant improvement in the enhancement at high duty cycles over measurements made without magnetic guiding. With the quadrupole field in place, the enhancement at $D = 90\%$ was $2.3\times$ the result without guiding and approached an overall enhancement of $5\times$. These results confirmed that transverse spreading was responsible for suppressing the enhancement at large interaction lengths in our previous data.

A permanent solution for this problem without introducing extra magnetic field effects into the experiment required system modifications to decrease the maximum cooling length and eliminate slow atom loss due to skimming at the second aperture. This type of upgrade would directly improve performance and would also lend itself to better tests of the miniaturization potential of the technique. These improvements were accomplished by switching the method through which the repump used for slowing the atomic beam was coupled into the system. Using the bichromatic fiber to inject the repump resulted in active slowing forces over the full 7.5 cm length between the first collimating aperture and the location of the MOT at the center of the science chamber.
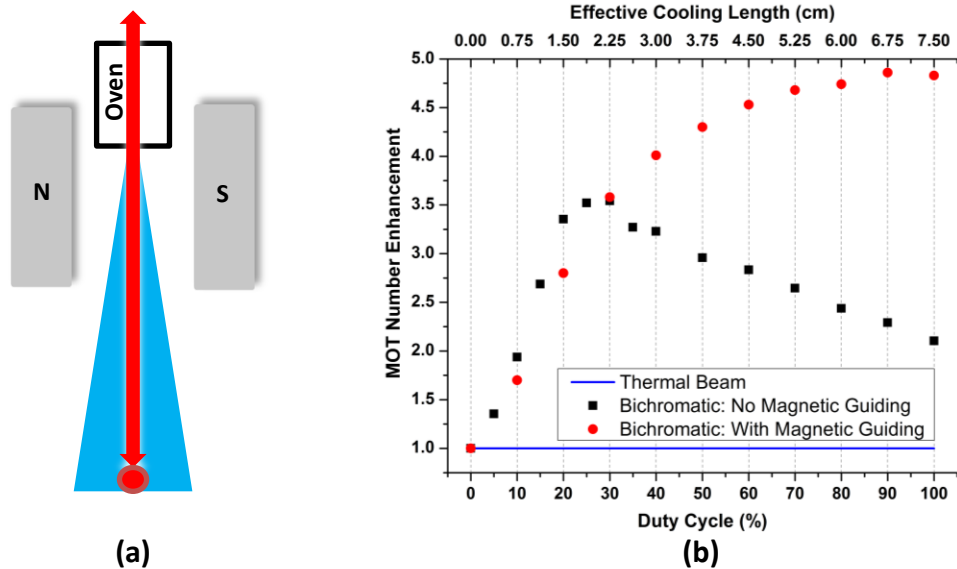
Figure 4.17: (a) Permanent magnet configuration for the magnetic guiding experiment. The magnetic pole on the visible face of each bar magnet is labeled. (b) Atom number enhancement vs. effective interaction length with and without magnetic guiding. The bichromatic fields were optimized for $\Delta = 20\gamma$.
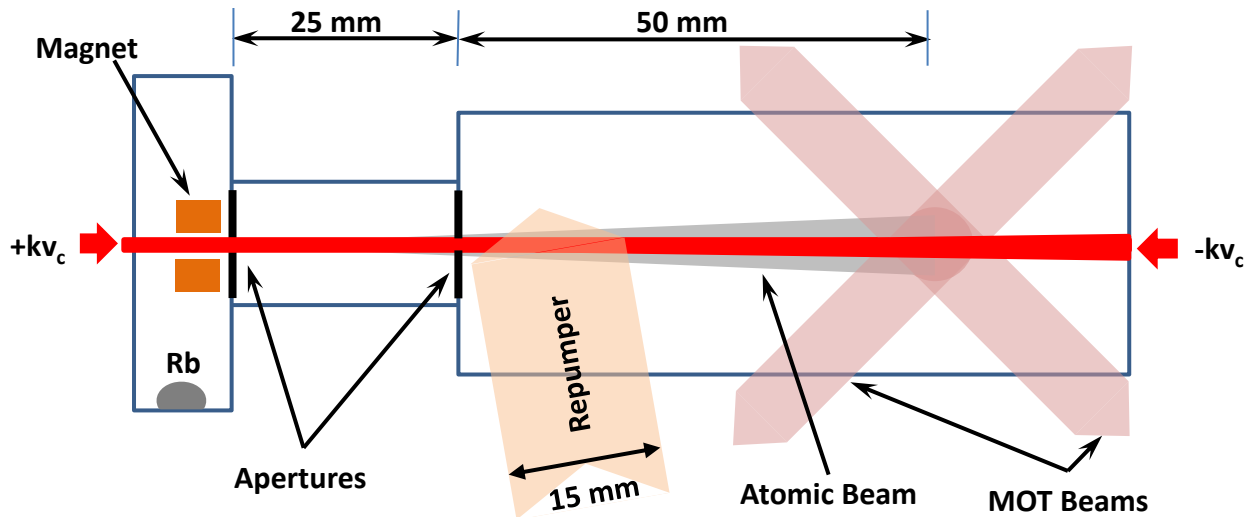
Figure 4.18: Modified experiment configuration with the slowing repump laser injected transversely in a 15 mm long stripe. This reduced the transverse spread problem and eliminated skimming from the collimator. The new maximum interaction length was $L_b = 15$ mm.

This maximum interaction length was reduced by coupling the repump laser into an independent polarization-maintaining optical fiber and injecting it into the system transversely through the 4.5" windows. The shape was manipulated with a 50 mm focal length cylindrical lens to create an elliptical repump beam that was 15 mm in length along the long axis. It was aligned at a $10°$ incident angle such that it overlapped the atomic beam just below the second collimating aperture. Since the slowing forces are only efficient with a repump field present, this injection technique set the maximum interaction length to 15 mm and eliminated atom loss due to skimming as the slowing forces were only active below the collimator. Additionally, the distance traveled by slowed atoms before reaching the trapping region was reduced, suppressing the transverse spread loss mechanism. The modified system geometry is shown in Fig. 4.18.

With the maximum interaction length at 15 mm, a true test of the feasibility of using bichromatic slowing in a chip-scale device was carried out by measuring the atom number enhancement for compact MOTs. In our system, miniaturized traps were simulated by reducing the optical power in the trap beams such that the capture velocity was equivalent to small saturated MOT beams (small d_{sat}). The results of this type of measurement are shown in Fig. 4.19 (a), where the atom number enhancement was measured as a function of optical power in the MOT beams. As shown in the data, the enhancement grew dramatically at low optical powers in the trapping beams, corresponding to capture velocities of $v_{cap} \lesssim 10$ m/s and mm-scale beam diameters. Similar behavior had been previously observed with the longitudinal repump injection, however the effect was not as dramatic.

With the decrease in interaction length and trapping power, it was necessary to re-optimize the bichromatic force parameters to ensure that the profile was as close to ideal as possible and capable of slowing atoms to the low capture velocity of the compact MOTs under consideration. An example of the optimization process showing the strong dependence of the enhancement on kv_c for a low power MOT (simulating a compact trap) is shown in Fig. 4.19 (b).

Our scalability study was completed by measuring the MOT atom number and loading rate enhancements as a function of effective interaction length for a MOT with 100 μW of power per trapping beam. This corresponded to a capture velocity of $v_{cap} \approx 5.5$ m/s and was equivalent to a MOT with fully saturated beams 0.5 mm in diameter (d_{sat}). The best reproducible results from these measurements are shown in Fig. 4.20. Compared to loading from a thermal beam, we observed a maximum MOT number enhancement of 14$\times$ for bichromatic slowing and 10$\times$ for spontaneous
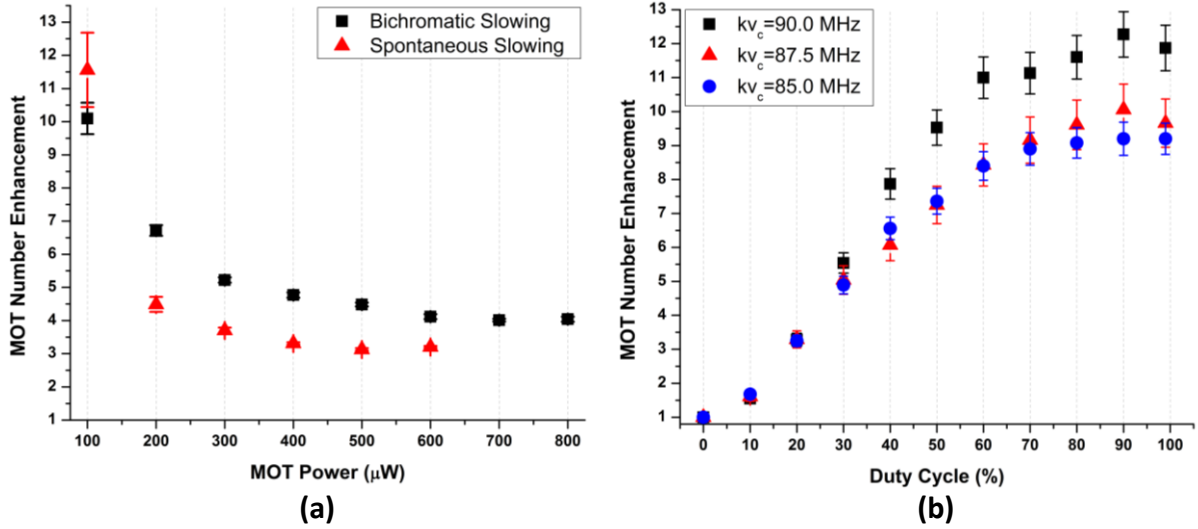
Figure 4.19: (a) Atom number enhancement as a function of laser power in each MOT beam. Bichromatic data was collected at a duty cycle of 90%. (b) Atom number enhancement vs. duty cycle for varied center frequency and 100 μW of power per MOT beam.
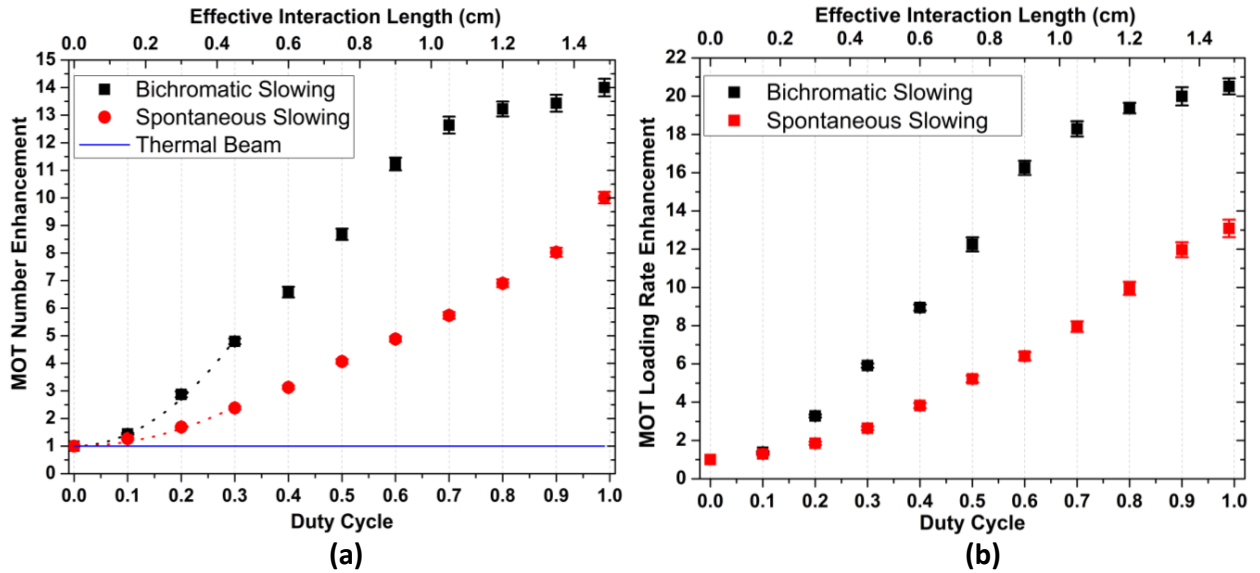
Figure 4.20: Atom number enhancement (a) and loading rate enhancement (b) as a function of interaction length for 100 μW of power in each MOT beam. The bichromatic parameters were $\Delta = 20\gamma$, $\Omega_R = 24.5\gamma$, and $kv_c = 15.7\gamma$ (center velocity of 74 m/s). Fits to the enhancement function defined in Eq. 4.8 (dotted lines) are shown in (a).

slowing, while measuring loading rate enhancements of up to $20\times$ for bichromatic forces and $13\times$ for spontaneous forces. From the basic equations for N_{ss}, we would expect the loading rate and number enhancements to be the same. They could differ because either our fluorescence detection method was saturated and artificially suppressed our atom-number measurement, or because the MOT atom density was saturated in our compact MOTs due to an additional loss mechanism. From absorption measurements, our peak MOT density was estimated to be 1×10^{10} cm^{-3}, which is smaller than the saturated density of 2×10^{11} cm^{-3} that has been observed in larger MOTs [96].

As expected from the enhancement model, the spontaneous signal grew steadily with effective slowing length, but the enhancement from bichromatic slowing began to saturate and depart from a quadratic dependence at an interaction length that roughly agrees with the stopping distance of 5.3 mm expected from the applied bichromatic force profile. After interacting with the field for ~ 5.3 mm, all of the atoms still within the slowing beams that had initial velocities within the force profile had been maximally slowed and no longer interacted with the bichromatic field. Thus, for this set of bichromatic force parameters, the full advantage of the stimulated slowing method was only realized for effective interaction lengths under ~ 1 cm.

In terms of enhancement, bichromatic slowing was more effective than spontaneous slowing in our system; however an analysis of the data in Fig. 4.20 in the context of the enhancement model from Section 4.2.2 suggests that the results could be improved even further. With $d_{sat} = 0.5$ mm and $L_b = 15$ mm, the spontaneous slowing data in Fig. 4.20 (a) was fitted to Eq. 4.8 with $\xi = 1$, and a value for η was extracted, obtaining $\eta = 0.057(4)$. With the coefficient accounting for poor mode-matching determined, the bichromatic slowing data was fitted with the same equation, resulting in $\xi = 2.2(2)$ for the applied force multiplier. This was a factor of $\sim 4\times$ lower than expected, a discrepancy caused by a range of issues related to our large apparatus that will be discussed in Section 4.3. Regardless of the weak applied bichromatic force, these results indicated that bichromatic slowing could be accomplished in a compact device.

4.2.4 Zeeman-Shifted Bichromatic Slowing

The effects of the magnetic field on the bichromatic force profile are particularly important for a field-grade device based on this stimulated slowing technique. The energy levels of an atom in the presence of a magnetic field shift due to the Zeeman effect, which describes the coupling between
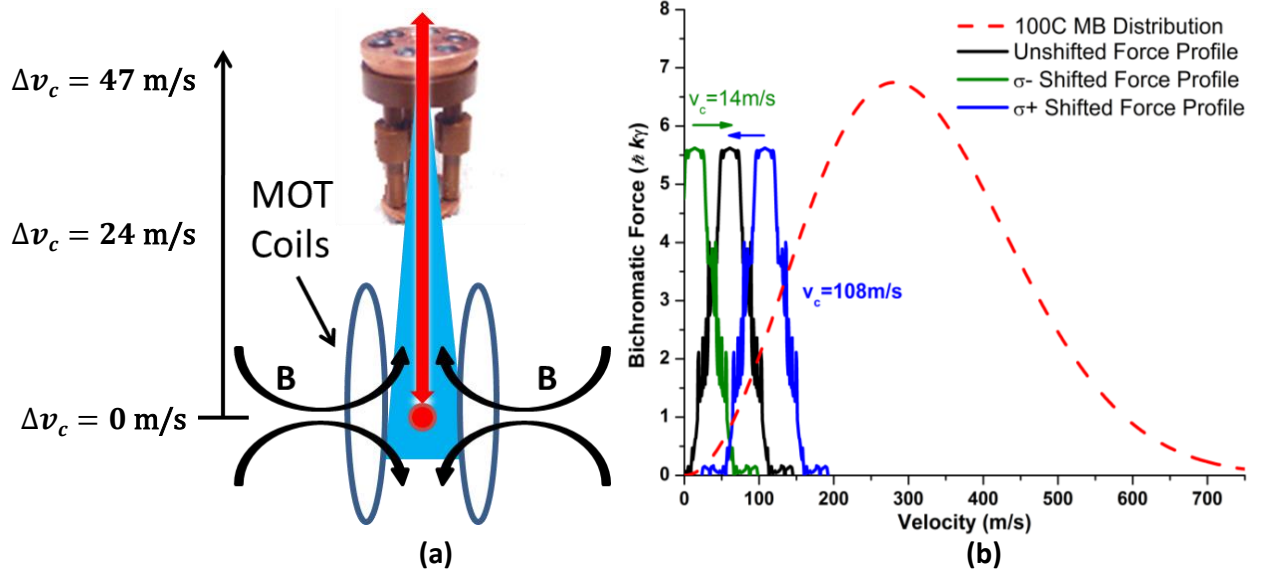
Figure 4.21: (a) Diagram illustrating the shift in the center of the force profile due to the magnetic gradient from the MOT coils. (b) Plot showing the shifted force profiles relative to the Maxwell-Boltzmann distribution for $\sigma\pm$ polarized bichromatic light.

the atomic magnetic moment and the external field. This coupling introduces a perturbation to the Hamiltonian given by [56]:

$$H' = \frac{\mu_B}{\hbar}\left(\vec{L} + 2\vec{S}\right) \cdot \vec{B}, \tag{4.9}$$

where μ_B is the Bohr magneton, $\vec{L}$ is the orbital angular momentum, $\vec{S}$ is the spin angular momentum, and $\vec{B}$ is the external magnetic field. In the low field limit, the shift of the energy levels for a field along the $\hat{z}$ axis is shown to be $\Delta E_z = g_F \mu_B B_z m_F$, where g_F is the Landé g-factor. In this expression, we have assumed that the Zeeman shift is small relative to the hyperfine splitting such that F is a good quantum number. Evaluating this for the $|F = 2\rangle \rightarrow |F' = 3\rangle$ cycling transition in ^{87}Rb, on which the bichromatic slowing operates, results in a Zeeman shift of 1.4 MHz/G. Thus, any magnetic field present in the system will shift the resonance frequency of the atom such that the location of the bichromatic force profile on the Maxwell-Boltzmann distribution becomes a function of the magnetic field.

The total magnetic field in our system was the sum of bias fields, the MOT quadrupole field, the field from the permanent magnets in the oven chamber, and any external background; however, the field gradient from the MOT coils was dominant within the science chamber, and other contributions were neglected. The magnetic field gradient for our trap was ~ 10 G/cm, resulting in an initial shift
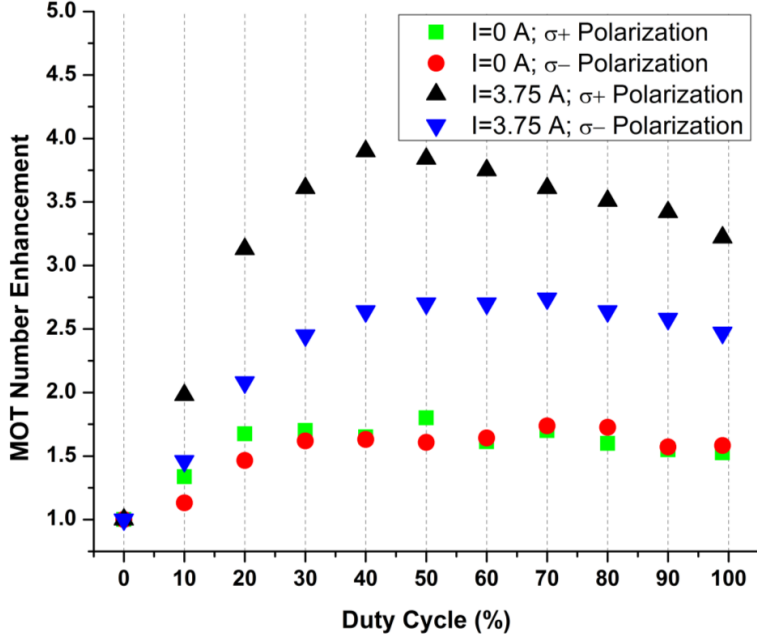
Figure 4.22: Atom number enhancement vs. duty cycle for $\sigma^{\pm}$ polarized bichromatic light for 3.75 A and 0 A running through the anti-Helmholtz coils. Data was collected with the repump laser applied longitudinally.

of the bichromatic force profile of 42 MHz at the lower aperture. The sign of the shift depended on the polarization of the bichromatic light as this determined whether $\Delta m_F = +1$ or -1 for the driven transition. For σ^+ light, the shift is positive and the force profile was pushed to higher velocities on the Maxwell-Boltzmann distribution; for σ^- light, the shift was negative, and the profile was translated to lower velocities (Fig. 4.21 (b)). In both cases, the Zeeman shift was largest near the second aperture and decreased to zero at the location of the MOT (Fig. 4.21 (a)). This had the effect of creating a Zeeman-shifted bichromatic force profile that slid continuously from its maximum shift near the apertures to its expected center velocity at the position of the MOT. For a σ^+ polarization, this could be advantageous as the force profile addressed a much larger number of atoms by shifting to a 108 m/s initial center velocity at the apertures. The opposite was true for σ^- light as the force profile was initially centered at 14 m/s, where a small velocity class was addressed and atoms were accelerated away from the trap ($v_{min} < 0$).

Based on this effect, we would expect to see larger enhancements for σ^+ over σ^- polarized bichromatic light, and this was confirmed in the data shown in Fig. 4.22. In this experiment, the atom number enhancement was measured for both polarizations with the MOT coils on and off,

loading the atoms into a molasses for the second case. The enhancement curves overlap for zero magnetic gradient but exhibit a significant difference with the anti-Helmholtz coils turned on. It is possible that in a future device, Zeeman shifted bichromatic slowing could be used in an analogous manner to chirped spontaneous slowing, potentially trapping even more atoms than we were able to demonstrate in our experiment. A Zeeman-shifted technique could be accomplished through careful control of the device size, beam mode-matching, bichromatic parameters, and magnetic fields in the system.

4.3   Conclusion and Outlook

By slowing a thermal atomic beam with the bichromatic force, we have demonstrated atom number enhancements of up to 12.5 and loading rate enhancements of 18 for effective slowing lengths under 1 cm [69]. The number and rate enhancements are $\sim 2.5\times$ larger than observed for spontaneous force slowing. While these results were promising, the true potential of the technique was obscured by the applied bichromatic force exceeding that of spontaneous slowing by a factor of only $\xi = 2.2$. This suppression of the bichromatic force arose from issues related to our apparatus design. One factor was the inhomogeneous intensity profile of the slowing laser beams, which resulted in deviations from the ideal π-pulse condition for optimized bichromatic forces. The π-pulse requirement was only satisfied along a cylindrical shell of the beams, and we estimate that the spontaneous force profile integrated over velocity was actually larger than the integrated bichromatic force profile for radii larger than $\sim 0.6\omega_0$, where ω_0 is the $1/e^2$ Gaussian waist diameter.

A second factor reducing the applied bichromatic force was the evolution of the beam profile over the interaction length. Focusing the slowing beams through the apertures resulted in an expansion of the beam diameter through the science chamber that caused the Rabi frequency to change by $\sim 2\gamma$ over the 7.5 cm interaction length (longitudinal repump). Similarly, the relative phase between the counter-propagating beams changed by $2.4°/\text{cm}$. These effects resulted in the applied force not matching the ideal force profile but rather an average of many profiles caused by the continuous variation in the phase and Rabi frequency. The effect of this is shown in Fig. 4.23, where the average force profile caused by an $18°$ change in relative phase is plotted with the ideal profile. These effects, coupled with the imperfect mode-matching between the atomic beam
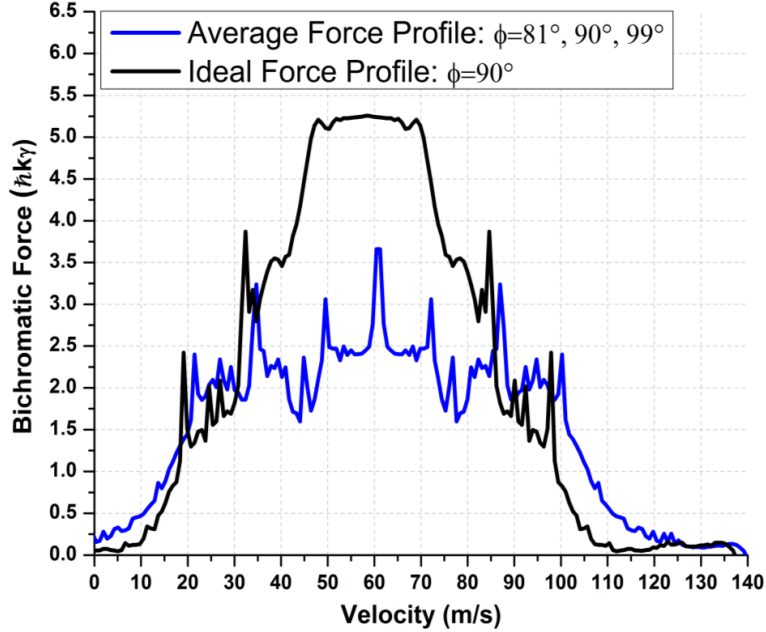
Figure 4.23: Ideal bichromatic force profile (black) and an averaged profile resulting from three different relative phases (blue).

and the slowing fields that caused half of the atoms to never see the slowing light, reduced the enhancement achievable with the bichromatic force in our system.

These various limiting factors could be mitigated with an improved experimental geometry based on a shortened overall apparatus length. This would facilitate improved mode matching of the atomic beam to the bichromatic light, which would increase the number of atoms addressed, and would enable a more optimized intensity distribution. Also, the enhancements observed in our large system were very sensitive to the precise alignment of the bichromatic beams. We observed brief MOT number enhancements of up to 20 and rate enhancements of up to 40. Consistently achieving optimal beam alignment would be easier in a compact system.

Bichromatic slowing could potentially be an important technique for achieving large cold-atom numbers in highly-miniaturized instruments; however, further experiments would be necessary to determine if the realized enhancements justify the technical complexity required to successfully implement the technique. We performed preliminary modeling to explore the possibility of an optical molasses formed by bichromatic forces operating orthogonally in three dimensions. However, the complexity involved and the intrinsic trade-off between the required optical power and trap volume in such a system made this a high-risk experiment and one we did not pursue.

CHAPTER 5

PHASE II COLD-ATOM COHERENT POPULATION TRAPPING CLOCK

As mentioned in Chapter 1, a field-grade version of a cold-atom coherent population trapping atomic clock, integrating laser-cooled atoms, optical interrogation of a microwave clock transition, and Ramsey interrogation, would be useful in a variety of applications including network synchronization, secure and jam-resistant communications, and inertial navigation. A post-doctoral researcher in our group, Dr. Francois-Xavier Esnault, constructed the first generation CACPT system and completed a performance evaluation. Based on lessons learned from the Phase I system, a second-generation CACPT clock was developed, featuring a smaller and more advanced physics package that would enable the Phase II performance requirements of the IMPACT program to be reached in a simpler system. Beyond demonstrating an improved long-term stability, the Phase II system was also used to characterize the AC-stark effect in the CACPT clock as light shifts were one of the principal concerns for a frequency reference based on lin||lin optical interrogation.

This chapter will provide an overview of the Phase II CACPT clock, beginning with a brief introduction to coherent population trapping. Following this, the method used to generate the CPT laser field and the principles of operation of the clock will be presented. The fourth section will discuss the apparatus itself, including the physics package, signal detection, and control software. The chapter will conclude with a summary of the current Phase II clock performance.

5.1 Coherent Population Trapping

Coherent population trapping is a process in which the internal state of an atom transitions to a coherent superposition of energy eigenstates through interaction with a specially configured optical field. Once in the superposition state, called the "dark state", quantum interference prevents further interaction between the atom and CPT laser field, creating a resonance phenomenon that has been thoroughly studied and employed in atomic clocks and magnetometers. The CPT literature is extensive, and several reviews have been written that contain a wealth of information on the
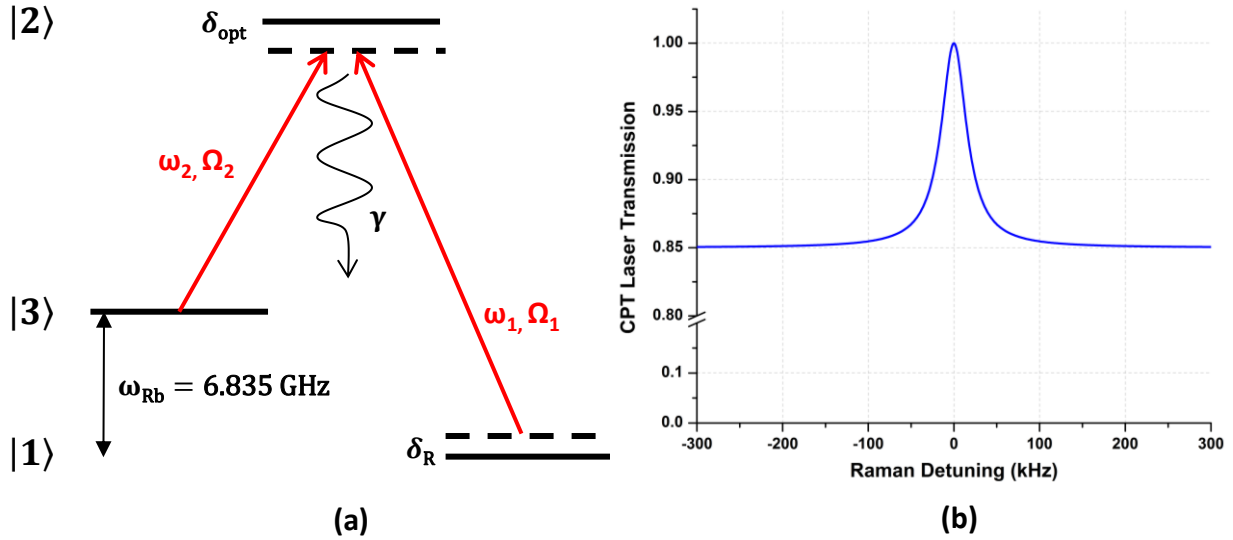
Figure 5.1: (a) Level diagram for a standard CPT system in ^{87}Rb, showing two long lived ground states $|1,3\rangle$ coupled via an excited state $|2\rangle$ by optical fields with frequencies $\omega_{1,2}$ and Rabi frequencies of $\Omega_{1,2}$. Also shown are the optical and Raman detunings given by δ_{OPT} and δ_R, respectively. (b) Simulated ideal CPT transmission resonance. As $\delta_R \to 0$, absorption decreases as atoms are pumped into the dark state.

subject [98–100]. In this section, a brief overview of the phenomenon is presented, followed by a discussion of the particular configuration used in the CACPT clock.

5.1.1 CPT Fundamentals

A standard coherent population trapping resonance is formed by the coupling of two long-lived states (typically ground state hyperfine levels) through an excited state in a so-called "Λ-system". This requires a coherent bichromatic optical field with frequencies corresponding to the transition between each ground and excited state. This configuration is shown in Fig. 5.1 (a), where ground states $|1\rangle$ and $|3\rangle$ are coupled via the excited state $|2\rangle$ by laser fields at frequencies $\omega_{1,2}$ with Rabi frequencies of $\Omega_{1,2}$. For this system, the optical detuning (δ_{OPT}) is defined as the difference between ω_2 and the resonant frequency for a $|3\rangle \to |2\rangle$ transition and the Raman detuning as $\delta_R = (\omega_1 - \omega_2) - \omega_{Rb}$, where ω_{Rb} is the frequency spacing of the ground state hyperfine levels in ^{87}Rb.

To quantitatively determine the effect of the optical fields on this three-level system, the matrix elements of the electric dipole operator must be calculated for the two possible superposition states

formed by linear combinations of the ground state hyperfine levels [98]:

$$
\begin{aligned}
|\alpha\rangle &= \frac{1}{\tilde{\Omega}_R} \left(\Omega_1^* |1\rangle + \Omega_2^* |3\rangle \right) \\
|\beta\rangle &= \frac{1}{\tilde{\Omega}_R} \left(\Omega_2 |1\rangle - \Omega_1 |3\rangle \right),
\end{aligned}
\tag{5.1}
$$

where the normalization Rabi frequency is given by $\tilde{\Omega}_R = \sqrt{|\Omega_1|^2 + |\Omega_2|^2}$. Using the rotating wave approximation and the electric dipole operator $\hat{d}_{dip}$, the matrix elements for transitions from the superposition states to level $|2\rangle$ in the presence of the bichromatic field are [98]:

$$
\begin{aligned}
\langle 2|\hat{d}_{dip}|\alpha\rangle &= \frac{\hbar}{2\tilde{\Omega}_R} \exp\left[-i\left(\Omega_1 + \omega_1\right)t - i\phi_1\right] \left(|\Omega_1|^2 + |\Omega_2|^2 \exp\left[i\delta_R t + i\Delta\phi\right] \right) \\
\langle 2|\hat{d}_{dip}|\beta\rangle &= \frac{\hbar\Omega_1\Omega_2}{2\tilde{\Omega}_R} \exp\left[-i\left(\Omega_1 + \omega_1\right)t - i\phi_1\right] \left(1 - \exp\left[i\delta_R t + i\Delta\phi\right]\right),
\end{aligned}
\tag{5.2}
$$

where ϕ_1 and ϕ_2 are the independent phases of the two frequency components of the optical field, and $\Delta\phi = \phi_1 - \phi_2$ is the relative phase between them. When the optical field is properly configured such that the two frequency components are in phase ($\Delta\phi = 0$) with a Raman detuning of $\delta_R = 0$, then the transition matrix elements become:

$$
\begin{aligned}
\langle 2|\hat{d}_{dip}|\alpha\rangle &= \frac{\hbar\tilde{\Omega}_R}{2} \exp\left[-i\left(\Omega_1 + \omega_1\right)t - i\phi_1\right] \\
\langle 2|\hat{d}_{dip}|\beta\rangle &= \frac{\hbar\Omega_1\Omega_2}{2\tilde{\Omega}_R} \exp\left[-i\left(\Omega_1 + \omega_1\right)t - i\phi_1\right] \times (1 - 1) = 0.
\end{aligned}
\tag{5.3}
$$

Thus, on Raman resonance, the transition amplitude from $|\beta\rangle$ to the excited state for in-phase CPT frequency components is zero, and $|\beta\rangle$ is a CPT dark state. When the Raman detuning of the CPT fields is non-zero, atoms will absorb photons, and the transmission of the CPT beams is < 1. As $\delta_R \to 0$, the frequency difference between the two CPT components approaches the splitting of the ground state hyperfine levels, optically pumping atoms into the coherent dark state, where they no longer interact with the laser fields. This causes an increase in transmission at $\delta_R = 0$ that forms the resonance feature in coherent population trapping. It is worth noting for the later chapter on AC-stark shifts in the CACPT clock that when $\delta_R \neq 0$, atoms can occupy the other hyperfine superposition state $|\alpha\rangle$. This precludes the formation of a perfect dark state and causes light shifts to arise.

5.1.2 Traditional vs. Lin||Lin CPT

Coherent population trapping resonances have been observed in a variety of different excitation schemes involving multiple atomic species, D1 and D2 transition manifolds, and varied field parameters. Different configurations have advantages and disadvantages in terms of performance and complexity as the contrast of the resonance can vary significantly depending on these different variables. For example, the choice of D1 or D2 excitation in [87]Rb greatly affects the achievable contrast in the presence of high pressure buffer gas. For circularly polarized CPT light, two Λ-systems are possible on each laser line; one system couples the hyperfine states via the $|F' = 1\rangle$ excited state, while the other pumps through $|F' = 2\rangle$. Different Clebsch-Gordon coefficients for the transitions on the D1 and D2 lines result in the two Λ-systems constructively interfering for D1 excitation and destructively interfering for D2 [100]. Due to the different phase relationships between the independent dark states in this case, as well as the additional hyperfine states present on the D2 line, the CPT resonance contrast achievable with [87]Rb in buffer gas is much higher for D1 excitation than D2.

In conventional CPT spectroscopy, atoms are interrogated with left or right circularly polarized laser beams to drive transitions between the same Zeeman sublevel, m_F, in each hyperfine state. Due to the vanishing first order Zeeman shift, this configuration with $m_F = 0$ is commonly used in atomic clocks and other applications where magnetic field sensitivity is a detriment. A typical CPT configuration featuring $\sigma^\pm$ polarized laser fields driving an $m_F \to m_F$ transition is shown in Fig. 5.2 (a). Since the structure of a real atom does not form an ideal, closed three level system, this CPT interrogation scheme is susceptible to atom loss from optical pumping to states that are not part of the Λ-system. Once in this trap state ($|F = 2, m_F = 2\rangle$ in Fig. 5.2 (a)), atoms no longer contribute to the resonance contrast and degrade the signal to noise ratio of a device featuring CPT interrogation [99].

With the atom number and S/N directly impacting the stability of an atomic clock, this decrease in contrast can be a significant issue. Fortunately, several schemes have been developed that eliminate trap states and improve the CPT resonance signal, including push-pull optical pumping [101] and double-Λ methods [102, 103]. Our CACPT clock features one of these techniques, lin||lin coherent population trapping [103], in which a bichromatic field with parallel linear polarizations
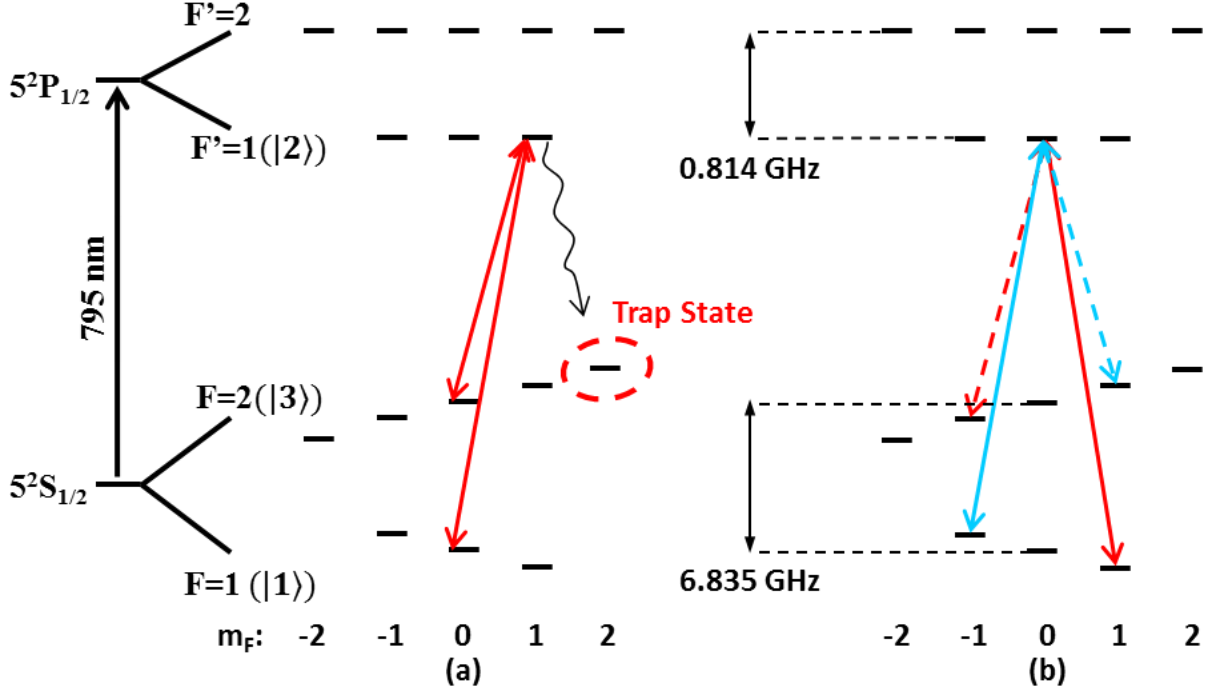
Figure 5.2: D1 level diagrams for ^{87}Rb. (a) Standard CPT configuration with circularly polarized light and a trap state. (b) Lin||lin CPT scheme with parallel, linear polarizations and no trap states. Same-colored lines form the two Λ-systems. Solid (dashed) lines are from the same laser.

generates the CPT resonance. The linearly polarized field can be decomposed into circular components, $\hat{s} = 1/\sqrt{2}\left(\hat{\sigma}^+ + \hat{\sigma}^-\right)$, that drive $\Delta m_F = \pm 1$ transitions, generating two independent Λ systems that couple ground state hyperfine levels with $\Delta m_F = 2$ (Fig. 5.2 (b)). In this double-Λ configuration centered on the excited $m'_F = 0$ sublevel, selection rules preclude the formation of trap states that siphon atoms from the CPT interaction, preventing the loss of resonance contrast.

Achieving a high-contrast resonance in lin||lin interrogation requires two conditions to be met: the atom must have ground state hyperfine levels with total angular momenta of $F = 1$ and $F = 2$ coupled by an excited state with $F' = 1$, and the hyperfine levels must be sufficiently separated to be spectrally resolved [103]. These conditions are both met for the D1 line of ^{87}Rb, used in the CACPT clock. In this case, the lin||lin CPT field is composed of two frequencies separated by the 6.835 GHz ground state hyperfine splitting and couples atoms into a double-Λ system connecting the $|F = 1, m_F = \pm 1\rangle$ and $|F = 2, m_F = \mp 1\rangle$ ground states via the $5^2\mathrm{P}_{1/2}$, $|F' = 1, m_F = 0\rangle$ level. This configuration has been previously shown to exhibit an improved resonance contrast over traditional CPT schemes [104, 105].

5.1.3 Magnetic Field Effects in Lin||Lin CPT

In addition to the primary resonance from the $\Delta m_F = 2$ Λ-systems, a pair of resonances arising from $\Delta m_F = 0$ Λ-systems also appear with high contrast in the lin||lin scheme. These two magnetically-sensitive resonances are caused by dark states formed from frequency components linking $|F = 1, m_F = \pm 1\rangle$ and $|F = 2, m_F = \pm 1\rangle$ (Fig. 5.3 (a)). With a small applied magnetic field, these lines are shifted tens or hundreds of kHz away from the primary resonance and do not affect the CPT contrast. From the perspective of operating an atomic clock, these transitions are useful as scanning the Raman detuning over one of these resonances provides a mechanism for measuring the magnetic field within the system. This will be discussed further in Section 5.3.

A second magnetic effect in the lin||lin configuration arises from the opposite Zeeman shifts of each independent Λ-system forming the primary resonance and is a disadvantage of using this scheme in an atomic clock. Due to the contribution of the nuclear spin ($I = \frac{3}{2}$) to the total angular momentum, the Landé g-factor is different for the $|F = 1\rangle$ and $|F = 2\rangle$ ground state hyperfine levels, causing each state to undergo a different Zeeman shift in the presence of an external magnetic field. Accordingly, since the lin||lin configuration features two Λ-systems connecting $m_F \neq 0$ states, the frequency of the two-photon transition that optically pumps atoms into the dark state via these Λ-systems will also exhibit a dependence on the external magnetic field.

This magnitude of this effect can be determined by expanding the Breit-Rabi equation to second order, where it can be shown that the Zeeman shift for each of the two Λ-systems is given by [103, 106]:

$$\Delta\nu_Z = 431.6 \text{ Hz/G}^2 \pm 2786 \text{ Hz/G}, \tag{5.4}$$

where the $\pm$ refers to the $\pm m_F \rightarrow \mp m_F$ transitions in the lin||lin scheme. This expression reveals first-order and second-order Zeeman shifts in each Λ-system that must be addressed individually in the experiment. The linear shift is equal and opposite for the two Λ-systems, introducing interference between the independent Ramsey fringes generated by each. A high contrast CPT resonance is only achieved at specific values of the external magnetic field where the first-order Zeeman shift matches the width of the Ramsey fringes such that constructive interference between the two Λ-systems occurs. The discrete field values resulting in a high contrast signal are given by:
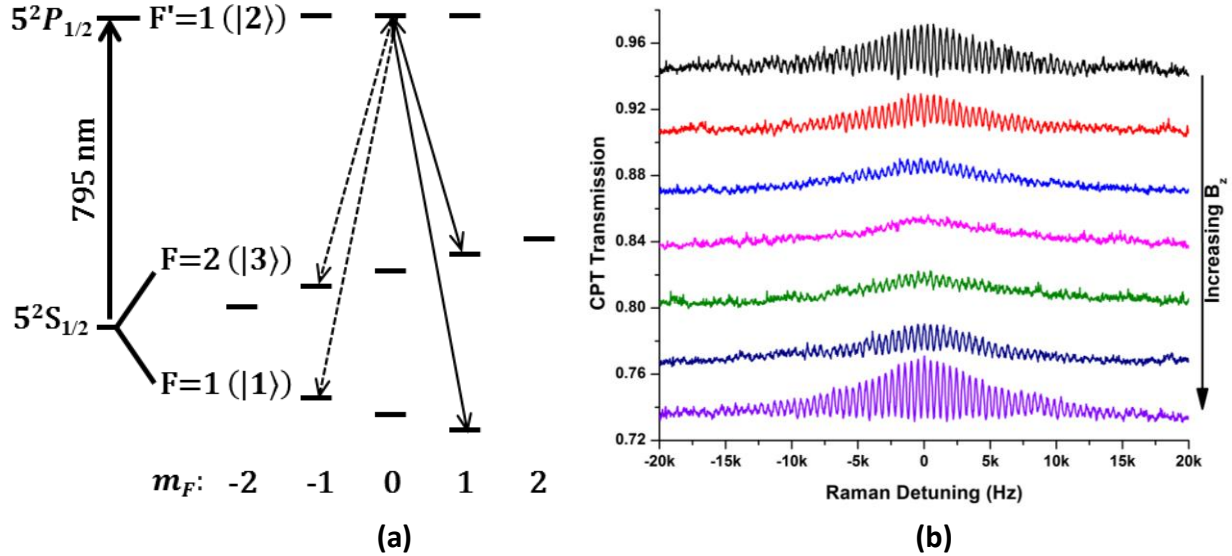
Figure 5.3: (a) Level diagram showing the two magnetically sensitive Λ-systems (solid and dashed lines) in lin‖lin CPT. (b) $T_R = 2$ ms Ramsey fringes as a function of applied magnetic field. Fringes have been artificially offset for clarity and are in top to bottom order of increasing applied magnetic field. Data collected by Dr. F.-X. Esnault.

$$|\vec{B}_n| = \frac{n \times 1/(2T_R)}{2786 \text{ Hz/G}}. \tag{5.5}$$

Experimentally, this constructive interference condition required tuning the magnetic field along the axis of the CPT lasers until one of the allowed values of B_n for a given Ramsey period was reached. This is illustrated in Fig. 5.3 (b), where $T_R = 2$ ms Ramsey fringes have been recorded as a function of the applied field along the CPT axis (the "c-field"). As the c-field was tuned away from an optimum given by Eq. 5.5, the fringe amplitude steadily decreased until only the envelope was visible. Beyond this point of destructive interference, the fringe amplitude grew until being fully recovered at the $n+1$ optimum field value.

The second-order Zeeman term in Eq. 5.4 is the same for both Λ systems and represents a shift of the CPT resonance frequency. Fluctuations in the magnetic environment cause shifts of the clock frequency due to this term, resulting in long-term stability limits for the clock; this will be discussed further below. Typically, the c-field applied in the experiment corresponded to the $n = 4$ optimum. This bias field of ~ 45 mG, was sufficient to separate the field-sensitive CPT resonances from the primary lin‖lin resonance and suppressed the effect of any gradients present

in the external magnetic environment.

While the magnetic field sensitivity is a drawback of the lin||lin scheme, it can be managed with proper tuning of the c-field to ensure constructive interference of the Λ-systems and magnetic shielding of the physics package to reduce frequency fluctuations from the quadratic Zeeman shift. With these simple measures, the advantages of the lin||lin scheme outweigh this limitation.

5.2 CPT Field Generation

For CPT interrogation of the microwave transition to be effective in an atomic clock, the laser field must fulfill certain requirements. First, there must be high relative coherence between the two frequency components driving the two-photon transitions that pump atoms into the dark state. Poor coherence results in inefficient pumping and an incompletely formed dark state with decreased resonance contrast. Secondly, the laser field must have stable absolute and relative intensities to minimize shifts of the clock frequency due to the AC-stark effect. Finally, there must be low overall phase noise to suppress the Dick Effect, an aliasing phenomenon that degrades the signal to noise ratio via laser frequency noise that is down-converted by the pulsed nature of the clock [12].

One technique to generate an optical spectrum meeting these requirements involves current modulating a laser diode to create first order sidebands separated by the ground state hyperfine splitting. While the sidebands are perfectly coherent, this approach introduces additional higher-order sidebands that can shift the clock frequency through long term variations of the sideband to carrier power ratio. Also, the availability of field-grade lasers with the proper modulation capabilities, linewidth, and output power is a concern.

To avoid these issues, the coherent population trapping field in our experiment was created by phase-locking two commercial 795 nm laser diodes. Optical phase locking has the potential to generate highly coherent fields with a very clean spectrum due to the lack of modulation sidebands. The details of our CPT laser system are presented in this section.

5.2.1 Laser Selection

The lasers selected to generate the interrogation field were chosen from the perspective of creating a field-grade device. While ECDLs provide superior linewidths, they are susceptible to
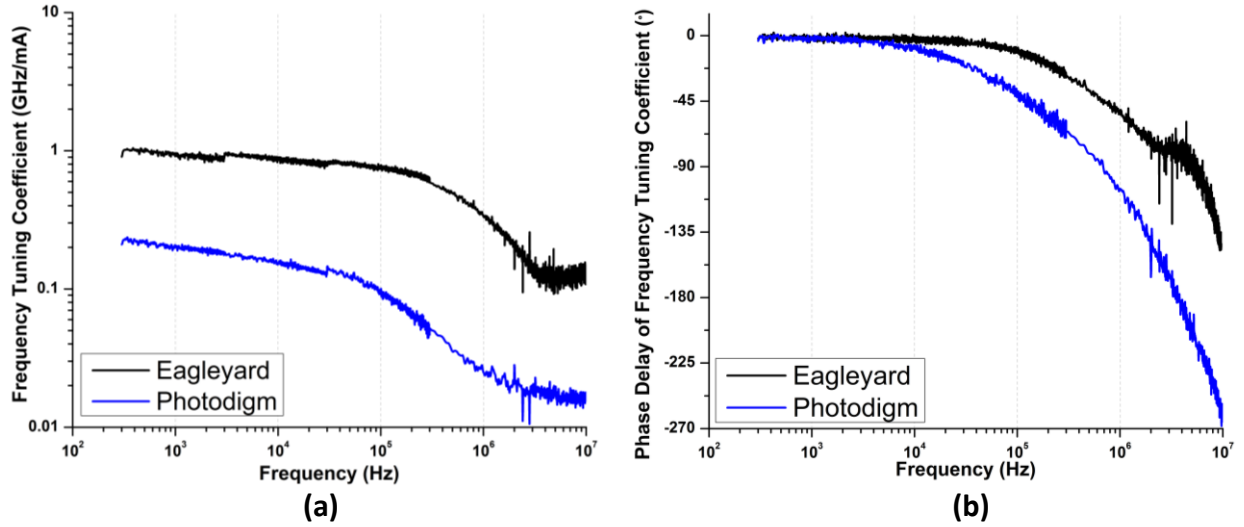
Figure 5.4: Current to frequency tuning coefficient amplitude (a) and phase delay (b) for the Eagleyard and Photodigm laser diodes.

vibration issues due to the sensitive alignment of the components required for frequency selective optical feedback. New ECDL designs currently arriving on the market may be sufficiently robust to operate outside of a lab environment; however at the start of this project, we chose to use DFB and DBR lasers as wavelength selection was done through current and temperature tuning, and no sensitive alignment was needed for the laser itself to operate reliably over long time periods.

In our optical system, the two CPT frequency components were generated from a Photodigm DBR laser diode (Fig. 3.9 (a)) and an Eagleyard DFB laser diode (Fig. 3.6 (b)), both of which operated at 795 nm on the D1 line of ^{87}Rb and had output powers of ~ 40 mW. The linewidths of the two diodes were determined by heterodyne measurements in which beatnote spectra were recorded between the two CPT lasers and between each CPT laser and a third diode (an extra Eagleyard DFB). By fitting the beat notes from each of these combinations, the linewidth of each individual laser could be calculated. The Photodigm DBR had a linewidth of 0.6 MHz, while the Eagleyard DFB was nearly twice as broad with a measured linewidth of 1.1 MHz. The broad linewidths of the DFB/DBR lasers used for the coherent population trapping field placed stringent requirements on the phase lock electronics (discussed below). Both lasers were mounted in home-built laser enclosures and driven by NIST current and temperature controllers.

To determine the optimal master/slave relationship between the Photodigm and Eagleyard diodes, the amplitude and phase of the frequency tuning coefficient for each laser was measured

using a delay-line frequency discriminator. In this technique, white noise from an FFT analyzer was injected into the fast modulation port of the diode undergoing the measurement. The two lasers were separated in frequency by the 6.835 GHz splitting of the ground state hyperfine levels, and a sample of each beam was overlapped on a high speed photodiode. The beat note signal was amplified and passed through an $8\times$ frequency divider. The signal was then split into two equal parts: half went directly into an RF mixer, while the other half propagated through a ~ 2 m long delay line before arriving at the mixer. Measuring the amplitude of the mixer output on the FFT provided the transfer function (T) specifying the spectral response of the laser diode to the noise injection. The tuning coefficient of the laser, given by the change in frequency (f) per change in applied voltage (V), was then calculated from:

$$\left(\frac{df}{dV}\right)|_{laser} = \frac{nT}{(dV/df)|_{DLD}},\tag{5.6}$$

where $n = 8$ corrected for the frequency divider in the measurement setup, and $dV/df|_{DLD}$ is a calibration factor for the delay-line discriminator determining the mixer response as a function of frequency. This factor was measured using the same delay-line frequency discriminator with direct injection from a synthesizer. The phase of the tuning coefficient was also determined from the mixer output using the FFT. The results of these measurements are shown in Fig. 5.4. The Eagleyard diode exhibited a $5\times$ to $10\times$ greater tuning coefficient than the Photodigm laser over the full frequency range and had a $\sim 5\times$ smaller phase delay, reaching a $\pi/2$ phase shift at ~ 4 MHz as opposed to < 1 MHz for the Photodigm laser. Based on these results, the Photodigm laser was chosen to be the master for the phase lock and Eagleyard diode the slave, making use of the large tuning coefficient and smaller phase delay to achieve a higher optical phase locked loop bandwidth than possible in the reverse configuration.

5.2.2 Optics Layout

The optics layout used in our experiment to generate a CPT light field at the proper frequencies is shown in Fig. 5.5. Since both the master and slave lasers were edge-emitting diodes, the beams first passed through anamorphic prism pairs to correct for the elliptical shape of the diode output. They then passed through free-space optical Faraday isolators to prevent back-reflections from
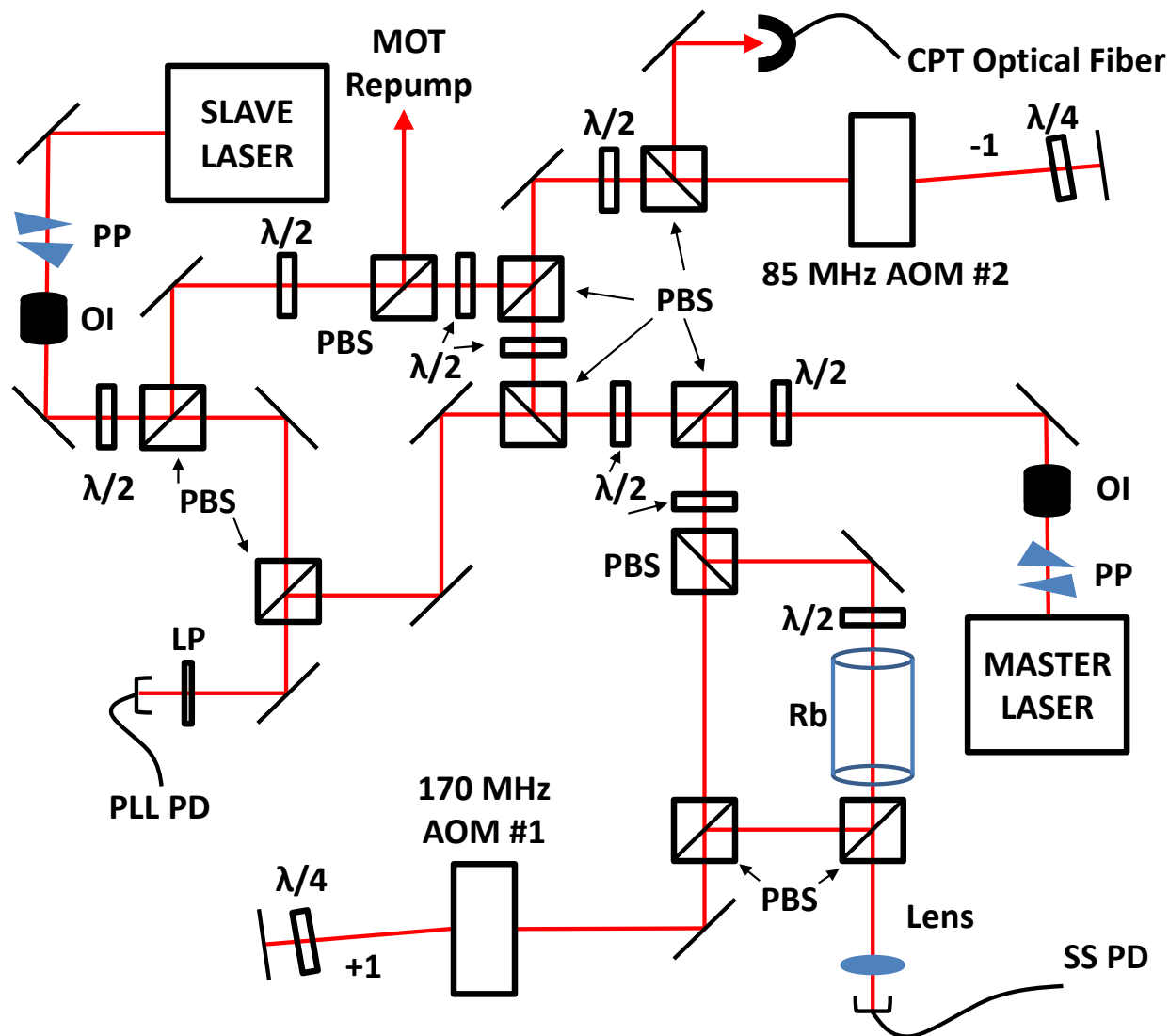
Figure 5.5: Diagram of the beam paths for the master and slave CPT lasers. The following label abbreviations are used: anamorphic prism pairs (PP), optical isolators (OI), half-wave plates ($\lambda/2$), quarter-wave plates ($\lambda/4$), linear polarizer (LP), polarizing beam splitter cubes (PBS), rubidium vapor cell (Rb), phase lock loop photodiode (PLL PD), saturated absorption spectroscopy photodiode (SS PD), and acousto-optic modulator (AOM). The laser system output consisted of phase-locked and spatially overlapped master and slave frequency components coupled into the CPT optical fiber.

downstream optics from causing laser noise via optical feedback. For the master laser, roughly 2 mW of power was picked off by a polarizing beam splitter cube (PBS) and sent to a saturated absorption spectroscopy setup. As in the bichromatic experiment, different frequencies were used for the pump and probe: the pump laser was blue-shifted by ~ 340 MHz by a double-pass AOM (#1 in Fig. 5.5) operating at 170 MHz, while the probe beam was not shifted. Locking a laser with this configuration places the frequency 170 MHz above the chosen transition (see Section 3.2.2). Thus, the master laser was locked 170 MHz above the $|F = 2\rangle \rightarrow |F' = 1\rangle$ transition using a NIST lock-in amplifier and loop filter, achieving a bandwidth of ~ 10 kHz.

A small fraction (~ 2 mW) of each frequency component was diverted toward a PBS, where the master and slave beams met and were carefully overlapped using mirrors in each beam path. The combined beam passed through a linear polarizer and was aligned onto a fast Hamamatsu G4176 photodiode with a 9 GHz bandwidth. The optical beat note measured on this photodiode was used by the PLL electronics to phase lock the slave laser to the master with an offset frequency equal to the ~ 6.835 GHz splitting of the ground state hyperfine levels. The offset frequency was set by a microwave synthesizer acting as the reference for the PLL electronics. With the master laser blue-detuned from the $|F = 2\rangle \rightarrow |F' = 1\rangle$ transition, this was equivalent to locking the slave laser 170 MHz above the $|F = 1\rangle \rightarrow |F' = 1\rangle$ transition. The slave laser then tracked frequency and phase fluctuations in the master, maintaining the correct frequency separation for the CPT field to remain on Raman resonance.

After the saturated absorption spectroscopy and phase lock arms, the master and slave laser beams were combined on a PBS, with a half-wave plate setting the power balance between the frequencies. Both components were then down-shifted by a double pass AOM operating at ~ 85 MHz (#2 in Fig. 5.5) such that the optical detuning of the CPT field was nearly zero. After the double-pass, the beams were coupled into a polarization maintaining optical fiber and sent to the physics package.

Finally, as shown in Fig. 5.5, the CPT slave laser was dual purposed to provide repump light for the MOT cooling and trapping sequence, eliminating the need for a fourth laser in the experiment. A few mW were picked off from the main beam and directed toward a frequency control arm for the cooling light. This is discussed in Section 5.4.

Regarding the frequency control scheme in our experiment, using AOM #1 (Fig. 5.5) to blue-

detune the lock point of the master and slave lasers by 170 MHz and AOM #2 to shift the frequencies back to resonance provided a convenient mechanism for adjusting the optical detuning. Instead of a VCO, the frequency of the second AOM was driven by an RF synthesizer controlled by the LabVIEW software running the experiment. Incorporating control of δ_{opt} into the software allowed the computer to automatically correct for frequency drift of the saturated absorption spectroscopy lock on the master laser using the cold-atoms in the clock as a reference. This will be discussed more in the next section. With one synthesizer referencing the PLL electronics and another driving the second AOM in the CPT optics, both the Raman and optical detuning of the CPT field were carefully controlled using our LabVIEW software.

5.2.3 Phase Locked Loop

To generate the CPT field, an optical phase locked loop was used to electronically lock the frequency and phase of the slave laser to the master. The performance of this system was critical for observing a coherent population trapping resonance, which required the relative phase difference between the master and slave lasers to remain $\ll \pi/2$ over the course of a 15-20 ms Ramsey sequence. This implied that the PLL had to achieve a lock with a low phase error variance (σ_Φ^2) such that the fraction of the CPT spectrum in the coherent carrier was sufficiently large for a high contrast resonance to be observed. However, obtaining a low phase error variance with the large linewidths of the DFB and DBR lasers was challenging. The dependence on the linewidths is roughly given by [107]:

$$\sigma_\Phi^2 \sim \frac{2\left(\Delta\nu_m + \Delta\nu_s\right)}{f_{BW}}, \tag{5.7}$$

where $\Delta\nu_{m,s}$ is the linewidth of the master and slave laser, respectively, and f_{BW} is the bandwidth of the PLL. With the 0.6 MHz and 1.1 MHz linewidths of our lasers, achieving a quality phase lock required broadband electronics and careful control of propagation delays and laser properties. This requirement motivated the choice of master/slave configuration based on the phase delay and amplitude of the diode tuning coefficients.

A block diagram of our phase locked loop is shown in Fig. 5.6 (a). The optical beat note at ~ 6.835 GHz was measured on the same ultra-fast photodiode discussed above, amplified, and down-converted to ~ 854 MHz by an $8\times$ frequency divider. It was then sent to a 1.3 GHz digital
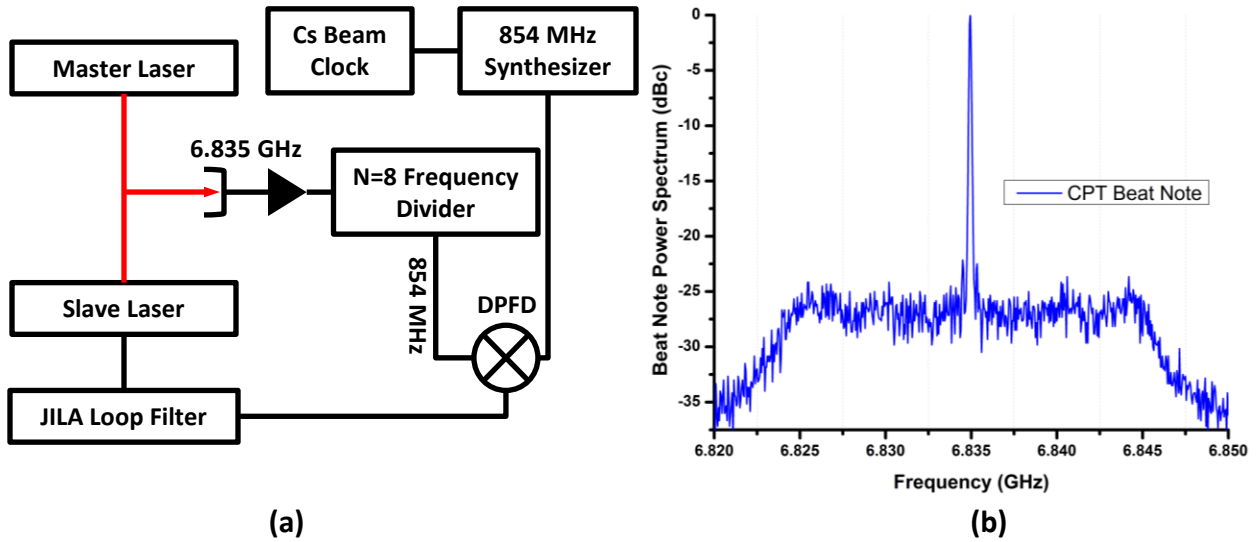
Figure 5.6: (a) Diagram of the phase-locked loop used in the CACPT clock. The broadband loop filter was designed by Terry Brown at JILA. (b) Optical spectrum (RBW=100 kHz) of the beat note between master and slave lasers locked using the PLL. A carrier power fraction of 0.72, corresponding to a phase error variance of $\sigma_\Phi^2 \cong 0.35$ rad^2, was typically achieved.

phase frequency detector (DPFD), where it was compared with an $\sim$ 854 MHz signal from an Agilent N5181 analogue signal generator, referenced to a Cesium beam atomic clock (Symmetricom 5071A). This reference synthesizer determined the frequency offset between the master and slave lasers through the PLL and was used to tune the Raman detuning via GPIB connections to the LabVIEW software. The phase error signal from the DPFD was sent to a broadband loop filter, purchased from JILA, that provided feedback to the slave laser via the high-speed current injection port. The JILA loop filter featured a proportional-integral stage, a lead stage, and a phase advance that compensated for phase delays at high frequencies in the slave laser. The circuit featured fast operational amplifiers and achieved a bandwidth of $\sim$ 4 MHz limited by the phase reversal of the frequency tuning coefficient in the slave.

The optical spectrum of a typical beat note between the master and slave lasers with the PLL engaged is shown in Fig. 5.6 (b). With this system, we routinely achieved a phase lock with $\sim$ 73% of the CPT optical power locked to the coherent carrier, determined by integrating the spectrum over 20 MHz centered on the carrier. The phase error variance corresponding to this carrier power is given by [108]:

$$e^{\left(-\sigma_\Phi^2\right)} \approx \frac{P\left(f_{carrier}\right)}{\int_{-\infty}^{+\infty} P\left(f\right) df}, \tag{5.8}$$

where $P(f_{carrier})$ is the fraction of power in the coherent carrier and $P(f)$ is the power spectrum. From this expression, the phase error variance achieved by our phase locked loop was $\sigma_\Phi^2 \cong 0.35$ rad^2. While this performance was certainly sufficient to observe a CPT resonance, the 27% of the CPT light not in the coherent carrier decreased the clock resonance contrast and contributed to the light shift. Further improvement of the PLL carrier fraction would require lasers with narrower linewidths and reduced phase delays or locking the master using a fast electro-optical modulator (EOM). The EOM technique will be tried in the near future.

5.3   Clock Operation

To achieve a narrow resonance with suppressed AC-stark shifts, the CACPT clock operated with the time-separated, pulsed Ramsey interrogation sequence shown in Fig. 5.7 (a). Each clock cycle began with a ~ 35 ms cooling period to trap an atomic sample for CPT interrogation. Following this, the MOT coil was turned off, and the cooling laser detuning was ramped by -8γ over a few ms to decrease the temperature of the atom cloud and increase the cycle to cycle recapture fraction. This was followed by a preparation stage, which was an optional step in the sequence that could be used to apply another laser pulse for atomic state selection or as a free-fall period to amplify the Doppler shift for characterization measurements. The first CPT pulse, typically of duration $\tau_1 = 400$ μs, then optically pumped the atoms into the non-interacting dark state. The atomic state vectors evolved freely at the hyperfine frequency during the Ramsey period with all laser fields off. After the Ramsey period (~ 16 ms), the accumulated phase shift between the coherent dark state and the local oscillator was probed via the absorption of a second CPT laser pulse, 50 μs in duration.

The time-separated interrogation sequence results in Ramsey fringes through interference of the excited state transition amplitudes of each individual pulse. For the mathematically simple case of a two level system with equal pump and probe pulse durations of $\tilde{\tau}$ and a Ramsey time of $T_R = T - \tilde{\tau}$, the excited state transition probability after the second pulse is [56]:

(a)　　　　　　　　　　　　　　　　　　**(b)**
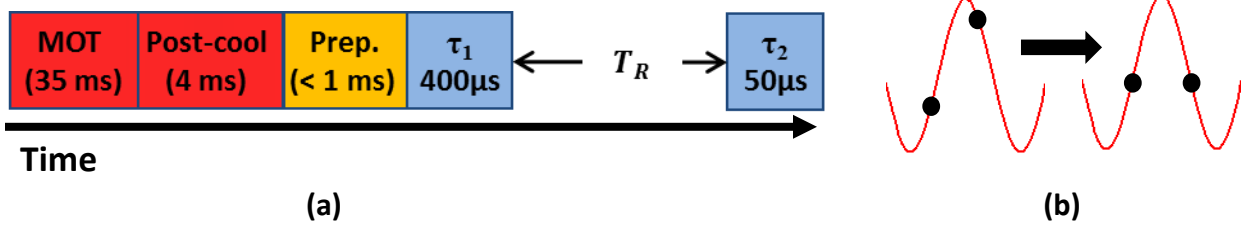
Figure 5.7: (a) Timing diagram for the CACPT clock. A roughly 40 ms cooling sequence (red) trapped and cooled the cloud, followed by a preparation pulse (yellow) for state selection ($|F_0 = 1\rangle$ or $|F_0 = 2\rangle$) or for freefall Doppler shift measurements. The CPT sequence (blue) occurred next, with a 400 μs pumping pulse and a 50 μs probe pulse separated by a Ramsey period of 8-16 ms. (b) Diagram showing the locking sequence for the CACPT clock. Transmission measurements (black dots) were made on either side of the central Ramsey fringe and the center frequency was adjusted until the transmission was equal.

$$P_{1\to 2} = |c_2|^2 = \left|\frac{\Omega\tilde{\tau}}{2}\right|^2 \left[\frac{\sin\left(\frac{1}{2}\delta\tilde{\tau}\right)}{\frac{1}{2}\delta\tilde{\tau}}\right]^2 \cos^2\left(\frac{\delta T}{2}\right), \tag{5.9}$$

where c_2 is the excited state amplitude, and Ω and δ are the Rabi frequency and detuning of the laser field, respectively. In this expression, the width of the central Ramsey fringe is determined by the $\cos^2$ function, from which the full width at half maximum is found to be $\Delta f_{FWHM} = 1/(2T)$. This Fourier-relationship between the fringe width and Ramsey period is a benefit of operating in a pulsed Ramsey configuration as the clock fringe can be narrowed by extending the Ramsey period as long as possible in the particular system. For the CACPT clock, T_R was limited to ~ 16 ms by the distance the atom cloud fell during the interrogation sequence. For longer times, the S/N was degraded by both the different intensities of the Gaussian CPT beams sampled during the first and second pulses and by a lower atom number caused by decreased cycle to cycle recapture.

When the CACPT clock was locked on resonance, the transmission of the CPT probe pulse at equal frequencies above and below the peak of the central fringe was the same (Fig. 5.7 (b)). This was the desired outcome of the digital servo used to maintain lock during clock operation. The locking procedure involved measuring the transmission of the probe pulse at $\pm\Delta\nu_R/2$ around the central fringe, where $\Delta\nu_R$ is the Ramsey fringe width. After measuring the transmission at $+\Delta\nu_R/2$, an error signal was generated based on the transmission difference between the current and previous clock cycle, and the synthesizer frequency referencing the optical PLL was tuned to shift the Raman detuning toward zero. This same procedure then occurred at $-\Delta\nu_R/2$, and the
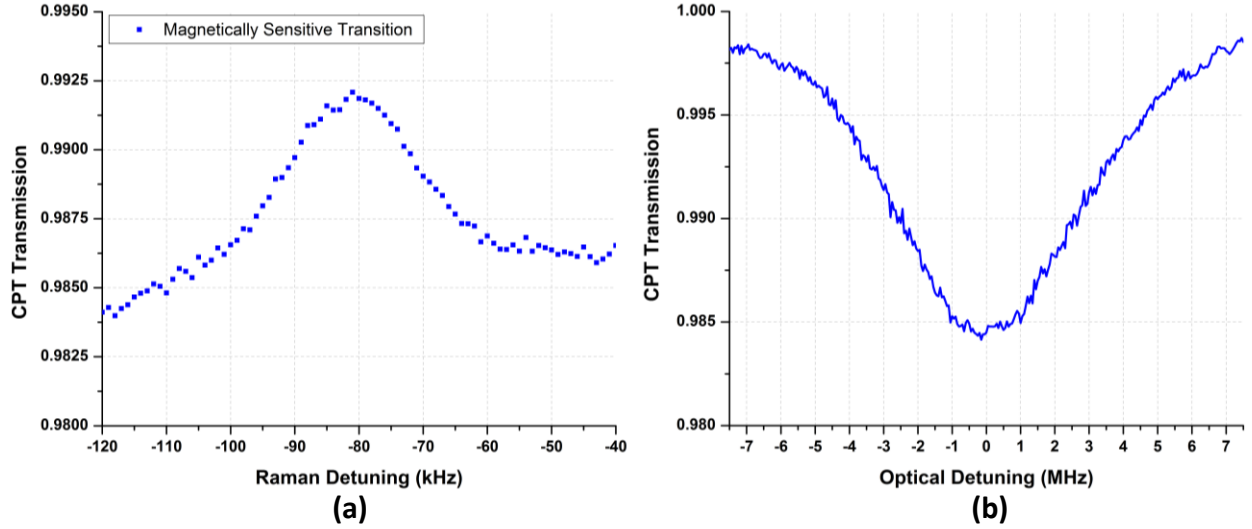
Figure 5.8: (a) Transmission of the first CPT pulse as a function of δ_R scanned over the $m_F = 1 \to m_F = 1$ magnetically sensitive CPT resonance. (b) Absorption of the first CPT pulse as a function of δ_{opt}. Fitting this data provided a correction to slow drift in the master laser frequency.

magnitude of the frequency corrections was recorded and used to calculate the Allan deviation of the clock. The gain of the clock servo was controlled in real-time with the LabVIEW software and was set to optimize the short-term stability of the CACPT clock.

During long data runs, the Ramsey sequence was performed repeatedly to average down the uncertainty and generate statistics on the measured clock frequency. After roughly 10 minutes of operation, the clock sequence was paused to execute in-situ diagnostic measurements to monitor drifts in the magnetic environment and in the master laser frequency. To measure the ambient magnetic field, the Raman detuning was swept over the $m_F = 1 \to m_F = 1$ magnetically sensitive CPT resonance, and the transmission was fitted with a Gaussian function. An example scan of the magnetic resonance is shown in Fig. 5.8 (a). The magnetic field causing the Zeeman shift of this resonance was calculated from the center frequency of the fit, providing a means of tracking drift in the magnetic environment in real-time. Following the magnetic diagnostic, the optical detuning of the CPT field was scanned, and the absorption from the cold-atoms was fitted. The center frequency of this fit was used to adjust the frequency of the CPT AOM to ensure that the optical detuning of the field remained at $\delta_{opt} = 0$. This provided a second feedback control for the master laser, correcting frequency drifts in the saturated absorption setup with scans of the cold atoms.

Tracking the magnetic field was very important in understanding long-term drifts in the Phase

I CACPT clock. In this un-shielded system, the stability was limited to 2×10^{-12} at 1000 s of integration time by drift in the magnetic environment of 0.25 mG over the five hour measurement period. By calculating the Allan deviation of the magnetic field data collected by the diagnostic scans throughout the full measurement period, the Zeeman shift was identified as the limiting drift mechanism [48]. In the Phase II system, optical detuning scans allowed us to attribute jumps in the clock frequency to light shift effects and reduced the instability by providing an extra servo control for the master laser frequency.

5.4 Phase II Apparatus

The Phase II CACPT apparatus was designed and constructed with miniaturization in mind, using lessons learned from the first-generation system. The volume of the UHV physics package was significantly reduced and featured a high-quality optical cell to reduce issues related to reflected light. A block diagram of the cold-atom coherent population trapping clock is shown in Fig. 5.9. To generate the CPT resonance and Ramsey fringes, the phase-locked master and slave lasers were sent via polarization-maintaining optical fiber to an output coupler near the chamber, where the interrogation beam was split into two arms. One arm was focused onto a photodiode used to servo the intensity of the CPT lasers, and the other arm propagated through the chamber, interrogating the atom cloud before being retro-reflected and detected on a second photodiode. This generated the Ramsey fringe signal used by the computer to calculate of the clock frequency corrections. Steering signals were generated and sent to the synthesizer acting as the reference for the optical phase locked loop, which then shifted the offset frequency of the phase lock such that the Raman detuning remained at zero. This formed the feedback loop for the clock, disciplining the local oscillator with frequency measurements of the atomic resonance. This section will provide an overview of the major components of the Phase II CPT apparatus, including the optics, physics package, detection system, and control software.

5.4.1 Laser Cooling Optics

To prepare an atomic sample for interrogation by the CPT field, ^{87}Rb atoms were confined in a standard 3D magneto-optical trap. The MOT laser was a 40 mW Photodigm DBR diode
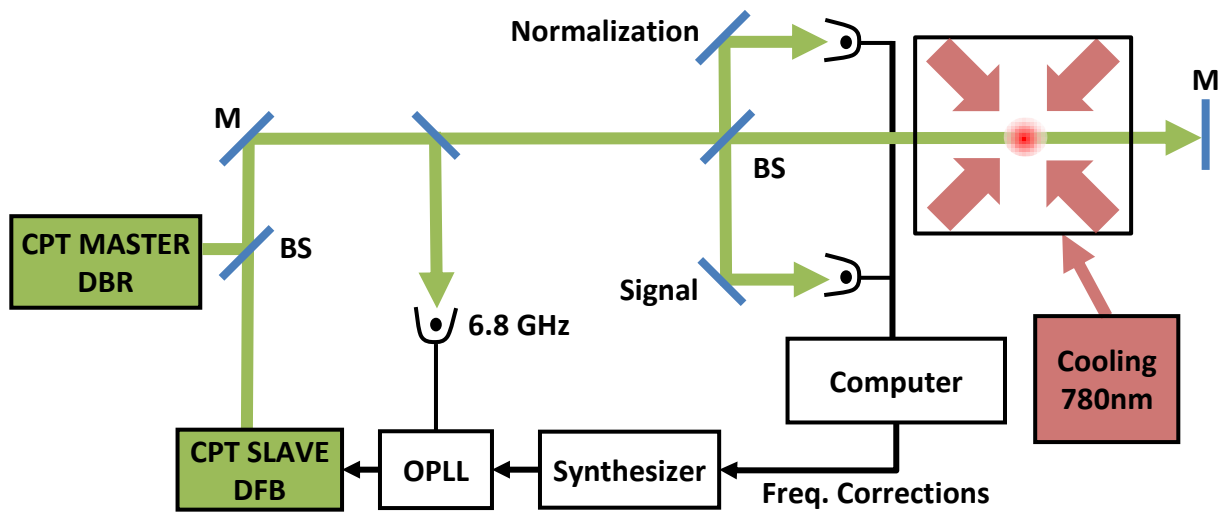
Figure 5.9: Block diagram of the Phase II CACPT clock. Abbreviations: M is a mirror, BS is a beam splitter, and OPLL is the optical phase locked loop. See text for discussion.
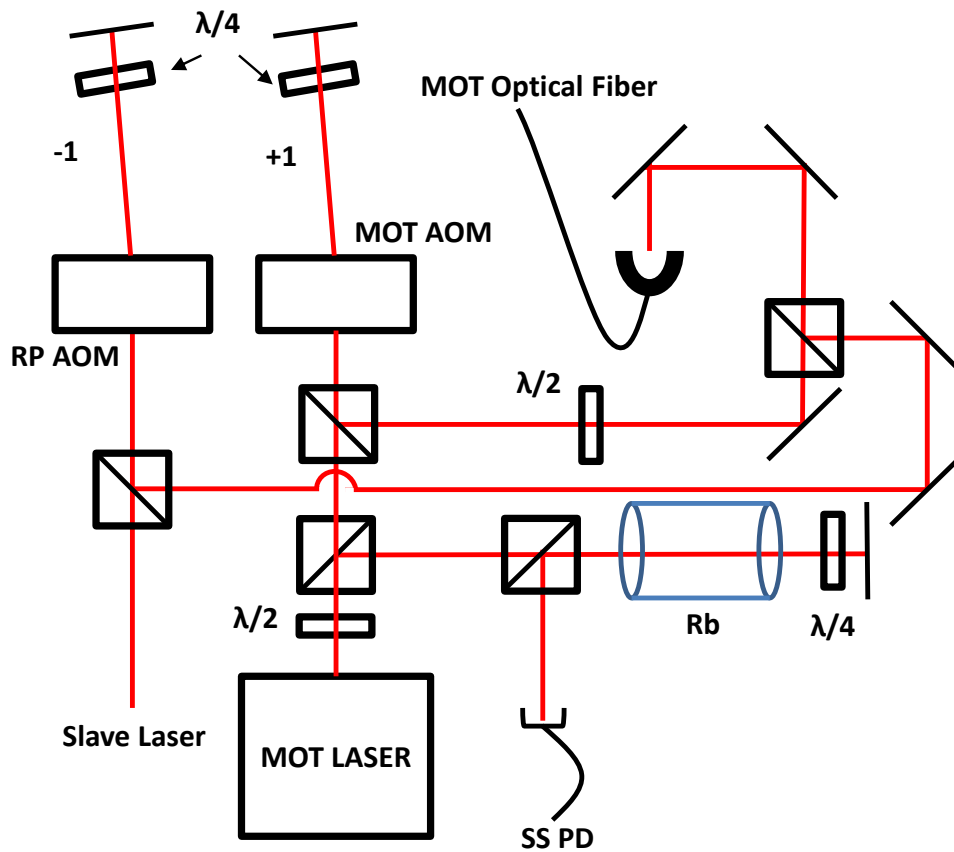
Figure 5.10: Optics layout for the repump and cooling beams used for the MOT. The MOT AOM operated at 100 MHz, and the repump (RP) AOM ran at 85 MHz.

operating at 780 nm on the D2 line. This was the same commercial model from Vescent Photonics used for the MOT laser in the bichromatic slowing experiment (Fig. 3.6 (a)), including the current controller and locking electronics. The trapping laser was locked to the $|F = 1', 3'\rangle$ cross-over resonance via a standard saturated absorption spectroscopy setup with pump and probe beams at equal frequencies, detuning the frequency ~ 212 MHz below resonance (Fig. 3.4 (a)). As shown in the optics layout in Fig. 5.10, the frequency was shifted back toward resonance by a double-pass AOM operating at ~ 100 MHz such that the trapping laser was red-detuned by $\sim 2\gamma$.

The repump laser was derived from the CPT slave. A fraction was diverted from the slave beam and sent through a double-pass AOM to down-shift the frequency by 170 MHz, correcting for the detuned master laser lock point and placing the frequency on resonance with the $|F = 1\rangle \rightarrow |F' = 1\rangle$ transition. The repump was aligned onto a polarizing beam splitter, where it was overlapped with the cooling light. Both beams were then coupled into a single optical fiber. To do so, the two mirrors closest to the input were used to optimize the injection of the MOT laser into the fiber; after this, the two mirrors directing the repump onto the PBS were used to walk the beam such that was efficiently coupled into the fiber as well. The polarization-maintaining optical fiber used for the MOT and repump light was from Oz Optics and had a three-way fiber splitter (based on partially reflecting mirrors) at the end, providing each MOT axis with an independent output coupler.

5.4.2 Physics Package

The second generation CACPT physics package was based on a compact vacuum system from ColdQuanta. It featured a 3.5 cm^3, high optical quality glass cell with an anti-reflection coating on both the inner and outer surfaces specified to suppress reflections below 0.05% for 780 nm and 795 nm light. The cell was attached via a glass to metal adapter to a 1.33" conflat flange that was bolted to a 0.4 L/s ion pump, giving the vacuum system a total volume of < 80 cm^3. To generate a Rb vapor inside the chamber, ~ 3.4 A of current was passed through a Rb dispenser inside the cell. The vacuum system was pumped out upon arrival and had a pressure below 10^{-9} torr during early stages of clock operation. Photographs of the physics package are shown in Fig. 5.11.

The physics package was designed to be as compact and self-contained as possible. A cubic mounting structure for the magnetic field coils and fiber output couplers was designed to slide into place around the optical cell, guided by four aluminum threaded rods and clamped in place by
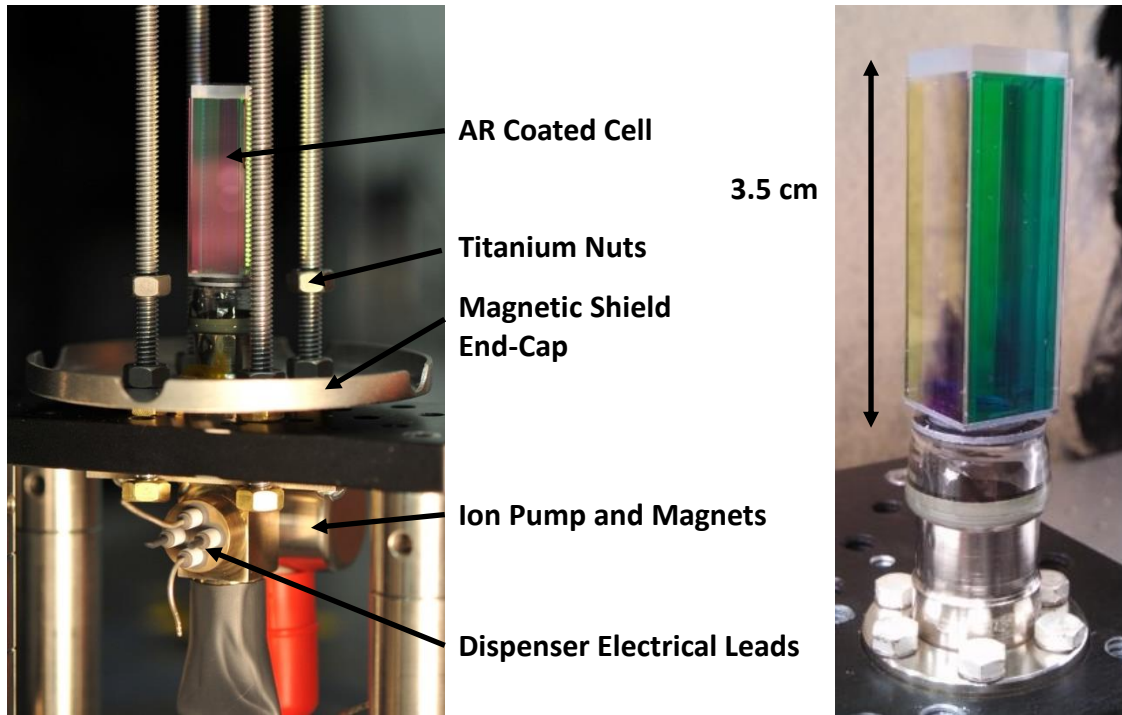
Figure 5.11: Photographs of the CACPT vacuum system. Total volume was below < 80 cm^3, including a 0.4 L/s ion pump. Non-magnetic components were used wherever possible, including titanium nuts and aluminum threaded rods.

(a) **(b)** **(c)**
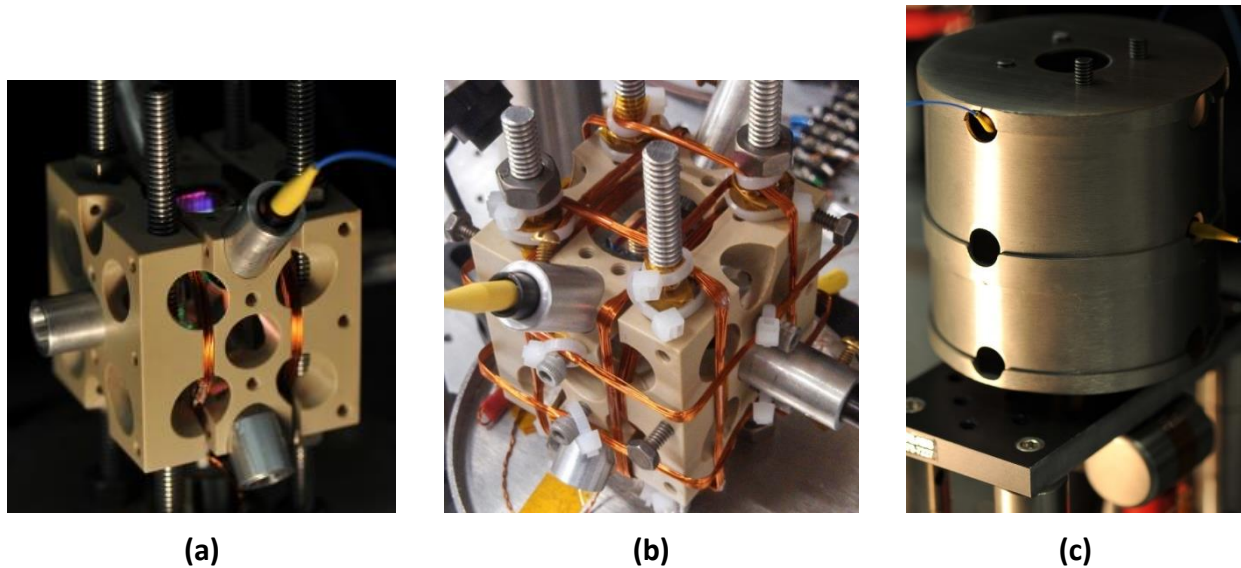
Figure 5.12: Photographs of the CACPT mounting block without (a) and with (b) bias coils attached to the structure and of the single layer μ-metal magnetic shield (c). The mounting block (5 cm tall) and shields (10 cm tall) were designed to slide onto the threaded rods around the optical cell to form a compact, fiber-coupled physics package.

titanium nuts. The mounting block (Fig. 5.12 (a,b)) was machined out of PEEK, a high strength, thermally stable plastic. The design featured two grooves for magnetic field coils to be wound directly onto the structure and had cylindrical holes along each axis, providing optical access for the MOT and CPT interrogation beams.

The MOT anti-Helmholtz coils were wound with 40 turns of copper wire directly into the grooves in the mounting structure (Fig. 5.12 (a)). With this coil geometry and a throughput current of 1.05 A, the magnetic field gradient measured with a Gaussmeter and translation stage was found to be $\nabla B_z = 8.6$ G/cm along the coil axis and $\nabla B_\rho = 4.2$ G/cm in the radial direction. To null the background magnetic field and apply the c-field, Helmholtz bias coils were added along each axis. These coils had ~ 10 turns and were fixed in place around the mounting block and optical cell using zip ties and titanium screws (Fig. 5.12 (b)). Bias fields on the order of a few 100 mG could be applied with these coils which was more than sufficient to zero the magnetic background and apply the roughly 40 mG field along the CPT axis.

To prevent drift in the magnetic environment from introducing Zeeman shifts with the potential to limit the long-term stability of the clock, the second generation CACPT system was encased in a single layer of magnetic shielding formed by a cylinder with end caps on top and bottom (Fig. 5.12 (c)). The shield was made of μ-metal, a nickel-iron alloy with small fractions of copper and chromium that has a very high magnetic permeability, directing magnetic field lines around the structure. While typical shielding configurations feature multiple layers of μ-metal, a single layer was sufficient for our purposes, providing shielding factors of $S_{||} = 20$ and $S_\perp = 100$. The shield was designed with holes along each axis for the MOT and CPT laser beams as well as a hole in the top end cap for fluorescence detection of the MOT.

As shown in Fig. 5.12, the mounting block was originally designed for fiber output couplers and retro-reflection mirrors to be clamped into place within the structure. The pig-tail output couplers of the three-way MOT fiber were inserted into aluminum sleeves with a quarter-wave plate glued onto the end. By rotating the aluminum sleeve, the correct polarization for the MOT beams was set, and the output couplers were clamped into place with set screws. The aluminum sleeves were then slid into the mounting structure, fixing the MOT optics within the physics package. This approach was taken in the spirit of building a field-grade device and sought to avoid the constant adjustments required to maintain a laboratory system. However, due to machining tolerance issues

(a) **(b)**
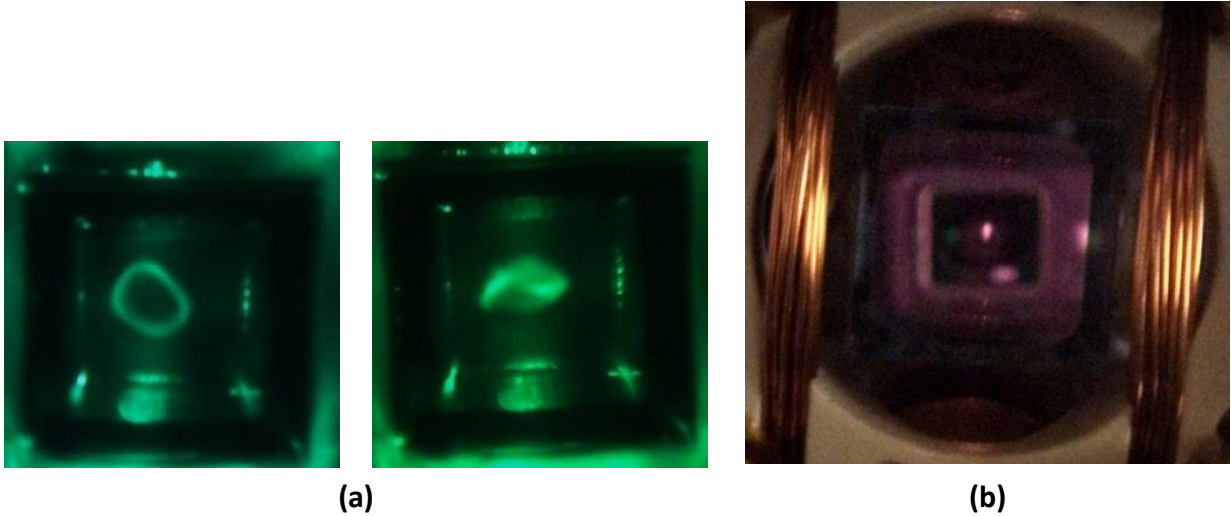
Figure 5.13: Photographs of the MOT in the Phase II CACPT clock taken from above the system, looking through the top end-cap of the magnetic shield. The images in (a) were taken using an IR viewer; the black square in each image is the optical cell with 8 mm long walls, and the green object in the center is the MOT. Both images were taken with the fibers clamped into the PEEK mounting structure and exhibit the poor MOT geometry characteristic of alignment problems. In (b), the MOT beams were directed through the system using free-space optics, providing sufficient control to achieve good relative alignment.

and thermal drifts caused by heat from the MOT coils, the alignment of the 3.8 mm $1/e^2$ diameter MOT beams proved exceedingly difficult to optimize and maintain in this configuration. Low atom numbers and unique MOT shapes were routinely observed (Fig. 5.13 (a)). To obtain a stable trap for characterizing the Phase II clock, we abandoned the fixed geometry and used free-space optics to align the MOT beams through the system. This resolved the issue, and with ~ 10 mW of cooling and ~ 500 μW of repump laser power, 2×10^5 atoms were consistently trapped in a Gaussian-shaped MOT (Fig. 5.13 (b)). During clock operation, a 4 ms post-cool stage resulted in a recapture percentage of $\sim 85\%$ cycle to cycle for a Ramsey period of 8 ms.

Despite significant effort to improve the atom number in the Phase II system, we were never able to trap more than 2×10^5 atoms, a factor of $\sim 5\times$ less than expected. The parameter space for the cooling laser and magnetic field (Fig. 5.14 (a)), as well as the beam alignment, was repeatedly optimized without success. We later discovered that the AR coating on our optical cell was not behaving as specified, and the resulting power imbalance between the input and retro-reflected beams may have been part of the issue.

The interrogation laser was coupled into the physics package with free space optics in the

107
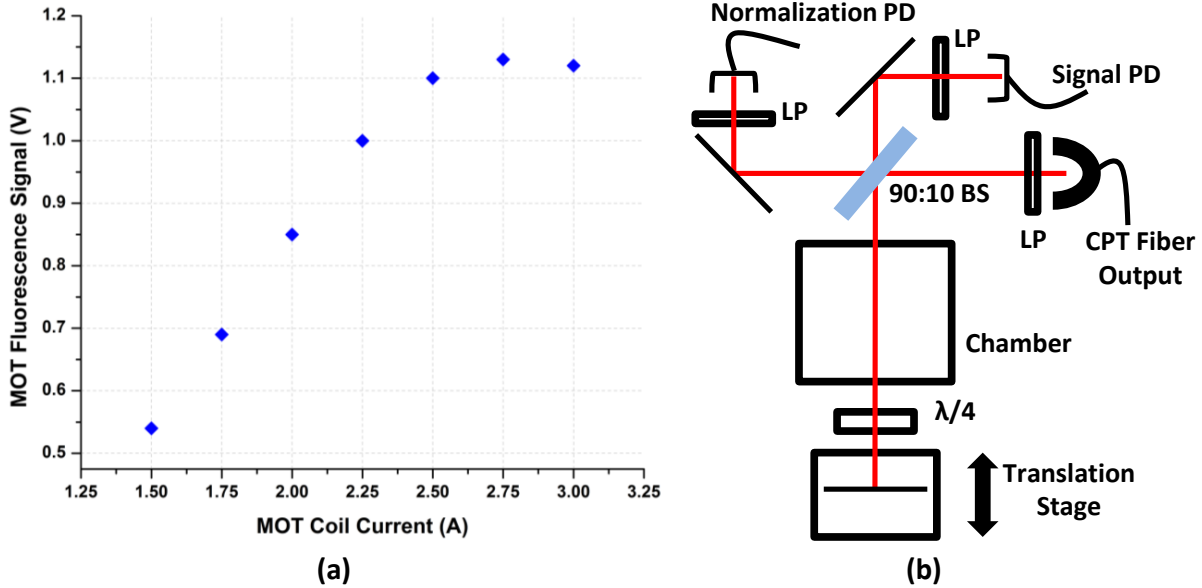
Figure 5.14: (a) MOT fluorescence signal vs. current through the anti-Helmholtz coils. Maximum N_{ss} was achieved for currents above ~ 2.5 A. (b) Optics layout for the CPT light near the chamber.

configuration shown in Fig. 5.14 (b). At the output of the CPT fiber, the laser passed through a linear polarizer to ensure a clean polarization for both frequency components. A 90:10 beam splitter transmitted most of the light, after which it was aligned onto the normalization photodiode. The reflected 10% propagated through the chamber, where it interrogated the atoms before being retro-reflected by a mirror, passing through the chamber a second time. It was then aligned onto the signal photodiode. The retro-reflection mirror was mounted on a linear translation stage such that the phase between the counter-propagating CPT beams could be tuned for constructive interference and maximum signal amplitude. As will be discussed in the next chapter, proper tuning of this mirror was critical for achieving good S/N and reduced Doppler shifts. An alternate optics configuration was used for some experiments in which the 90:10 beam splitter was replaced by a polarizing beam splitter cube with a half-wave plate after the CPT fiber output. This was used when a large CPT interrogation intensity was needed as it provided a more efficient distribution of the interrogation power between the signal and normalization arms.

5.4.3 Signal Detection

During typical operation of the CACPT clock, three signals were collected and processed: fluorescence from the magneto optical trap, power in the CPT normalization arm, and power in the

CPT signal arm. Fluorescence from the MOT was monitored during every run in order to correlate changes in the S/N or stability of the clock with fluctuations in the atom number. Generally, the atom number was very stable in the short term and was not a source of variation in the clock performance; tracking the fluorescence was more useful for achieving the same alignment and cooling system optimization day to day. To measure the MOT atom number, fluorescence emitted vertically by the trapped atoms was collected by a 1.5" focal length Fresnel lens and measured on a photodiode. The photodiode voltage was sent to the LabVIEW software via the data acquisition system described below, where it was monitored in real-time as the clock ran. Based on the photodiode signal, the atom number was calculated as described in Section 3.3.2.

Ramsey fringes, the primary signal of interest in the clock, were obtained by measuring the transmission of the CPT beam during the two interrogation pulses. The CPT light interrogated the atoms in a retro-reflected, counter-propagating configuration, and the laser power was detected on the signal photodiode in Fig. 5.14 (b), recording a voltage S. To determine the transmission through the atom cloud, a fraction of the interrogation light was picked off and measured on the normalization photodiode without passing through the chamber, producing a voltage L. With no trapped atoms, the voltages L and S were balanced by tuning the linear polarizers in front of each photodiode. Then, with atoms absorbing some light during clock operation, the transmission of each CPT laser pulse was calculated by dividing these signals: $T = S/L$. Finally, to compensate for drift in the balance of the signal and normalization arms, the transmission recorded at the end of each sequence was the ratio of the individual transmissions from the first and second CPT pulses: $T = T_2/T_1$. In this equation, the transmission (T_1) of the first pulse was measured at the end of τ_1, when the dark state had already formed and transmission was maximum. This procedure normalized the measured second pulse transmission by accounting for fluctuations on a cycle to cycle basis, resulting in higher S/N fringes.

The photodiode signals were collected by a National Instruments PXI-6281 data acquisition card with 16 analogue inputs, a 500 kS/s sampling rate, and two analogue outputs. This board and a PXIe-6535 10 MHz digital input/output card were used to interface between the experiment and the LabVIEW control software. Data collection was done using the DAQ inputs, and the digital I/O card generated the TTLs used to pulse the CPT, cooling, and repump lasers as well as the magnetic field coils. These cards, and the GPIB connection linking the computer and RF

synthesizers, enabled the LabVIEW software to run the CACPT clock in a straightforward fashion.

5.4.4 LabVIEW Control Software

The majority of the LabVIEW code controlling the CACPT clock was written by Dr. Francois-Xavier Esnault for the first generation system. It was modified and tailored for the Phase II CACPT clock which had a simpler detection scheme due to the retro-reflected CPT geometry. Screen shots of the front panel are shown in Fig. 5.15 for a broad scan of the Ramsey fringes. In Fig. 5.16, the data collection pane is shown for light shift and long term stability measurements.

The LabVIEW software incorporated all aspects of running the experiment into one program. The sequencer, based on the same software used in the bichromatic slowing experiment, was simplified and integrated into the code. It included each of the stages in the timing sequence (Fig. 5.7 (a)) and allowed the user to turn each of the lasers and MOT coils on and off with a TTL signal from the digital I/O card. The AOM drivers for each laser had a switch built in such that the RF power to the AOM was turned off when the control TTL was LOW, and on when it was HIGH. The frequency of the CPT AOM (optical detuning) and of the reference for the OPLL (Raman detuning) were both controlled by the software using GPIB connections to the two synthesizers. The intensity of the CPT beams was controlled using an attenuator on the RF power supply for the CPT AOM. The signal from the normalization photodiode was used to generate an error signal, and corrections were sent to the attenuator using an analogue output on the DAQ card, forming a feedback loop for I_{CPT}.

The software had the ability to program six different sequences at one time and run them sequentially. Each sequence could have different timing, state selection, CPT laser intensity, optical detuning, and post-cool parameters. It had an additional loop that could run the six sequences, vary the optical detuning or CPT laser intensity, and run the six sequences again; this could be done for nine different detunings and intensities. The light shift measurements in Fig. 5.16 are an example of this interleaved measurement process. The figure shows three sets of average clock frequency measurements for six different CPT laser intensities (colored dots in the Frequency Data Run pane) at one optical detuning. The ability to sequentially run multiple experiments with different intensities and detunings was very useful for the light shift study, where the parameter space was quite large.
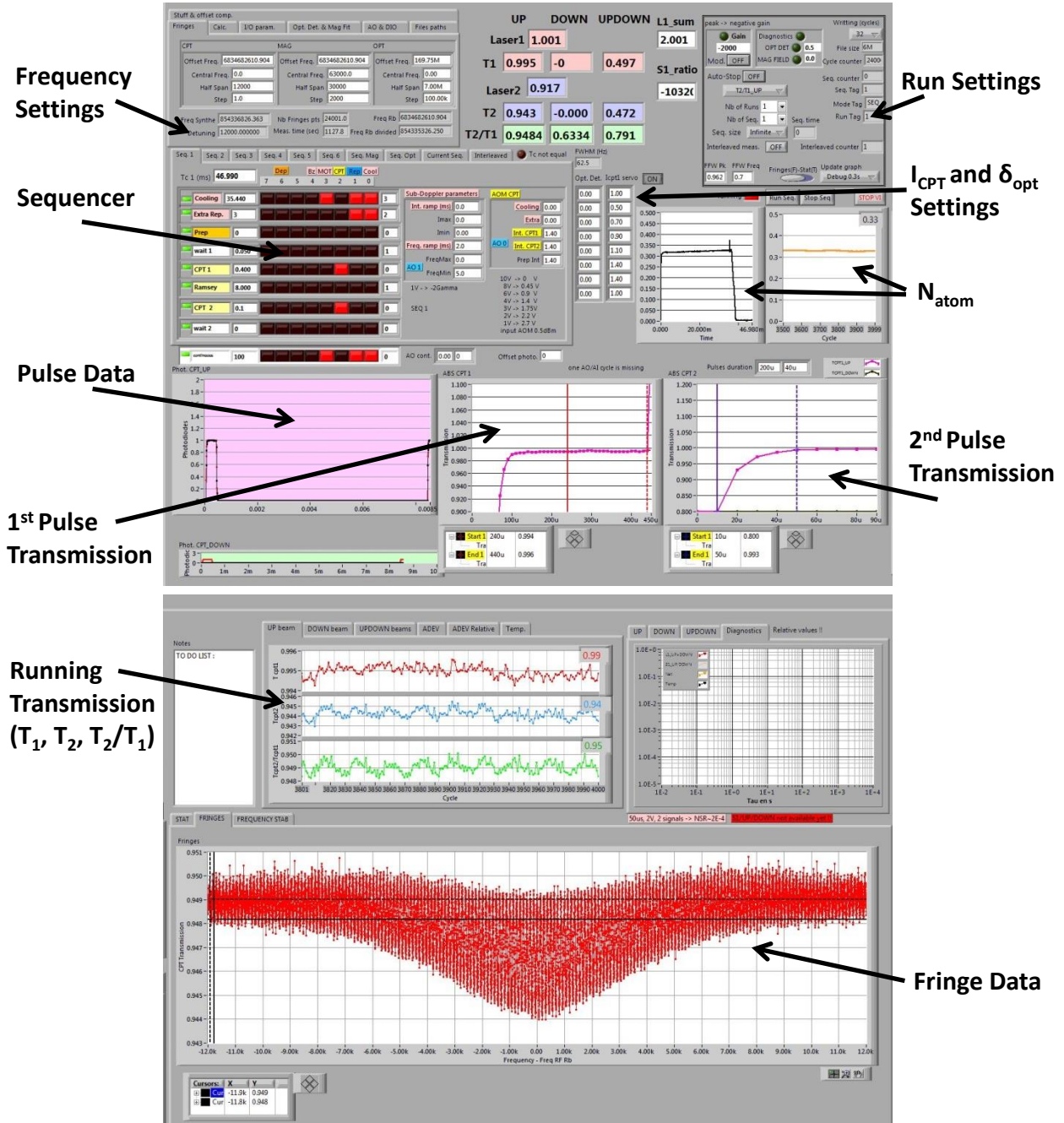
Figure 5.15: Screen shots of the LabVIEW control software front panel. The pane on top contained the sequencer, intensity and frequency controls, first and second pulse transmission measurements, and monitors for the MOT atom number for an individual sequence and over multiple runs. The lower pane displayed the running transmissions (top to bottom: T_1 T_2, T_2/T_1) and a larger plot of the T_2/T_1 transmission for the entire run. The system was configured in this case to scan the Raman detuning over the full Ramsey fringe pattern.

111
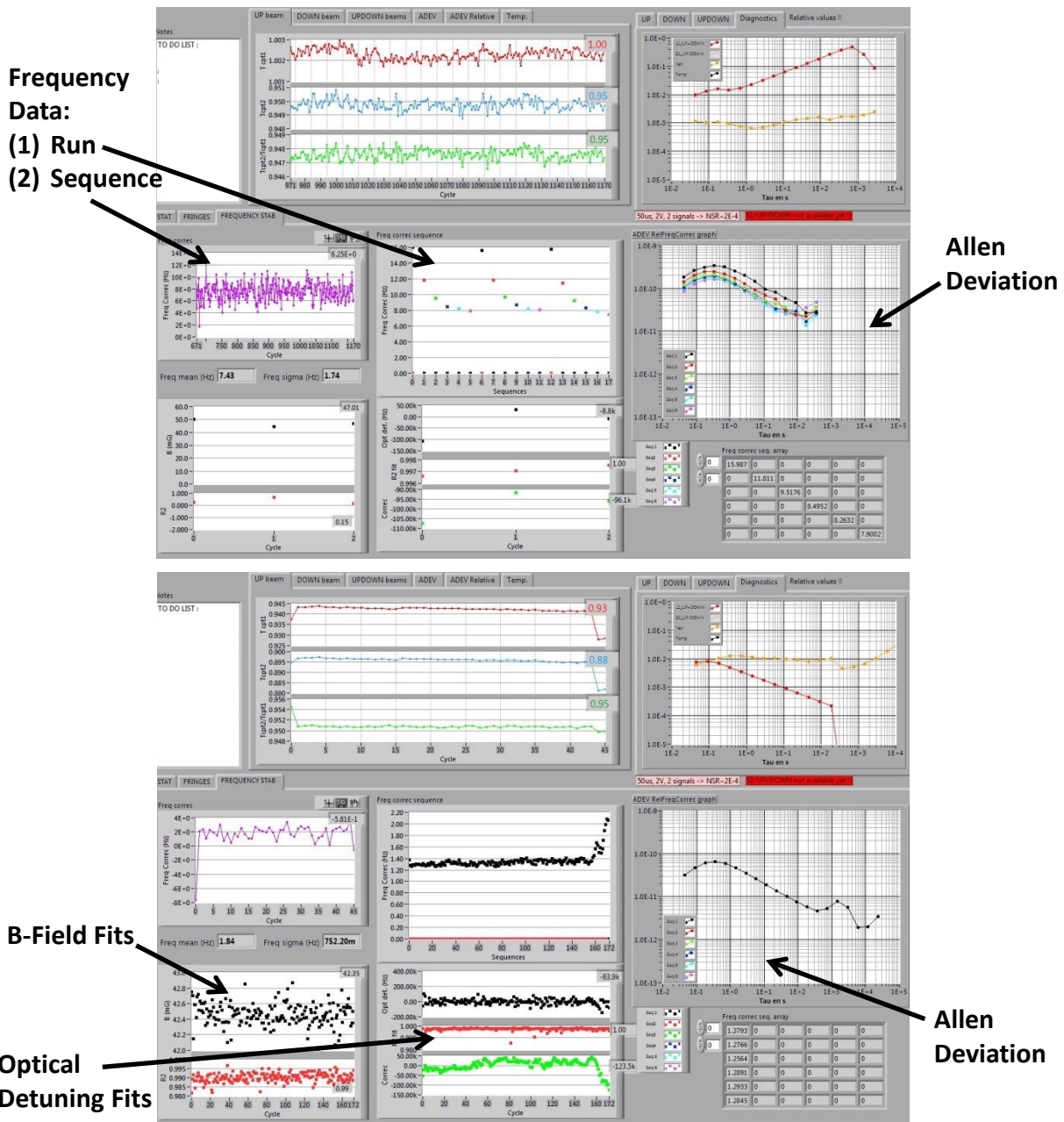
Figure 5.16: Screen shots of the LabVIEW control software showing data panes on the front panel for light shift measurements (top) and long-term stability measurements (bottom). The sequence frequency data showed measurements of the clock frequency for each individual cycle. Each point in the run frequency data was the average clock frequency of all cycles (several thousand) in a given run. Allan deviations were calculated in real time from the corrective steers of the central frequency and plotted in the bottom right.

With this program, the clock could run in two different modes of operation. In scan mode, the software would either display the Ramsey fringes or a scan of the CPT resonances as a function of the Raman detuning depending on whether the first or second pulse was chosen for display. The program also had a statistics mode of operation that could be used to optimize the resonance signal or lock the clock and collect frequency measurements. For optimization, the Raman detuning would be jumped from the peak to the valley of a Ramsey fringe (T_2/T_1) or of the central CPT resonance (T_1), and the software would output the amplitude difference in a scrolling plot, calculating the signal to noise ratio continuously. This allowed the different parameters affecting the CPT signal size (laser frequencies, MOT number, magnetic fields, absolute intensity, relative intensity, etc.) to be adjusted in real time such that the best S/N ratio possible for a given measurement could be achieved. Statistics mode with the Raman detuning configured to jump side to side on the central Ramsey fringe was used to lock the clock (Section 5.3). When locked, the software would calculate running Allan deviations based on the steers to the central clock frequency applied by the feedback loop. Allan deviations were calculated for each of the different sequences that were active in a given run, allowing for immediate stability comparisons between different CPT parameters. At the end of a run, all of the collected data was output in text files for additional analysis in Origin or for a more sophisticated statistical treatment using overlapping Allan deviations, etc.

5.5   Phase II CACPT Clock Performance

A typical measurement of the CPT resonances in the lin||lin configuration, obtained by scanning the Raman detuning over the clock resonance and recording the transmission of the first CPT pulse (T_1), is shown in Fig. 5.17. The peaks in the data correspond to the formation of dark states in which the atoms no longer absorb photons from the CPT field, resulting in increased transmission at the end of the pumping pulse. The central resonance at a Raman detuning of $\delta_R = 0$ arose from the double-Λ systems driving the $m_F = \pm 1 \rightarrow m_F = \mp 1$ transitions. The high-contrast peaks surrounding the central resonance at $\delta_R = \pm 65$ MHz were from dark states loaded by the magnetically sensitive $m_F = \pm 1 \rightarrow m_F = \pm 1$ transitions that are also allowed in the lin||lin scheme. For the magnetic diagnostic scans, these are the resonances that were tracked to monitor the magnetic environment during long runs of the CACPT clock.
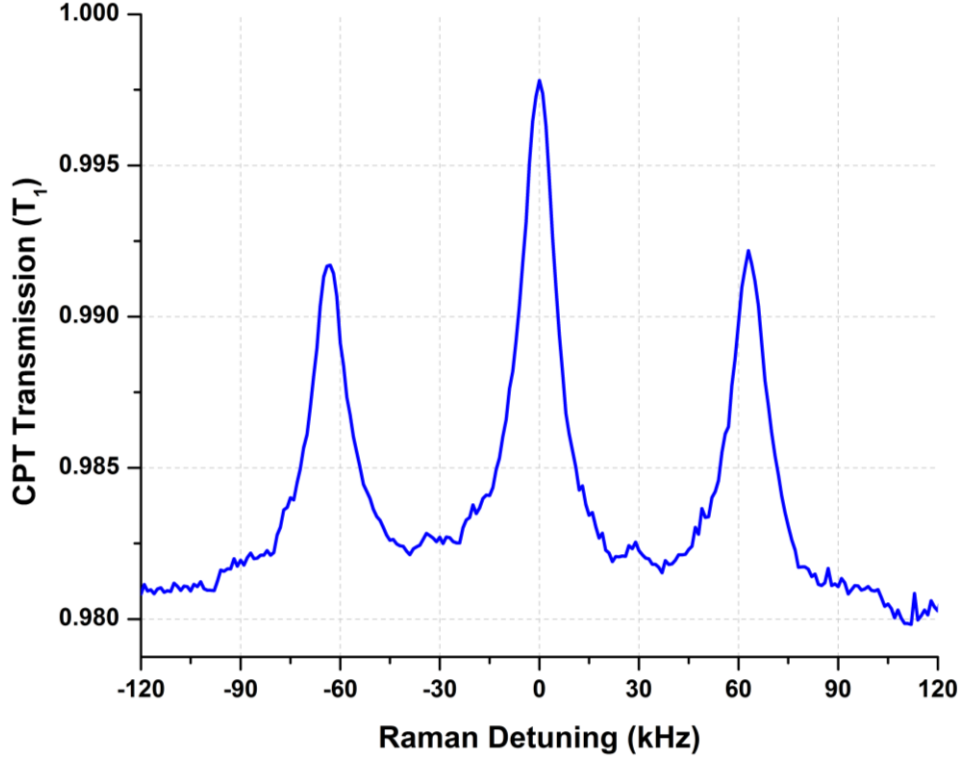
Figure 5.17: Transmission (T_1) measurement of the CPT resonances in the lin||lin configuration obtained by scanning the frequency offset between the master and slave lasers, i.e. varying the Raman detuning of the CPT field.

When the transmission of the second pulse was measured instead of the first, then quantum interference between the transition amplitudes from the two pulses resulted in Ramsey fringes, shown in Fig. 5.18 (see Section 5.3). These Ramsey fringes were measured with 2×10^5 atoms for Ramsey periods of 8 ms (top) and 16 ms (middle) with cycle times of 45 ms and 53 ms, respectively. The signal to noise ratio in a 1 Hz bandwidth was ~ 176, and the quality factor of the 16 ms resonance was $Q = \nu_{HF}/\Delta\nu_R = 2T_R\nu_{HF} \sim 2.1 \times 10^8$. The scans over a broad Raman detuning exhibit both the narrow Ramsey fringes and the Lorentzian envelope, the width of which was determined by the shape and parameters of the first pulse in the Ramsey sequence. Higher quality factors and improved clock performance would arise from longer Ramsey periods; however, our system was limited to 16 ms by decreasing atom numbers at long T_R caused by a lower cycle to cycle recapture fraction. The recapture efficiency decreased due to the distance the atoms fell during long interrogation sequences. The central Ramsey fringe used for locking the clock is shown in the narrow Raman detuning scan at the bottom of Fig. 5.18.

114
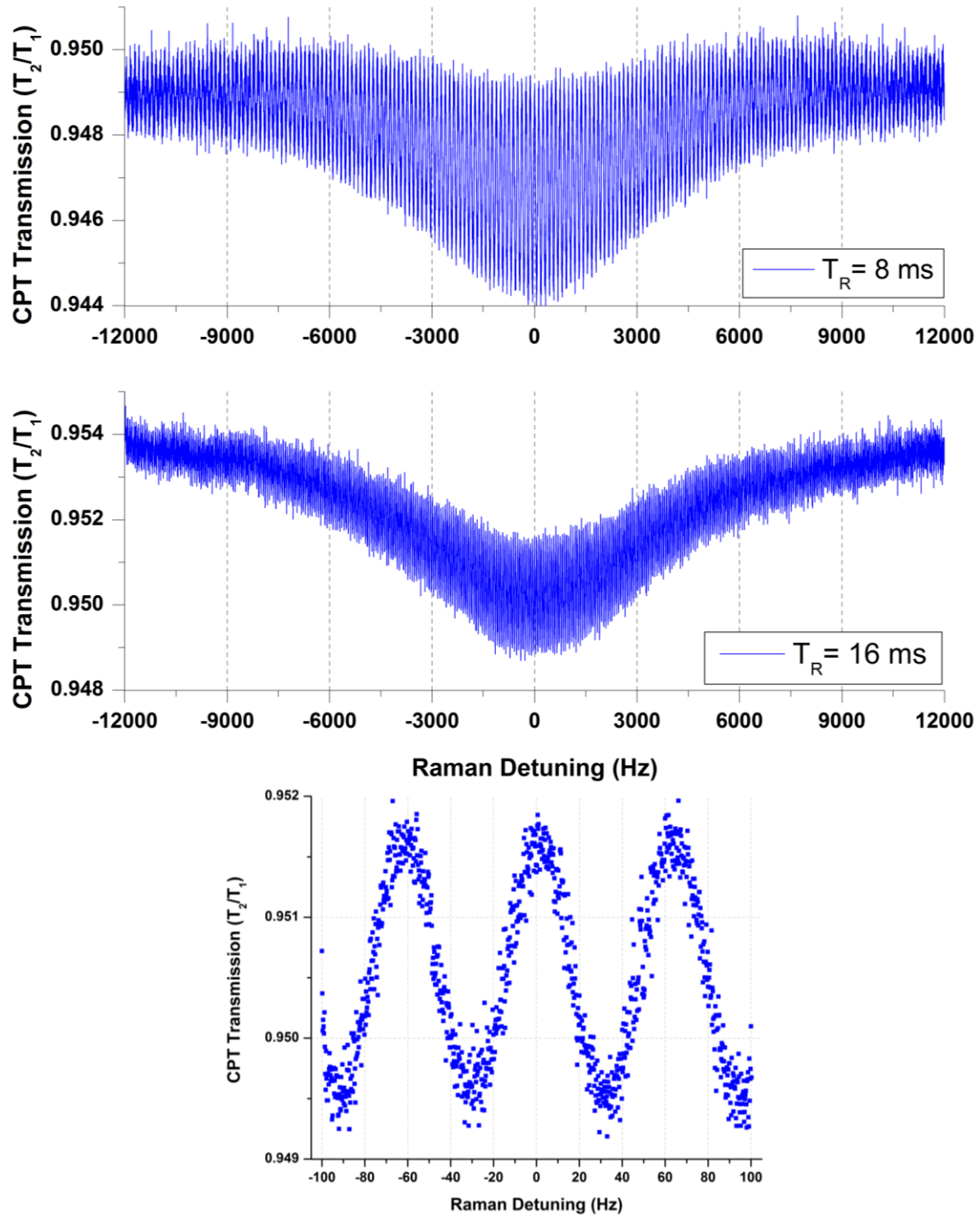
Figure 5.18: Transmission (T_2/T_1) measurement of the Ramsey fringes in the Phase II CACPT system. The top two plots show scans over a broad Raman detuning for Ramsey periods of 8 ms and 16 ms. The bottom figure is a narrowband scan for $T_R = 16$ ms. The decrease in fringe amplitude at $T_R = 16$ ms was caused by a reduced atom number due to lower recapture fractions at longer Ramsey times.

5.5.1 Signal Optimization

Obtaining high-contrast CPT resonances and Ramsey fringes with sufficient S/N for the long-term stability goals of the program required careful optimization the magnetic field and laser parameters. For the lin||lin configuration to be effective, the magnetic field inside the physics package during the interrogation sequence must meet the constructive interference requirements discussed in Section 5.1.3 and be oriented along the axis of the CPT beams to cleanly define the light polarization. This required tuning the bias coils to precisely zero the background magnetic fields orthogonal to the CPT axis. To accomplish this, the clock was locked on one of the magnetically sensitive transitions shown in Figs. 5.8 (a) and 5.17, and the current through the bias coils orthogonal to the CPT axis was tuned to minimize the measured resonance frequency using real-time data displayed in the LabVIEW software (statistics mode). When the frequency of the $m_F = \pm 1 \rightarrow m_F = \pm 1$ resonance was minimized for both orthogonal axes, then the only remaining magnetic field was the c-field applied along the CPT beams. The c-field could then be tuned to one of the discrete values providing maximum fringe amplitude. Scans of the CPT resonances showing the steps of this procedure are shown in Fig. 5.19.

The intensity of the CPT field was one of the more critical parameters to optimize as it affected the fringe amplitude, fringe width (via power broadening), and noise characteristics as well as Doppler shifts and AC-stark effects. While the frequency biases will be discussed in later chapters, Fig. 5.20 shows the effect of the field intensity on the observed signal to noise ratio during clock measurements. For this data, the signal was the peak to peak amplitude of sinusoidal fits to the Ramsey fringes (T_2/T_1), and the noise amplitude was the average of the residuals from the fitting routine. The highest signal to noise ratio occurred for a range of CPT intensities between 0.22 W/m^2 and 0.36 W/m^2. We typically operated the clock within this regime and narrowed the optimum range based on light shift measurements discussed later in this thesis.

Setting the relative phase between the counter-propagating CPT beams was important to ensure constructive interference between the two sets of Ramsey fringes and, as will be discussed in the next chapter, to mitigate Doppler shifts. To optimize the relative phase, the retro-reflection mirror in the CPT optics layout was mounted on a translation stage that could be adjusted based on either the fringe amplitude or the stability of the clock. An optimization measurement using the
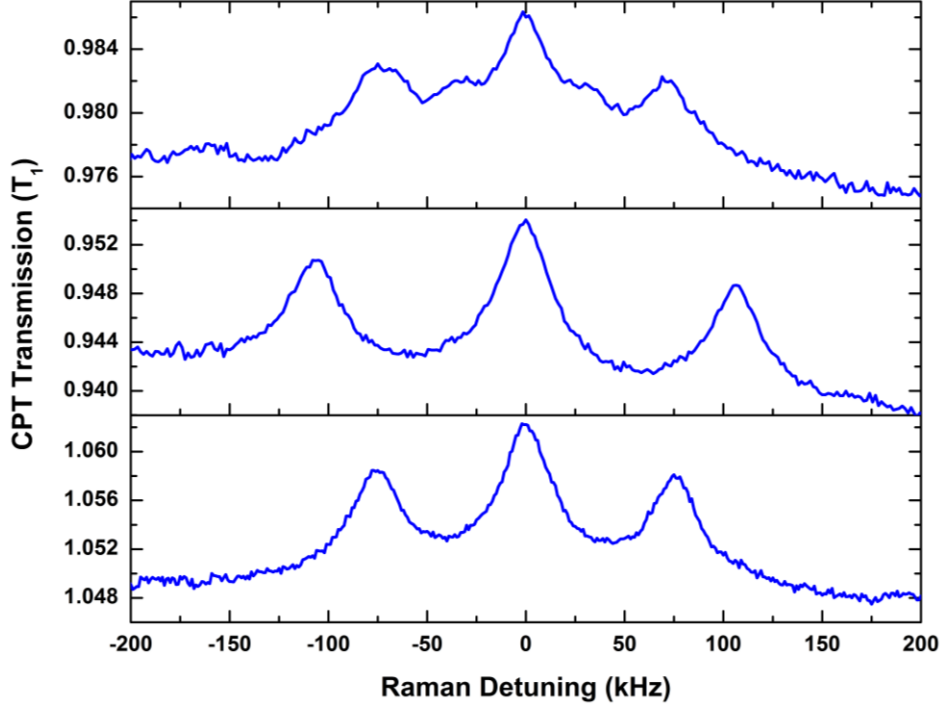
Figure 5.19: Measurements of the CPT resonances for different background magnetic fields. The top scan had poorly configured magnetic fields with off-axis components resulting in peaks appearing at half the resonance frequency of the magnetically sensitive lines. In the middle plot, the c-field has been increased to spread out the resonances, and the off axis components have been zeroed (see text). In the lower image, the c-field has been reduced to a value given by Eq. 5.5.

short-term clock stability ($\tau = 1.4$ s and $\tau = 11.2$ s) is shown in Fig. 5.21 (a). This data indicated that for a 16 ms Ramsey time, there was a large range over which the stability did not deviate significantly from optimum; however, the clock performance degraded quickly if the delay mirror was poorly placed.

A characterization of the signal amplitude as a function of the first CPT pulse duration is shown in Fig. 5.21 (b) for two different CPT intensities. This data is consistent with the earlier measurements of the fringe amplitude at different I_{CPT}, with the 0.18 W/m^2 intensity (1 V) providing the larger signal. However, while the higher intensity data is lower in amplitude, it is consistent over the entire range of pulse durations, whereas the 0.18 W/m^2 data does not saturate until $\tau_1 \cong 400$ μs. This is due to a smaller dark state loading rate at the lower intensity; a longer duration pulse is necessary to completely form the dark state for a CPT laser intensity of 0.18 W/m^2 than for 0.36 W/m^2. This concept will be very important in the light shift chapter.

As mentioned in Section 5.4.4, the control software allowed most of the CPT parameters to be
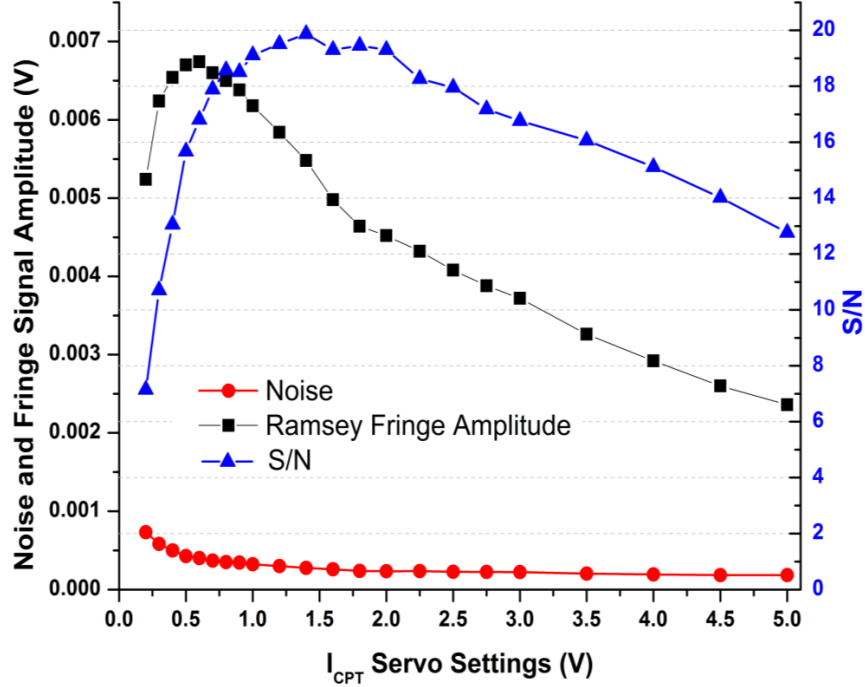
Figure 5.20: Measured Ramsey fringe and noise amplitude as well as the signal to noise ratio for varied CPT laser intensity and a Ramsey period of 4 ms. For this data, a servo setting of 1 V corresponded to 0.18 W/m^2 of laser intensity.

optimized in real-time by monitoring the amplitude of the central CPT resonance or Ramsey fringe as the laser or magnetic field parameters were tuned. Generally, the large central CPT resonance was used for course optimization and the Ramsey fringes for the final, fine-tuning. The results of this process are shown in Fig. 5.22, where Ramsey fringes for $T_R = 8$ ms measured before (left) and after (right) optimizing the relative phase, off-axis magnetic fields, c-field, and CPT intensity are plotted. While the difference in Fig. 5.22 is extreme, optimizing the parameter space for the CPT interrogation and laser cooling was a daily part of operating the CACPT clock.

5.5.2 Long-Term Performance and Error Budget

A critical performance metric for a frequency standard is the stability, specified by the Allan deviation of the clock frequency as a function of integration time. For the Phase II CACPT clock, the best long-term performance through summer 2014 is shown in Fig. 5.23. The clock demonstrated a stability of 3×10^{-11} at an integration time of $\tau = 1$ s and averaged down for ~ 5000 s, reaching a stability of 7×10^{-13} after roughly an hour of integration. The short-term
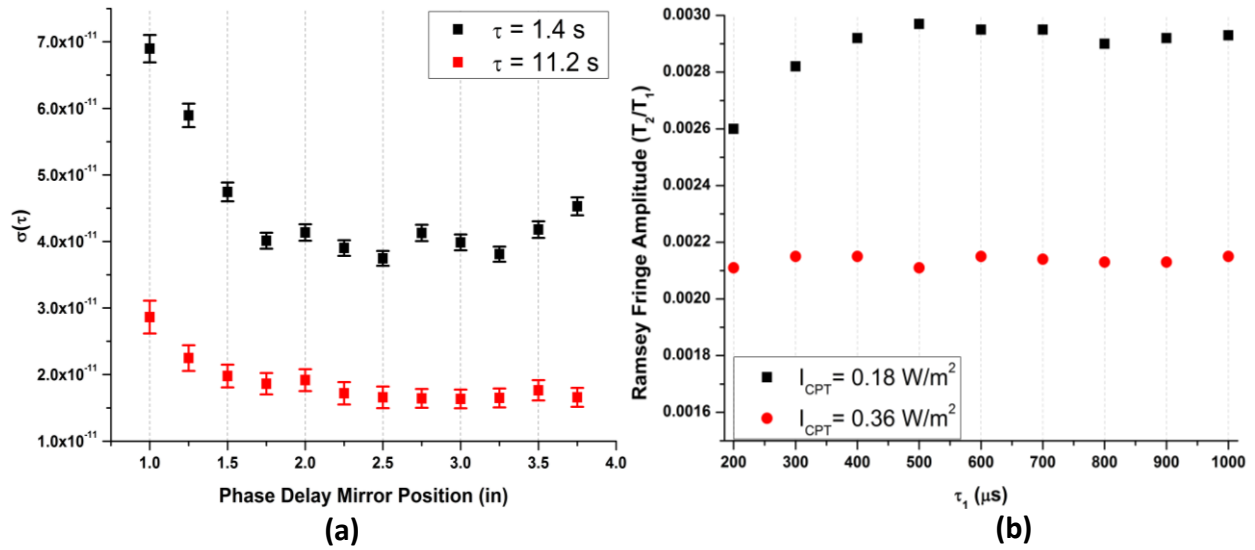
Figure 5.21: (a) Stability as a function of position for the CPT phase delay mirror for integration times of 1.4 s and 11. 2 s and a Ramsey time of 16 ms. (b) Ramsey fringe amplitude as a function of first pulse duration for different CPT laser intensities.
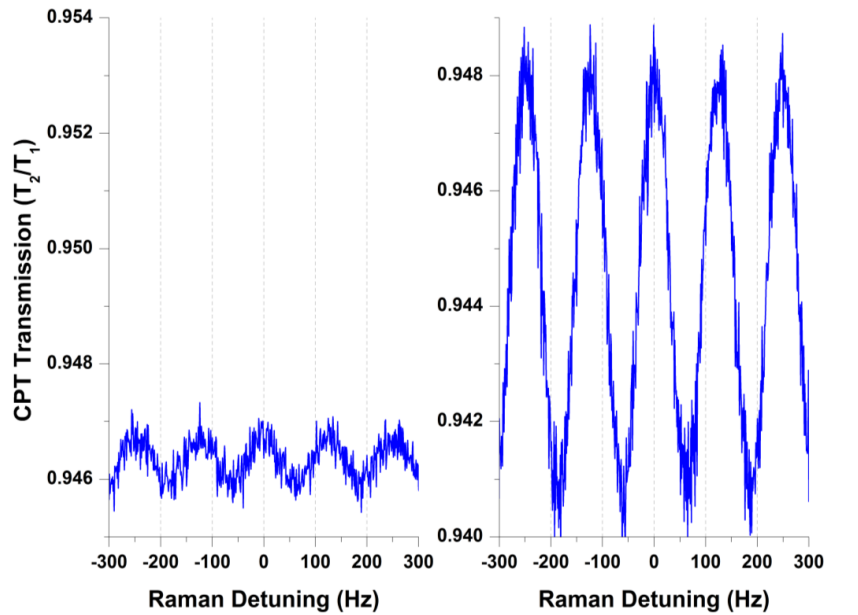
Figure 5.22: Results of the CPT optimization process. The left plot is a set of Ramsey fringes measured after modifying the system and re-acquiring the CPT signal. The right plot shows the significant increase in signal size achieved after optimizing the phase, I_{CPT}, and magnetic fields.

stability of the clock was limited by frequency noise in the CPT laser system, mostly associated with the master. Tuning the gain and filters of the locking electronics for the master laser frequently affected the Allan deviation at short time scales on the order of one second. As the laser system drifted over time, the lock-in amplifier and loop filter had to be re-optimized, balancing the need for the laser to remain locked for a long measurement with the requirement for good short-term clock stability. This was accomplished by monitoring the laser lock while optimizing the electronics for clock performance, tuning the filters and gain based on stability measurements from continuous short clock runs. At time scales exceeding an hour, the Allan deviation of the clock frequency measurements began to rise due to instability introduced by residual Doppler shifts. This will be discussed further in later chapters.

Also plotted in Fig. 5.23 is the Allan deviation of the Zeeman shift from the background magnetic field, measured by diagnostic scans of the magnetically sensitive CPT transition collected throughout the clock run. This data shows that the current stability of the CACPT clock at integration times exceeding 1000 s is a factor of $5 - 7\times$ higher than limit imposed by drift in the background magnetic field, implying that the Zeeman shift is not yet a limiting frequency bias in the clock. However, this has not always been the case. The Phase I CACPT clock did not have the μ-metal magnetic shield that surrounds the Phase II physics package and was much more susceptible to drifts in the magnetic environment. This is illustrated in Fig. 5.24, where the Allan deviation of the Zeeman shift is plotted for both the Phase I and Phase II CACPT systems. In the Phase I clock, the stability was observed to reach a minimum of roughly 2×10^{-12} at 1000 s of integration time, matching the Allan deviation of the Zeeman shift shown in Fig. 5.24. Drifts in the magnetic field were limiting the performance of the Phase I system and motivated the inclusion of magnetic shielding into the Phase II package design.

As additional upgrades to the Phase II system are completed, or if a Phase III system is constructed, then the limit imposed by Zeeman shifts may again become an issue. However, this could be overcome by suppressing the effect with additional layers of shielding in a next generation device. As it stood at the end of my involvement in the lab, the second generation system met the IMPACT Phase II performance requirements for integration times up to one hour. We were not able to meet the one day goal due to residual frequency biases, the mitigation of which is an ongoing effort in the lab.
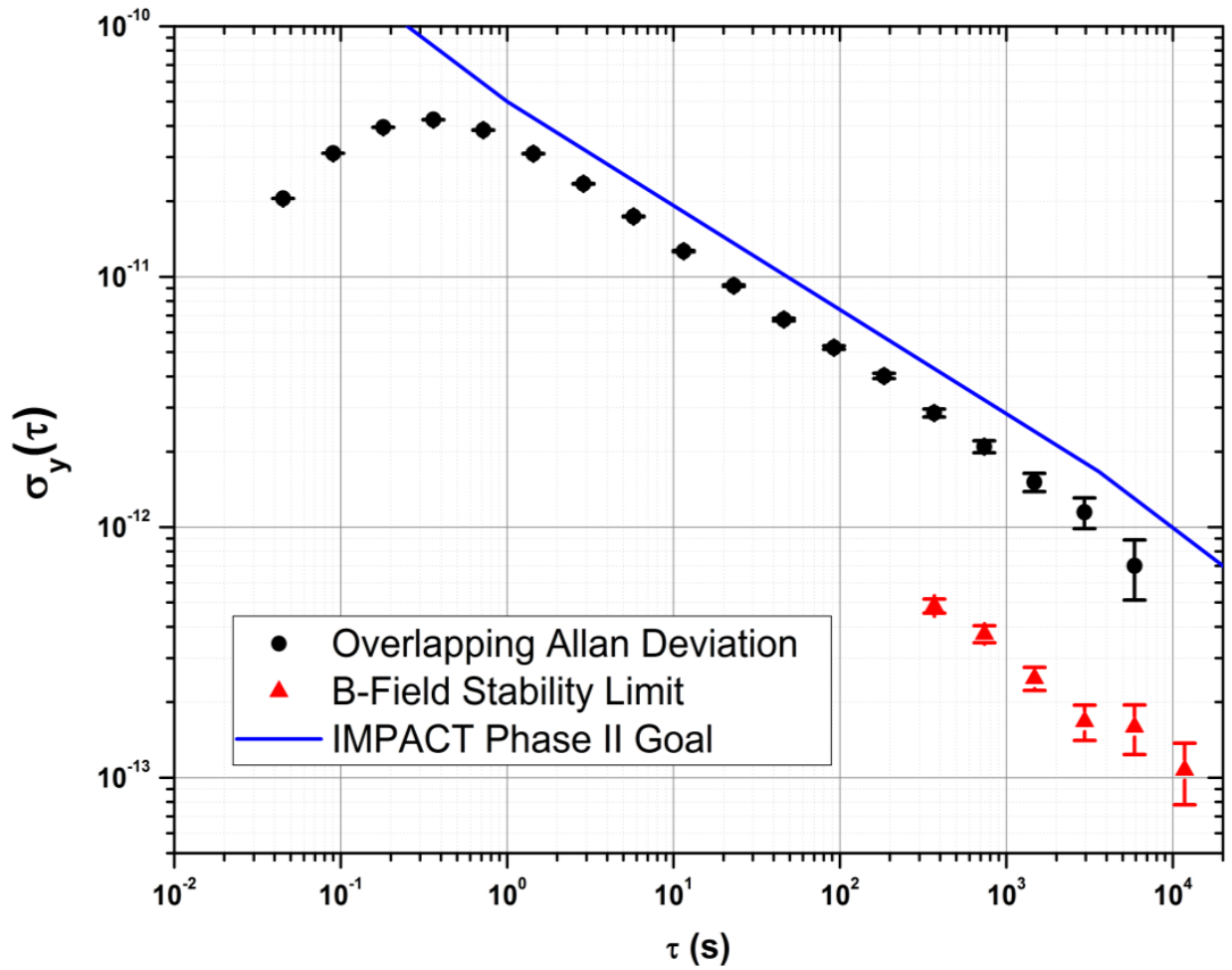
Figure 5.23: Allan deviation of the clock frequency for the second generation CACPT system as a function of integration time out to ~ 5000 s. Drift from residual Doppler shifts prevented the stability from continuing to average down over longer interrogation times.
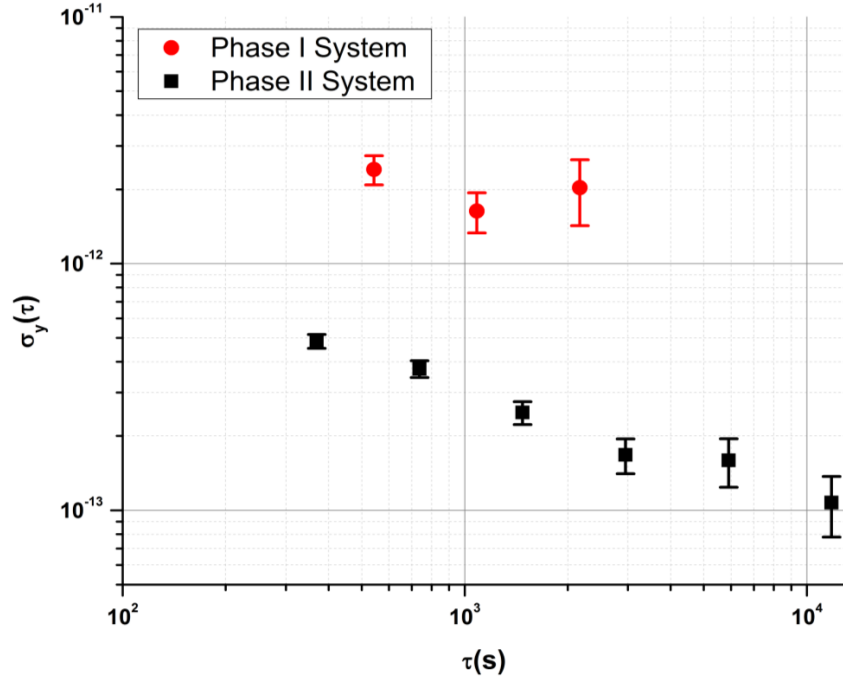
Figure 5.24: Allan deviation of the Zeeman shift caused by the background magnetic field for both CACPT clocks.

Complementing the frequency stability in characterizing the performance of an atomic clock is the error budget, in which noise contributions are broken down into independent physical effects and measured. The components of the error budget will vary depending on the type of atomic clock and the stability level achieved. As the performance increases and large noise sources are suppressed, ever smaller contributions to the instability are identified and included in the budget. For the Phase II CACPT clock, the dominant noise terms are mostly technical and related to the laser system and detection electronics. The error budget is given in Table 5.1. The combination of these four noise

Table 5.1: Phase II CACPT Clock Error Budget

Noise Term	$\sigma_y \left(\tau = 1 \text{ s} \right) / 10^{-11}$
Electronics	0.8
Laser Intensity	1.3
Laser FM/AM	1.7
Local Oscillator	2.5
TOTAL	3.4

sources determined the short-term stability of the clock, and the $\sigma_y \left(\tau = 1 \text{ s} \right) = 3.4 \times 10^{-11}$ stability calculated from these measured noise terms agrees very well with the measured $\sim 3.5 \times 10^{-11}$

stability of the Phase II system at an integration time of 1 s (Fig. 5.23).

To calculate the stability limitation from each noise term in Table 5.1, the signal to noise ratio for each term was measured and a variant of Eq. 1.2 was used [10]:

$$\sigma_y \left(\tau = 1 \text{ s} \right) = \frac{\sqrt{T_c}}{\pi Q} \times \left(\frac{S}{N} \right)^{-1}. \tag{5.10}$$

For the S/N ratio of each term, the signal was defined as the measured peak to peak amplitude of the Ramsey fringes and the noise amplitude as the standard deviation of transmission measurements (T_2/T_1) collected in a manner that isolated each noise contribution. For electronic noise, a set of clock frequency measurements was collected with the interrogation and MOT lasers physically blocked, and the current supply for the MOT coils turned off. The clock feedback loop was open, and the modulation used to jump the Raman detuning to either side of the central fringe was off. In this case, the only detected signal was from electronic noise: $\sigma_y \left(\tau \right) |_E$. To isolate the laser intensity noise, clock frequency measurements were recorded with the cooling light and MOT coils off, but the CPT lasers on and passing through the physics package. The detected signal was purely from the CPT lasers as no trapped atoms were present, providing a measure of the laser intensity noise (AM) and electronics noise: $\sigma_y \left(\tau \right) |_{E+AM}$. By subtracting these signals in quadrature, the laser intensity noise was isolated:

$$\sigma_y \left(\tau \right) |_{AM} = \sqrt{\sigma_y \left(\tau \right)^2 |_{E+AM} - \sigma_y \left(\tau \right)^2 |_E}. \tag{5.11}$$

To measure the laser FM to AM conversion noise (FM), all laser beams were unblocked, and the MOT coils were on such that the clock was in full operation. The central offset frequency was set to 0 Hz, and a series of clock frequency measurements were recorded at the peak of the Ramsey fringe, where FM/AM conversion, intensity, and electronics noise all contributed. The FM/AM noise was then found by subtracting the intensity noise measurement from this data:

$$\sigma_y \left(\tau \right) |_{FM} = \sqrt{\sigma_y \left(\tau \right)^2 |_{E+AM+FM} - \sigma_y \left(\tau \right)^2 |_{E+AM}}. \tag{5.12}$$

The final contribution to the short-term instability arose from the phase noise of the local oscillator and the Dick effect [12]. While local oscillator noise depends on the performance of

the particular device used in the clock, the Dick effect is more fundamental. It is an aliasing phenomenon in which the periodic feedback on the local oscillator due to the pulsed nature of the interrogation sequence can down-convert high frequency oscillator noise into the bandwidth of the servo loop. This noise appears in the applied corrections and contributes to the clock instability [10]. The instability from the Dick effect depends on the phase noise spectrum of the local oscillator and the response of the clock to that phase noise. For the CACPT clock, this was calculated by Dr. Esnault and found to be $\sim 0.5 \times 10^{-11}$. For simplicity, the Dick effect contribution was left within the local oscillator (LO) noise term as both are related to the LO's noise properties. This final contribution was measured by recording clock frequency data with the central frequency shifted to the side of the Ramsey fringe. On the fringe slope, all previous noise terms are present plus the combined local oscillator and Dick effect contributions, which were again isolated by subtracting in quadrature:

$$\sigma_y \left(\tau \right)|_{LO+Dick} = \sqrt{\sigma_y \left(\tau \right)^2 |_{E+AM+FM+LO+Dick} - \sigma_y \left(\tau \right)^2 |_{E+AM+FM}}. \qquad (5.13)$$

To further suppress the noise contributions listed in Table 5.1 and improve the short-term clock stability, the laser system used to generate the interrogation light would require an upgrade. However, the performance was sufficient to meet the $\tau = 1$ s Phase II milestones for the IMPACT program and addressing the long-term stability issues was more critical for demonstrating that the CACPT clock could be a viable option for a future device. Primary frequency shifts affecting the long-term performance will be discussed in the following two chapters.

CHAPTER 6

DOPPLER SHIFT MITIGATION

The cold-atom coherent population trapping clock was designed to operate without a buffer gas in order to eliminate the temperature-dependent pressure shifts that degrade the accuracy and stability of compact vapor cell clocks. However, the lack of a buffer gas reintroduces Doppler shifts of the clock frequency since atoms are free to move through the phase fronts of the interrogation field during the Ramsey sequence and therefore do not fall within the Lamb-Dicke regime [109]. When illuminated by a CPT light field from a single direction, the component of the atomic velocity along the axis of the interrogation beams causes an atom to be at different positions during the pump pulse (τ_1) and probe pulse (τ_2). Since the phase of the CPT field varies linearly with position, the phase of the field pumping atoms into the coherent dark state will be different than the phase at the point where the atoms are probed, introducing a phase shift that changes the frequency of the central clock fringe. This is the Doppler shift and has a magnitude given by:

$$\Delta\nu_D = \frac{\phi_1 - \phi_2}{2\pi T_R} = \frac{k_{HF}\delta z}{2\pi T_R} = k_{HF}\bar{v}, \tag{6.1}$$

where ϕ_i is the phase of the interrogation field at the position of the ith pulse, k_{HF} is the wave number of the frequency difference between the ground state hyperfine levels, δz is the position difference along the CPT axis during the Ramsey period (T_R), and $\bar{v}$ is the mean velocity. The total velocity of the atom arises from a combination of multiple effects and can be written as:

$$\vec{v}_{atom} = T_R\vec{g} + \vec{v}_0 + N_{CPT}\vec{v}_r, \tag{6.2}$$

where $\vec{g}$ is the acceleration due to gravity, $\vec{v}_0$ is the initial atomic velocity, N_{CPT} is the number of photons absorbed from a traveling wave CPT field, and $\vec{v}_r$ is the recoil velocity. The initial atomic velocity is from the expansion of the atom cloud due to residual thermal motion as well as from an imperfect MOT release. If the background magnetic fields are not completely zeroed by the bias coils, then the atom cloud experiences a force when the quadrupole field is turned off that can

accelerate it away from the center of the system. However, the acceleration due to gravity is the dominant term in this expression, and in the discussion that follows, imperfect MOT release and recoil effects from the CPT field will be neglected.

Controlling Doppler shifts is critically important if the CACPT clock is to become a viable option for a future compact frequency standard. Assuming a relatively short Ramsey period of 10 ms, the fractional frequency Doppler shift in a cold-atom clock interrogated with a traveling wave CPT laser would be on the order of 1×10^{-10}. This large shift would preclude the use of this type of clock in most applications. A widely used miniature CACPT clock would need to be sufficiently robust to operate in the field, where it would be subject to random, environment-dependent accelerations and would have no preferential orientation. To meet these requirements for a field-grade clock, we interrogate the atom cloud not with a single CPT beam but in a counter-propagating configuration that suppresses the Doppler shift. This chapter will discuss this interrogation technique and will present the results of evaluation experiments measuring its effectiveness.

6.1 Standing Wave Interrogation

To cancel Doppler shifts arising from the spatially varying phase of the CPT field, we interrogated the atoms with a pair of counter-propagating CPT beams tuned to establish maximum coherence and a constant phase over the trajectory of the atom cloud. This configuration is shown in Fig. 6.1 (a), where the counter-propagating field was established using independent CPT laser beams aligned along the axis of gravity (UP beam and DOWN beam). As the MOT fell downward due to gravitational acceleration during the Ramsey sequence, atoms interacted with the composite CPT field by sampling the average phase of the oppositely oriented beams, reducing the Doppler shift for balanced UP and DOWN parameters.

As discussed in the previous chapter, achieving maximum CPT coherence in this configuration required the phase between the counter-propagating beams to be set for constructive interference at the position of the atom cloud. For the previously studied counter-propagating CPT geometry with circularly polarized beams aligned along the $\hat{z}$-axis and room-temperature atomic vapors [110, 111], this condition was met and complete dark states where atoms do not absorb light could only be created at positions z_{max}, determined by the interference condition $2\left(k_1 - k_2\right) z_{max} = \left(2n + 1\right)\pi$,
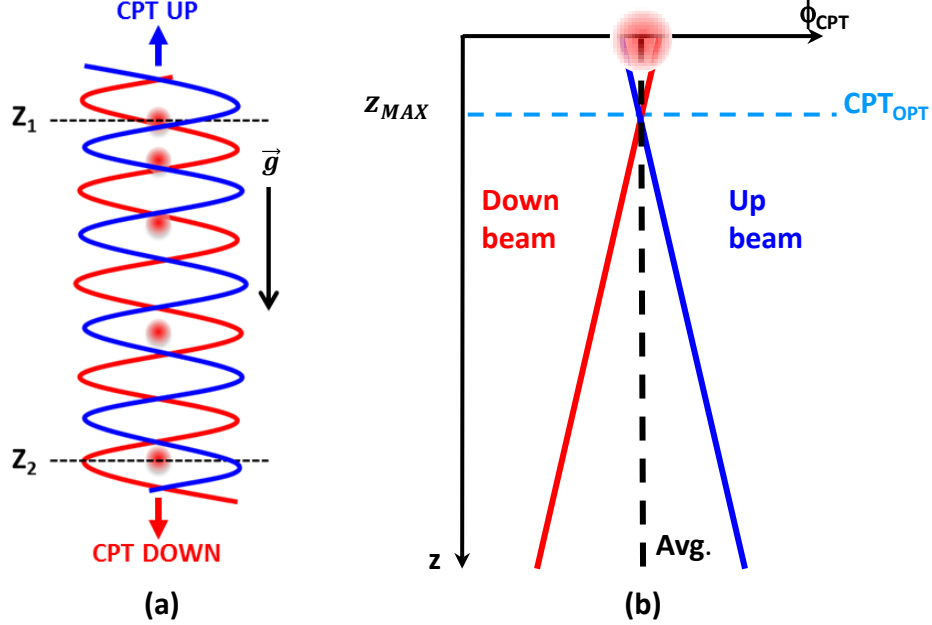
Figure 6.1: (a) Diagram of the counter-propagating interrogation scheme with CPT beams oriented along the axis of gravity. The position of the atom cloud during the two Ramsey pulses is $z_{1,2}$. (b) Phase diagram for each of the beams in the counter-propagating configuration, where the position of maximum constructive interference between the CPT fields is z_{max}. In both diagrams, the MOT is represented by the red circle.

where k_i is the wave number of the ith CPT frequency component. At z_{max}, the counter-propagating excitation fields interfere constructively in the atom, and the atomic coherence is maximal. There is no pure dark state at other positions, and atoms absorb light from each CPT beam, reaching maximum absorption at $2(k_1 - k_2) z_{min} = 2n\pi$. The same field interference occurs for the lin$\|$lin configuration used in the CACPT clock, and the transition amplitude of the Λ systems is modulated as a function of position, with a modulation length given by the hyperfine ground-state splitting (λ_{HF}). The retro-reflection mirror in an optical delay line was used to adjust the interrogation field such that the atom cloud was initially trapped at the position z_{max}, providing maximum constructive interference and signal contrast.

With the phase appropriately set, the counter-propagating interrogation geometry excites atoms in both directions simultaneously, removing the spatial phase variation and introducing the spatial amplitude modulation described above. During the first Ramsey pulse, atoms are pumped into a coherent dark state with the average phase of the upward- and downward-propagating CPT fields (z_1). Since the average phase of the independent CPT beams does not change along the

interrogation axis, falling atoms will be probed during the second pulse (z_2) by an optical field with the same phase as the pumping field. For perfect CPT beams with equal intensities in both directions and a precisely tuned phase, this reduces the $\phi_1 - \phi_2$ factor in Eq. 6.1 to zero, canceling the Doppler shift. In practice, the suppression achieved in the CACPT clock depends critically on the intensity balance of the counter-propagating fields and to a slightly lesser degree, on the relative phase.

6.2 Doppler Shift Experiments

To evaluate the effectiveness of the counter-propagating interrogation geometry in mitigating Doppler shifts in the CACPT clock, a series of experiments were performed in which the clock frequency was simultaneously measured for the upward traveling beam and the downward traveling beam. In these measurements, the counter-propagating field was established not by retro-reflecting the CPT beam, but by splitting the interrogation light into independent up and down beams and overlapping them through the system. The absorption of the upward- and downward-traveling CPT lasers was independently measured during the probe pulse, and clock frequency corrections were calculated for each beam. The CACPT clock was then locked using the corrections from the upward traveling beam, the downward traveling beam, or the averaged frequency corrections from both. Locking to the average of the two signals cancels the Doppler shift, while as discussed above, shifts will occur when locking to the individual traveling wave fields. The frequency shift in each independent beam due to the Doppler effect is equal and opposite:

$$\Delta \nu_D|_{\uparrow,\downarrow} = \pm \frac{k_{HF}\left(z_{max} - z_m\right)}{2\pi T_R}, \tag{6.3}$$

where z_m is the position of the atoms during the probe pulse. Since the symmetric excitation scheme loads atoms into a dark state with the average phase of the counter-propagating beams during the first pulse, the Doppler shift depends only on the location of the atom cloud with respect to z_{max} during the second pulse. This is shown in Fig. 6.1 (b); when $z_m = z_{max}$, the atoms are probed at a position where the upward and downward traveling beams have a phase equal to their average, and neither beam will exhibit a Doppler shift ($\phi_{avg} - \phi_2 = 0$). When $z_m \neq z_{max}$, then the upward and downward traveling beams will exhibit a Doppler shift given by Eq. 6.3 due to the deviation

of their phase from the average of the two ($\phi_{avg} - \phi_2 \neq 0$).

The Doppler shift was amplified in our experiments by releasing the atoms from the MOT and letting them free-fall for a period T_f before the first CPT pulse. The atoms accelerated due to gravity for a period ranging from 0-10 ms, providing larger Doppler shifts to measure. Experimentally, this was implemented by varying the duration of the preparation stage in the clock timing sequence (Fig. 5.7 (a)).

The Doppler shift arising from atomic motion during the free-fall period and Ramsey interrogation sequence for the upward- and downward-traveling beams can be calculated using basic kinematics. For atoms released at a position z_0 with an initial velocity of v_0 along the $\hat{z}$-axis, the distance from z_{max} to the atomic position at the start of the probe pulse is:

$$z_{max} - z_m = z_0 + v_0\left(T_f + T_R\right) - \frac{1}{2}g\left(T_f + T_R\right)^2. \tag{6.4}$$

Inserting this expression into Eq. 6.3, we find the Doppler shift measured by each beam to be:

$$\Delta\nu_D = \pm\frac{k_{HF}}{2\pi T_R}\left[z_0 + v_0\left(T_f + T_R\right) - \frac{1}{2}g\left(T_f + T_R\right)^2\right], \tag{6.5}$$

where the shift is positive for one beam and negative to the other. This model facilitated a theoretical comparison with the data presented below, where the frequency shifts as a function of free-fall time were measured while locking the clock to the up beam, down beam, and average of the two. These experiments were performed in our Phase I CACPT clock, discussed next.

6.2.1   Phase I System

The Doppler shift characterization was performed in the first-generation cold-atom coherent population trapping clock which featured a differentially pumped system with separate two- and three-dimensional MOTs [48]. The commercial vacuum chamber had a total volume below 0.2 L and was composed of two optical cells mounted on opposite sides of a six-way cross with a 2 L/s ion pump connected to the top port (Fig. 6.2). The 2D MOT was formed in a 12.5 mm by 12.5 mm by 25 mm cell with high alkali pressure from a Rb dispenser located in a glass offshoot. Atoms were trapped using 10 mW of laser power and two neodymium permanent magnets mounted
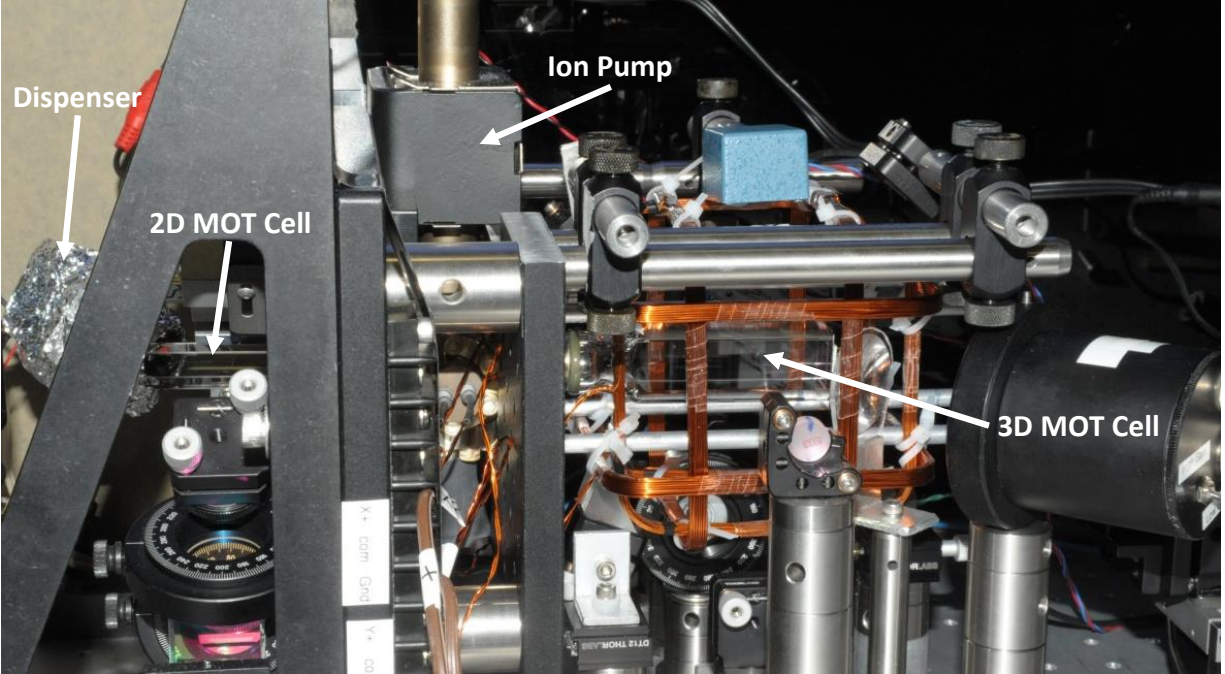
Figure 6.2: Photograph of the first-generation CACPT system showing the dispenser, 2D MOT chamber, 3D MOT chamber, and ion pump.

on translation stages to create a longitudinal quadrupole field with a gradient of 15 G/cm. The 2D MOT served as a cold-atom source for the science chamber. A red-detuned laser beam was aligned through the center of the 2D MOT, creating a cold atomic beam that passed through an aperture into the low pressure science chamber. The slow atoms were then trapped in a traditional 3D MOT using anti-Helmholtz coils and 6 mW of optical power, red-detuned by 1.5γ from the cycling transition. In addition to the MOT coils, three sets of Helmholtz coils were used to cancel the residual magnetic field and apply the c-field along the vertical direction, parallel to the CPT beams. In this system, $\sim 10^6$ atoms were trapped in a 45 ms cooling stage with a cycle to cycle recapture fraction of 80% for a Ramsey period of 8 ms. In the first generation system, exceeding 8 ms for the Ramsey period was not possible due to magnetic field gradients arising from the ion pump. The spatially-varying Zeeman shift caused destructive interference between the Λ-systems, destroying the S/N ratio of the Ramsey fringes for $T_R > 10$ ms.

The CPT light was generated in the same manner as for the Phase II system discussed in the previous chapter. As shown in the simplified block diagram of the Phase I system in Fig. 6.3, the only difference was in the injection of the interrogation field into the system as independent
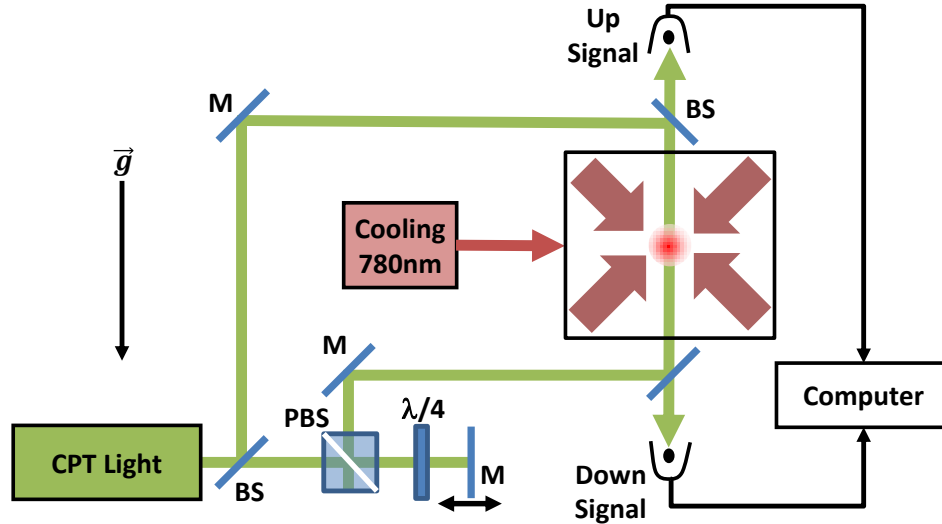
Figure 6.3: Block diagram of the Phase I CACPT Clock. The vertical alignment of the beams maximized the Doppler shifts for evaluation purposes. Upward and downward beams were overlapped in the system and independently detected on two photodiodes. The phase between the beams was controlled with an optical delay line on the up beam.

CPT beams were used for the Doppler shift mitigation experiments. After being phase locked, the interrogation lasers were coupled into a polarization maintaining optical fiber and directed toward the system, where the 3.5 mm diameter $(1/e^2)$ output beams were divided by a 50:50 beam splitter. The downward beam was aligned directly through the system, while the upward beam first passed through an optical delay line where it was reflected off a mirror on a translation stage. This delay line was used to set the relative phase between the two counter-propagating beams.

Independent photodiodes monitored the absorption of the CPT beams, while a third photodiode measuring light from a pick-off at the CPT fiber output was used for normalization. The transmission signals (T_1 and T_2) and frequency corrections for the up and down beams were calculated by the software in the same manner as in the second generation system. The correction signals from the up beam, down beam, or average of the two were then used in the feedback loop to servo the synthesizer providing the frequency reference for the PLL, locking the clock.

6.2.2   Evaluation Results

The Doppler shift mitigation was evaluated by measuring the clock frequency as a function of free-fall time for Ramsey periods of 1, 2, and 6 ms, while locking the clock using frequency corrections from the upward beam, downward beam, and the average of the two. The results of

this experiment are shown in Fig. 6.4, along with theory curves calculated from Eq. 6.5. Close agreement between measured Doppler shifts and the kinematic model was observed, particularly at low free-fall times. At higher values of T_f, measured Doppler shifts for the up and down beams were slightly smaller than the values predicted by Eq. 6.5. This occurred as both up and down beams were interacting with the atoms during the probe pulse, pulling the measurement toward the average phase instead of providing a clean measurement using the phase of the individual beams. This effect was explored further in the shutter experiments discussed below.

As shown in each pane of Fig. 6.4, there was significant cancellation of the Doppler shift when the clock was locked using the average frequency corrections from the upward and downward traveling beams. The symmetric excitation scheme was quite effective at minimizing the phase shift arising from atom movement between the Ramsey pulses ($\phi_1 - \phi_2$ in Eq. 6.1). From multiple measurements with a Ramsey period of 6 ms, we determined that the Doppler shift in normal clock operation was consistent with zero under 1 g of acceleration, canceling to $< 1 \times 10^{-11}$ residual shift for the symmetric interrogation scheme. These measurements indicated that in the Phase II system, where the interrogation beams were aligned horizontally to minimize effects from gravitational acceleration, the residual Doppler shifts should be reduced to the 10^{-13} scale or lower. The degree of cancellation would depend on the orthogonality of the CPT field relative to the axis of gravity as well as the intensity balance and relative phase of the counter-propagating beams.

The data plotted in Fig. 6.4 reveals an offset in the frequency of the up and down beams at a free-fall time of $T_f = 0$, indicating that at the time of the second Ramsey pulse, the atoms were not at the position z_{max}. Assuming a clean MOT release and neglecting expansion of the atom cloud, this implied that the initial position of the MOT relative to the point of maximum CPT coherence was not set such that $z_0 - \frac{1}{2}gT_R^2 = 0$, the condition for zero Doppler shift of the up and down beams for $T_f = 0$. Since adjusting the position of the trap center to change z_0 was not an option, this offset at $T_f = 0$ was investigated by adding a relative phase shift between the counter-propagating interrogation beams using the optical delay line in the beam path of the upward-propagating laser. A change in the optical path length of dL, achieved by varying the position of the retro-reflection mirror (Fig. 6.3), moved the position of z_{max} by $dL/2$. From Eq. 6.1, this caused the magnitude of the Doppler shift to change by:
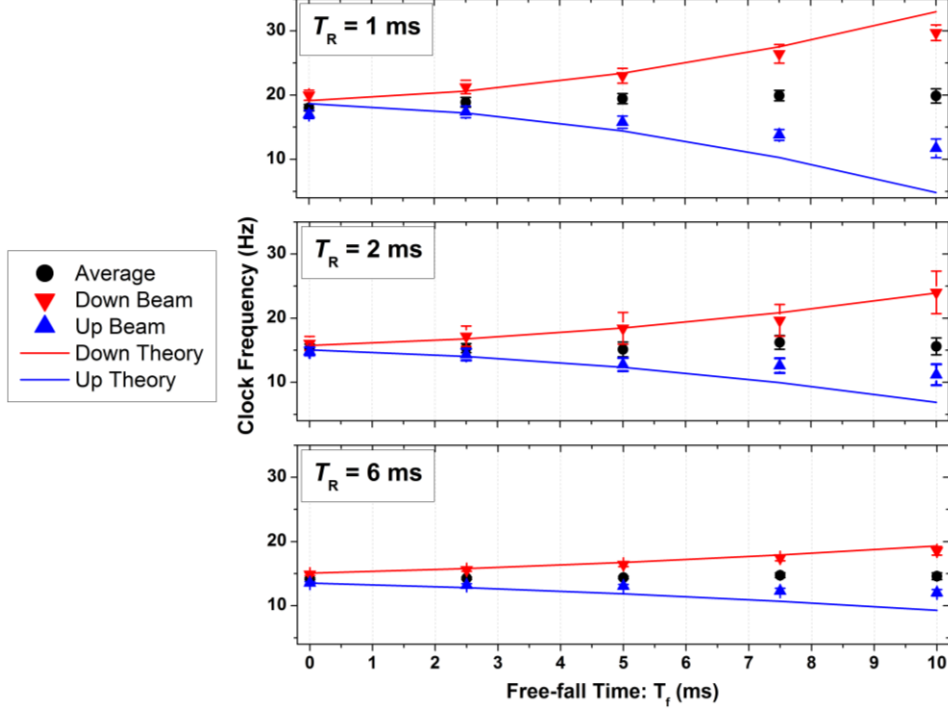
Figure 6.4: Measured frequency shifts as a function of free-fall time for Ramsey periods of 1, 2, and 6 ms compared to our model from Eq. 6.5 with $v_0 = 0$ and $z_0 = 0$. The clock was locked with frequency corrections calculated from the average of the up and down signals, only the down signal, and only the up signal.

$$\Delta\nu_D = \frac{k_{HF}\left(\frac{dL}{2}\right)}{2\pi T_R} \rightarrow \frac{d\Delta\nu_D}{dL} = \pm\frac{k_{HF}}{4\pi T_R}. \tag{6.6}$$

Evaluating this expression for the expected shift from changes in the delay line results in 11.4 Hz/mm for a Ramsey period of 1 ms and 1.9 Hz/mm for $T_R = 6$ ms. To verify that this was the cause of the offset at $T_f = 0$, the clock was locked using the up, down, and averaged signals, and the frequency and stability at $\tau = 1$ s was measured as a function of dL. This data is shown in Fig. 6.5, where the measured clock frequency when locked to the average of the corrections from the up and down beams was again consistent with zero. The frequencies measured for the downward-propagating beam agree well with the predicted shift from Eq. 6.6; however, the upward-propagating beam exhibited significantly smaller shifts than expected. This asymmetry between the up and down beams was due to the extreme sensitivity of the data to collinear alignment and the relative power between the counter-propagating fields. The measurements were also affected by a small traveling-wave component introduced by reflections from the optical cell, which in
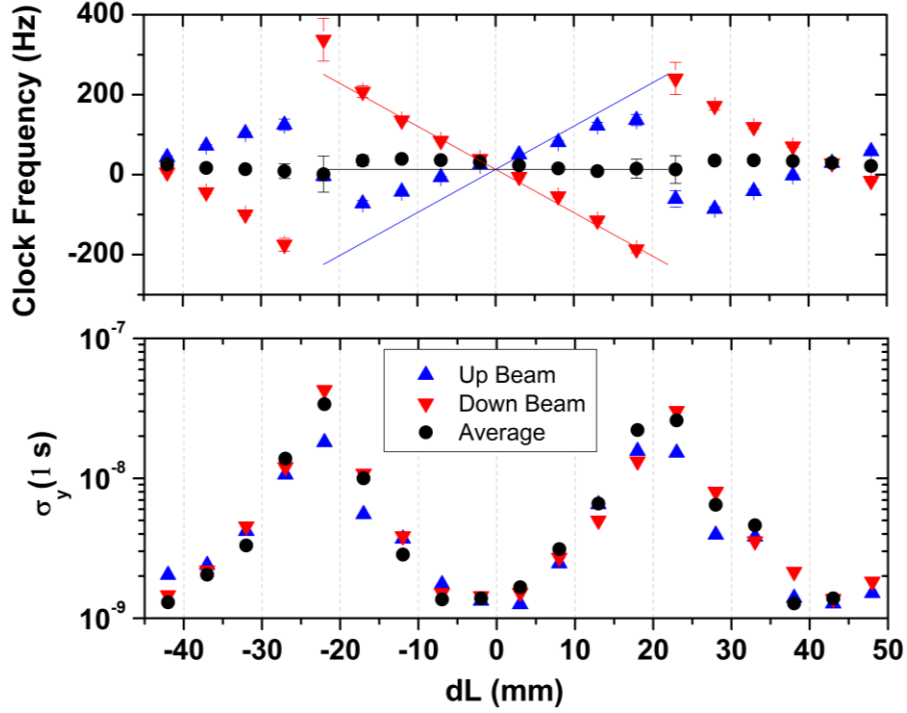
Figure 6.5: TOP: Doppler frequency shift versus change in optical path length of the up beam shown with theory curves calculated from Eq. 6.6. This data was collected with $T_R = 1$ ms and the corresponding theory curves are ± 11.4 Hz/mm. BOTTOM: Measured fractional frequency stability versus dL. The positions where the clock stability deteriorates ($\sim \pm 23$ mm) correspond to values of z_{min}.

the first-generation system, did not have an anti-reflection coating. Finally, the presence of both interrogation fields during the second Ramsey pulse again biased the measurements toward the average phase.

The stability measurements in the bottom plot of Fig. 6.5 emphasize the importance of tuning the relative phase such that the atom cloud was positioned near z_{max} during the probe pulse. The fractional frequency stability was degraded by a factor of $15\times$ when the atoms were interrogated at z_{min}, where the Λ-systems driven by the counter-propagating fields destructively interfere. These positions occur in the data at $\sim \pm 23$ mm, agreeing well with the expected 43.8 mm (c/ν_{HF}) modulation wavelength of the CPT field.

To investigate the asymmetry and suppressed frequency shifts measured for the up and down beams, an additional experiment was performed in which a mechanical shutter was used to block either the up or down beam during the second Ramsey pulse. During the first pulse, the atoms interacted with both counter-propagating fields and were loaded into a dark state with the average
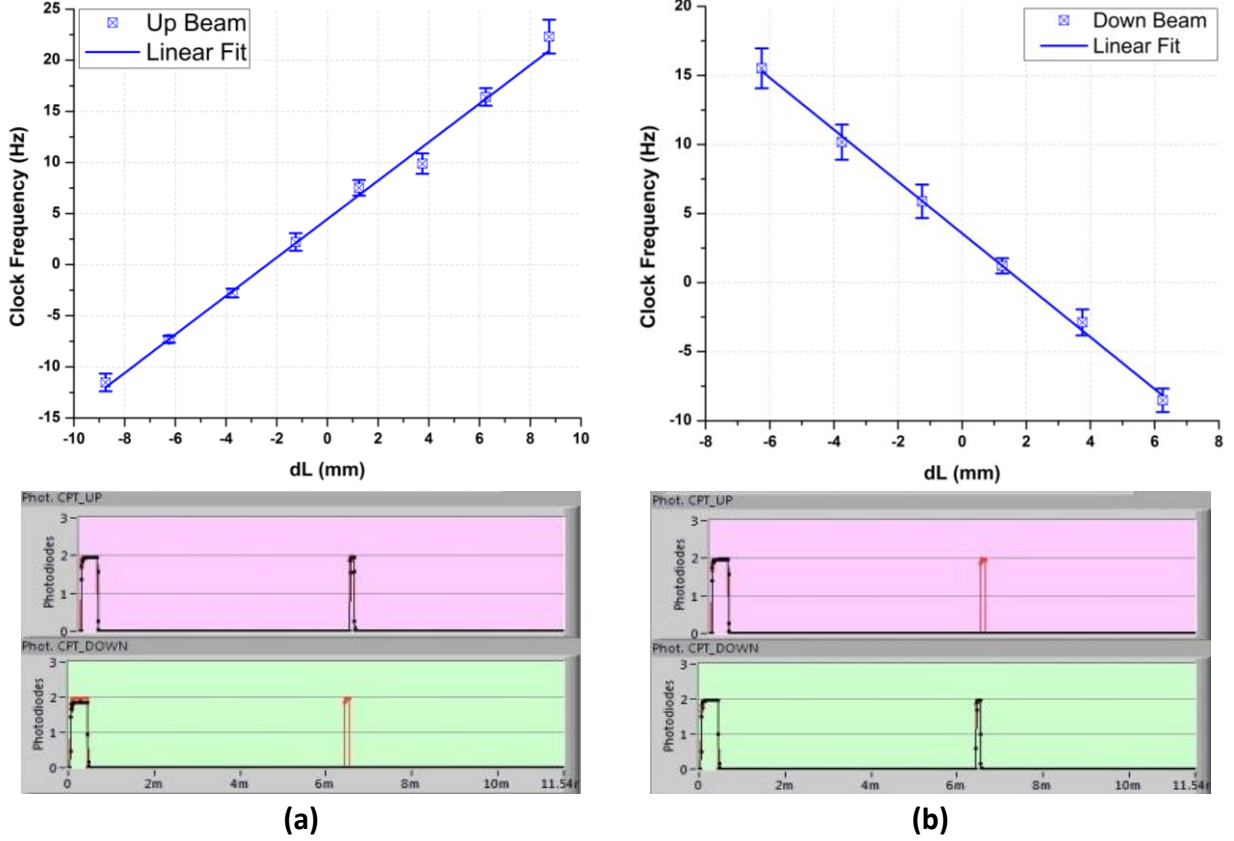
Figure 6.6: (a) Clock frequency measurements for the upward-propagating beam and a linear fit with a slope of 1.88 ± 0.05 Hz/mm. Below the plot is a screen-shot from the control software showing the photodiode measurements of the Ramsey pulses for the up and down beams. The normalization signal is red and the CPT signal is black. The shutter blocked the down beam during the second pulse. (b) Same measurement for the downward-propagating beam with a fitted slope of -1.87 ± 0.04 Hz/mm. The upward beam was blocked in this case. For both measurements, $T_R = 6$ ms.

phase of the two beams. To measure the Doppler shift of the up beam, the shutter was placed in the path of the down beam to block that interrogation field during the second pulse, providing a clean measurement of the upward-propagating frequency without biasing the data toward the average phase. Placing the shutter in the upward-propagating beam path facilitated the same measurement of the down beam frequency. The results of these measurements and screen-shots from the control software showing the photodiode signals for the up and down beams during the Ramsey sequence are shown in Fig. 6.6. This data agrees very well with the prediction from Eq. 6.6 for $T_R = 6$ ms, differing by $\sim 1\%$. Repeated measurements of $d\Delta\nu_D/dL$ with the shutter in place consistently observed larger shifts than with both up and down beams present during

135

the second Ramsey pulse, agreeing to within 10% of the theoretical expectation. Variations in the measurements were again due to the sensitivity of the system to the alignment and relative intensity of the counter-propagating beams.

The large apparatus size made achieving perfect overlap particularly difficult, while the lack of an anti-reflection coating on the optical cell introduced intensity imbalances and traveling wave components. These factors limited our ability to perform further measurements in the Phase I system but provided lessons used in the design of the second generation CACPT clock. Regardless of these technical problems, we were able to demonstrate that under the worst case scenario of interrogation along the axis of gravity, Doppler shifts in the CACPT clock were suppressed below the 10^{-11} level. When scaling this for horizontal interrogation, these results show that despite the lack of a buffer gas in the physics package, Doppler shifts would not restrict the CACPT clock from reaching the stability goals of the program as long as sufficient care is taken to ensure balanced intensities and optimized relative phase between the counter-propagating CPT fields. This would be a critical engineering task for a field-grade version of the CACPT clock.

CHAPTER 7

LIGHT SHIFT CHARACTERIZATION

The AC-stark effect refers in general to the shift of the energy eigenstates in an atom due to a perturbation in the Hamiltonian introduced by a time-varying electric field. In our case, the perturbation is caused by the interrogation lasers used in the atomic clock. For a two-level atom, the shift of the resonant transition frequency due to the presence of a monochromatic laser field with a Rabi frequency Ω and a detuning δ is [56]:

$$\Delta\omega_{LS} = \frac{\Omega^2}{4\delta}. \tag{7.1}$$

In a three-level system interacting with a continuous bichromatic field (Fig. 5.1), a more complicated dependence on the field detuning and Rabi frequencies arises ($\Omega_{1,2}$) [112, 113]:

$$\Delta\omega_{LS} = -\frac{1}{4}\frac{\delta}{\delta^2 + (\gamma/2)^2}\left(\Omega_1^2 - \Omega_2^2\right). \tag{7.2}$$

For this case of continuous excitation, the shift of the two-photon resonance frequency vanishes when the Rabi frequencies driving the two transitions forming the Λ-system are equal.

The AC-stark effect is beneficial in some atomic physics techniques, such as reaching sub-Doppler temperatures via polarization gradient cooling; however, in atomic frequency standards it causes shifts of the clock frequency that generally depend on the detuning and intensity of the interrogation field in a more complicated manner than predicted by Eq. 7.1 or even Eq. 7.2 [71–73, 112]. Because of the dependencies of this "light shift", it can be a significant source of instability in some types of atomic clocks, and much effort has been expended to characterize and suppress it [114, 115]. One successful technique in CPT clocks to address light shifts from off-resonant couplings involves operating at an intensity ratio of the two frequency components that balances the opposite shifts of the CPT resonance, canceling light shifts from higher excited states [105, 116].

Couplings with excited states other than $|F' = 1\rangle$ are not the primary issue in the CACPT clock, where the light shift response is dominated by resonant shifts from the coherent and incoherent

fractions of the CPT field. Characterizing and reducing these frequency shifts is critical for the successful development of a field-grade CPT clock. The coherent AC-stark shift for the Raman-Ramsey interrogation used in the CACPT clock has been previously studied in a sodium beam clock [117] as well as in vapor-cell clocks [118]. This light shift does not follow the simple relationship of Eq. 7.1 as it counter-intuitively vanishes for large interrogation laser intensities and in the limit of long first pulse duration. However, low intensity and/or detuned CPT fields generate low excitation rates that prevent the dark state from completely forming during reasonable durations of the pump pulse, introducing a coherent light shift that scales inversely with the Ramsey period and depends on the initial atomic state and interrogation laser parameters [117]. This light shift will be referred to as the "coherent shift" throughout this chapter. For typical laser parameters used in the CACPT clock, the coherent shift is predicted to be on the order of tens of μHz.

However, measured light shifts in our CACPT clock do not fit this model for the coherent shift and are as large as 0.5 Hz per MHz of optical detuning at intensities that produce high-contrast Ramsey fringes. These light shifts are associated with population transfer caused by incoherent light in the CPT spectrum and scale as T_R^{-1} but are independent of laser intensity, pulse duration, and initial hyperfine state. This atypical response is due to a dynamic equilibrium driven by incoherent light in which atoms continuously scatter out of and re-enter the dark state. This cycle precludes the formation of a complete dark state with the precise optical phase of the interrogation laser field, causing potentially large light shifts at desired laser intensities. Due to its origin in the incoherent part of the CPT laser spectrum, we refer to this light shift as the "incoherent shift".

This chapter focuses on our characterization study of the light shift in a double-Λ coherent population trapping configuration. Measured coherent shifts are compared with an established theory [117], and that model is expanded to describe the observed high-intensity shift in terms of optical pumping driven by incoherent light. Finally, experiments with a different CPT laser configuration that cancels incoherent shifts in the Phase II CACPT clock is presented.

7.1 Light Shift Characterization Measurements

Evaluating the light shift response in the lin||lin CPT configuration required measuring the clock frequency as a function of total CPT intensity (I_{CPT}) for multiple optical detunings (δ_{OPT})
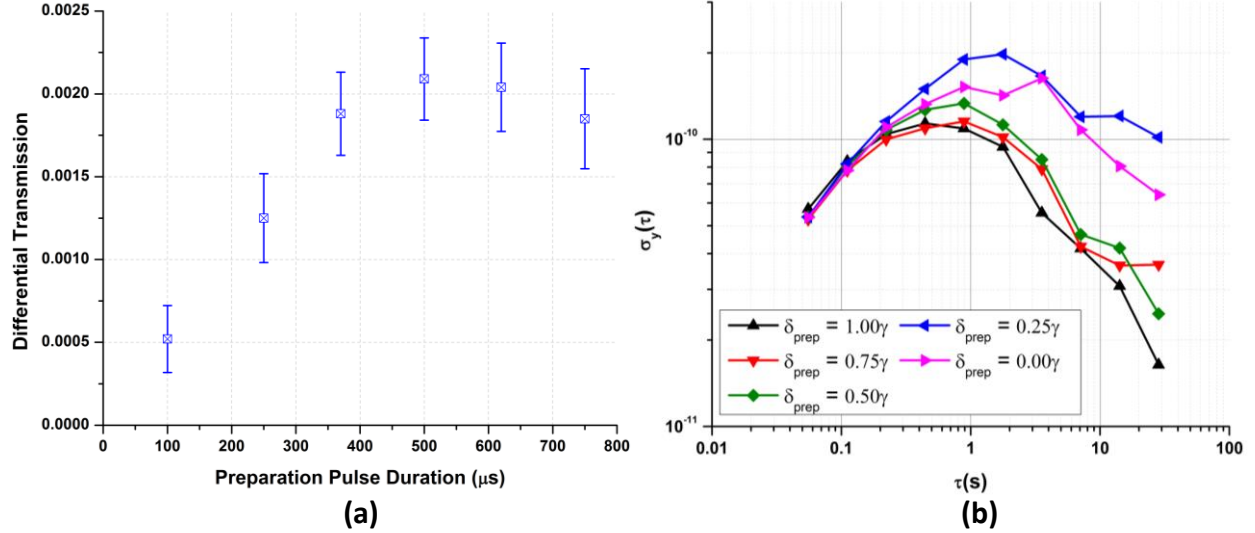
Figure 7.1: (a) Differential transmission of the CPT master laser resonant with the $|F = 2\rangle \to |F' = 1\rangle$ transition as a function of preparation pulse duration. In this data, the difference was taken between the transmission of the CPT master beam through the atom cloud with no preparation pulse (atoms remain in $|F = 2\rangle$) and with a preparation pulse of varied duration (population of the $|F = 2\rangle$ state is reduced). Higher differential transmission corresponds to more atoms in the $|F = 1\rangle$ state. The preparation pulse was on resonance in this data ($\delta_{prep} = 0$) (b) Allan deviation of clock frequency measurements for a 500 μs preparation pulse of varied detuning with $T_R = 4$ ms.

such that the sensitivity to frequency fluctuations at different operating intensities could be determined. Measurements were performed for varied Ramsey pulse duration (τ_1), Ramsey period (T_R), frequency component intensity ratio (I_R), and initial hyperfine state of the atom cloud (F_0).

To prepare the atom cloud in the $|F_0 = 2\rangle$ state, no additional steps in the timing sequence were necessary as this level is naturally populated by the cooling process on the closed D2 cycling transition $|F = 2\rangle \to |F' = 3\rangle$. However, to perform a light shift measurement with the atoms initially in $|F_0 = 1\rangle$, a pulse from the MOT cooling laser was applied immediately following the post-cool stage, during the preparation step of the clock sequence (Fig. 5.7). The MOT laser continued to drive the cycling transition, however during each excitation, there was a small but non-vanishing probability of off-resonant excitation that allowed atoms to leak out of the closed cooling transition and accumulate via optical pumping in the $|F = 1\rangle$ ground state. Generally, a repump laser is applied to overcome this leakage and form a MOT; however, by turning off the repump during this step, the MOT laser pulse acted as a state selection mechanism loading the $|F = 1\rangle$ level. The frequency and duration of this pulse was tuned to ensure that the cloud was fully pumped into $|F_0 = 1\rangle$ while minimizing heating from the additional photon recoils. As shown

in Fig. 7.1 (a), for zero detuning of the preparation pulse, the $|F = 1\rangle$ state was loaded with a ~ 400 μs pulse. However, the stability of the clock was significantly degraded from a decreased trapped atom number caused by heating of the atom cloud (Fig. 7.1 (b)). To balance these effects, the detuning of the MOT laser during the preparation pulse was set to $\sim \gamma$, and the duration was extended to 900 μs. Whether the longer pulse and detuned pumping field were necessary depended on the required resolution of the measurement. For experiments where large shifts were measured, the shorter, on resonance pulse could be used as the error bars were acceptable relative to the shift magnitude. Most measurements with a Ramsey period of 4 ms used a 400 μs, on resonance pulse, while data collected at 16 ms used the detuned, longer pulse.

7.1.1 Dependence on T_R, F_0, and τ_1

The clock frequency as a function of I_{CPT} is shown in Fig. 7.2 for different Ramsey periods and both initial hyperfine states. The coherent light shift is clearly visible for interrogation intensities below $I_{CPT} \cong 0.125$ W/m^2, where low excitation rates to the dark state cause a significant phase shift that exhibits an opposite sign depending on the initial hyperfine state. This shift is suppressed at high intensities ($I_{CPT} \gtrsim 0.125$ W/m^2), leaving the residual incoherent shift dominant in the intensity regime with the highest signal-to-noise ratio for clock operation. The incoherent shift for $T_R = 16$ ms is 0.54 Hz/MHz for both $|F_0 = 1, 2\rangle$, requiring laser frequency stabilization of ~ 1 kHz to reduce instability from the AC-stark effect to the 10^{-13} level. The T_R^{-1} dependence of both coherent and incoherent contributions to the light shift is clearly shown in Fig. 7.2. For longer Ramsey periods, the same phase shift results in a smaller frequency shift due to the reduced Fourier line-width of the Ramsey fringes: $\Delta\nu_{LS} = \Delta\phi/(2\pi T_R)$. This data agrees fairly well with this relationship as for $|F_0 = 2\rangle$, incoherent shifts of 2.60 ± 0.03, 1.17 ± 0.04, and 0.54 ± 0.01 Hz/MHz have been measured for Ramsey times of 4, 8, and 16 ms, respectively. These values were determined from a linear fit to the data, plotted as a function of optical detuning, at high intensities where the coherent shift had vanished ($I_{CPT} = 0.25$ W/m^2). The magnitude and error of the fitted slope quantified the incoherent shift.

The duration of the first Ramsey pulse had a significant effect on the magnitude of the coherent light shift. This is demonstrated by the clock frequency measurements in Fig. 7.3 and in the top left plot of Fig. 7.2 ($\tau_1 = 400$ μs). The dependence on τ_1 can be quantitatively estimated by
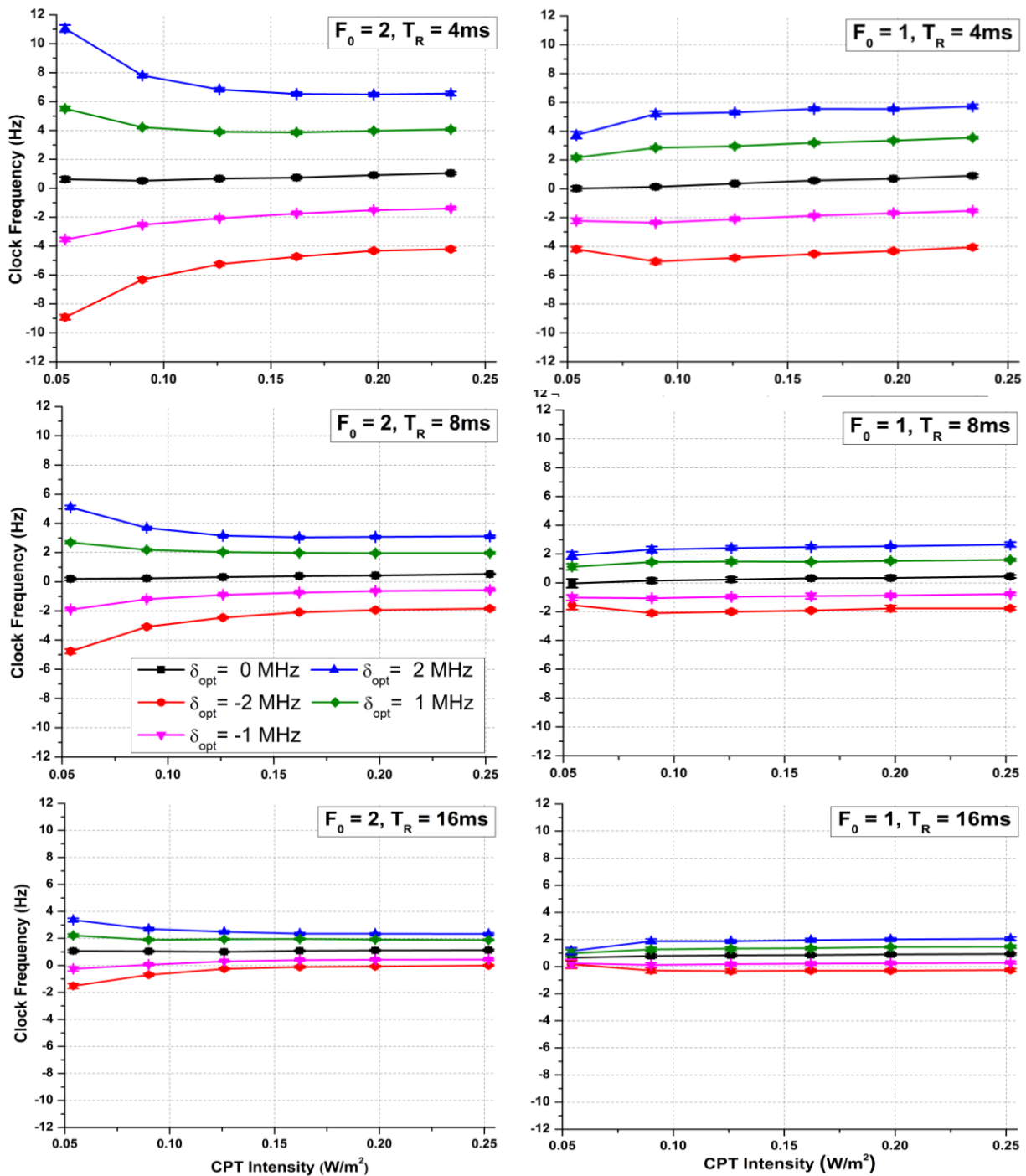
Figure 7.2: Measured light shifts for varied Ramsey period (T_R = 4, 8, and 16 ms) and initial hyperfine state ($|F_0 = 1, 2\rangle$). The first Ramsey pulse was 400 μs in duration, and the integration time was ~ 1000 s per point.
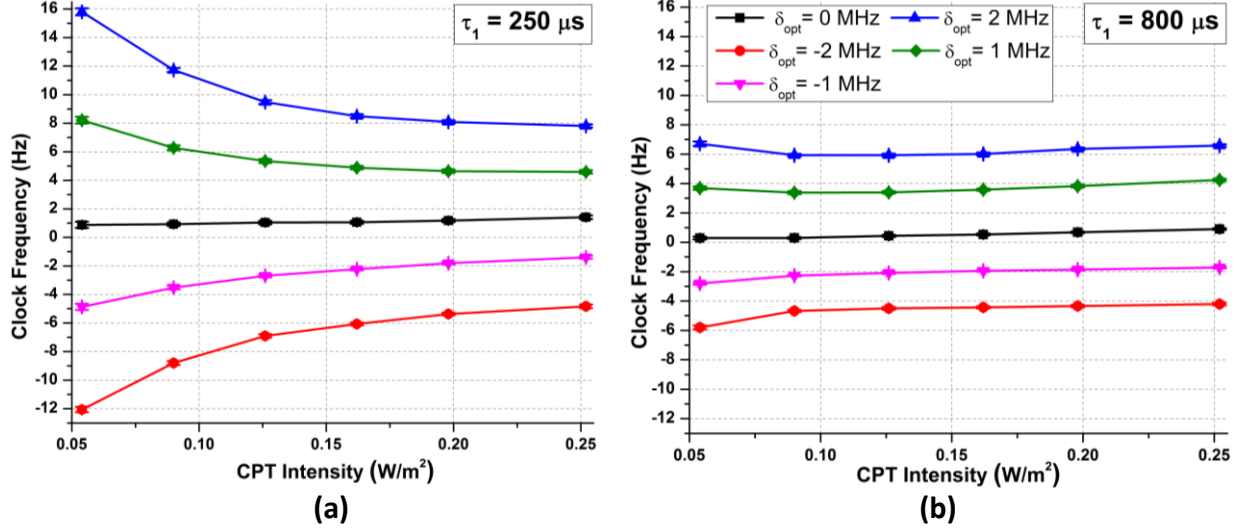
Figure 7.3: Measured light shifts for first Ramsey pulse durations of $\tau_1 = 250$ μs (a) and $\tau_1 = 800$ μs (b) for $T_R = 4$ ms and $|F_0 = 2\rangle$. The integration time was ~ 1000 s per point.

performing a linear fit to the data in the high-intensity regime, where the coherent shift is zero, and extrapolating the fit to zero intensity. Taking the difference between the measured frequency and this extrapolated fit at $I_{CPT} \cong 0.06$ W/m^2 provides a rough value for the coherent shift. This procedure results in coherent shifts of 5.73 ± 0.82, 3.94 ± 0.39, and 1.04 ± 0.37 Hz for pumping pulse durations of $\tau_1 = 250$, 400, and 800 μs, respectively. The data for $\tau_1 = 800$ μs shows that despite the small excitation rates occurring at low interrogation intensities, the coherent shift can be reduced by extending τ_1 such that the system has sufficient time to eventually reach a steady state during the first pulse. The measurements in Figs. 7.2 and 7.3 confirm the predictions in [117] that the coherent shift can be made vanishingly small by operating the clock with large interrogation field intensities or with long pulse durations.

7.1.2 Coherent Shift Parametrization

Since the coherent light shift arises when the duration of τ_1 is insufficient for the dark state to fully form, either due to low excitation rates or a short pulse, the magnitude of the shift depends critically on the dark state loading rate. Mathematically, this physical behavior originates with an exponential in the AC-stark phase shift [117]:

$$\tan(\Delta\phi) \propto (\rho_{11}^0 - \rho_{33}^0)\exp(-\Omega^2 S\tau_1), \tag{7.3}$$
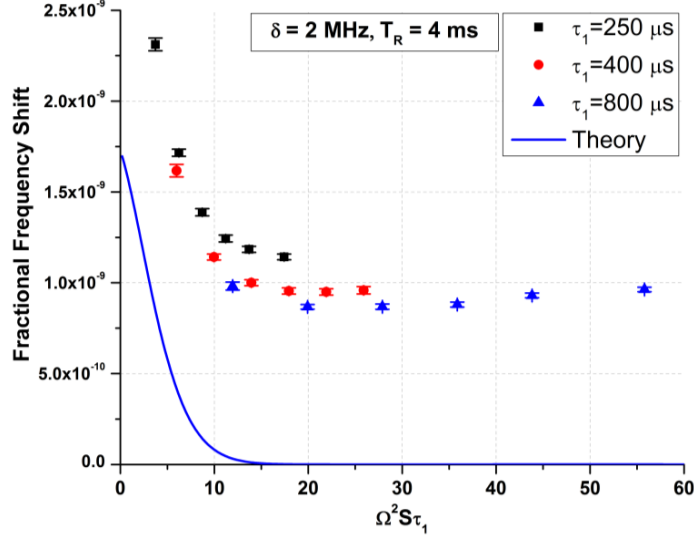
Figure 7.4: Measured fractional frequency light shifts (points) vs. $\Omega^2 S\tau_1$ for different τ_1 and the theoretically predicted coherent shift (line) [117]. The poor agreement is due to the lack of incoherent coupling in the model. $\Omega^2 S\tau_1$ was varied by tuning the CPT laser intensity.

where $\rho_{11}^0 - \rho_{33}^0$ is the population difference of the ground states, Ω is the average Rabi frequency of the CPT frequency components, and $\Omega^2 S = \Omega^2 \gamma/(\gamma^2 + 4\delta^2)$ is the Raman damping rate. When $\Omega^2 S\tau_1 \gg 1$, the dark state is efficiently loaded, and the system approximately reaches equilibrium before the end of the first pulse, resulting in a minimal shift of the Ramsey fringes.

The light shift characterization measurements can be concisely represented in terms of the dimensionless parameter $\Omega^2 S\tau_1$. This is demonstrated in Fig. 7.4, where clock fractional frequency data for a Ramsey period of 4 ms, an optical detuning of 2 MHz, and three different pumping pulse durations have been plotted as a function of $\Omega^2 S\tau_1$. Both the large coherent shifts at low intensities ($\Omega^2 S\tau_1 \lesssim 15$) and the transition to the incoherent shift at high intensities (high $\Omega^2 S\tau_1$ data for $\tau_1 = 250$ μs) and long pulse durations (low $\Omega^2 S\tau_1$ data for $\tau_1 = 800$ μs) appear clearly in this representation. Also shown in Fig. 7.4 is a theory curve for the expected fractional frequency shift as a function of $\Omega^2 S\tau_1$ calculated using the full expression from which Eq. 7.3 was approximated [117]. The disagreement between the measured fractional frequency shifts and the theoretical prediction is significant and results from the theory not including the effects of optical pumping from incoherent light in the CPT spectrum that dominate the light shift response above $\Omega^2 S\tau_1 \approx 15$. The data for each pulse duration in Fig. 7.4 approaches a non-zero steady state offset absent from the treatment of the coherent shift, causing the large discrepancy between theory and measurement.

To account for this offset, the coherent shift must be isolated from the incoherent contribution.

7.2 Coherent Shift Analysis

The parameterized representation of the light shift characterization measurements in Fig. 7.4 illustrates that removing the residual high-intensity shift from the data is necessary to facilitate a direct comparison between measured coherent shifts and the theory developed in [117]. As shown in Eq. 7.3, and by the data in Fig. 7.2, the sign of the coherent shift inverts between $|F_0 = 1\rangle$ and $|F_0 = 2\rangle$, whereas the incoherent shift was observed to be equal for both hyperfine states. The total light shift for each case can be expressed as:

$$\delta\nu_i = \delta\nu_{Ci} + \delta\nu_{IC}, \tag{7.4}$$

where $\delta\nu_i$ and $\delta\nu_{Ci}$ are the total and coherent shift for the ith hyperfine state, and $\delta\nu_{IC}$ is the common incoherent shift. The average coherent shift between the two ground states can then be isolated through the following linear combination:

$$\overline{\delta\nu}_{C12} = \frac{1}{2}(\delta\nu_2 - \delta\nu_1) = \frac{1}{2}(\delta\nu_{C2} + |\delta\nu_{C1}|) \equiv \delta\nu_{\text{diff}}. \tag{7.5}$$

Calculating this linear combination of the clock frequency data removes the incoherent shift and provides the average coherent shift of the $|F_0 = 1\rangle$ and $|F_0 = 2\rangle$ states. To further improve the theory comparison, the average coherent shift between the two states was amplified by measuring the clock frequency at low interrogation intensities ranging from 0.04-0.18 W/m^2 and large optical detunings of $\sim \pm 2\gamma$. These laser parameters are well within the low Raman damping regime and exhibit low excitation rates that cause large phase shifts. The measured clock frequencies within this regime are shown in Fig. 7.5, where the data is plotted against both I_{CPT} and δ_{opt}.

When plotted as a function of δ_{opt}, the measurements taken in the low Raman damping regime (small $\Omega^2 S\tau_1$) exhibit interesting nodal features that were the original motivation for comparing our data with the theoretical formalism in [117]. In that paper, the authors calculate the phase shift of the Ramsey fringes caused by the AC-stark effect, beginning with the optical Bloch equations governing a three-level atom interacting with a bichromatic interrogation field in a Λ configuration.
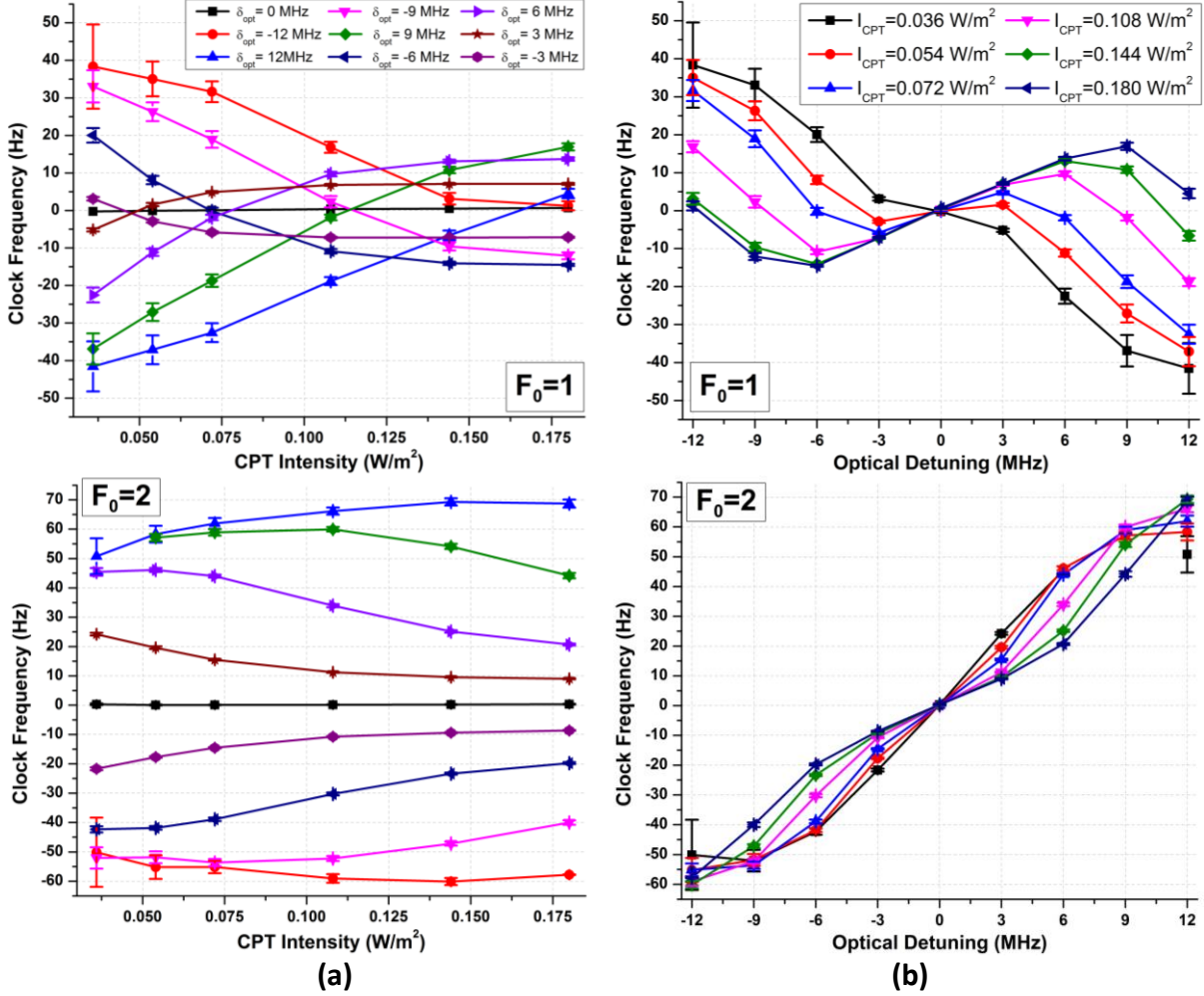
Figure 7.5: Measured light shifts vs. CPT laser intensity (a) and optical detuning (b) for $|F_0 = 1\rangle$ (top) and $|F_0 = 2\rangle$ (bottom). Data was collected using large δ_{opt} and low I_{CPT} to amplify the coherent light shift. To lower the error bars, the integration time was ~ 1500 s per point and 21 hours for a full data set.

After assuming a short lived excited state and comparable detunings of each frequency component, the authors were able to derive a closed form solution that accounts for the Zeeman sublevels via unequal decay rates to the ground state hyperfine levels. The phase shift they obtain is [117]:

$$\tan(\Delta\phi_c) = \frac{\left(\rho_{11}^0 - \rho_{33}^0\right)\sin\left(\Omega^2 D\tau\right)\exp\left(-\Omega^2 S\tau\right) - r\zeta}{N\left[1 - \exp\left[-\left(f - rdf\right)\Omega^2 S\tau\right]\right] + d\tilde{\xi} - r\eta}, \tag{7.6}$$

where $\Omega^2 D = \Omega^2\delta/(\gamma^2 + 4\delta^2)$ is the Raman dispersion, N is the atom number, and $r = (\Gamma_{21} - \Gamma_{23})$ is the parameter accounting for the Zeeman structure. The authors of [117] estimate r to be $r = 0.275$. The rest of the parameters in Eq. 7.6 (ζ, f, d, $\tilde{\xi}$, and η) are complicated functions
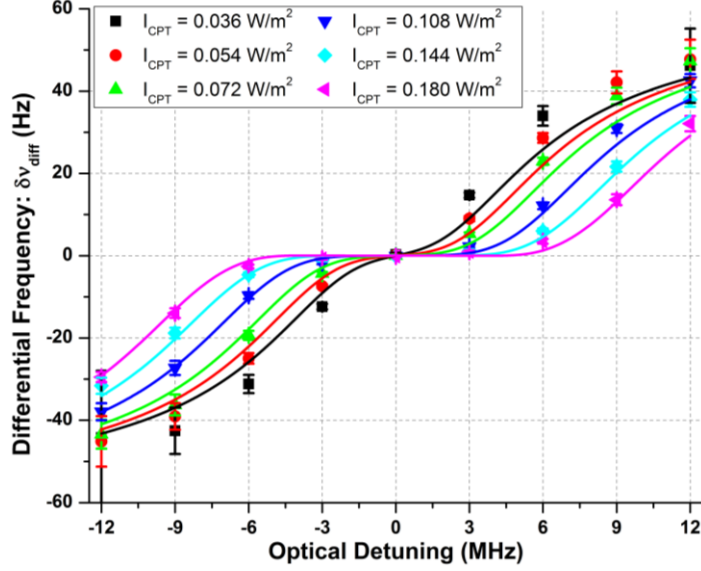
Figure 7.6: Comparison of measured differential frequency light shifts (points) to the full theoretical model (lines) calculated from Eq. 7.6 with no adjustable parameters [117]. Here, $T_R = 4$ ms and $\tau_1 = 400$ μs.

of the Rabi frequencies, detunings, pulse length, and initial population difference. The details of these functions are not critical here as the interesting behavior arises from the sine and exponential functions in the numerator.

Theory curves corresponding to the linear combination in Eq. 7.5 were generated using Eq. 7.6 and are compared with measured values of $\delta\nu_{diff}$ in Fig. 7.6. Excellent quantitative agreement is demonstrated with no adjustable parameters, particularly at high CPT intensities. Small variations of the MOT position within the interrogation beam introduced a discrepancy between the average Gaussian intensity used to calculate the Rabi frequencies for the theory curves and the intensity applied in the experiment. Since the theory is particularly sensitive to the Rabi frequencies, this could explain the small difference between the predicted and measured shifts at low I_{CPT}.

7.3   Incoherent Light Shift

While the observed coherent shifts agreed well with theoretical expectations (Fig. 7.6), the behavior of the incoherent shift deviated from dependencies typical of AC-stark effects. Measurements of the residual shift were independent of the intensity of the CPT light, the duration of the first Ramsey pulse, and the initial hyperfine state. The cause of this unusual phenomenon will be

146

discussed in this section.

7.3.1 Dynamic Equilibrium Model

The observed light shifts in the CACPT clock deviate significantly from the standard shift (Eq. 7.1) and from the coherent shift arising in the Ramsey interrogation scheme (Eq. 7.6). The mechanism behind this unusual behavior is optical pumping driven by incoherent light in the spectrum of the CPT interrogation field. As discussed in Chapter 5 (Fig. 5.6 (b)), the PLL typically achieved a fractional power in the coherent carrier (P_{carrier}) of 0.73, which corresponded to a phase error variance of $\sigma_\Phi^2 \cong 0.35$ rad^2 when integrated over 20 MHz. With this phase-lock performance, 27% of the optical power in the CPT laser spectrum did not contribute to the clock signal but could scatter atoms out of the dark state.

Delayed self-heterodyne measurements of the master and slave optical spectra with and without the frequency locks engaged were used to determine the distribution of the incoherent light among the two CPT frequency components. In our implementation of this technique, light from each laser was split into two arms. One beam passed through an AOM operating at 110 MHz that up-shifted the frequency, while the other arm was coupled into a 320 m single mode optical fiber. The beams were then overlapped on a beam splitter and aligned onto a photodiode, producing a beat note that was sent to an HP8562A spectrum analyzer. The optical fiber delay line introduced a time delay that broke the coherence between the two beams such that when superimposed on the photodiode, they were uncorrelated, and the linewidths could be determined. The results of these measurements for the slave laser are plotted in Fig. 7.7. A comparison of the line shapes with and without the PLL engaged revealed a noise pedestal on the slave laser, while no additional noise was observed on the master. The significant increase in the optical power located in the wings indicated that the slave laser was the dominant source of incoherent light in the CPT spectrum.

With the slave laser offset locked by the PLL to the $|F = 1\rangle \rightarrow |F' = 1\rangle$ transition, the incoherent light in the CPT spectrum was also nearly resonant with this transition. Since this light was not coherent with the interrogation field determining the phase of the dark state, $\Delta\phi \neq 0$ in Eq. 5.2, and the matrix element for the interaction of this part of the CPT spectrum with the dark state was non-vanishing. Accordingly, atoms in the dark state would absorb photons from the incoherent light and be excited out of the dark state. Since the incoherent part of the spectrum
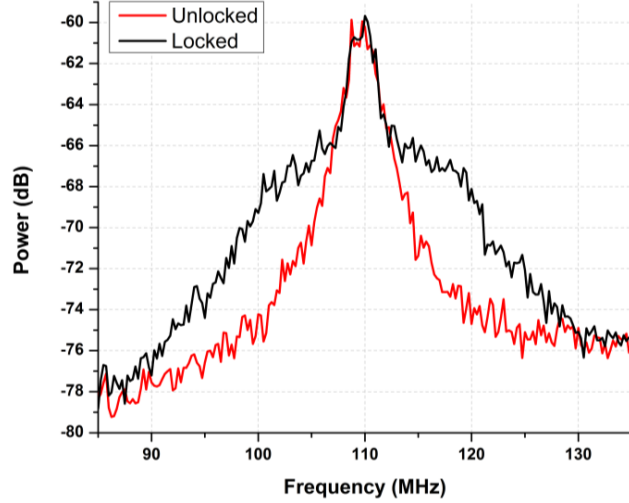
Figure 7.7: Optical spectra measured with the delayed self-heterodyne technique of the slave laser with and without the PLL engaged. Data was collected by Nathan Abrams, a 2013 SURF student.

was dominantly on the $|F = 1\rangle \to |F' = 1\rangle$ transition, affected atoms were preferentially optically pumped to $|F = 2\rangle$, where they then re-entered the dark state through a second interaction with the coherent field. This established a dynamic equilibrium during the first Ramsey pulse in which atoms continuously left and re-joined the dark state. Labeling interaction with the coherent CPT field and the incoherent part of the spectrum as CPT and IC, respectively, this sequence can be written as:

$$|F_0 = 1, 2\rangle \xrightarrow{CPT} |dark\rangle \xrightarrow{IC} |F = 2\rangle \xrightarrow{CPT} |dark\rangle, \tag{7.7}$$

This optical pumping cycle modified the dark state loading process such that regardless of the duration of τ_1, the complete dark state achievable in the absence of the incoherent light was never formed. Rather, equilibrium consisted of a dark state with a population and phase that depended critically on the ratio of the incoherent to coherent components of the CPT spectrum. This is illustrated in Fig. 7.8, where the dependence of the incoherent shift on P_{carrier} was measured. To vary the fraction of light in the central carrier from 0.43-0.73, the gain on the PLL electronics was decreased by 10 dB and the lead filter was increased by 5 kHz, tuning each parameter away from their optimum value. With these PLL settings, the clock frequency at high CPT intensities was recorded as a function of optical detuning, and the incoherent shift was determined by applying a linear fit to the data. The results of this measurement indicated that suppression of the incoherent shift was possible if the performance of the PLL could be improved. In our current configuration,
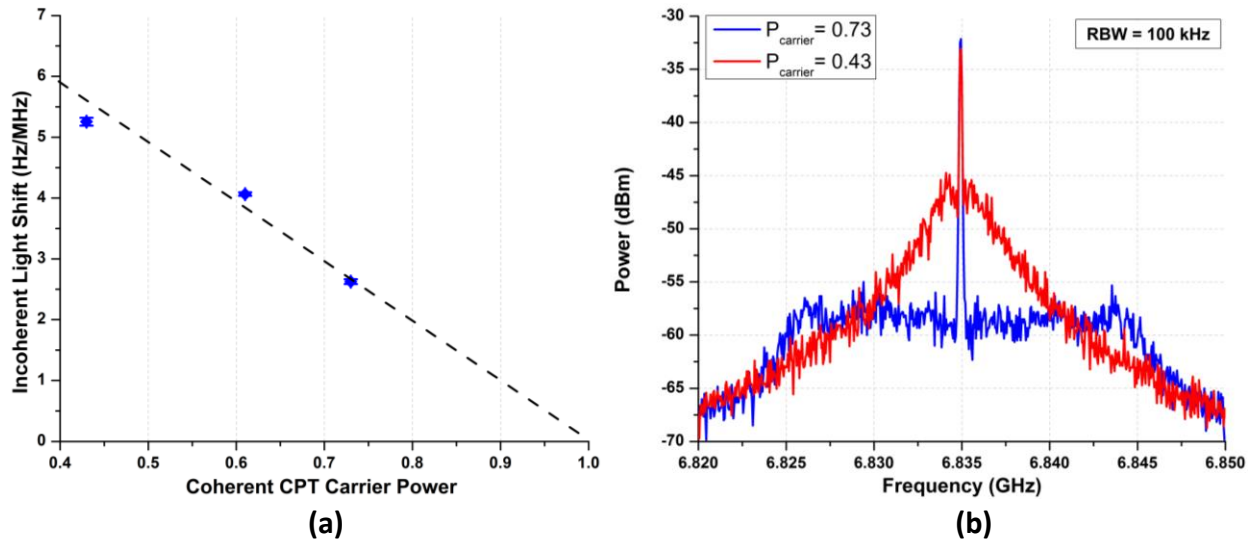
Figure 7.8: (a) Incoherent light shift versus P_{carrier} for $T_R = 4$ ms. A trend line shows the shift reduction as the coherent fraction is improved. (b) Beat note spectrum between master and slave lasers for $P_{\text{carrier}} = 0.43$ and 0.73.

this would require exchanging the master and slave diodes for narrow-line lasers with reduced phase delays or implementing the PLL with fast feedback via an EOM.

As a test of the dynamic equilibrium model, the incoherent light shift was measured as a function of the intensity ratio between the two CPT frequency components, where the intensity ratio was defined as $I_R = I_{\text{master}}/I_{\text{slave}}$. Based on a simple model where the light shift is proportional to the Rabi frequency squared, we would expect the incoherent shift to grow with increasing I_R as the Clebsch-Gordan coefficient for the $|F = 2, m_F = \pm 1\rangle \rightarrow |F' = 1, m_F = 0\rangle$ transitions is $\mp\sqrt{1/4}$, while for $|F = 1, m_F = \pm 1\rangle \rightarrow |F' = 1, m_F = 0\rangle$, the coefficient is $\pm\sqrt{1/12}$ [92]. Thus, transferring more optical power into the master laser frequency component would result in larger Rabi frequencies and larger traditional light shifts. As shown by the data in Fig. 7.9, this is not the case as the incoherent shift decreased by $\sim 3\times$ as I_R was increased from 0.33 to 3.0. However, this trend is consistent with the optical pumping mechanism as higher intensity ratios correspond to a decrease of the slave laser power. Since the incoherent light originates from from the broadband residual noise on the slave laser, this decreases the incoherent power in the CPT beams and reduces the shift arising from the optical pumping cycle described in Eq. 7.7. The high I_R data can be viewed as continuing down the trend-line shown in Fig. 7.8 (a), not by increasing the fraction in the coherent carrier, but by decreasing the incoherent power coupled into the physics package.
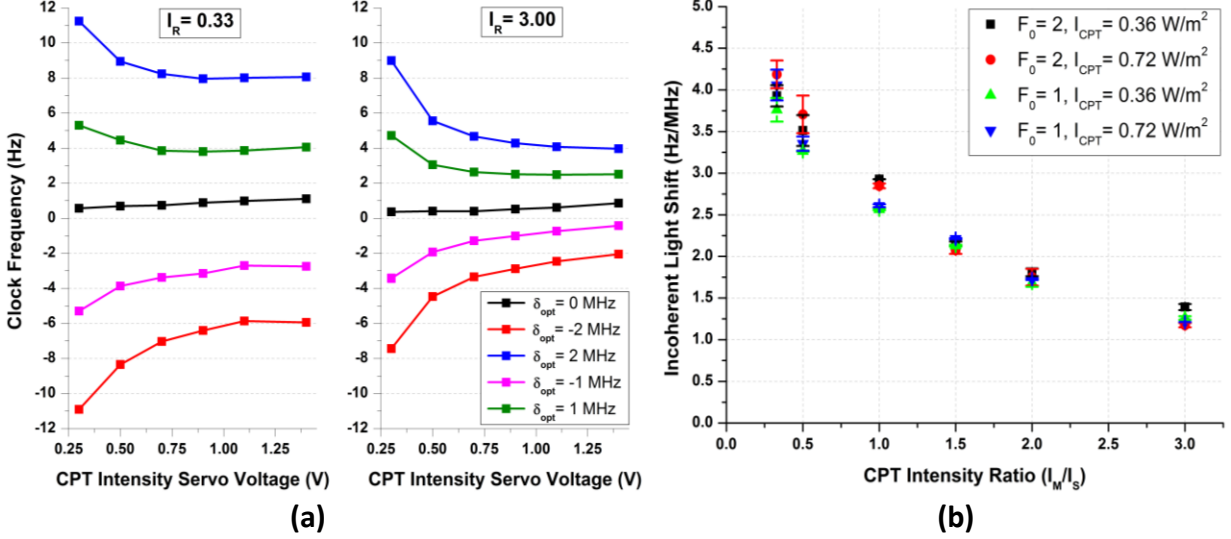
Figure 7.9: (a) Clock frequency vs. CPT intensity servo voltage (1 V→0.18 W/m^2) for intensity ratios of 0.33 and 3.00. (b) Incoherent shift as a function of intensity ratio for two CPT intensities and both hyperfine states. For both plots, the Ramsey period was 4 ms.

7.3.2 Density Matrix Calculation

To place the optical pumping model of the incoherent shift on a firm theoretical foundation, the framework developed in [117] was modified to account for the incoherent part of the CPT spectrum. This was implemented by introducing additional laser couplings parameterized by β_{12} and β_{32}, the incoherent scattering rate between the $|F = 1\rangle$ and $|F = 2\rangle \rightarrow |F' = 1\rangle$ levels, respectively. Calculating the AC-stark phase shift required re-deriving the optical Bloch equations describing the interaction of the three-level atom with the double-Λ system and the added incoherent couplings. With a few physical assumptions, this was reduced to a set of three coupled, linear, first-order differential equations that were numerically solved to obtain the phase shift and the predicted change of the clock frequency.

Fig. 7.10 defines the various laser parameters involved in the calculation, including the coherent and incoherent couplings as well as the spontaneous decay rates to each of the ground state hyperfine levels. This diagram only includes one Λ-system, but since the Clebsch-Gordan coefficients are squared throughout the derivation, the phase shift of the other system was identical. Not present in Fig. 7.10 are couplings corresponding to stimulated emission from the incoherent light driving $|2\rangle \rightarrow |1, 3\rangle$ transitions (Einstein B_{21} coefficients). These terms would be equivalent to an effective spontaneous emission rate that exceeds Γ_{21} and Γ_{23}. However, with the relatively weak intensities
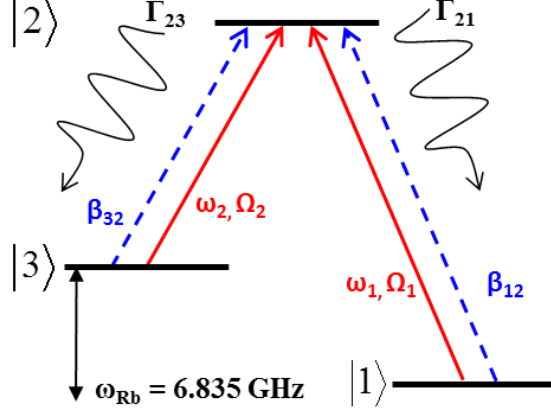
Figure 7.10: Level diagram showing the coherent CPT couplings (Ω_1 and Ω_2), the incoherent couplings (β_{12} and β_{32}), and the spontaneous decay rates (Γ_{21} and Γ_{23}). The frequencies of the CPT fields are $\omega_{1,2}$.

used in the CPT interrogation, the stimulated emission terms are small relative to the spontaneous emission rate and were neglected.

The starting point for the calculation is the Hamiltonian for the system without spontaneous emission and incoherent scattering, which will be added independently later: $H = H_0 + H_{int}$. For this system, the unperturbed Hamiltonian for the three-level system, H_0, and the interaction Hamiltonian representing the perturbation caused by the presence of the CPT Λ-system, H_{int}, are given by [86]:

$$H_0 = \begin{pmatrix} E_1 & 0 & 0 \\ 0 & E_2 & 0 \\ 0 & 0 & E_3 \end{pmatrix} \qquad H_{int} = -\frac{\hbar}{2} \begin{pmatrix} 0 & \Omega_1^* & 0 \\ \Omega_1 & 0 & \Omega_2 \\ 0 & \Omega_2^* & 0 \end{pmatrix}, \qquad (7.8)$$

where E_i is the energy of the ith state. Note that the electric-dipole and rotating wave approximations are assumed in this derivation. Exchanging the level energies for frequencies $\tilde{\omega}_i$, the total Hamiltonian is then:

$$H = \begin{pmatrix} \hbar\tilde{\omega}_1 & -\frac{\hbar}{2}\Omega_1^* & 0 \\ -\frac{\hbar}{2}\Omega_1 & \hbar\tilde{\omega}_2 & -\frac{\hbar}{2}\Omega_2 \\ 0 & -\frac{\hbar}{2}\Omega_2^* & \hbar\tilde{\omega}_1 \end{pmatrix}. \qquad (7.9)$$

There is no direct coupling between levels $|1\rangle$ and $|3\rangle$ due to selection-rule restrictions.

The effects of spontaneous emission and incoherent optical pumping are now incorporated by independently adding these contributions to the density matrix Schrodinger equation describing

the evolution of the system with time [57]:

$$\dot{\rho} = -\frac{i}{\hbar} [H, \rho] + \left(\frac{d\rho}{dt}\right)_{spont} + \left(\frac{d\rho}{dt}\right)_{ic},$$ (7.10)

where the label ic refers to the incoherent pumping contribution and the density matrix for the three level system is:

$$\rho = \begin{pmatrix} \rho_{11} & \alpha_{12} & \alpha_{13} \\ \alpha_{21} & \rho_{22} & \alpha_{23} \\ \alpha_{31} & \alpha_{32} & \rho_{33} \end{pmatrix}.$$ (7.11)

In this version of the density matrix operator, ρ_{ii} is the population of the ith state and α_{ij} is the coherence between levels $|i\rangle$ and $|j\rangle$. From the detailed derivation of the density operator master equation in [119] and the application of it to a three-level system in [120], the spontaneous emission terms can be written as:

$$\left(\frac{d\rho}{dt}\right)_{spont} = -\frac{1}{2}\Gamma_{21}\left(\hat{\sigma}_{22}\rho + \rho\hat{\sigma}_{22} - 2\hat{\sigma}_{12}\rho\hat{\sigma}_{21}\right) - \frac{1}{2}\Gamma_{23}\left(\hat{\sigma}_{22}\rho + \rho\hat{\sigma}_{22} - 2\hat{\sigma}_{32}\rho\hat{\sigma}_{23}\right),$$ (7.12)

where $\hat{\sigma}_{ij} \equiv |i\rangle\langle j|$ is the quantum projection operator between states $|i\rangle$ and $|j\rangle$. This expression describes the de-excitation of an atom from state $|2\rangle$ to the ground state hyperfine levels $|1\rangle$ and $|3\rangle$ via spontaneous emission at the decay rates defined above. The incoherent excitation can be written in an analogous fashion, with similar terms describing transitions from levels $|1\rangle$ and $|3\rangle$ to $|2\rangle$ with excitation rates of β_{12} and β_{32}, respectively:

$$\left(\frac{d\rho}{dt}\right)_{ic} = -\frac{1}{2}\beta_{12}\left(\hat{\sigma}_{11}\rho + \rho\hat{\sigma}_{11} - 2\hat{\sigma}_{21}\rho\hat{\sigma}_{12}\right) - \frac{1}{2}\beta_{32}\left(\hat{\sigma}_{33}\rho + \rho\hat{\sigma}_{33} - 2\hat{\sigma}_{23}\rho\hat{\sigma}_{32}\right).$$ (7.13)

With the terms corresponding to coherent excitation, incoherent couplings, and spontaneous emission defined, each part of the density matrix Schrodinger equation can now be independently evaluated. For the coherent contribution, multiplying out the matrices in the commutator between the density operator (Eq. 7.11) and Hamiltonian (7.9) results in the following set of equations:

$$\dot{\rho}_{11} = \frac{i}{2}\left(-\Omega_1\alpha_{12} + \Omega_1^*\alpha_{12}^*\right)$$
$$\dot{\rho}_{22} = \frac{i}{2}\left(\Omega_1\alpha_{12} - \Omega_1^*\alpha_{12}^* + \Omega_2\alpha_{32} - \Omega_2^*\alpha_{32}^*\right)$$ (7.14)

152

$$\dot{\rho}_{33} = \frac{i}{2}\left(-\Omega_2\alpha_{32} + \Omega_2^*\alpha_{32}^*\right)$$

$$\dot{\alpha}_{12} = \frac{i}{2}\Omega_1^*(\rho_{22} - \rho_{11}) - \frac{i}{2}\Omega_2^*\alpha_{13} - i\delta_1\alpha_{12}$$

$$\dot{\alpha}_{32} = \frac{i}{2}\Omega_2^*(\rho_{22} - \rho_{33}) - \frac{i}{2}\Omega_1^*\alpha_{13}^* - i\delta_2\alpha_{32}$$

$$\dot{\alpha}_{13} = \frac{i}{2}\left(\Omega_1^*\alpha_{32}^* - \Omega_2\alpha_{12}\right) - i(\delta_1 - \delta_2)\alpha_{13}.$$

The relationship $\alpha_{ij} = \alpha_{ji}^*$ (valid since the density matrix operator is hermitian) has been used to reduce the set of equations from nine to six, and the detuning of the coherent CPT beams, defined as $\delta_1 = \tilde{\omega}_1 - \tilde{\omega}_2$ and $\delta_2 = \tilde{\omega}_3 - \tilde{\omega}_2$, has been used to eliminate $\tilde{\omega}_i$. This set of equations would describe the evolution of the three-level atom if the only interaction arose from the coherent part of the spectrum. The contributions from spontaneous emission and the incoherent couplings are obtained by evaluating Eq. 7.12 and Eq. 7.13 for the six independent density matrix components. For spontaneous emission, the terms are:

$$\dot{\rho}_{11}|_{spont} = \langle 1|\left(\frac{d\rho}{dt}\right)_{spont}|1\rangle = \Gamma_{21}\rho_{22}$$

$$\dot{\rho}_{22}|_{spont} = \langle 2|\left(\frac{d\rho}{dt}\right)_{spont}|2\rangle = -\left(\Gamma_{21} + \Gamma_{23}\right)\rho_{22} = -\gamma\rho_{22}$$

$$\dot{\rho}_{33}|_{spont} = \langle 3|\left(\frac{d\rho}{dt}\right)_{spont}|3\rangle = \Gamma_{23}\rho_{22}$$

$$\dot{\alpha}_{12}|_{spont} = \langle 1|\left(\frac{d\rho}{dt}\right)_{spont}|2\rangle = -\frac{1}{2}\left(\Gamma_{21} + \Gamma_{23}\right)\alpha_{12} = -\frac{\gamma}{2}\alpha_{12} \qquad (7.15)$$

$$\dot{\alpha}_{32}|_{spont} = \langle 3|\left(\frac{d\rho}{dt}\right)_{spont}|2\rangle = -\frac{1}{2}\left(\Gamma_{21} + \Gamma_{23}\right)\alpha_{32} = -\frac{\gamma}{2}\alpha_{32}$$

$$\dot{\alpha}_{13}|_{spont} = \langle 1|\left(\frac{d\rho}{dt}\right)_{spont}|3\rangle = 0.$$

The contributions from the incoherent couplings are:

$$\dot{\rho}_{11}|_{ic} = \langle 1|\left(\frac{d\rho}{dt}\right)_{ic}|1\rangle = -\beta_{12}\rho_{11}$$

$$\dot{\rho}_{22}|_{ic} = \langle 2|\left(\frac{d\rho}{dt}\right)_{ic}|2\rangle = \beta_{12}\rho_{11} + \beta_{32}\rho_{33}$$

$$\dot{\rho}_{33}|_{ic} = \langle 3|\left(\frac{d\rho}{dt}\right)_{ic}|3\rangle = -\beta_{32}\rho_{33} \qquad (7.16)$$

$$\dot{\alpha}_{12}|_{ic} = \langle 1|\left(\frac{d\rho}{dt}\right)_{ic}|2\rangle = -\frac{1}{2}\beta_{12}\alpha_{12}$$

$$\dot{\alpha}_{32}|_{ic} = \langle 3|\left(\frac{d\rho}{dt}\right)_{ic}|2\rangle = -\frac{1}{2}\beta_{32}\alpha_{32}$$

$$\dot{\alpha}_{13}|_{ic} = \langle 1| \left(\frac{d\rho}{dt}\right)_{ic} |3\rangle = -\frac{1}{2}\left(\beta_{12} + \beta_{32}\right)\alpha_{13}.$$

Returning to the density matrix Schrodinger equation (Eq. 7.10) and inserting the terms calculated in Eqs. 7.14, 7.15, and 7.16, we obtain the full set of optical Bloch equations for the lin||lin coherent population trapping interrogation scheme with incoherent optical couplings:

$$\begin{aligned}
\dot{\rho}_{11} &= \frac{i}{2}\left(-\Omega_1\alpha_{12} + \Omega_1^*\alpha_{12}^*\right) + \Gamma_{21}\rho_{22} - \beta_{12}\rho_{11} \\
\dot{\rho}_{22} &= \frac{i}{2}\left(\Omega_1\alpha_{12} - \Omega_1^*\alpha_{12}^* + \Omega_2\alpha_{32} - \Omega_2^*\alpha_{32}^*\right) - \gamma\rho_{22} + \beta_{12}\rho_{11} + \beta_{32}\rho_{33} \\
\dot{\rho}_{33} &= \frac{i}{2}\left(-\Omega_2\alpha_{32} + \Omega_2^*\alpha_{32}^*\right) + \Gamma_{23}\rho_{22} - \beta_{32}\rho_{33} \\
\dot{\alpha}_{12} &= \frac{i}{2}\Omega_1^*(\rho_{22} - \rho_{11}) - \frac{i}{2}\Omega_2^*\alpha_{13} - \frac{1}{2}(\gamma + 2i\delta_1 + \beta_{12})\alpha_{12} \\
\dot{\alpha}_{32} &= \frac{i}{2}\Omega_2^*(\rho_{22} - \rho_{33}) - \frac{i}{2}\Omega_1^*\alpha_{13}^* - \frac{1}{2}(\gamma + 2i\delta_2 + \beta_{32})\alpha_{32} \\
\dot{\alpha}_{13} &= \frac{i}{2}\left(\Omega_1^*\alpha_{32}^* - \Omega_2\alpha_{12}\right) - i(\delta_1 - \delta_2)\alpha_{13} - \frac{1}{2}\left(\beta_{12} + \beta_{32}\right)\alpha_{13}.
\end{aligned} \tag{7.17}$$

With the governing system of equations established, the next step in calculating the AC-stark phase shift for our experiment was adopting three assumptions to reduce Eqs. 7.17 to a more manageable form. We assume that the excited state is short-lived, that the difference in detunings of the two CPT frequency components is small, and that the states form a closed three-level system. These conditions are mathematically expressed as [117]:

$$\begin{aligned}
\dot{\rho}_{22} &\ll \gamma\rho_{22} \\
\dot{\alpha}_{12} &\ll \frac{1}{2}(\gamma + 2i\delta_1)\alpha_{12} \\
\dot{\alpha}_{32} &\ll \frac{1}{2}(\gamma + 2i\delta_2)\alpha_{32} \\
\delta_1 - \delta_2 &\ll \delta_1, \delta_2 \\
\Gamma_{21} + \Gamma_{23} &= \gamma,
\end{aligned} \tag{7.18}$$

where the first three equations arise from the assumption of a short-lived excited state. To further simplify the calculation, we now assume equal detunings and Rabi frequencies for the two CPT components and equal spontaneous decay rates to each hyperfine level: $\delta_1 = \delta_2 \equiv \delta$, $\Omega_1 = \Omega_2 \equiv \Omega$, and $\Gamma_{21} = \Gamma_{23}$. With these simplifications, the system of equations can be algebraically reduced to coupled differential equations for $\text{Re}(2\dot{\alpha}_{13})$, $\text{Im}(2\dot{\alpha}_{13})$, and $(\dot{\rho}_{11} - \dot{\rho}_{33})$. Using the second and third

equation in Eq. 7.18, expressions for α_{12} and α_{32} from Eq. 7.17 can be written down:

$$
\begin{aligned}
\alpha_{12} &= \frac{\gamma_+ \beta_{12} - 2i\delta}{(\gamma + \beta_{12})^2 + 4\delta^2} \left[i\Omega^* \left(\rho_{22} - \rho_{11} - \alpha_{13} \right) \right] \\
\alpha_{32} &= \frac{\gamma_+ \beta_{32} - 2i\delta}{(\gamma + \beta_{32})^2 + 4\delta^2} \left[i\Omega^* \left(\rho_{22} - \rho_{33} - \alpha_{13}^* \right) \right].
\end{aligned}
\tag{7.19}
$$

Inserting this result into the equation for $\dot{\rho}_{22}$ and using the first expression in Eq. 7.18, an equation for the excited state population can be derived. After multiple algebraic steps, one obtains:

$$
\begin{aligned}
\rho_{22} = {} & F \left[\Omega^2 \left(S_1 + S_2 \right) \operatorname{Re} \left(\alpha_{13} \right) - 2\Omega^2 \left(D_2 - D_1 \right) \operatorname{Im} \left(\alpha_{13} \right) \right. \\
& \left. + \frac{1}{2} \left[\beta_{12} - \beta_{32} + \Omega^2 \left(S_1 - S_2 \right) \right] \left(\rho_{11} - \rho_{33} \right) + \frac{N}{2} \left[\beta_{12} + \beta_{32} + \Omega^2 \left(S_1 + S_2 \right) \right] \right],
\end{aligned}
\tag{7.20}
$$

where, to simplify the notation, the following definitions have been made:

$$
\begin{aligned}
S_1 &\equiv \frac{\gamma_+ \beta_{12}}{(\gamma + \beta_{12})^2 + 4\delta^2} \\
S_2 &\equiv \frac{\gamma_+ \beta_{32}}{(\gamma + \beta_{32})^2 + 4\delta^2} \\
D_1 &\equiv \frac{\delta}{(\gamma + \beta_{12})^2 + 4\delta^2} \\
D_2 &\equiv \frac{\delta}{(\gamma + \beta_{32})^2 + 4\delta^2} \\
F &\equiv \frac{1}{\gamma + \frac{1}{2} \left[\beta_{12} + \beta_{32} + 3\Omega^2 \left(S_1 + S_2 \right) \right]}.
\end{aligned}
\tag{7.21}
$$

Next, the expressions for α_{12} and α_{32}, with Eq. 7.20 substituted in for ρ_{22}, are inserted into $\dot{\alpha}_{13}$. After extensively manipulating the expression and making use of the fact that for $z \in \mathbb{C}$, $\operatorname{Re}(z) = \frac{1}{2}(z + z^*)$ and $\operatorname{Im}(z) = \frac{1}{2i}(z - z^*)$, the differential equations for $\operatorname{Re}(2\dot{\alpha}_{13})$ and $\operatorname{Im}(2\dot{\alpha}_{13})$ are found to be:

$$
\begin{aligned}
\operatorname{Re}(2\dot{\alpha}_{13}) = {} & \left[-\frac{1}{2}\Omega^2 \left(S_1 + S_2 \right) F \left(\gamma + \frac{1}{2}\beta_{12} + \frac{1}{2}\beta_{32} \right) - \frac{1}{2} \left(\beta_{12} + \beta_{32} \right) \right] \operatorname{Re}(2\alpha_{13}) \\
& + \left[\Omega^2 \left(D_2 - D_1 \right) F \left(\gamma + \frac{1}{2}\beta_{12} + \frac{1}{2}\beta_{32} \right) \right] \operatorname{Im}(2\alpha_{13}) \\
& + \frac{1}{2} F \Omega^2 \left[\left(S_2 - S_1 \right) \left(\gamma + \frac{1}{2}\beta_{12} + \frac{1}{2}\beta_{32} \right) + \frac{3}{2} \left(S_1 + S_2 \right) \left(\beta_{12} - \beta_{32} \right) \right] \left(\rho_{11} - \rho_{33} \right) \\
& + \frac{1}{2}\Omega^2 \left(S_1 + S_2 \right) N F \left(-\gamma + \beta_{12} + \beta_{32} \right)
\end{aligned}
\tag{7.22}
$$

and

$$\mathrm{Im}\,(2\dot{\alpha}_{13}) = \left[-\Omega^2\,(D_2 - D_1)\,F\left(\gamma + \frac{1}{2}\beta_{12} + \frac{1}{2}\beta_{32}\right)\right]\mathrm{Re}\,(2\alpha_{13})$$
$$+\left[-\frac{1}{2}\Omega^2\,(S_1 + S_2) - \frac{1}{2}\,(\beta_{12} + \beta_{32}) - 3\Omega^4\,(D_2 - D_1)^2\,F\right]\mathrm{Im}\,(2\alpha_{13})$$
$$+\left[\Omega^2\,(D_1 + D_2) + \frac{3}{2}\Omega^2\,(D_2 - D_1)\left(\beta_{12} - \beta_{32} + \Omega^2\,(S_1 - S_2)\right)F\right](\rho_{11} - \rho_{33})$$
$$+NF\Omega^2\,(D_2 - D_1)\,(-\gamma + \beta_{12} + \beta_{32})\,. \tag{7.23}$$

Two required differential equations have now been derived. For the last equation, $\dot{\rho}_{33}$ is subtracted from $\dot{\rho}_{11}$ in Eq. 7.17, and Eqs. 7.19 and 7.20 are substituted for α_{12}, α_{32}, and ρ_{22}. After multiplying out the expression and grouping terms, ρ_{11} and ρ_{33} are eliminated with the following substitution:

$$\rho_{11} = \frac{1}{2}\,(\rho_{11} - \rho_{33}) + \frac{1}{2}\,(\rho_{11} + \rho_{33}) = \frac{1}{2}\,(\rho_{11} - \rho_{33}) + \frac{1}{2}\,(N - \rho_{22})$$
$$\rho_{33} = \frac{1}{2}\,(\rho_{33} - \rho_{11}) + \frac{1}{2}\,(\rho_{11} + \rho_{33}) = -\frac{1}{2}\,(\rho_{11} - \rho_{33}) + \frac{1}{2}\,(N - \rho_{22})\,, \tag{7.24}$$

where the normalization of the density matrix populations ($\rho_{11} + \rho_{22} + \rho_{33} = N$) has been used. After completing these steps and additional algebraic manipulations, the third differential equation for the system is found to be:

$$(\dot{\rho}_{11} - \dot{\rho}_{33}) = \frac{1}{2}F\Omega^2\left[\frac{1}{2}\,(S_1 + S_2)\,(\beta_{12} - \beta_{32}) - (S_1 - S_2)\left(\gamma + \frac{1}{2}\beta_{12} + \frac{1}{2}\beta_{32}\right)\right]\mathrm{Re}\,(2\alpha_{13})$$
$$+\left[-\Omega^2\,(D_1 + D_2) - \frac{1}{2}\left(\beta_{12} - \beta_{32} + 3\Omega^2\,(S_1 - S_2)\right)F\Omega^2\,(D_2 - D_1)\right]\mathrm{Im}\,(2\alpha_{13})$$
$$+\left[-\frac{1}{2}\left(\beta_{12} + \beta_{32} + \Omega^2\,(S_1 + S_2)\right)\right.$$
$$\left.+\frac{1}{4}F\left(\beta_{12} - \beta_{32} + 3\Omega^2\,(S_1 - S_2)\right)\left(\beta_{12} - \beta_{32} + \Omega^2\,(S_1 - S_2)\right)\right](\rho_{11} - \rho_{33})$$
$$+\frac{1}{2}NF\left[(\beta_{12} + \beta_{32} - \gamma)\,\Omega^2\,(S_1 - S_2) - (\beta_{12} - \beta_{32})\left(\gamma + \Omega^2\,(S_1 + S_2)\right)\right]\,. \tag{7.25}$$

Combining Eqs. 7.22, 7.23, and 7.25, the final system of equations describing CPT interrogation in the presence of incoherent light is:

$$\frac{d}{dt}\begin{pmatrix} \mathrm{Re}\,(2\alpha_{13}) \\ \mathrm{Im}\,(2\alpha_{13}) \\ (\rho_{11} - \rho_{33}) \end{pmatrix} = A\begin{pmatrix} \mathrm{Re}\,(2\alpha_{13}) \\ \mathrm{Im}\,(2\alpha_{13}) \\ (\rho_{11} - \rho_{33}) \end{pmatrix} + B, \tag{7.26}$$

where A is a 3×3 matrix with the following elements:

$$A_{11} = \left[-\frac{1}{2} \Omega^2 \left(S_1 + S_2 \right) F\chi - \frac{1}{2} \left(\beta_{12} + \beta_{32} \right) \right]$$

$$A_{12} = \left[\Omega^2 \left(D_2 - D_1 \right) F\chi \right]$$

$$A_{13} = \left[\frac{1}{2} F\Omega^2 \left[\left(S_2 - S_1 \right) \chi + \frac{3}{2} \left(S_1 + S_2 \right) \left(\beta_{12} - \beta_{32} \right) \right] \right]$$

$$A_{21} = \left[-\Omega^2 \left(D_2 - D_1 \right) F\chi \right]$$

$$A_{22} = \left[-\frac{1}{2} \Omega^2 \left(S_1 + S_2 \right) - \frac{1}{2} \left(\beta_{12} + \beta_{32} \right) - 3\Omega^4 \left(D_2 - D_1 \right)^2 F \right] \qquad (7.27)$$

$$A_{23} = \left[\Omega^2 \left(D_1 + D_2 \right) + \frac{3}{2} \Omega^2 \left(D_2 - D_1 \right) FG \right]$$

$$A_{31} = \left[\frac{1}{2} F\Omega^2 \left[\frac{1}{2} \left(S_1 + S_2 \right) \left(\beta_{12} - \beta_{32} \right) - \left(S_1 - S_2 \right) \chi \right] \right]$$

$$A_{32} = \left[-\Omega^2 \left(D_1 + D_2 \right) - \frac{1}{2} \left(G + 2\Omega^2 \left(S_1 - S_2 \right) \right) F\Omega^2 \left(D_2 - D_1 \right) \right]$$

$$A_{33} = \left[-\frac{1}{2} \left(\beta_{12} + \beta_{32} + \Omega^2 \left(S_1 + S_2 \right) \right) + \frac{1}{4} FG \left(G + 2\Omega^2 \left(S_1 - S_2 \right) \right) \right],$$

and B is a 3×1 matrix formed by:

$$B_{11} = \left[\frac{1}{2} NF\tilde{\chi}\Omega^2 \left(S_1 + S_2 \right) \right]$$

$$B_{21} = \left[NF\tilde{\chi}\Omega^2 \left(D_2 - D_1 \right) \right] \qquad (7.28)$$

$$B_{31} = \left[\frac{1}{2} NF \left[\tilde{\chi}\Omega^2 \left(S_1 - S_2 \right) - \left(\beta_{12} - \beta_{32} \right) \left(\gamma + \Omega^2 \left(S_1 + S_2 \right) \right) \right] \right].$$

The following functions have been defined to further simplify the notation:

$$G \equiv \beta_{12} - \beta_{32} + \Omega^2 \left(S_1 - S_2 \right)$$

$$\chi \equiv \gamma + \frac{1}{2} \left(\beta_{12} + \beta_{32} \right) \qquad (7.29)$$

$$\tilde{\chi} \equiv \beta_{12} + \beta_{32} - \gamma.$$

The system of equations derived above reduces to the result obtained in [117] when the incoherent optical couplings are removed by setting $\beta_{12} = \beta_{32} = 0$.

The final step necessary to model the optical pumping induced light shift is to calculate the incoherent scattering rates, β_{12} and β_{32}. These parameters are modeled after the Raman damping rate that determines how quickly atoms are pumped into the dark state. In our calculation, the

157

incoherent scattering rate is given by:

$$\beta_{ij} = \epsilon \frac{\Omega_{IC}^2 \gamma}{\gamma^2 + 4\delta^2}, \qquad (7.30)$$

where Ω_{IC}^2 is the Rabi frequency of the incoherent light, and ϵ is a scaling factor. This expression is equivalent to the standard two-level scattering rate (see Eq. 2.1) in the intensity regime in which the clock operates ($\Omega \ll \gamma$). To incorporate the spectrum of the incoherent noise into the model, the β_{ij} parameter was calculated by integrating a white noise spectrum with an intensity given by $(1 - P_{\text{carrier}}) I_{CPT}$ spread over a 16 MHz wide band centered on the coherent carrier.

The AC-stark shift was calculated by numerically solving the coupled, first-order differential equations in Eq. 7.26 using Eqs. 7.27 and 7.28 with the functions defined in Eqs. 7.21 and 7.29 and the definition of the incoherent scattering parameter in Eq. 7.30. The numerical calculation was performed using the NDSolve function in Mathematica, resulting in interpolated solutions for $\text{Re}\,(2\alpha_{13})$, $\text{Im}\,(2\alpha_{13})$, and $(\rho_{11} - \rho_{33})$ as functions of time. The last term provided information on the evolution of the population difference as the system was pumped into the dark state, while the real and imaginary parts of the α_{13} coherence were used to obtain the phase shift [117]:

$$\phi_{LS} = \tan^{-1} \left(\frac{\text{Im}\,(\alpha_{13})}{\text{Re}\,(\alpha_{13})} \right). \qquad (7.31)$$

The shift of the clock frequency from the AC-stark effect was then calculated from the Fourier width of the Ramsey fringes discussed in Section 7.1.1.

7.3.3 Simulation Results

The first set of simulation results are shown in Fig. 7.11, where the clock frequency shift as a function of interrogation intensity was calculated for different fractions of incoherent power in the CPT optical spectrum. For a perfectly coherent spectrum with $P_{\text{carrier}} = 1.00$, the incoherent shift completely vanishes, leaving only the coherent shift at $I_{CPT} \lesssim 0.075$ W/m^2 (top plot). As the percentage of incoherent light in the spectrum increases to 15% (middle) and 30% (bottom), the coherent shift at low intensities grew slightly, while a constant shift appears at high intensities that exhibits a linear dependence on optical detuning. These qualitative features agree very nicely
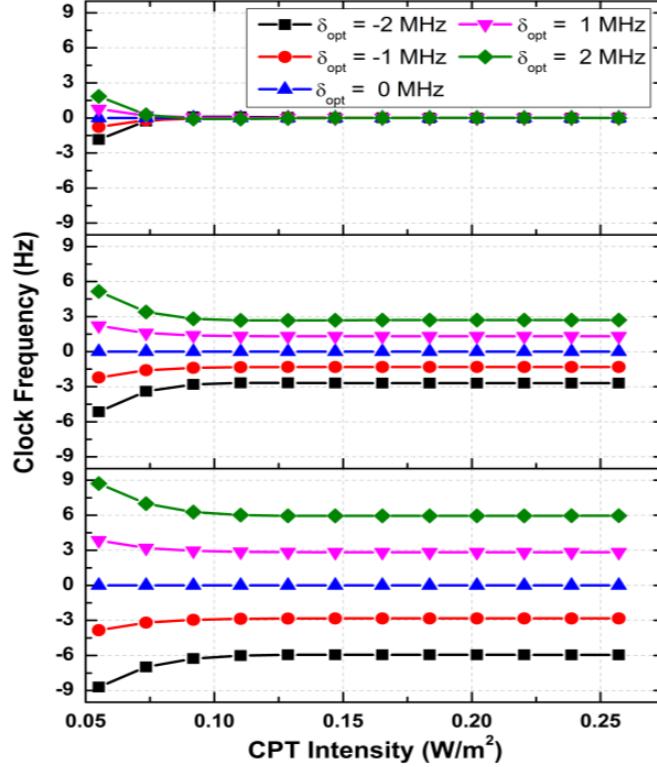
Figure 7.11: Simulation results for the clock frequency as a function of intensity for $P_{\text{carrier}} = 1.00$, 0.85, and 0.70 (top to bottom). For these calculations, the Ramsey period was 4 ms, $\tau_1 = 400$ μs, $|F_0 = 2\rangle$, and $\epsilon = 2.7$.

with the measured shifts shown in Section 7.1.1.

Simulations were also run to verify that the modeling of the incoherent shift captured the dependence on the initial hyperfine state of the atoms as well as the effects of varying the duration of the first Ramsey pulse. The results of these calculations are shown in Fig. 7.12. Plots (a) and (b) demonstrate the expected inversion of the coherent shift between the initial hyperfine states and show no difference between the incoherent shifts, in agreement with the data in Fig. 7.2. Similarly, the strong dependence of the coherent shift on τ_1 is exhibited in plots (c) and (d) in Fig. 7.12, while the incoherent shift is again unaffected. For $\tau_1 = 250$ μs, the coherent shift for $\delta_{opt} = 2$ MHz exceeds 6 Hz, while for $\tau_1 = 800$ μs, the shift is barely visible having been suppressed below 0.25 Hz. This matches the qualitative behavior of the observed shifts shown in Fig. 7.3, where the coherent shift was suppressed by a factor of $\sim 8\times$ by extending the first pulse duration from 250 μs to 800 μs.

The modeled light shifts plotted in Figs. 7.11-7.12 exhibit the qualitative features observed in
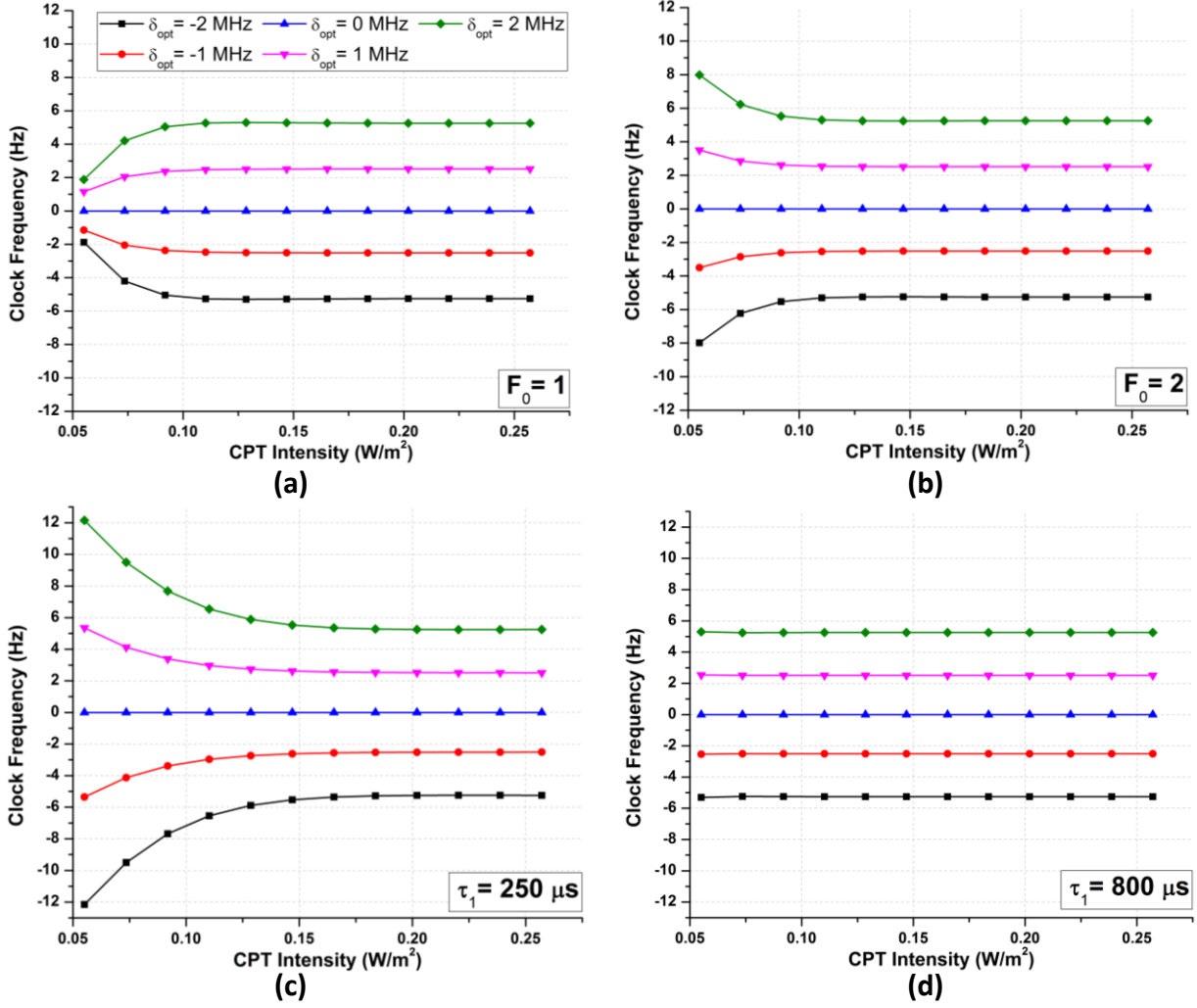
Figure 7.12: Simulation results for the clock frequency as a function of intensity for $|F_0 = 1\rangle$ (a) and $|F_0 = 2\rangle$ (b) for $\tau_1 = 400~\mu s$. Also shown are the simulated shifts for $|F_0 = 2\rangle$ with first Ramsey pulse times of $\tau_1 = 250~\mu s$ (c) and $\tau_1 = 800~\mu s$ (d). For all plots, the Ramsey period was 4 ms, $\epsilon = 2.7$, and $P_{\text{carrier}} = 0.73$ to match the CPT spectrum of the experiment.

the CACPT clock data, accurately reproducing the dependence of the coherent shift on τ_1, I_{CPT}, and F_0 and revealing a constant residual shift at high intensities. As shown in Fig. 7.13, the simulated data roughly agrees with measured light shifts quantitatively with the scaling factor in Eq. 7.30 set to $\epsilon = 2.7$. This scaling factor in the definition of β_{ij} accounts for simplifications in the calculation, including the assumption of equal Rabi frequencies and detunings of the two CPT frequency components and not accounting for the Zeeman substructure. These effects, plus variations in the applied light intensity across the Gaussian profile of the CPT beams, obscured subtleties of the light shift and reduced the calculated magnitude at low intensities. A more
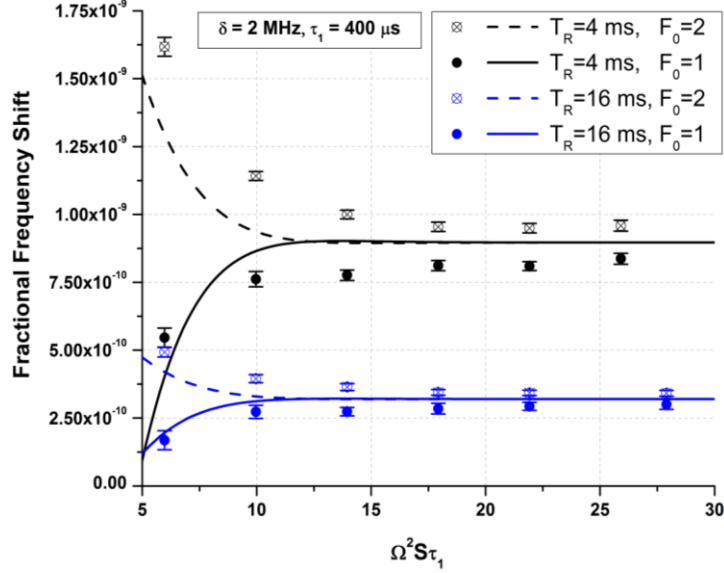
Figure 7.13: Fractional frequency shifts (points) for varied Ramsey period and initial hyperfine state with the corresponding theory curves (solid/dashed lines) calculated from Section 7.3.2. The agreement is much better than in Fig. 7.4 due to the inclusion of the incoherent couplings into the calculation. A Zeeman shift of 0.87 Hz (1.3×10^{-10} fractional) was added to the theory curves to account for the clock bias field. For the theory calculation, $\epsilon = 2.7$.

complete theoretical treatment accounting for these effects would be necessary to carefully compare our observed light shifts to the theory without a scaling factor.

Despite the simplifications included in the model of the incoherent light shift, the qualitative agreement between our theory and data is excellent and provides strong support for our understanding of these shifts in terms of optical pumping. With the constant shift at high interrogation intensities understood, efforts shifted toward developing a technique to eliminate the shift without completely updating the CPT laser system. This is discussed next.

7.3.4 Master/Slave Configuration Exchange

The optical detuning dependence of the incoherent light shift is determined by the level to which atoms are optically pumped after scattering out of the dark state. For the CPT laser configuration with the slave locked to the $|F = 1\rangle \rightarrow |F' = 1\rangle$ transition, atoms preferentially accumulate in and re-enter the dark state from $|F = 2\rangle$. The incoherent shift thus exhibits an optical detuning dependence with the same sign as the coherent shift for atoms initially in $|F_0 = 2\rangle$. This introduces an opportunity to suppress the incoherent light shift as if the laser system could be adjusted such
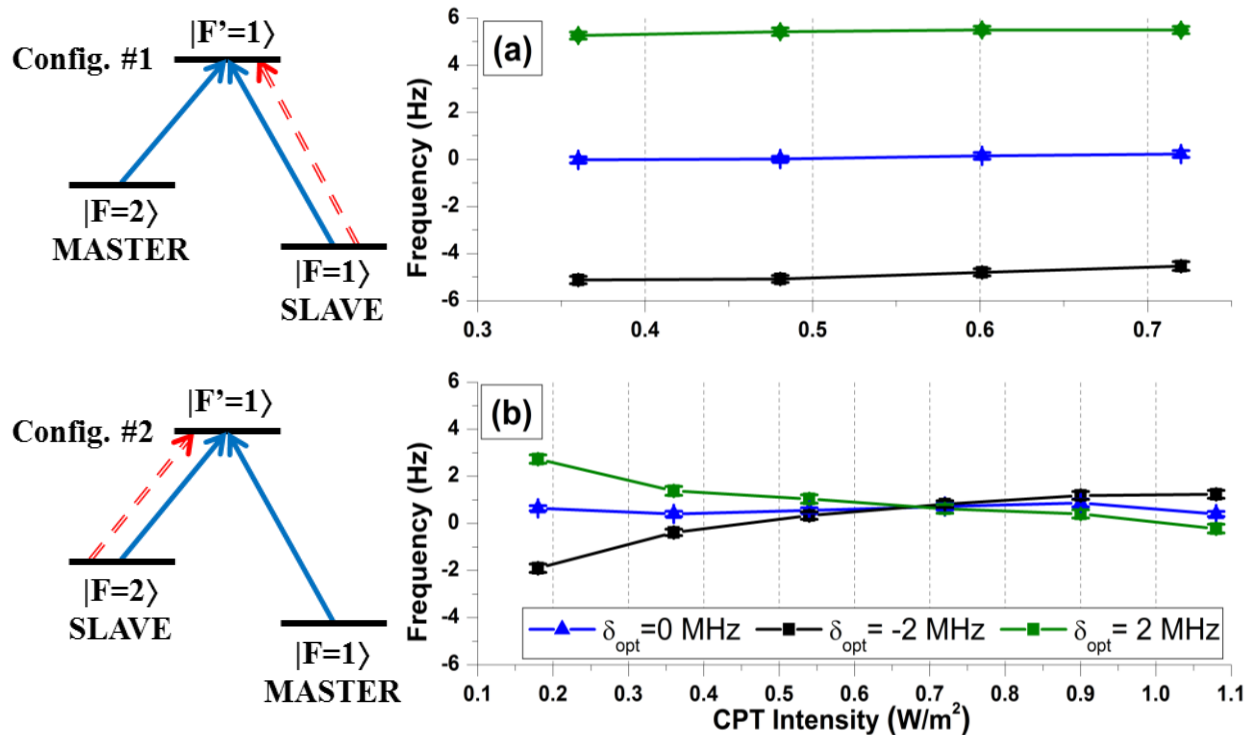
Figure 7.14: LEFT: Two laser configurations enabling the incoherent light (red) to be placed on either $|F = 1, 2\rangle \to |F' = 1\rangle$. RIGHT: Clock frequency data for $T_R = 4$ ms with the CPT laser system in Config. #1 (a) and Config. #2 (b). Locking the slave laser to the $|F = 2\rangle \to |F' = 1\rangle$ line resulted in a $6\times$ suppression of the incoherent shift and introduced a zero-point in the light shift response.

that the incoherent noise caused atoms to accumulate in the $|F = 1\rangle$ level, then for atoms starting in $|F_0 = 2\rangle$, the detuning dependence of the coherent and incoherent light shifts would be opposite. For a positive optical detuning, the incoherent shift would be negative, and the coherent shift would be positive. For a small range of interrogation intensities near the transition between coherent and incoherent shifts, the dependence of the clock frequency on the optical detuning would be very small.

To verify the detuning dependence of the optical pumping effect and test this idea for mitigating the shift, the transitions for the master and slave frequency locks were exchanged such the master laser was locked via saturated absorption spectroscopy to the $|F = 1\rangle \to |F' = 1\rangle$ transition, and the slave laser was offset locked by the PLL to the $|F = 2\rangle \to |F' = 1\rangle$ line. This switch required reconfiguring the optics layout for the CPT lasers such that a fraction of the master output was coupled into the MOT optical fiber to provide repump during the trapping sequence. With this

change, the laser system was placed in Config. #2 in Fig. 7.14. The incoherent light preferentially drove optical pumping to the $|F = 1\rangle$ level which should invert the detuning dependence of the shift at high intensities. This expectation was confirmed by the frequency measurements in Fig. 7.14 (b), where the shift for negative optical detunings was positive at high I_{CPT}.

The magnitude of the observed incoherent shift at high intensities in Config. #2 was significantly suppressed over Config. #1, falling from 2.7 Hz/MHz to 0.4 Hz/MHz for $T_R = 4$ ms. This reduction was caused by the smaller number of Zeeman sublevels in the $|F = 1\rangle$ state. Atoms accumulating in $|F = 2\rangle$ (Config. #1) decay into one of five m_F levels, three of which are not in the double-Λ system and require additional excitation cycles before re-entering the dark state. For Config. #2, atoms accumulate in the three m_F levels of $|F = 1\rangle$, reducing the time required to re-enter the dark state and suppressing the incoherent shift. Measurements of the $|F_0 = 1\rangle$ coherent light shift were consistently smaller than the corresponding shift for the $|F_0 = 2\rangle$ case due to the same effect. This is shown in Fig. 7.15 (a), where the coherent shift has been estimated by performing a linear fit to the data at high intensities and taking the difference between the measured shift and the extrapolated fit at low intensity. The smaller shifts observed for $|F_0 = 1\rangle$ indicated that the number of Zeeman sublevels had a larger impact on the CPT interaction time required to load the dark state than the difference in pumping rates due to unequal Clebsch-Gordan coefficients ($\Omega_1 < \Omega_2$ for equal intensities).

In addition to the general suppression of the incoherent shift shown in Fig. 7.14 (b), the data for Config. #2 also exhibits the expected intersection of the light shifts for opposite optical detunings. This zero-point crossing was caused by the inverted detuning dependence between the coherent shift at low intensities and the incoherent shift at high intensities. The transition occurs near the value of I_{CPT} that maximizes the signal to noise ratio of the Ramsey fringes (Fig. 5.20) and has a light shift response of $\Delta\nu_{LS} = 0.01 \pm 0.05$ Hz/MHz, determined by multiple measurements with $T_R = 4$ ms (Fig. 7.15 (b)). A light shift limited performance bound for our CACPT clock can be calculated by scaling this measured response to the 16 ms Ramsey time the clock typically operates with. Assuming a worst-case long-term laser stability of 10 kHz, operating at this cross-over point would correspond to a light shift limited stability of 4×10^{-15}, well below the requirements for most applications.

Successfully operating the clock at this point of insensitivity to the incoherent shift would require
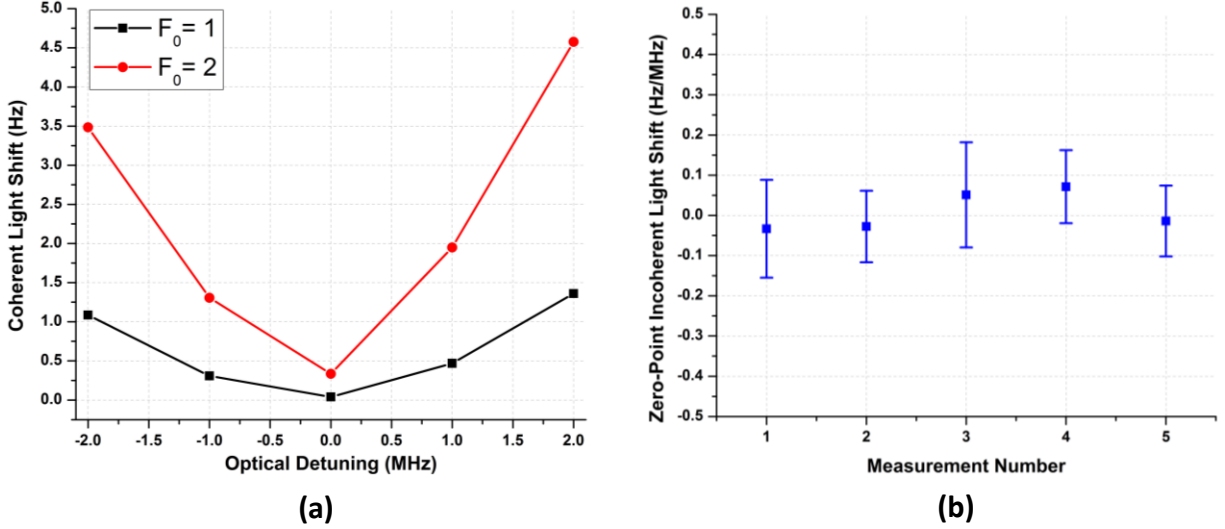
Figure 7.15: (a) Coherent light shift vs. optical detuning for atoms beginning in both the $|F_0 = 1\rangle$ and $|F_0 = 2\rangle$ states. (b) Repeated measurements of the light shift at the zero-point crossing with the laser system in Config. #2. For both figures, the Ramsey time was 4 ms and $\tau_1 = 400~\mu$s.

careful control of the intensity ratio between the two CPT frequency components. Measurements of the shift at the zero point as a function of I_R revealed strong sensitivity to this parameter as a $2\times$ change in the intensity ratio resulted in an order of magnitude increase in the measured incoherent shift for $T_R = 4$ms. While a factor of two fluctuation in the ratio is extreme, this effect did lead to variations in the intensity of the zero-crossing in our measurements. In our system, these fluctuations arose from small polarization variations that changed the power coupled into the CPT fiber by the polarizing beam splitters used to combine the master and slave frequency components. This problem has recently been significantly reduced by an improved optics layout; in future designs, active control of the intensity ratio using feedback could also be implemented.

7.4   Light Shift Summary and Outlook

The AC-stark shift, initially a concern for cold-atom clocks based on CPT, has been shown to be a technical concern that can be mitigated through attention to the PLL spectrum. We have characterized the light shift in a CACPT clock, including contributions from coherent and incoherent couplings. Careful measurements of the coherent shift agree closely with theoretical expectations. We have developed an initial model for the high-I_{CPT} incoherent shift and have demonstrated a configuration in which shifts in the intensity regime relevant for clock operation

164
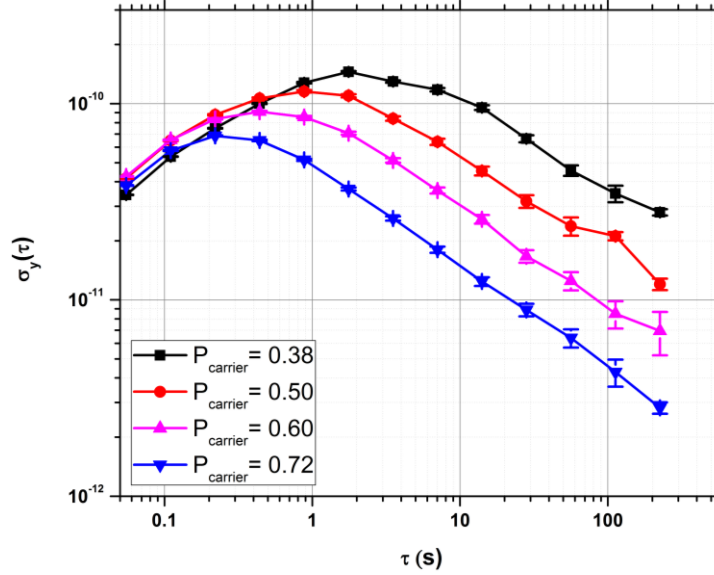
Figure 7.16: Stability of CACPT clock frequency measurements for varied P_{carrier}. The coherent fraction was changed by tuning the settings on the PLL electronics.

are suppressed below the 10^{-14} level [74]. With this degree of sensitivity, light shifts would not be a fundamental limit for a compact CACPT atomic clock.

While the light shift would directly benefit from improved coherence between the master and slave lasers, the advantages do not stop there. As shown in Fig. 7.16, the stability of the CACPT clock continued to improved with higher values of P_{carrier}. If improved lasers with narrow linewidths and reduced phase delays were used in the CPT laser system, or a technique for generating the interrogation field was used that exhibited higher coherence, then the stability of the CACPT clock would immediately improve. This is a strategy being considered for future versions of the clock.

CHAPTER 8

CONCLUSION

The series of experiments discussed in this thesis have demonstrated progress toward a compact atomic clock based on coherent population trapping interrogation of laser-cooled atoms. Using bichromatic stimulated laser forces to slow a thermal atomic beam over 10 mm, we achieved a $12.5\times$ improvement in the number of atoms trapped in a MOT with an equivalent beam diameter of 0.5 mm. This enhancement factor would immediately improve the signal to noise ratio and would directly cause a $\sim 3.4\times$ improvement in the projection-noise limited fundamental performance of an atomic clock. Regarding the CACPT clock, we constructed and characterized a second-generation system that exhibited a short-term fractional frequency stability of 3×10^{-11} at one second of integration time and averaged down for ~ 5000 s, reaching a stability of 7×10^{-13} after one hour. Considerable effort was spent to understand and mitigate the main frequency biases in the CACPT clock. Doppler shifts were suppressed through a counter-propagating interrogation configuration in which atoms were symmetrically excited, reducing the phase shift caused by movement during the Ramsey sequence. With this technique, we canceled the Doppler shift to less than 1×10^{-11} for a worst-case orientation with the CPT beams aligned along the gravitational acceleration vector. When interrogated horizontally, the shift is expected to be below 10^{-13}. Finally, a thorough study of the AC-stark effect in the lin||lin CPT configuration was performed. Observed shifts were modeled and explained in terms of the loading rate of the dark state and population transfer via optical pumping induced by incoherent light. The light shift was canceled to $< 10^{-14}$ for a 16 ms Ramsey time using a laser configuration with an opposite detuning dependence between the coherent and incoherent shifts. This degree of sensitivity is well below the requirements of most target applications.

In the immediate future, efforts are under way to remove the residual drift that limited the long-term stability of the clock at interrogation times of ~ 5000 s. Recently, it was discovered that the anti-reflection coating on the cell in our Phase II CACPT physics package was not performing up to specification, resulting in an intensity imbalance between the two counter-propagating interrogation

beams. As discussed in Chapter 6, this significantly degrades the effectiveness of the symmetric excitation upon which the Doppler mitigation scheme is based. Thus, residual Doppler shifts are likely the limiting factor in the long-term performance of the Phase II system. This is being remedied by changing the optics layout near the physics package such that independent CPT beams can be used, allowing the intensity balance to be carefully tuned. Once this is complete, measurements of the long-term stability will be made to determine whether this corrective measure is sufficient to enable the clock to reach the one-day stability milestones of the IMPACT program.

Beyond this, the future of the clock is yet to be determined. Developing a Phase III device based on a chip-scale physics package is a potential next step. A small system featuring MOTs trapped within pyramidal or conical reflectors is a good candidate, though recent results with tetrahedral MOTs formed from planar triplets of diffraction gratings [121] are extremely promising due to the extra optical access relative to other single beam configurations. Regardless of whether or not a Phase III CACPT clock is developed in the near future, the proof of principle experiments completed in the Atomic Devices and Instrumentation group over the last several years have successfully demonstrated that there is not a physical limitation that would prevent the clock from serving as a frequency standard with 1×10^{-13} long-term stability. With magnetic shielding, balanced counter-propagating CPT interrogation, and careful attention to the CPT optical spectrum, each of the principal frequency biases can be controlled.

However, the component technology required for miniature cold-atom devices is currently a significant obstacle as low power AOMs, compact ion pumps, and robust narrow-line lasers do not exist. While the CACPT clock developed at NIST was a successful demonstration of the technical approach, the equipment required for the experiment occupied half of an optics table and a two-meter tall electronics rack (Figs. 8.1-8.2). While the laboratory system could have been built in a more compact fashion, a field-grade CACPT clock would have a minimum size dictated by the currently available cold-atom enabling technology. Significant innovation in this field is necessary for a commercial version of the CACPT clock to become a reality.

While much of the volume of the laboratory system was occupied by electronics (Fig. 8.1), this is not a major focus of miniaturization efforts. Previous compact clock programs have succeeded in integrating the electronics required for an atomic frequency reference into very small physics packages [31]. Even with the complexity added by the phase lock circuitry and extra laser
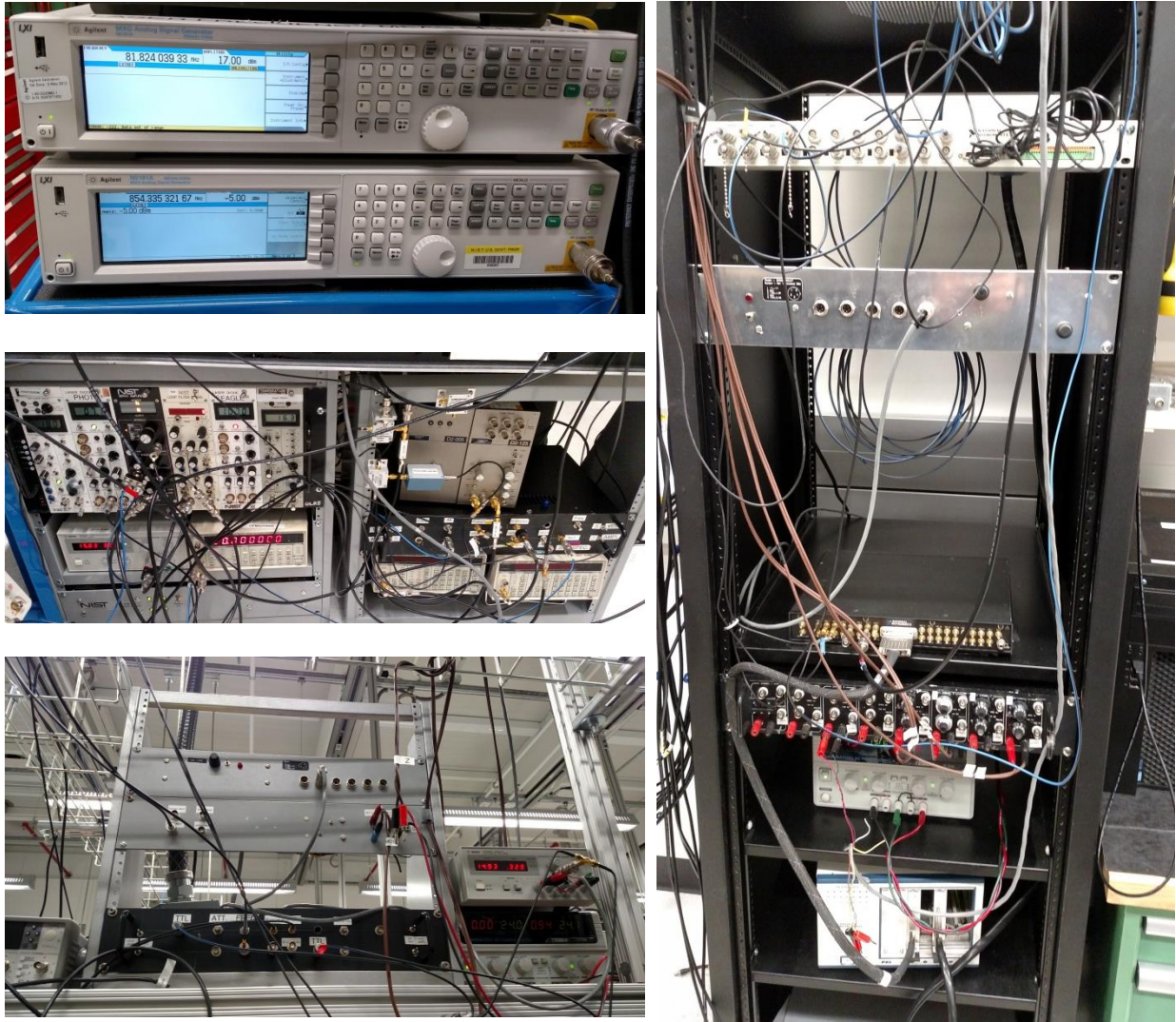
Figure 8.1: Photographs of the electronics racks used in the laboratory CACPT clock. Top Left: frequency synthesizers generating the reference signal for the PLL and the modulation signal for AOM #2 (Fig. 5.5). Middle Left: frequency control electronics and current supplies for the master and slave CPT lasers as well as the RF control box for AOM #1 (Fig. 5.5). Bottom Left: RF control box for the trapping laser and repump. Also shown is the power supply and TTL-controlled switch for the MOT coils. Right: Electronics rack containing the DAQ and DIO cards, breakout boxes for the computer control system, and current supplies for the three sets of bias coils.
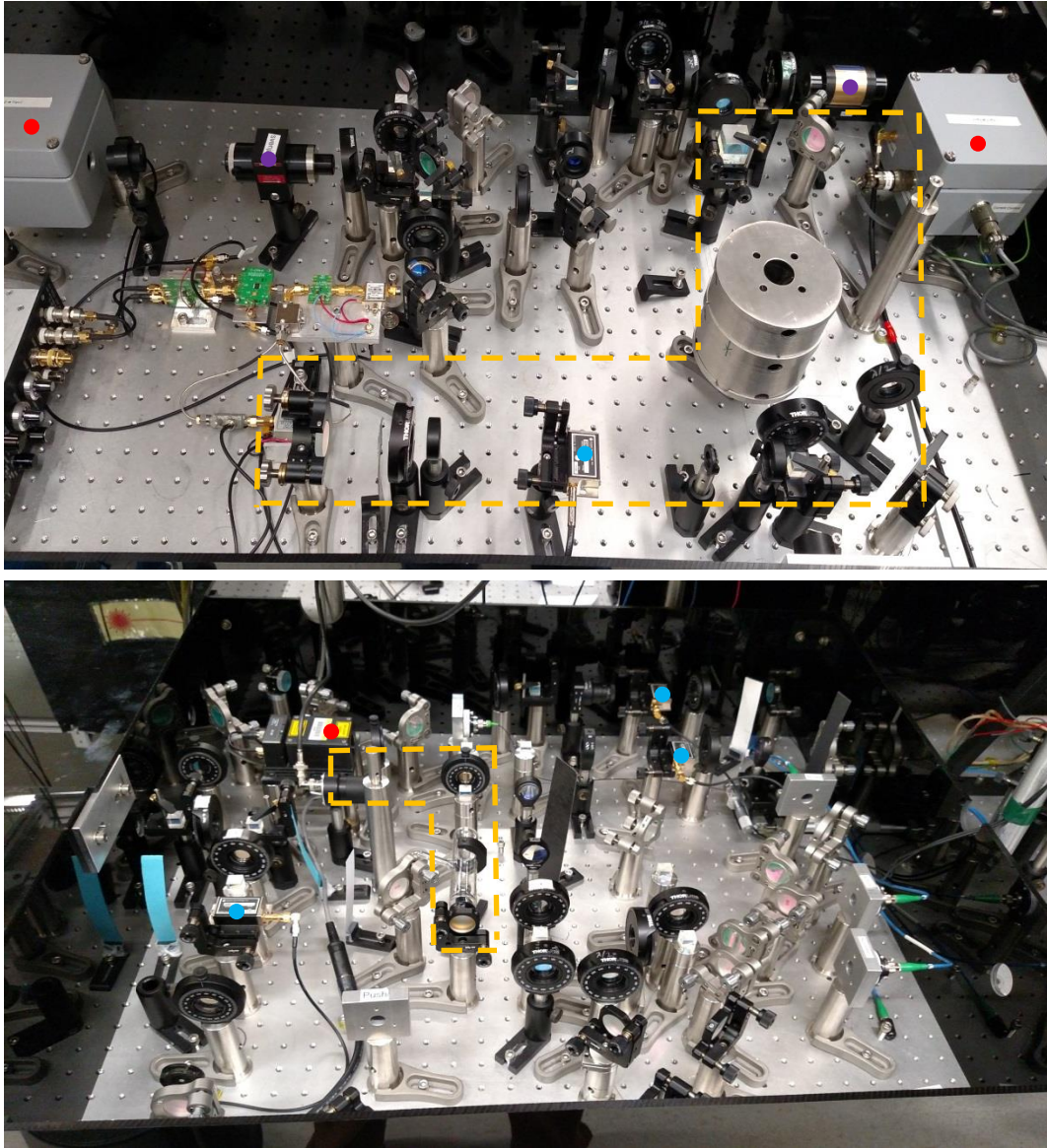
Figure 8.2: Photographs of the optical table. In the top photo, the optics required for phase locking the CPT beams and locking the master laser are shown. The bottom photo shows the optics used to lock the trapping laser as well as the beam path of the overlapped master and slave lasers. Colored dots mark components that require miniaturization, including lasers (red), optical isolators (purple), acousto-optical modulators (blue), and the saturated absorption spectroscopy configuration (gold dashed lines). The screw holes in the table are spaced in a 1" by 1" grid.

frequency control requirements in a CACPT clock, this should be a straight forward electrical engineering task. The phase lock requirements could also be avoided by generating the frequencies required for coherent population trapping by modulating the injection current of a laser diode at a frequency equal to half the hyperfine splitting. The frequency difference between the first order side-bands then matches the resonance condition for the CPT interaction. If this method were adopted, particular care would be required to ensure higher order sidebands are filtered from the optical spectrum. Regardless of the frequency synthesis technique, the more pressing challenge to the viability of an IMPACT-scale CACPT clock resides in the development of high performance, miniaturized versions of the optical components highlighted in Fig. 8.2 and compact ultra-high vacuum technology.

The DBR and DFB lasers used for this thesis research were sufficient for our proof of principle experiments but would not suffice for a field-grade clock. Lasers for a commercial CACPT system would need to be highly compact and robust, with minimal sensitivity to the vibration and thermal effects of a non-laboratory environment. Ideally, these lasers would also possess improved technical capabilities, exhibiting narrower linewidths and larger modulation bandwidths than the current CPT lasers. This would reduce the phase error variance in two ways, suppressing the numerator in Eq. 5.7 with the reduced linewidths and increasing the denominator by achieving a PLL bandwidth limited by the electronics instead of by the phase delay of the laser diodes (Fig. 5.4). If this could be accomplished in an integrated chip-scale package containing both lasers, then the miniaturization requirement would be met while also achieving improved coherence over the Phase II system. Laser technology is already moving in this direction, as demonstrated by the release of Vescent Photonics' Chip External Cavity Laser. These lasers feature short, mm-scale cavities with no moving components and exhibit typical linewidths of 50 kHz [122]. While the vibrational sensitivity and modulation bandwidth would require evaluation, these lasers could be an option for a Phase III system, though further package miniaturization would be required for a commercial device. As this type of technology continues to develop, striving to achieve lasers with 10 kHz linewidths and modulation bandwidths of 10 MHz in packages sufficiently robust to meet MIL-STD requirements is a reasonable goal. Using these numbers in Eq. 5.7 results in a phase error variance of $\sigma_\phi^2 = 0.004$ and a coherent carrier fraction of $P_{carrier} = 0.999$. With this degree of phase lock performance, incoherent light shifts would be significantly reduced even when operating away from the crossing

point in Fig. 7.14 (b). Furthermore, if the trend exhibited in Fig. 7.16 continues, then the improved signal to noise ratio provided by lasers with these specifications could cause a significant improvement in the stability of the CACPT clock.

Future development efforts should also focus on the optical components required for frequency control and feedback suppression in cold-atom laser systems. Low SWAP, high-performance modulators, saturated absorption spectroscopy modules, optical isolators, and shutters are all necessary for a fully integrated commercial CACPT clock. In the optics system shown in Fig. 8.2, the interrogation and MOT laser detunings are controlled with AOMs that require $\sim$1.5 W of RF power to achieve large diffraction efficiencies. While this technique in its current form would not be suitable for a compact clock, perhaps an innovative approach could still employ acoustic waves to achieve the required laser frequencies. Such a modulator would need a volume below 1 cm^3 and should exhibit a large diffraction efficiency at RF frequencies of a few hundred MHz while drawing tens of mW of power. A tapered-fiber acousto-optical frequency shifter is one possible option as it has been demonstrated to operate on just one mW of electrical power [123, 124]. Commercial devices based on this technique could meet the requirements for a highly compact, low SWAP modulator.

Obtaining a stable frequency lock for the master laser is important for maintaining suppression of light shifts in the CACPT clock. As shown in Fig. 8.2, the saturated absorption spectroscopy (SATSPEC) optics for the CPT and trapping lasers require significant table space in the laboratory system. For a commercial CACPT clock, a highly robust, compact SATSPEC module that could be integrated directly into the laser assembly and limit frequency drift to $<$ 1 kHz over long time periods would be necessary. Development efforts are underway with Vescent Photonics producing a high-performance fiber-coupled SATSPEC module for alkali atoms [125]. A significantly miniaturized version of this commercial package, similar to a laboratory system demonstrated at NIST [126], featuring integrated components and high bandwidth electronics would be well suited for an IMPACT-scale clock.

Preventing optical feedback and accurately pulsing lasers can be difficult in a chip-scale sensors. Optical isolators are a standard component in most laser systems, using the Faraday effect to suppress optical feedback by allowing light to pass in only one direction. Developing mm-scale optical isolators requires material science research as the minimum size is dictated by the length of Faraday rotator material required to shift the polarization angle by 45° for a particular wavelength.

However, progress is being made in this field as a $\sim$3 mm long isolator with 38 dB of isolation for 780 nm light is now available [127]. Miniature high speed optical shutters with large extinction ratios and low power requirements are needed for generating the laser pulses used in trapping and Ramsey interrogation sequences. An ideal shutter for a commercial CACPT clock would have a response time of roughly one μs with an extinction ratio of $\sim$80 dB and would not introduce vibrational noise into the system. Current shutter designs feature mechanical, liquid crystal, or frequency shifting techniques that are not well suited for a highly miniaturized system due to slow response times, power requirements, and/or noise issues. This is an active area of research as overcoming these challenges will likely require an innovative approach.

Finally, low SWAP vacuum technology is necessary for a commercial CACPT clock to become a reality. The Phase II physics package featured the smallest ion pump available at the time, a 0.4 L/s system with a volume of $\sim$50 cm^3. Ideal pumping technology for a field-grade clock would maintain a pressure at or below $\sim$10^{-7} torr, preserving reasonable MOT loading times, while occupying volume of a few cm^3 and eliminating the high voltages required for traditional ion pumps. Research focused on new active and passive pumping technologies capable of meeting these difficult requirements is ongoing. The Chip-Scale Vacuum Micro Pumps program [128], launched by DARPA in 2008, spurred new technical approaches for compact pumps that show promise for the future, despite not yet achieving pressures in the UHV regime [129, 130]. Passive vacuum maintenance using non-evaporable getter pumps is another option. These devices maintain low vacuum pressures by absorbing gases in hermetically sealed systems and have been evaluated in compact cold-atom experiments, where UHV pressures were preserved for several hours [131]. However non-evaporable getters do not absorb helium which limits their use over long time periods in chambers that are susceptible to helium permeation. Advances in getter technology or the development of chamber materials that are impermeable to helium could make passive getter-pumping a viable option for maintaining UHV pressure in a chip-scale cold-atom device.

While cold-atom enabling technology is currently a significant obstacle to the development of a field-grade version of the CACPT clock, new government-funded research programs targeting atomic device components could overcome this within the next 5-10 years. If these efforts are successful, then realizing a commercial CACPT clock with the stability of a primary standard would be possible with sufficient engineering to control the frequency biases discussed in this thesis.

The field of atomic devices has significantly expanded in the last two decades and will continue to move forward at a rapidly increasing pace. With industry and government customers realizing the potential of sensors based on atomic physics principles, new atomic clocks, accelerometers, gravimeters, and gyroscopes will likely emerge. It will be very interesting to see what kind of novel applications are found and where this field will be in twenty years.

Bibliography

[1] N. Hinkley, J. A. Sherman, N. B. Phillips, M. Schioppo, N. D. Lemke, K. Beloy, M. Pizzocaro, C. W. Oates, and A. D. Ludlow, Science **341**, 1215 (2013).

[2] B. Bloom, T. Nicholson, J. Williams, S. Campbell, M. Bishof, X. Zhang, S. Bromley, and J. Ye, Nature **506**, 71 (2014).

[3] C. Chou, D. Hume, T. Rosenband, and D. Wineland, Science **329**, 1630 (2010).

[4] T. Rosenband, D. B. Hume, P. O. Schmidt, C. W. Chou, A. Brusch, L. Lorini, W. H. Oskay, R. E. Drullinger, T. M. Fortier, J. E. Stalnaker, S. A. Diddams, W. C. Swann, N. R. Newbury, W. M. Itano, D. J. Wineland, and J. C. Bergquist, Science **319**, 1808 (2008).

[5] P. Gill, Phil. Trans. R. Soc. A **369**, 4109 (2011).

[6] F. Riehle, Physics **5**, 126 (2012).

[7] H. Margolis, Science **341**, 1185 (2013).

[8] Bureau International des Poids et Mesures, ed., *The International System of Units (SI)*, 8th ed. (Organisation Intergouvernementale de la Convention du Metre, 2006).

[9] D. Allan, Proceedings of the IEEE **54**, 221 (1966).

[10] F. Riehle, *Frequency Standards: Basics and Applications* (Wiley-VCH, 2006).

[11] G. Santarelli, P. Laurent, P. Lemonde, A. Clairon, A. G. Mann, S. Chang, A. N. Luiten, and C. Salomon, Phys. Rev. Lett. **82**, 4619 (1999).

[12] G. J. Dick, in *Proceedings of the 19th Annual Precise Time and Time Intervals Meeting* (1987) pp. 133–147.

[13] G. Santarelli, C. Audoin, A. Makdissi, P. Laurent, G. Dick, and C. Clairon, IEEE Transactions on Ultrasonics, Ferroelectrics, and Frequency Control **45**, 887 (1998).

174

[14] W. M. Itano, J. C. Bergquist, J. J. Bollinger, J. M. Gilligan, D. J. Heinzen, F. L. Moore, M. G. Raizen, and D. J. Wineland, Phys. Rev. A **47**, 3554 (1993).

[15] D. J. Wineland, J. J. Bollinger, W. M. Itano, F. L. Moore, and D. J. Heinzen, Phys. Rev. A **46**, R6797 (1992).

[16] C. W. Chou, D. B. Hume, J. C. J. Koelemeij, D. J. Wineland, and T. Rosenband, Phys. Rev. Lett. **104**, 070802 (2010).

[17] C. Vian, P. Rosenbusch, H. Marion, S. Bize, L. Cacciapuoti, S. Zhang, M. Abgrall, D. Chambon, I. Maksimovic, P. Laurent, G. Santarelli, A. Clairon, A. Luiten, M. Tobar, and C. Salomon, IEEE Transactions on Instrumentation and Measurement **54**, 833 (2005).

[18] T. L. Nicholson, M. J. Martin, J. R. Williams, B. J. Bloom, M. Bishof, M. D. Swallows, S. L. Campbell, and J. Ye, Phys. Rev. Lett. **109**, 230801 (2012).

[19] T. P. Heavner, E. A. Donley, F. Levi, G. Costanzo, T. E. Parker, J. H. Shirley, N. Ashby, S. Barlow, and S. R. Jefferts, Metrologia **51**, 174 (2014).

[20] E. Tiesinga, B. J. Verhaar, H. T. C. Stoof, and D. van Bragt, Phys. Rev. A **45**, R2671 (1992).

[21] Microsemi Corporation, *5071A Primary Frequency Standard Data Sheet* (2014).

[22] C. J. Campbell, A. G. Radnaev, A. Kuzmich, V. A. Dzuba, V. V. Flambaum, and A. Derevianko, Phys. Rev. Lett. **108**, 120802 (2012).

[23] P. J. Chantry, B. R. McAvoy, J. M. Zomp, and I. Liberman, in *Proceedings of the 1992 IEEE Frequency Control Symposium* (1992).

[24] P. J. Chantry, I. Liberman, W. R. Verbanets, C. F. Petronio, R. L. Cather, and W. D. Partlow, in *Proceedings of the 1996 IEEE Frequency Control Symposium* (1996) pp. 1002–1010.

[25] H. Fruehauf, in *Proceedings of the 33rd Annual Precise Time and Time Intervals Meeting* (2001) pp. 359–369.

[26] J. Kitching, GPS World **18**, 52 (2007).

[27] J. Murphy and T. Skidmore, in *Proceedings of the 7th International Technical Meeting of the Satellite Division of The Institute of Navigation* (1994) pp. 1329–1336.

[28] 3rd Generation Partnership Project 2 (3GPP2), C.S0010-E Version 1.0 (2011).

[29] M. Lombardi, IEEE Instrumentation and Measurement Magazine **15**, 14 (2012).

[30] IEEE, *IEEE Standard for Synchrophasor Data Transfer for Power Systems* (IEEE C37.118.2-2011, 2011).

[31] R. Lutwak, in *Proceedings of the Joint Meeting of 2009 IEEE Frequency Control Symposium and European Frequency and Time Forum* (2009) pp. 573–577.

[32] S. Knappe, *Comprehensive Microsystems*, edited by Y. Gianchandani, O. Tabata, and H. Zappe, Vol. 3 (Elsevier Ltd., 2008) pp. 571–612.

[33] J. R. Vig, IEEE Transactions on Ultrasonics, Ferroelectrics, and Frequency Control **40**, 522 (1993).

[34] J. Kitching, S. Knappe, and L. Hollberg, Appl. Phys. Lett. **81**, 553 (2002).

[35] L. Hollberg and J. Kitching, "Miniature frequency standard based on all-optical excitation and a micro-machined containment vessel," (2004), U.S. Patent 6,806,784.

[36] N. Cyr, M. Tetu, and M. Breton, IEEE Trans. Instrum. Meas. **42**, 640 (1993).

[37] R. King, D. Wiedenmann, P. Schnitzer, R. Jaeger, R. Michalzik, and K. J. Ebeling, in *Conference Digest-IEEE International Semiconductor Laser Conference* (1998) pp. 103–104.

[38] C. Affolderbach, A. Nagel, S. Knappe, C. Jung, D. Wiedenmann, and R. Wynands, Appl. Phys. B Lasers Opt. **70**, 407 (2000).

[39] S. Knappe, S. Shah, P. D. Schwindt, L. Hollberg, L.-A. Liew, J. Moreland, and J. Kitching, Appl. Phys. Lett. **85**, 1460 (2004).

[40] L.-A. Liew, S. Knappe, J. Moreland, H. Robinson, L. Hollberg, and J. Kitching, Appl. Phys. Lett. **84**, 2694 (2004).

[41] Microsemi Corporation, *Quantum SA.45s Chip Scale Atomic Clock* (2014).

[42] N. Allard and J. Kielkopf, Rev. Mod. Phys. **54**, 1103 (1982).

[43] J. Vanier and C. Mandache, Applied Physics B **87**, 565 (2007).

[44] S. Knappe, V. Gerginov, P. D. Schwindt, H. G. Robinson, L. Hollberg, and J. Kitching, Opt. Lett. **30**, 2351 (2005).

[45] R. Lutwak, in *Proceedings of the 43rd Annual Precise Time and Time Intervals Meeting* (2011) p. 207.

[46] Defense Advanced Research Projects Agency, *Broad Agency Announcment: Integrated Micro Primary Atomic Clock Technology (DARPA-BAA-08-32)* (2008).

[47] V. Shah, M. Mescher, R. Stoner, V. Vuletic, and R. Lutwak, ArXiv e-prints (2011), arXiv:1111.5890 [physics.atom-ph] .

[48] F.-X. Esnault, E. Blanshan, E. N. Ivanov, R. E. Scholten, J. Kitching, and E. A. Donley, Phys. Rev. A **88**, 042120 (2013).

[49] J. Sebby-Strabley, K. Salit, K. Nelson, J. Ridley, and J. Kriz, in *Proceedings of the 43rd Annual Precise Time and Time Interval (PTTI) Meeting* (2011) pp. 231–238.

[50] P. D. D. Schwindt, Y.-Y. Jau, H. Partner, D. K. Serkland, R. Boye, L. Fang, A. Casias, R. P. Manginell, M. Moorman, J. Prestage, and N. Yu, in *SPIE Proceedings*, Vol. 8031 (2011) p. 80310O.

[51] A. A. Savchenkov, A. B. Matsko, W. Liang, V. S. Ilchenko, D. Seidel, and L. Maleki, Opt. Express **20**, 27290 (2012).

[52] E. L. Raab, M. Prentiss, A. Cable, S. Chu, and D. E. Pritchard, Phys. Rev. Lett. **59**, 2631 (1987).

[53] M. H. Anderson, J. R. Ensher, M. R. Matthews, C. E. Wieman, and E. A. Cornell, Science **269**, 198 (1995).

[54] S. Dutta, J. Lorenz, A. Altaf, D. S. Elliott, and Y. P. Chen, Phys. Rev. A **89**, 020702 (2014).

[55] J. Hald, J. L. Sorensen, C. Schori, and E. S. Polzik, Phys. Rev. Lett. **83**, 1319 (1999).

[56] C. J. Foot, *Atomic Physics* (Oxford University Press Inc., New York, 2005).

[57] H. J. Metcalf and P. van der Straten, *Laser Cooling and Trapping* (Springer-Verlag, New York, 1999).

[58] C. Wieman, G. Flowers, and S. Gilbert, American Journal of Physics **63**, 317 (1995).

[59] C. Monroe, W. Swann, H. Robinson, and C. Wieman, Phys. Rev. Lett. **65**, 1571 (1990).

[60] K. E. Gibble, S. Kasapi, and S. Chu, Opt. Lett. **17**, 526 (1992).

[61] K. Lindquist, M. Stephens, and C. Wieman, Phys. Rev. A **46**, 4082 (1992).

[62] S. Pollock, J. P. Cotter, A. Laliotis, F. Ramirez-Martinez, and E. A. Hinds, New Journal of Physics **13**, 043029 (2011).

[63] G. W. Hoth, E. A. Donley, and J. Kitching, Opt. Lett. **38**, 661 (2013).

[64] S. Chu, L. Hollberg, J. E. Bjorkholm, A. Cable, and A. Ashkin, Phys. Rev. Lett. **55**, 48 (1985).

[65] W. D. Phillips and H. Metcalf, Phys. Rev. Lett. **48**, 596 (1982).

[66] W. Ertmer, R. Blatt, J. L. Hall, and M. Zhu, Phys. Rev. Lett. **54**, 996 (1985).

[67] A. Aspect, J. Dalibard, A. Heidmann, C. Salomon, and C. Cohen-Tannoudji, Phys. Rev. Lett. **57**, 1688 (1986).

[68] M. Prentiss and A. Cable, Phys. Rev. Lett. **62**, 1354 (1989).

[69] T. C. Liebisch, E. Blanshan, E. A. Donley, and J. Kitching, Phys. Rev. A **85**, 013407 (2012).

[70] N. F. Ramsey, Phys. Rev. **78**, 695 (1950).

[71] J. P. Barrat and C. Cohen-Tannoudji, J. Phys. Radium **22**, 329 (1961).

[72] C. Cohen-Tannoudji and J. Dupont-Roc, J. Phys. Radium **5**, 968 (1972).

[73] B. S. Mathur, H. Tang, and W. Happer, Phys. Rev. **171**, 11 (1968).

[74] E. Blanshan, E. A. Donley, and J. Kitching, In Preparation (2014).

[75] J. Dalibard and C. Cohen-Tannoudji, J. Opt. Soc. Am. B **6**, 2023 (1989).

[76] S. Chu, J. E. Bjorkholm, A. Ashkin, and A. Cable, Phys. Rev. Lett. **57**, 314 (1986).

[77] A. Ashkin, J. M. Dziedzic, J. E. Bjorkholm, and S. Chu, Opt. Lett. **11**, 288 (1986).

[78] A. P. Kazantzev and I. V. Krasnov, JETP Lett. **46**, 332 (1987).

[79] R. Grimm, Y. B. Ovchinnikov, A. I. Sidorov, and V. S. Letokhov, Phys. Rev. Lett. **65**, 1415 (1990).

[80] J. Söding, R. Grimm, Y. B. Ovchinnikov, P. Bouyer, and C. Salomon, Phys. Rev. Lett. **78**, 1420 (1997).

[81] M. R. Williams, F. Chi, M. T. Cashen, and H. Metcalf, Phys. Rev. A **60**, R1763 (1999).

[82] M. R. Williams, F. Chi, M. T. Cashen, and H. Metcalf, Phys. Rev. A **61**, 023408 (2000).

[83] M. Partlow, X. Miao, J. Bochmann, M. Cashen, and H. Metcalf, Phys. Rev. Lett. **93**, 213004 (2004).

[84] M. A. Chieda and E. E. Eyler, Phys. Rev. A **84**, 063401 (2011).

[85] V. S. Voitsekhovich, M. V. Danileiko, A. M. Negriiko, V. I. Romanenko, and L. P. Yatsenko, JETP Lett. **49** (1989).

[86] L. Allen and J. H. Eberly, *Optical Resonance and Two-Level Atoms* (Dover, Mineola, N.Y., 1987).

[87] M. Williams, *Ph.D. Thesis* (State University of New York at Stony Brook, 1999).

[88] L. Yatsenko and H. Metcalf, Phys. Rev. A **70**, 063402 (2004).

[89] J. Söding, *Ph.D. Thesis* (University of Heidelberg, 1996).

[90] M. Cashen, *Ph.D. Thesis* (State University of New York at Stony Brook, 2002).

[91] R. Grimm, G. Wasik, J. Soding, and Y. B. Ovchinnikov, in *Proceedings of the Fermi School CXXXI* (IOS Press, 1996).

[92] D. A. Steck, "Rubidium 87 d line data," http://steck.us/alkalidata (2008).

[93] M. G. Littman and H. J. Metcalf, Appl. Opt. **17**, 2224 (1978).

[94] K. C. Harvey and C. J. Myatt, Opt. Lett. **16**, 910 (1991).

[95] E. A. Donley, T. P. Heavner, F. Levi, M. O. Tataw, and S. R. Jefferts, Review of Scientific Instruments **76**, 063112 (2005).

[96] C. G. Townsend, N. H. Edwards, C. J. Cooper, K. P. Zetie, C. J. Foot, A. M. Steane, P. Szriftgiser, H. Perrin, and J. Dalibard, Phys. Rev. A **52**, 1423 (1995).

[97] J. A. Richmond, B. P. Cantwell, S. N. Chormaic, D. C. Lau, A. M. Akulshin, and G. I. Opat, Phys. Rev. A **65**, 033422 (2002).

[98] R. Wynands and A. Nagel, Applied Physics B: Lasers and Optics **68**, 1 (1999).

[99] J. Vanier, Applied Physics B **81**, 421 (2005).

[100] J. Kitching and V. Shah, *Advances in Coherent Population Trapping for Atomic Clocks* (Elsevier, 2001) pp. 21–74.

[101] Y.-Y. Jau, E. Miron, A. B. Post, N. N. Kuzma, and W. Happer, Phys. Rev. Lett. **93**, 160802 (2004).

[102] T. Zanon, S. Guerandel, E. de Clercq, D. Holleville, N. Dimarcq, and A. Clairon, Phys. Rev. Lett. **94**, 193002 (2005).

[103] A. V. Taichenachev, V. I. Yudin, V. Velichansky, and S. A. Zibrov, JETP Lett. **82**, 398 (2005).

[104] E. Breschi, G. Kazakov, R. Lammegger, G. Mileti, B. Matisov, and L. Windholz, Phys. Rev. A **79**, 063837 (2009).

[105] S. A. Zibrov, I. Novikova, D. F. Phillips, R. L. Walsworth, A. S. Zibrov, V. L. Velichansky, A. V. Taichenachev, and V. I. Yudin, Phys. Rev. A **81**, 013833 (2010).

[106] S. A. Zibrov, V. Velichansky, A. Zibrov, and A. V. Taichenachev, Phys. Rev. A **82**, 477 (2005).

[107] M. Ohtsu, *Highly Coherent Semiconductor Lasers* (Artech House, 1992).

[108] M. Zhu and J. L. Hall, J. Opt. Soc. Am. B **10**, 802 (1993).

[109] R. H. Dicke, Phys. Rev. **89**, 472 (1953).

[110] C. Affolderbach, S. Knappe, R. Wynands, A. V. Taichenachev, and V. I. Yudin, Phys. Rev. A **65**, 043810 (2002).

[111] S. V. Kargapoltsev, J. Kitching, L. Hollber, A. V. Taichenachev, V. L. Velichansky, , and V. I. Yudin, Laser Phys. Lett. **1**, 495 (2004).

[112] G. Orriols, Il Nuovo Cimento B Series 11 **53**, 1 (1979).

[113] F. Levi, A. Godone, and J. Vanier, IEEE Transactions on Ultrasonics, Ferroelectrics, and Frequency Control **47**, 466 (2000).

[114] S. Knappe, R. Wynands, J. Kitching, H. G. Robinson, and L. Hollberg, J. Opt. Soc. Am. B **18**, 1545 (2001).

[115] D. Miletic, C. Affolderbach, M. Hasegawa, R. Boudot, C. Gorecki, and G. Mileti, Applied Physics B **109**, 89 (2012).

[116] V. Gerginov, S. Knappe, V. Shah, P. D. D. Schwindt, L. Hollberg, and J. Kitching, J. Opt. Soc. Am. B **23**, 593 (2006).

[117] P. R. Hemmer, M. S. Shahriar, V. D. Natoli, and S. Ezekiel, Journal of the Optical Society of America B **6**, 1519 (1989).

[118] T. Zanon-Willette, E. de Clercq, and E. Arimondo, Phys. Rev. A **84**, 062502 (2011).

[119] C. Cohen-Tannoudji, J. Dupont-Roc, and G. Grynberg, *Atom-Photon Interactions: Basic Processes and Applications* (Wiley VCH, 1998).

[120] M. Fleischhauer, A. Imamoglu, and J. P. Marangos, Rev. Mod. Phys. **77**, 633 (2005).

[121] M. Vangeleyn, P. F. Griffin, E. Riis, and A. S. Arnold, Opt. Lett. **35**, 3453 (2010).

[122] Vescent Photonics, "Chip External Cavity Laser (CECL): DFB/DBR Stability with ECDL Flexibility," www.vescent.com/technology/short-cavity-lasers (2014).

[123] T. A. Birks, S. G. Farwell, P. S. J. Russell, and C. N. Pannell, Opt. Lett. **19**, 1964 (1994).

[124] T. Birks, P. Russell, and D. Culverhouse, Lightwave Technology, Journal of **14**, 2519 (1996).

[125] Vescent Photonics, "D2-210 Spectroscopy Module," http://www.vescent.com/products/electro-optics/d2-210-spectroscopy-module (2014).

[126] S. A. Knappe, H. G. Robinson, and L. Hollberg, Opt. Express **15**, 6293 (2007).

[127] Deltronic Crystal Industries, "Miniature Optical Isolators at 780nm and 800nm," http://deltroniccrystalindustries.com/ISOWAVEProducts/miniatureopticalisolators (2014).

[128] Defense Advanced Research Projects Agency, *Broad Agency Announcment: Chip-Scale Vacuum Micro Pumps (DARPA-BAA-08-75)* (2008).

[129] T. Grzebyk and A. Gorecka-Drzazga, Journal of Micromechanics and Microengineering **23**, 015007 (2013).

[130] H. Zhou, H. Q. Li, V. Sharma, and M. A. Schmidt, in *Proceedings of the IEEE 24th Invitational Conference on Micro Electrical Management Systems (MEMS)* (2011) pp. 1095–1098.

[131] D. R. Scherer, D. B. Fenner, and J. M. Hensley, ArXiv e-prints (2012), arXiv:1203.1202 [physics.atom-ph] .

[132] K. I. Lee, J. A. Kim, H. R. Noh, and W. Jhe, Opt. Lett. **21**, 1177 (1996).

[133] S. Pollock, J. P. Cotter, A. Laliotis, and E. A. Hinds, Opt. Express **17**, 14109 (2009).

[134] G. N. Lewis, Z. Moktadir, C. Gollasch, M. Kraft, S. Pollock, F. Ramirez-Martinez, J. P. Ashmore, A. Laliotis, M. Trupke, and E. A. Hinds, Journal of Microelectromechanical Systems **18**, 347 (2009).

[135] M. Trupke, F. Ramirez-Martinez, E. A. Curtis, J. P. Ashmore, S. Eriksson, E. A. Hinds, Z. Moktadir, C. Gollasch, M. Kraft, G. Vijaya Prakash, and J. J. Baumberg, Applied Physics Letters **88**, 071116 (2006).

[136] M. Vangeleyn, P. F. Griffin, E. Riis, and A. S. Arnold, Opt. Express **17**, 13601 (2009).

APPENDIX A

PYRAMIDAL MOT TEST APPARATUS

In between transitioning from the bichromatic slowing experiments to the Phase II CACPT clock, I spent roughly 7 months working on an experiment that sought to demonstrate a micro-fabricated pyramidal MOT. Pyramidal MOTs [62, 132–136] are formed by directing a single, circularly polarized laser beam at a pyramidal retro-reflector filled with alkali atom vapor. The incident light and reflections within the pyramid form counter-propagating trapping beams along three orthogonal axes with the correct polarizations such that upon placing anti-Helmholtz coils around the pyramid, a MOT is able to form. This technique is particularly attractive for compact cold-atom devices as it provides a means of generating an atom sample using a single laser beam and a micro-fabricated reflector.

Previous micro-fabricated pyramidal traps [62, 133] used an etching procedure that resulted in 54.7° sidewalls in silicon, producing traps that had 70.5° angles between opposite reflecting surfaces. The reflections inside this pyramid caused the optical force within the trap to be unbalanced along the axis of the incident laser beam. It also introduced beam paths with three reflections within the pyramid that distorted the polarization of the trapping light. These effects combined to reduce the efficiency of the pyramidal trap and suppressed the atom number.

The goal of our project was to use a technique developed by Dr. Max Perez, a MEMS scientist in our group, to trap atoms in balanced, 90° pyramids with 45° sidewalls etched from silicon wafers. I was responsible for designing the test apparatus and searching for a MOT. A CAD schematic for the test apparatus is shown in Fig. A.1. The vacuum chamber was based off of a high quality optical cell with built-in Rb dispensers that was mounted on a 2.75" flange (manufactured by Technical Glass). The cell was attached to the bottom of a cross flange that had horizontal arms leading to an ion pump and an all-metal valve used to attach a turbo-pump. At the top of the cross flange was a blank mounting flange from Kimball physics with internal rings to attach Groove Grabbers. These are mounting structures that allow you to fix components in place within the vacuum system. In our case, they held in place four long aluminum rods that ran through the UHV system into

the optical cell. Mounted within the cell were aluminum structures designed to hold two pyramid samples as well as a reflecting corner cube to provide optical access to the upper pyramid. These internal components are shown in the bottom row of Fig. A.1. This system was designed such that the pyramid samples could be easily exchanged by detaching the upper mounting blank to remove the internal structure.

Despite significant effort with multiple detection schemes (CCD camera, fluorescence, lock-in detection), we were never able to observe a MOT in the micro-fabricated pyramidal reflectors. It is unclear what the exact reason for the failure was, but the most likely candidates include poor placement of the magnetic field due to the large coils used in the apparatus or poor reflected beam quality due to pyramid wall surface roughness and curvature. After searching in vain, the project was canceled, and I moved on to the clock project. Despite never observing a MOT, this was a useful experiment as I developed additional skills with CAD design and had the opportunity to machine small components using both the lathe and mill. Pyramidal MOTs remain a potential candidate for a compact, cold-atom source in a future atomic sensor.
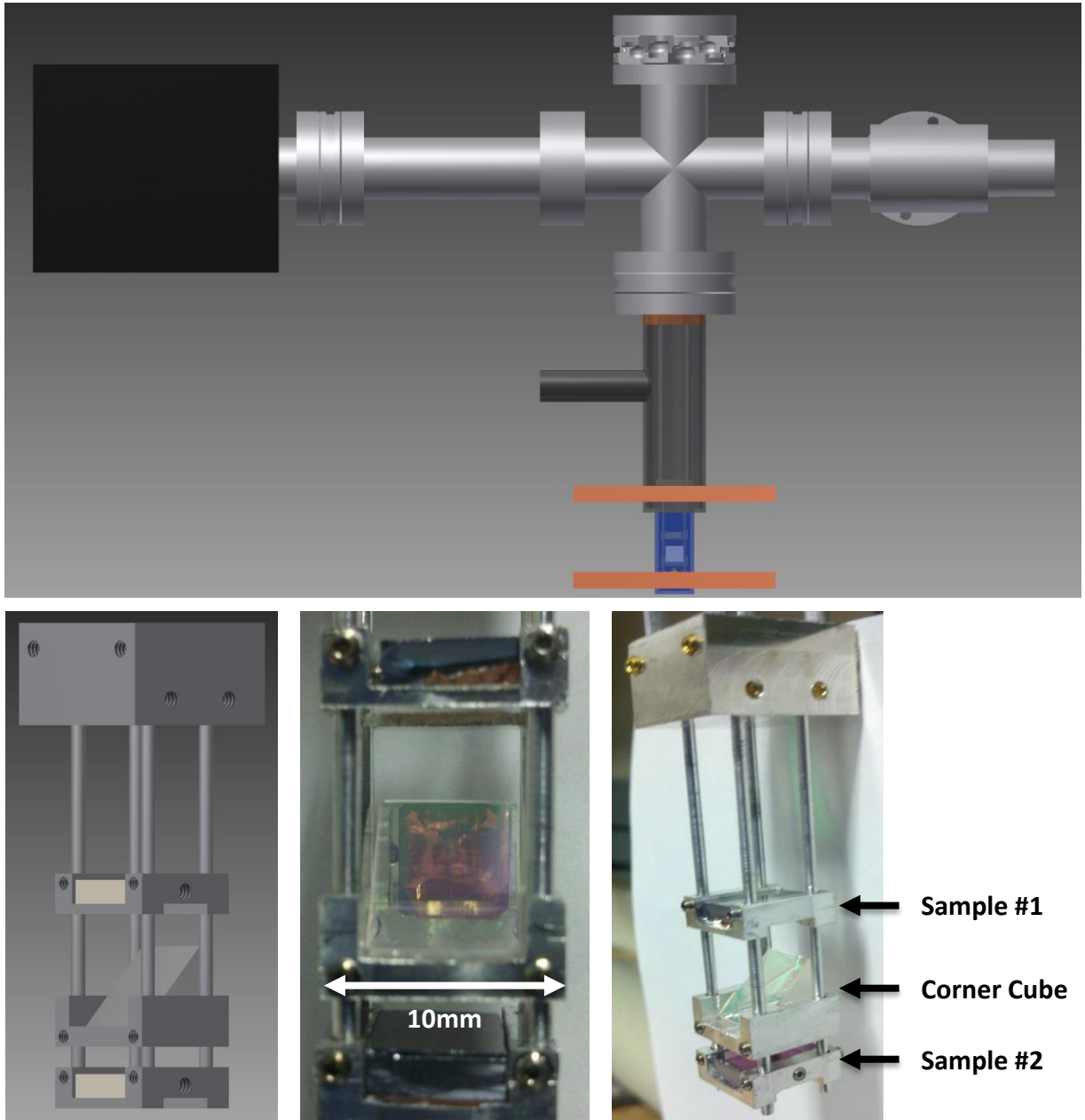
Figure A.1: TOP: Inventor rendering of the pyramidal MOT test apparatus. The ion pump is on the left, connected to a four-way cross flange with the optical cell mounted below. The square magnetic field coils are shown surrounding the bottom of the cell. BOTTOM: Inventor rendering (left) and photographs of the internal mounting structure for the two pyramid samples and corner cube. The image on the right is a close up of the structure showing the reflection off the cube that provided access to Sample #1.